To cite this document: ILYAS Muhammad. Génie mécanique. *Damage modeling of carbon epoxy laminated composites submitted to impact loading.* Toulouse : Institut Supérieur de l'Aéronautique et de l'Espace, 20 July 2010, 241p.

THÈSE

En vue de l'obtention du

DOCTORAT DE L'UNIVERSITÉ DE TOULOUSE

Délivré par *Institut Supérieur de l'Aéronautique et de l'Espace*
Discipline ou spécialité : *Génie Mécanique*

Présentée et soutenue par *Muhammad ILYAS*
Le *20 July 2010*

Damage modeling of carbon epoxy laminated composites submitted to impact loading

Modélisation de l'endommagement de composites stratifiés carbone époxy sous impact

---

JURY

Mr. Christian HOCHARD	*Professeur des Universités*	*Président*
Mr. Daniel COUTELLIER	*Professeur des Universités*	*Rapporteur*
Mr. Laurent GUILLAUMAT	*Professeur des Universités*	*Rapporteur*
Mr. Michel SALAÜN	*Professeur ERE*	*Directeur de Thèse*
Mr. Frédéric LACHAUD	*Professeur Associé*	*Co-directeur de Thèse*
Mme. Christine ESPINOSA	*Professeur Associé*	*Co-directrice de Thèse*
Mr. Laurent CHAMBON	*Ingénieur de recherche EADS-IW*	*Examinateur*
Mr. Jérôme LIMIDO	*Ingénieur de recherche Impetus Afea*	*Examinateur*

Ecole doctorale : *Mécanique, Energétique, Génie Civile, & Procédé*
Unité de recherche : *Institut Clément Ader*
Directeur(s) de Thèse : *Michel SALAUN, Frédéric LACHAUD, Christine ESPINOSA*
Rapporteurs : *Daniel COUTELLIER, Laurent GUILLAUMAT*

Acknowledgments

This work would not have been possible without a team which has offered me the possibility to acquire a variety of competencies related to composites (fabrication, test techniques, numerical simulation techniques) – The team at Department of Mechanics of Structures and Materials at Institut Supérieur de l'Aéronautique et de l'Espace (ISAE) Toulouse under direction of Mr. Jacques Huet, I thank you all.

I would like to thank profoundly my advisors Pr. Michel Salaün, Assoc. Pr. Christine Espinosa and Assoc. Pr. Frédéric Lachaud as they always believed in my abilities and provided whatever advice and resources necessary for me to accomplish my goals. They spent countless hours meeting with me to discuss various aspects of my research. This work would not have been possible without their interesting ideas, guidance and help.

It is an honor for me to have Pr. Christian Hochard as president of jury. I owe my deepest gratitude to Pr. Daniel Coutellier and Pr. Laurent Guillaumat for honoring me by evaluating this work and Dr. Laurent Chambon for accepting to be a jury member.

I have to thank Dr. Jérôme Limido and Dr. Jean-Luc Lacome, of Impetus Afea France, for their advices in SPH usage and related development.

A special thanks goes to research engineers Engr. Michel Labarrère and Dr. Samuel Rivallant for teaching me from scratch about impact and Hopkinson's bar test techniques.

A large number of experiments conducted during this study would not have been possible without help from Mr. Pierre Erizé, Mr. Daniel Boîtel and Mr. Thierry Martin as they helped me learn the use of material fabrication and specimen preparation equipments, and non destructive testing apparatus.

The workshop team led by Engr. Daniel Gagneux and comprising of Mr. Phillipe Corria, Mr. Serge Dayde, and Mr. Bernard Riviere are thanked for various fixtures manufactured during test equipment modifications.

Big thanks to Engr. Joël Xuereb, Mr. Marc Chartrou for their invaluable assistance in Hopkinson's bar tests.

The library staff especially Mme. Sylvie Mersadier and Mme. Naçira El-Yacoubi are thanked for arranging documents for this study. Mr. Claude Palaysi and Mr. Jacques Villemur have to be thanked for assuring the prompt software installations of software required during this study.

I would like to thank all the students and friends who chose to do their internships related to this study and generated some valuable numerical as well as experimental results. Especially, Nasir Shahzad, Florian Briche, Jatinkumar Patel, Harsh Shah, Jalpenkumar Patel, Maria Royon and Miriam Ruiz are thanked for their important contributions.

All of my friends in Toulouse, back in Pakistan and abroad have to be thanked for inspiring and motivating discussions.

I would like to show my gratitude to my faimly friends Shaheen Raja and Nazish Saher for their contributions to schematic representations shown in this study.

Last but not least, this important milestone of my life would not have been possible without the precious support from my grand parents, my mother and father, my wife Sadaf, my daughter Dania, my son Rabee, my brothers and sisters. Without their sacrifices the ups and downs of life would have been more difficult.

Muhammad Ilyas

Contents

List of Figures **vii**

List of Tables **xi**

Glossary **xv**

General Introduction **1**

1 Introduction **5**

- 1.1 Industrial Context 6
  - 1.1.1 Aircraft Type Certification 7
  - 1.1.2 Composite Requirements 8
    - 1.1.2.1 Composite Airworthiness Requirements 9
    - 1.1.2.2 Composite Materials - The Current Situation 9
    - 1.1.2.3 Durability and Damage Tolerance 10
  - 1.1.3 Impact Key Problems/Points 11
    - 1.1.3.1 Non-penetrating Impact 11
    - 1.1.3.2 Penetrating Impact 12
  - 1.1.4 Synthesis 12
- 1.2 Scientific Context 13
  - 1.2.1 Constitutive Modeling 14
    - 1.2.1.1 Explicit Models 14
    - 1.2.1.2 Implicit Models 15
    - 1.2.1.3 Hybrid Models 15
    - 1.2.1.4 Summary 15
  - 1.2.2 Composite Failure 15
    - 1.2.2.1 Failure Mechanisms 16
    - 1.2.2.2 Failure Criteria 17
  - 1.2.3 Impact Induced Rate Effects on Failure Mechanisms 20
  - 1.2.4 Damage Modeling 23
    - 1.2.4.1 Continuum Damage Mechanics 23

1.2.4.2 Interface Elements . . . 24
1.2.4.3 Meshless Methods . . . 24
1.3 Objectives . . . 25

2 Constitutive Law: Interface **27**
2.1 State of the Art . . . 27
2.1.1 Experimental Characterization . . . 28
2.1.1.1 Strain Energy Release Rate . . . 28
2.1.1.2 Quasi-Static Tests . . . 30
2.1.1.3 Dynamic Tests . . . 34
2.1.2 Liner Elastic Fracture Mechanics Based Numerical Modeling . . . 37
2.1.2.1 Different Methods for in Plane Nodal Opening . . . 37
2.1.2.2 Cohesive Fracture Mechanics . . . 38
2.1.2.3 Strain Rate Effects . . . 40
2.1.3 Emerging Discrete Methods/Use of SPH . . . 41
2.1.4 Concluding Remarks . . . 41
2.2 Developed Cohesive Interface Model . . . 42
2.2.1 2D Plane Strain Study . . . 44
2.3 Numerical Parameter Identification . . . 47
2.3.1 Numerical Parameter Sensitivity Study . . . 47
2.3.2 Identification of Mode I Parameters . . . 51
2.3.3 Identification of Mode II Parameters . . . 52
2.3.4 Validation by Mixed-Mode I+II Correlation . . . 54
2.4 Conclusions . . . 57

3 Constitutive Law: Ply **61**
3.1 Literature Survey . . . 62
3.1.1 Experimental Characterization of Rate Sensitive Behavior . . . 62
3.1.1.1 Split Hopkinson's Pressure Bar apparatus . . . 63
3.1.1.2 Dynamic Compression . . . 65
3.1.1.3 Dynamic Tension . . . 66
3.1.1.4 Dynamic Shear Loading . . . 66
3.1.2 Continuum Damage Models . . . 66
3.1.2.1 Damage Modeling through Energy Computations . . . 69
3.1.2.2 Failure Criteria Based Damage Model . . . 71
3.1.3 Numerical Models . . . 74
3.1.4 Concluding Remarks . . . 75
3.2 Physical Properties Characterization . . . 75
3.2.1 Quasi-static Tension Tests . . . 75
3.2.2 Dynamic Compression Tests . . . 78
3.2.2.1 Compression $[0]_{16}$ . . . 82
3.2.2.2 Compression $[90]_{16}$ . . . 83
3.2.2.3 Compression $[\pm 45]_{3s}$ . . . 83
3.2.2.4 Compression $[\pm\theta]_{3s}$ . . . 85
3.2.2.5 Summary of Dynamic Compression Results . . . 87
3.3 Constitutive Law . . . 89

3.3.1 Proposed/Modified MLT Model 90
3.3.2 Modified and Reference MLT Models: 1–D Comparison 93
3.3.3 Quasi-static Tension Simulation 95
3.3.4 1-D Parametric Study of SHPB 97
3.3.4.1 Mesh and Boundary Conditions 97
3.3.4.2 Influence of Impactor Length (L_{imp}) 99
3.3.4.3 Influence of Impactor Velocity (v_{imp}) 99
3.3.4.4 Influence of Specimen Length (L_s) 100
3.3.4.5 Strain Rate Effects 100
3.3.5 Dynamic Compression Simulation 101
3.3.5.1 Compression $[\pm 45]_{3s}$ 102
3.3.5.2 Compression $[\pm\theta]_{3s}$ 102
3.4 Conclusions 104

4 Impact Tests on Coupon Specimen 105
4.1 Specimen Preparation 106
4.2 Drop Tower Tests (Large Mass Low Velocity) 107
4.2.1 Global Force/Displacement Transitory Behavior 108
4.2.1.1 Influence of Impact Energy 109
4.2.1.2 Influence of lay–up Sequence 109
4.2.1.3 Conclusions 111
4.2.2 Post–impact Defects Examination 111
4.2.2.1 Profile of Impacted Zone 112
4.2.2.2 C–Scan Examination 114
4.2.2.3 X–ray Examination 114
4.2.2.4 Microscopic Examination 116
4.3 Canon Tests (Small Mass Medium Velocity) 117
4.3.1 Transitory Strain Gage Signals 119
4.3.2 Post–impact Defects Examination 121
4.3.2.1 Profile of Impacted Zone 121
4.3.2.2 C–Scan Examinations 123
4.3.2.3 X–ray Examinations 123
4.3.2.4 Microscopic Examination 124
4.4 Conclusions 126

5 Impact Modeling of Coupon Specimen 129
5.1 Impact Modeling: Cohesive Damage Law 129
5.1.1 Finite Element Model 130
5.1.2 Comparison: Test and Simulation 131
5.1.2.1 Specimen Global Behavior 131
5.1.2.2 Comparison of Delamination Area 132
5.1.3 Conclusions 134
5.2 Impact Modeling: Continuum Damage Law 134
5.2.1 Finite Element Models 134
5.2.2 Comparison: Test and Simulation 136
5.2.2.1 Specimen Global Behavior 136

5.2.2.2 Strain Rate Dependent Local Damage 138
5.2.2.3 Impacted Face Dent Depth Prediction 143
5.3 Conclusions 145
5.4 Low Velocity Impact Modeling using SPH 146
5.4.1 Feasibility Study 146
5.4.1.1 Anisotropy and SPH 147
5.4.1.2 Bending of a Laminate: Comparison SPH and FE 147
5.4.2 Application to impact 148
5.4.2.1 FE and Coupled FE–SPH Models 148
5.4.2.2 Comparison Tests and Simulations 149
5.4.3 Conclusions 152

Conclusions and Perspectives **158**

Bibliography **159**

Appendices **171**

A Material Fabrication, Mechanical Tests. **173**
A.1 Laminate Fabrication 173
A.2 Mechanical Characterization 180

B $\mathcal{G}_{Ic}$ and $\mathcal{G}_{IIc}$ for T800S/M21 **183**
B.1 DCB tests 183
B.2 ELS tests 184

C Impact Tests **185**

D Mathematical Formulation of SPH method **189**

Résumé en Français **195**

List of Figures

1 A concept airship, 85 years into future. 1
2 Fan blade out accident National Airlines DC-10 flight (November 3, 1973). 2
3 Organization of the thesis (in light of building block approach). 3

1.1 Increasing usage of composites in commercial planes by Airbus. 5
1.2 Pyramid tests or building block approach [135]. 8
1.3 Accidental tool drop and a typical BVID curve [135]. 12
1.4 Fan blade out accident and uncontained assessment by simulation. 13
1.5 Description of unidirectional ply axes 17
1.6 Low velocity impact induced damages, Zagainov and Lozino-Lozinski [162]. 21
1.7 Different types of impact damage, Mitrevski et al. [115]. 22
1.8 Initiation and propagation of low velocity impact induced damage. 22
1.9 Effect of velocity on laminate response, López-Puente et al. [105]. 23

2.1 Resin rich layer in a T800S/M21 laminate. 27
2.2 The three modes of delamination (a) Mode I; (b) Mode II and (c) Mode III. 28
2.3 Double cantilever beam (DCB) specimen for Mode I testing [152]. 30
2.4 End Notch Flexure (ENF) specimen for Mode II testing [152]. 31
2.5 End Loaded Split (ELS) specimen for Mode II testing [152]. 32
2.6 Mixed-Mode Bending (MMB) apparatus for Mode I+II testing [152]. . . . 33
2.7 Two variants of wedge insert fracture (WIF) specimen. 35
2.8 FEA simulation of a Brazilian disk specimen [52]. 35
2.9 CNF specimen for mode II testing [110]. 35
2.10 ONF specimen for mixed-mode testing [90]. 36
2.11 Uni-axially loaded structure, note re-meshed crack fracture, [54]. 37
2.12 Traction-relative displacement law. 38
2.13 Mixed-mode traction separation law. 43
2.14 Schematic representation of MATLAB® finite element model. 44
2.15 Influence of critical strain energy release rate, $\mathcal{G}_{Ic} \in \{200, 400, 800\}$ J/m^2. . 45
2.16 (a) Normal stress as a function of opening displacement and (b) damage parameter as a function of opening displacement for $\mathcal{G}_{Ic} = 800$ J/m^2. . . . 45

2.17 Influence of critical time τ for $\kappa = 1$. 46
2.18 A typical finite element mesh for DCB specimen. 47
2.19 Numerical model, load and boundary conditions (DCB). 47
2.20 Effect of damping and type of loading on numerical model. 48
2.21 DCB specimen numerical failure due to hourglass mode. 49
2.22 Schematic representation of hourglass modes. 49
2.23 Retained numerical model, load and boundary conditions for DCB. 50
2.24 Comparison of different hourglass controls with Pinho et al. [126]. 50
2.25 Influence of length of cohesive finite elements. 51
2.26 DCB specimen loaded in a servo-hydraulic machine. 52
2.27 DCB: Force displacement curves numerical and experimental results, [78]. . 52
2.28 ELS specimen loaded by screw driven machine. 53
2.29 Numerical model, load and boundary conditions (ELS). 53
2.30 ELS: Force displacement curves, numerical and experimental results, [81]. . 54
2.31 Mixed mode bending (MMB) test setup, Prombut [128]. 55
2.32 MMB: Numerical model, load and boundary conditions. 55
2.33 MMB: Force displacement curves, numerical and experimental results, [81]. 56
2.34 Modified Hopkinson's bar setup of 3-point bending test on ENF specimen. 57
2.35 A typical signal of 3-point bending test with an SHPB apparatus. 58
2.36 SHPB 3-point bending (a) ENF specimen and (b) ONF specimen. 58

3.1 Regimes of $\dot{\epsilon}$ and associated experimental setups [117]. 62
3.2 Schematic representation of an SHPB. 64
3.3 Schematic representation of damage by cracking. 67
3.4 Non-smooth loading surfaces in strain space [111]. 72
3.5 Displacement controlled quasi-static test. 76
3.6 Typical response of T700S/M21 [65] and T800S/M21 $[\pm 45]_{2s}$ laminates. . . 76
3.7 T700S/M21 and T800S/M21 $[\pm 45]_{2s}$ laminates cross-section along 45° plies. 77
3.8 Schematic of a loaded $\pm\theta$ laminate in global reference frame. 78
3.9 Hopkinson's bars setup at ISAE. 78
3.10 Impactor speed measuring system and a typical signal. 79
3.11 Compression of $[\pm 60]_{3s}$ laminate at $\dot{\epsilon} = 380 s^{-1}$. 79
3.12 Schematic representation of incident bar and specimen interface. 80
3.13 Equilibrium verification of input and output forces for a $[\pm 60]_{3s}$. 81
3.14 Asymmetric failure (on left) and symmetric failure (on right). 81
3.15 Schematic representation of incident/transmission bar and discs. 82
3.16 Compression along fibers $[0]_{16}$ laminate, nominal stress vs nominal strain. . 82
3.17 Transverse compression $[90]_{16}$ laminate, nominal stress vs nominal strain. . 83
3.18 Compression of $[\pm 45]_{3s}$ laminate, nominal stress vs nominal strain. 84
3.19 Yield stress (σ^y) versus strain rate for $[\pm 45]_{3s}$ laminate. 85
3.20 Dynamic compression of (a): $[\pm 15]_{3s}$ and (b): $[\pm 75]_{3s}$ laminates. 85
3.21 Dynamic compression of (a): $[\pm 30]_{3s}$ and (b): $[\pm 60]_{3s}$ laminates. 86
3.22 Tendency of effective Young's modulus as a function of specimen angle and strain rate. 87
3.23 Tendency of longitudinal failure stress as a function of specimen angle and strain rate. 88

3.24 Tendency of longitudinal yield stress as a function of specimen angle and strain rate. . . . 89
3.25 Tension and compression failure in fiber direction. . . . 91
3.26 (a) Compression and (b) tension in transverse direction. . . . 92
3.27 (a) Compression and (b) tension in out of plane direction. . . . 93
3.28 Illustration of numerical integration schemes for the two models. . . . 94
3.29 Four variant models based on MLT continuum damage mechanics model. . 95
3.30 Quasi-static tension FEA model. . . . 96
3.31 Comparison between test and numerical prediction of tensile behavior of T700S/M21 and T800S/M21, $[\pm 45]_{2s}$ laminates. . . . 97
3.32 Comparison experiment and MATLAB® results, $v_{imp} = 9.13$ m/sec. . . . 98
3.33 Influence of impactor length, $v_{imp} = 5$ m/sec. . . . 99
3.34 Influence of impact velocity, $L_{imp} = 0.6$ m. . . . 99
3.35 Influence of specimen length $v_{imp} = 5$ m/sec, $L_{imp} = 0.6$ m. . . . 100
3.36 Influence of constant $\mathcal{C}_1$. . . . 100
3.37 Dynamic compression model and boundary conditions. . . . 101
3.38 3-D SHPB simulation of $[\pm 45]_{3s}$ laminate at $\dot{\epsilon} = 850 s^{-1}$ . . . 102
3.39 (a) $[\pm 15]_{3s}$ laminate at $\dot{\epsilon} = 290 s^{-1}$ and (b) $[\pm 75]_{3s}$ laminate at $\dot{\epsilon} = 295 s^{-1}$. 103
3.40 (a) $[\pm 30]_{3s}$ laminate at $\dot{\epsilon} = 386 s^{-1}$ and (b) $[\pm 60]_{3s}$ laminate at $\dot{\epsilon} = 380 s^{-1}$. 103

4.1 Typical (a) large mass and (b) small mass impact response, [122] . . . 105
4.2 Strain gages pasted on test specimen (opposite to impact side). . . . 106
4.3 Large mass, low velocity Drop Tower impact setup. . . . 107
4.4 Specimen support plate with rectangular pocket. . . . 107
4.5 Force and displacement curves, $E_{imp} \approx 20$ J on 4.5 mm thick T800S/M21. 109
4.6 Drop tower tests for T800S/M21 $[-45, 45, 0, 90, 0, 0, -45, 45, 0]_s$ laminate. . 110
4.7 Force–time response of T700S/M21, 2 mm thick laminate. . . . 110
4.8 Force–time response of T800S/M21, 4.5 mm thick laminate. . . . 111
4.9 A typical indentation mark on T800S/M21, $[-45, 45, 0, 90, 0, 0, -45, 45, 0]_s$, laminate, $E_{imp} \approx 20$ J. . . . 112
4.10 Measurement of indentation for drop tower tests. . . . 113
4.11 Fiber breakage and impact energy. . . . 113
4.12 Ultrasonic C–Scan images for different impact energies. . . . 114
4.13 Cutting plans for microscopic examinations. . . . 115
4.14 X–ray image of $[-45, 45, 0, 90, 0, 0, -45, 45, 0]_s$ laminate, $E_{imp} = 30$ J. . . . 115
4.15 Scanning Electron Microscope (SEM) images of T700S/M21 quasi-isotropic, $[0_2, 45_2, 90_2, -45_2]_s$, laminate, [80]. . . . 116
4.16 Optical microscope image of T800S/M21 specimen impacted at 10 J with lay-up sequence as $[-45, 45, 90, 90, 0]_s$. . . . 116
4.17 Optical microscope image of T800S/M21 specimen impacted at 10 J with lay-up sequence as $[45, -45, 90, 0, 90, 90, 45, -45, 90]_s$. . . . 117
4.18 Optical microscope image of T800S/M21 specimen impacted at 20 J with lay-up sequence as $[45, -45, 90, 0, 90, 90, 45, -45, 90]_s$. . . . 117
4.19 Small mass, medium velocity impact test setup. . . . 118
4.20 Strain (ϵ_x) in T800S/M21, $[-45, 45, 0, 90, 0, 0, -45, 45, 0]_s$, laminate at different impact energies. . . . 119

4.21 Strain (ϵ_x) in T800S/M21, $[-45, 45, 0, 90, 0, 0, -45, 45, 0]_s$, laminate ($E_{imp}$ = 100 J). 120
4.22 Comparison of ϵ_x registered in drop tower and canon tests, E_{imp} = 15 J. . . 120
4.23 Comparison indentation after Drop Tower and Canon tests. 122
4.24 Comparison C–Scan images for different Canon and Drop Tower tests. . . . 123
4.25 X–ray image of $[-45, 45, 0, 90, 0, 0, -45, 45, 0]_s$ laminate, E_{imp} = 30 J. . . . 124
4.26 Optical microscope image of T800S/M21 laminate. 124

5.1 (a) Quarter Finite Element Model, (b) Location of cohesive elements . . . 130
5.2 Comparison of experiment and simulation results, $E_{imp} \approx 10$ J 131
5.3 C–Scan images (a) impacted face (b) opposite to impacted face. 132
5.4 Damage variable d ($0.9 < d < 1.0$) for finite elements, [78]. 133
5.5 Visualization of delamination at 2.5 msec 133
5.6 Transitory evolution of shear and normal stresses in (a) interface [+45/−45] (Coh-6) and (b) the interface [90/0] (Coh-4), [78]. 134
5.7 Impact finite element models and stacking sequence. 135
5.8 Force/displacement as a function of time. 137
5.9 Elements with damage variable $d_4 \in \{0.87, 1.0\}$, Drop Tower impact at 15 J. 138
5.10 Elements with damage variable $d_4 \in \{0.87, 1.0\}$, Canon impact at 15 J. . . 139
5.11 Failure criteria, f_4 and f_5, and damage variable, d_4, for Drop Tower simulation $E_{imp} \approx 15$ J. 139
5.12 Failure criteria, f_4 and f_5, and damage variable, d_4, for Canon simulation $E_{imp} \approx 15$ J. 139
5.13 Damage variable d_4 for second last ply from impact side. 140
5.14 Damage from microscopic image compared with failure criteria f_5 in simulation of $E_{imp} = 30$ J. 140
5.15 Illustration of impact dent prediction. 143
5.16 Dent depth, numerical models predictions compared with experimental value, $E_{imp} = 15J$. 143
5.17 Stress distribution in FE and SPH models for a bending case. 148
5.18 Models of laminated plate FE on left and EF–SPH on right hand side. . . 148
5.19 Transitory force and displacement, FE and FE–SPH impact simulation. . . 149
5.20 σ_x in last ply (0°) for FE–SPH and FE $[-400, 1950]$ above and σ_y in second last ply (90°) for FE–SPH and FE $[-16, 240]$ below. 150
5.21 Contact surface from FE–SPH and FE numerical models. 151
5.22 Qualitative prediction of damage initiation along global xz-plane. 151

A.1 Definition of an eight ply laminate. 174
A.2 Preparation for cutting of pre-impregnated plies. 175
A.3 Cutting of plies at 0 and 90. 176
A.4 Cutting of plies at 45. 176
A.5 Stacking/lay-up of plies. 177
A.6 Compaction of plies. 177
A.7 Placement in silicon frame. 178
A.8 Plate preparation in the high temperature, high pressure press. 179
A.9 Temperature and pressure cycle used for plate preparation. 179

A.10 Typical A-Scan of a plate for impact test specimen. 180
A.11 Tensile testing of T700S/M21, curves from Gohorianu [65]. 181
A.12 Tensile testing of T800S/M21, curves from Rahmé [129]. 182

B.1 DCB test curve (a) crack length versus opening displacement (b) Critical Strain energy release rate versus opening displacement. 183
B.2 ELS tests curve (a) Force versus specimen end displacement (b) Critical strain energy release rate $\mathcal{G}_{IIc}$ versus end displacement. 184

C.1 Stacking sequences of T800S/M21 impact specimen. 185
C.2 Stacking sequences of T700S/M21 impact specimen. 186

D.1 Particle approximation over a domain Ω by the interpolation kernel W. . . 191

List of Tables

2.1 Material properties used for ELS and MMB simulations of T700S/M21 . . 53
2.2 Material parameters for interface elements. 54

3.1 Material properties of SHPB test apparatus at ISAE. 80
3.2 T800S/M21 in plane material properties. 83
3.3 Dynamic compression of $[\pm15]_{3s}$ laminate. 86
3.4 Dynamic compression of $[\pm75]_{3s}$ laminate. 86
3.5 Dynamic compression of $[\pm30]_{3s}$ laminate. 86
3.6 Dynamic compression of $[\pm60]_{3s}$ laminate. 87
3.7 Material model data for T700S/M21 simulation. 96
3.8 Material model data for T800S/M21 simulation. 96

4.1 Stacking/Lay-up sequences. 106
4.2 Indentation profiles for Drop Tower Tests 114
4.3 Comparison of indentation profiles for Drop Tower and Canon tests 122

5.1 Elastic orthotropic material properties for plies (T800S/M21). 130
5.2 Material parameters for interface elements (T800S/M21 simulation). 131
5.3 Material model data for T800S/M21 impact simulations. 136
5.4 Force (N) versus time (msec) results. 137
5.5 Delamination bounding box comparison test results and simulation predictions. 142
5.6 Elastic orthotropic material properties for plies, T700S/M21. 147
5.7 Comparison of experiments, FE and FE–SPH numerical models 149
5.8 Stresses σ_x, σ_y, σ_{yz} and σ_{zx} in last two plies. 150

A.2 Results of tensile tests on T700S/M21 specimen, $[0°]_4$, [65]. 181
A.3 Results of tensile tests on T700S/M21 specimen, $[90°]_8$, [65]. 181
A.4 Results of tensile tests on T800S/M21 specimen, $[0°]_4$, [129]. 182
A.5 Results of tensile tests on T800S/M21 specimen, $[90°]_8$, [129]. 182

C.1 Impact experiments on T700S/M21 and T800S/M21 specimen. 186

Glossary

δ	Load-point displacement
δ_{I_0}	Mode I initiation separation
δ_{I_m}	Mode I maximum separation
δ_{II_0}	Mode II initiation separation
δ_{II_m}	Mode II maximum separation
$\dot{\epsilon}$	Strain rate
ϵ	Green-Lagrange Strain
$\epsilon_I(t)$	Strain measured during incident pulse/wave
$\epsilon_R(t)$	Strain measured during reflected pulse/wave
$\epsilon_T(t)$	Strain measured during transmitted pulse/wave
$\langle\times\rangle$	$= \times$ if $\times$ is positive, $= 0$ if $\times$ is negative
$\mathcal{C}$	Experimentally determined constant for viscosity function
$\mathcal{C}_1$	Experimentally identified constant for strength increase due to $\dot{\epsilon}$
$\mathcal{C}_2$	Experimentally identified constant for modulus increase due to $\dot{\epsilon}$
$\mathcal{F}$	Viscosity function
$\mathcal{G}$	Strain energy release rate
$\mathcal{Z}$	Acoustic impedance
ψ	Gibb's specific free enthalpy
ρ	Mass density

ρ_b	Density of Hopkinson's bars
ρ_s	Density of specimen
σ	Cauchy Stress
σ_n	Maximum normal stress
σ_s	Maximum shear stress
θ	Angle from global x-axis to ply 1-axis
A_b	Area of Hopkinson's bars
A_s	Area of specimen
c_o	Speed of sound in bar
E_b	Young's modulus of Hopkinson's bars
E_s	Young's modulus of specimen
F	Force
f	Failure criteria
k_I	Mode I penalty stiffness
k_{II}	Mode II penalty stiffness
L_s	Length of specimen
M	Mass of impactor/projectile
m	Softening parameter
q	Damage coupling matrix
S_{del}	Delamination scale factor
u_{DOF}	Displacement of nodes (rigid bodies), where DOF = x, y, z
v_{inc}	Incident bar-end velocity
v_{tra}	Transmission bar-end velocity
v_{imp}	Impactor velocity
BVID	Barely Visible Impact Damage
DCB	Double Cantilever Beam
DOF	Degree(s) of freedom
ELS	End Load Split

ENF	End Notched Flexure
MMB	Mixed Mode Bending
ONF	Open Notched Flexure
SHPB	Split Hopkinson's Pressure Bars
WIF	Wedge Insert Flexure

To cite this document: ILYAS Muhammad. Génie mécanique. *Damage modeling of carbon epoxy laminated composites submitted to impact loading*. Toulouse : Institut Supérieur de l'Aéronautique et de l'Espace, 20 July 2010, 241p.

environment friendly composites, the aerospace industry is inventing the newer generations of fibers and resins. The thermoplastic resin systems show better recyclibilty as compared to thermoset resins. An added advantage of thermoplastic resins is the strain rate sensitivity i.e at higher strain rates the failure strength and effective modulus may be enhanced. An alternative for the carbon fibers is yet to be found in order to have fully recyclable aerospace composites. Thus, with the advent of novel materials the aeronautic industry requires reliable and robust numerical tools to explore the "*what-if*" scenarios often encountered during the design and certification process.

There have been some dramatic aviation accidents e.g., see Figure 2, an uncontained shrapnel from the right engine penetrated the cabin causing loss in pressure. One passenger lost his life. To prevent such fatal accidents the European aviation has adopted the philosophy: "one world, one goal: aviation safety", De Florio [49].

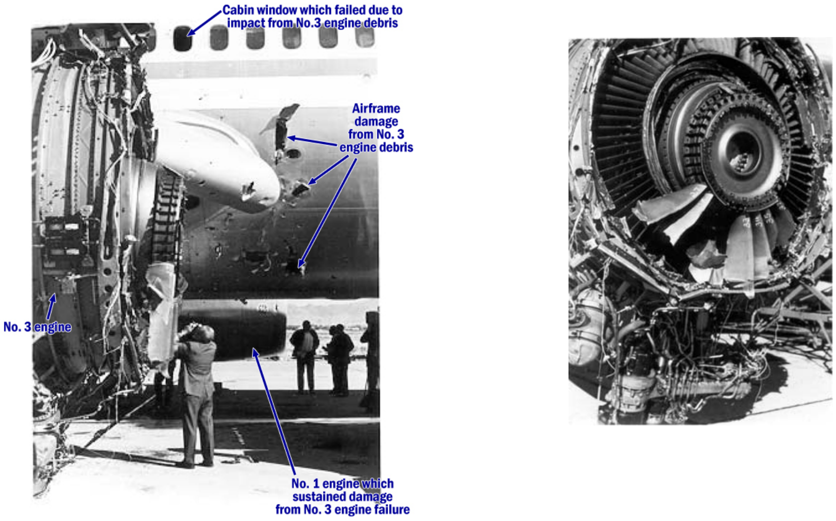

Figure 2: Fan blade out accident National Airlines DC-10 flight (November 3, 1973).

The present work has been carried out in light of the building block (or pyramid tests) approach, see Figure 3. The **First Chapter** outlines the problems treated in light of the certification requirements.

The interface behavior is treated in **Chapter 2**. Characterization experiments are carried out in accordance with available standards. A cohesive interface law is implemented in commercial code LS-DYNA® cohesive finite elements. The material parameters determined from tests are used as inputs and characterization tests are simulated.

Chapter 3 details the tests and numerical simulations carried out to study and explain the behavior of a unidirectional ply. Split Hopkinson's pressure bars are used to characterize the high strain rate behavior of balanced angle ply laminates. A damage mechanics based material model is then developed to carry out numerical simulations by finite element method.

1

Introduction

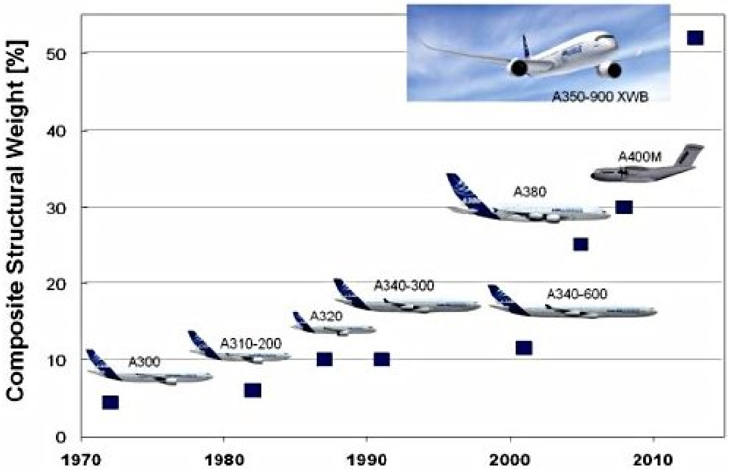

Figure 1.1: Increasing usage of composites in commercial planes by Airbus.

Since the last three decades the usage of composite materials for structure components in the aircraft industry is increasing due to definite advantages in comparison to traditional metallic materials. The most important advantage is the weight of this material based on its low density with accompanying high specific modulus and high specific strength as well as the adaptability to specific applications. First application in commercial aircraft structures was introduced by Airbus in 1972 only for secondary structure components which were not heavily loaded. It was concerning fairings of the vertical tail plane and the radome of the aircraft A300B. Followed by positive experience and extended research, other components like the rudder, spoiler and air brakes were substituted by composite components. The first primary structure, the vertical tail plane torsion box, was substituted by 1985 in the aircraft A310. In the following years the impulse for the intensive deployment of fiber reinforced materials was caused by competition between aircraft manufactures. This competition is mainly based on improvement of the aircraft performance by design of structure components with light weight materials and adapting of advanced engines. A significant reduction of aircraft weight is an important factor regarding the operational costs of an airliner and will be taken into account during strategic investment decisions. Figure 1.1 illustrates the percentage of structural weight of composites by the aircraft manufacturer Airbus.

However the behavior of composite components under impact is a major concern. The reason being absence of, sometimes useful, plasticity and thus chaotic brittle failure of composite materials requires to: (i) meet the expectations of manufacturers wishing to ensure that the impacted structure supports loads at least until the next inspection, (ii) answer scientific questions of understanding of physical phenomena at the origin of resistance or loss of strength of composite structures under shock and (iii) be able to link the deterministic simulation modeling of behavior to safety insurance of industrial design and in service maintenance.

During the design of an aircraft impact damages have been taken into account by fail safe design, where alternate load paths were investigated in order to have damage tolerance against impact of moderate severity. Also lowering the design allowable strength values to an extent where the barely visible impact damage (BVID) can be sustained even at the highest load and for all the time with no degradation in performance. Any damage that exceeds the BVID level (i.e visible damage) may lower the intermediate performance and should be repaired immediately. Therefore concerns in use of composites arise mainly due to demands of high degree of reliability and safety of aerospace structures as against the complexity of composite behavior and consequent difficulties in building prediction models. This creates an excessive reliance on testing at all stages like design and development, proving and certification, and in-service inspection and repairs. The costs of testing are enormous and led to some skepticism in use of composites. These issues shall be discussed in following section.

1.1 Industrial Context

It is estimated that in order to ensure a safe design, the aerospace companies spend an estimated $350 million per year for testing [1]. In case of composite structures there are no proven reliable analytical methods to predict fatigue and damage tolerance as well as impact induced damages. Since assessment of cost and management of risk for new and untried systems is a difficult task, the risk mitigation is attained by employing multiple conservative factors of safety and significant inspection requirements, hence avoiding the costly full scale tests.. The downside of this approach is that it leads to excessively conservative designs and the full potential of composite materials is not exploited.

1.1.1 Aircraft Type Certification

An aircraft is considered to be airworthy when it conforms to its type design and is in a condition for safe operation. These requirements are defined by certification authorities, whereas a certification itself is dependent upon the continent an aircraft is manufactured, purchased or operated in. For example, in case of a European type certification, the authority EASA (European Aviation Safety Agency) is responsible for the issuing, whereas a type certificate for US has to be applied at FAA (Federal Aviation Administration). Until 2003, the European certification of aircraft was overseen by the JAA (Joint Airworthiness Authorities) and prior to that many countries certified aircraft through their own agencies, e.g. CAA (Civil Airworthiness Authority) in the UK.

The certification process consists of all the operations ensuring that an airplane, as a whole and its constituting parts, meets a set of prescribed technical conditions known as Certification Basis. It depends upon whether an aircraft has: (i) New structure i.e changes in the design philosophy regarding structures and loads have been made or it is the first time the manufacturer is going to build a particular aircraft, (ii) Similar new structure, i.e similar design to an existing tested aircraft and (iii) Derivative/similar structure, i.e structural design concepts almost identical to those on which analytical methods have been validated. It is obvious that more similarity a particular aircraft type has with an existing design or design approach, the simpler is the design and certification process.

Standards are the technical documents issued to define design criteria, and referred to as the requirements (in the JAA terminology) or regulations (in the FAA terminology) - the compulsory standards. Over recent years, there has been considerable effort to rationalize the US and European codes and for most issues they are now the same, though there have been different rates of incorporating changes [49]. To cover the type certification of large commercial aircraft, the FAA and EASA have issued FAR-25 and CS-25 documents, respectively. The FAR-25 contains basic regulations and any additional material is contained within AC's (Advisory Circulars). The CS-25 Book 1 contains certification specifications which are standard technical interpretations of the essential airworthiness requirements; the book is further divided into a number of subparts together with appendices. The key subparts for loads and aeroelasticity issues are Subpart B (Flight), C (Structure) and D (Design and Construction). Loads requirements are mainly in Subpart C as the prescription of the loading cases that have to be accounted for in design is a primary prerequisite for assuring structural integrity over the operating environment of the aircraft. Most of the structural airworthiness requirements are related to static (as opposed to fatigue) loads. The CS-25 Book 2 contains what are known as AMC's (Additional Means of Compliance) which are non-exclusive means of demonstrating compliance with airworthiness codes or implementing rules. The AMC (previously termed ACJ when published by JAA) is related to the AC in FAR-25.

Traditionally the aerospace industry relies on the so called “pyramid tests” or “building blocs” approach, Figure 1.2. Determination of allowable material and structural properties is a time consuming task as a considerable amount of testing has to be carried out. In order to reduce product lead time and cost, virtual testing can be used to reduce the physical tests and determine allowable limits.

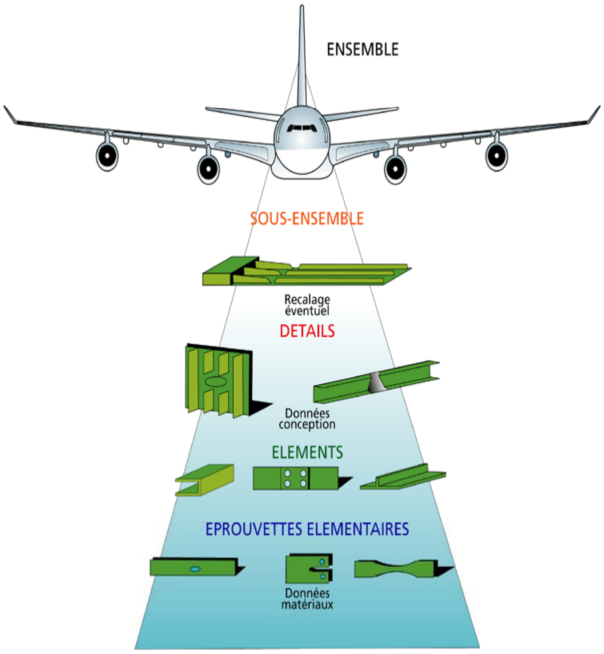

Figure 1.2: Pyramid tests or building block approach [135].

The process of test and analysis depends on what previous evidence is available. An introduction to the compliance with different loading conditions is given in the certification specification under CS-25.307 (Proof of Structure); e.g. the appropriateness of standard methods and formulas, and the use of the finite element method for complex structures are discussed together with the need for testing.

In accordance to JAR/FAR/CS 25.571 an evaluation of the strength, detail design and fabrication must show that catastrophic failure due to fatigue, corrosion or accidental damage will be avoided throughout the operational life of an airplane. CS-25.603 (AMC # 1) and FAA-AC 20.107A sets forth an acceptable means of showing compliance for composite aircraft structures, involving fiber reinforced materials, e.g. carbon (graphite), boron, aramid (Kevlar), and glass reinforced plastics.

1.1.2 Composite Requirements

We will not go into detailed reasons or essential criteria of material or technology selection, processes for their implementation, guiding designers to define the best composite solutions according to different specifications.

From a general point of view, the fundamental mechanical properties leading to the choice of composites over metals are the specific mass and fatigue resistance, the range of lamination possibilities and anisotropic materials constituting the basis for achieving the specific mechanical performance. It is well known, however, that these materials have a low impact resistance, and damages generated are much more extended deep inside structures than the external impact imprint, without being detectable by an outside visual inspection. Therefore, a risk exists that an inspection would qualify a structure but its resistance would be far less than the required one to ensure the CS requirements.

1.1.2.1 Composite Airworthiness Requirements

Some of the categories of material related airworthiness requirements are (**i**) static strength (capability to resist gust, man-oeuvre, ground loads etc.), (**ii**) endurance (to retain above capability in the long run) and (**iii**) others e.g. (a) emergency landing, ditching, rapid decompression, flutter, etc. and (b) accidental hazards (fire, lightning strikes, bird impact, accidental tool drop and fuselage impact etc.).

1.1.2.2 Composite Materials - The Current Situation

In order to demonstrate that structural failure of a single component does not occur and that the part has an adequate life during its entire operation, a comprehensive fatigue and fracture mechanics analysis is required. Safe-life analysis is based on fracture mechanics data which might or might not be available. When available this data is generated based on the ASTM or some other testing standards. Since fracture toughness is thickness dependent property and structural components with different sizes and thicknesses require numerous fracture toughness tests e.g. plane strain, plane stress, and the mixed-mode conditions. If fatigue driven data is also taken into account these tests become costly and time consuming.

The CS-25.603 deals with material substantiating testing. In case of composite materials there is no standardization system available,to date, with which various manufacturers could comply. Hence each composite material is identified under its own trademark (T800S/M21 from HEXCEL® or CYCOM 977-2 from CYTEC). The consequence of this is that no exact equivalence can be established between two different suppliers. Henceforth, a material approved for a certified structural application has a unique reference, usable for one product only and coming from one supplier. Any modification of one of these parameters leads to a material change, which needs a new approval procedure. Therefore, any method that can reduce the number of tests, e.g reliable robust virtual testing tools, will be useful to the industry to avoid unnecessary costs.

1.1.2.3 Durability and Damage Tolerance

The life assessment of aircraft components is divided into two parts: "durability" and "damage tolerance". "Durability" refers to the number of cycles to initiate a crack, where crack reaches to a visible measurable size ≈ 0.25 mm in length, and "damage tolerance" describes the number of cycles from initiation to final failure. Damage tolerance is definitely a "Safety Issue" not to be confused with durability which is an "Economical Issue".

Following are the FAA categories of damage and defect considerations for primary composite aircraft structures [1]:

Category 1 Damage that may go undetected by field inspection methods (or allowable defects)

- ***Examples*** BVID, minor environmental degradation, scratches, gouges, allowable manufacturing defects
- ***Safety Considerations*** Demonstrate reliable service life, retain Ultimate Load capability

Category 2 Damage detected by field inspection methods at specified intervals (repair scenario)

- ***Examples*** VID (ranging from small to large), manufacturing defects/aberrations, major environmental degradation
- ***Safety Considerations*** Demonstrate reliable inspection, retain Limit Load capability

Category 3 Obvious damage detected within a few flights by focal operations (repair scenario)

- ***Examples*** Damage obvious to operations in a "walk-around" inspection or due to loss of form/fit/function
- ***Safety Considerations*** Demonstrate quick detection, retain Limit Load capability

Category 4 Discrete source damage known by pilot to limit flight maneuvers (repair scenario)

- ***Examples*** Damage in flight from events that are obvious to pilot (rotor burst, bird-strike, lightning)
- ***Safety Considerations*** Retain "Get Home" capability

Category 5 Severe damage created by anomalous ground or flight events (repair scenario)

- ***Examples*** Damage occurring due to rare service events or to an extent beyond that considered in design

Safety Considerations Requires new substantiation, requires operations awareness for safety (immediate reporting)

Author's objective in this document is not focused on durability but hes has limited himself to the study of damage tolerance. With regard to the above paragraphs the two categories are of his particular interest i.e. Category 1 and Category 4. The loading conditions and strain rates generated during these types of impact events are considerably different from one another (see paragraph 1.2.3).

1.1.3 Impact Key Problems/Points

In accordance with AC 20-107 revision 1983, a damage tolerance demonstration (e.g the case of lightening strike) is required, unless it is not practical. The same AC also introduces the issue of accidental impact damage that may occur during fabrication or service. No-growth approach for fatigue damage tolerance is proposed. It is interesting to mention that there is a subtle difference in the area of static strength demonstration where, depending on the experience with similar structure, FAA may accept demonstrations only up-to "limit loads". In JAA advisory circular "limit load" has been replaced by an "agreed load level".

As defined by AC 25-571 1F (April 98), damage tolerance is the attribute of the structure that permits it to retain its residual strength without detrimental structural deformation for a period of use after the structure has sustained a given level of fatigue, corrosion, accidental or discrete source damage.

Therefore we are interested in a methodology which could be predictive and able to cover a large range of impact loadings. For the purpose of this study we have categorized the impact event into (i) non-penetrating impact and (ii) penetrating impact. These are two extreme cases in themselves. For first case the damage could be present but undetectable thus catastrophic failure can arrive any time and for second case failure has occurred but is it catastrophic or not.

1.1.3.1 Non-penetrating Impact

Non-penetrating accidental impacts due to tool drop or luggage trolley collisions etc. can have drastic consequences on residual strength of composite structures see Figure 1.3. Such type of impacts, with enough energy to cause damage induce barely visible impact damage (BVID). Fatigue / Damage tolerance requirements, as per CS or FAR 25-571, are applicable to all structures, regardless the material (metallic or composite).

ACJ 25 603 § 5.8 states that it should be shown that impact damage that can be realistically expected from manufacturing and service: (i) will always be less than the established threshold of detectability for the selected inspection procedure and (*ii*) will not reduce the structural strength below “limit load” capability.

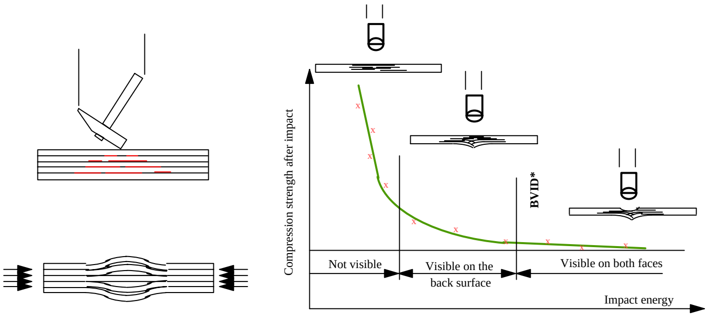

Figure 1.3: Accidental tool drop and a typical BVID curve [135].

Let us assume that accidental impact occurrence is reasonably probable ($10^{-5} < Po < 10^{-3}$/Flight Hour) according to JAR ACJ 25-1309 definitions. For a short-medium range aircraft (50,000 FH), if “Most of the structures” means 90% of the population, the realistic level of energy should not be lower than : 40 joules (50 joules were used for most of JAR certified programs, 137 joules is recommended in USA) [135]. Therefore a structure has to sustain the above energy without reduction in strength and also show that the visible impact damage at this energy will not be below the limit which a common inspector may overlook. The statistics on impact hazard on composite structures service life are very limited therefore appropriate models capable of predicting these defects are highly needed.

1.1.3.2 Penetrating Impact

One of the most challenging component design and certification requirements for commercial jet engines is to try and prevent a “blade-out” rotor failure event, which can result in catastrophic loss of aircraft and/or passengers. Engine blade-out occurs when a sudden change in speed causes a fluctuation in rotor spin resulting in a blade over-stress condition, or when a blade, or group of blades, fatigues from repeated cyclic stresses.

Although manufacturers are required to demonstrate through a test that engine casing is capable of containing debris resulting from this accident. The possibility of a shrapnel impacting the fuselage cannot be ruled out. The failure of critical piping and transmission lines has to be anticipated. A risk mitigation study is thus inevitable.

1.1.4 Synthesis

CS-25.307 requires compliance for each critical loading condition e.g an impact and the compression loads afterwards. Compliance can be shown by analysis supported by previous test evidence, analysis supported by new test evidence or by test only. As compliance by test only is impractical in most cases, a large portion of the substantiating data has

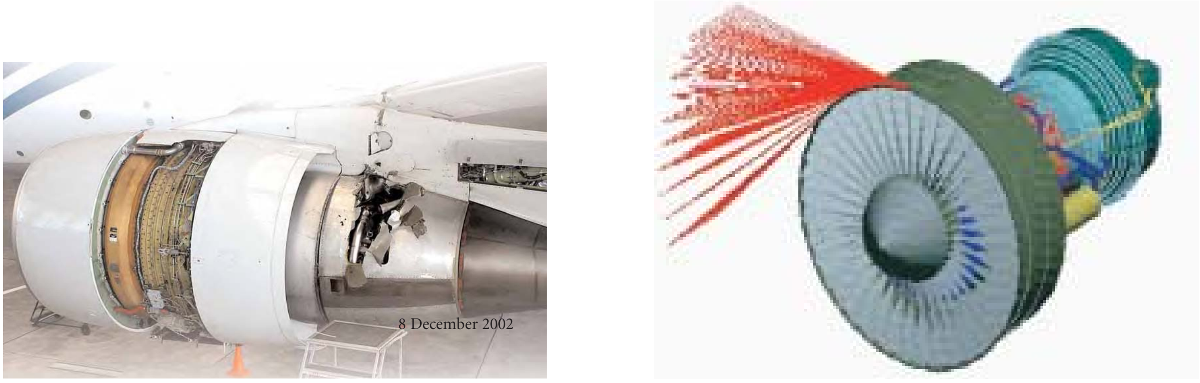

(a) Uncontained engine failure Boeing 767 (Australian Airline).

(b) Possible trajectories for uncontained assessment (Credit: NASA).

Figure 1.4: Fan blade out accident and uncontained assessment by simulation.

to base on analysis. Therefore, these analysis methods have to be feasible, robust and predictive at the same time.

There are a number of standard engineering methods and formulas which are known to produce acceptable, often conservative results especially for structures where static load paths are well defined. These standard methods and formulas, applied with a good understanding of their limitations, are considered reliable analyses when compliance with CS 25.307 is shown. Conservative assumptions must be applied in assessing whether or not an analysis may be accepted without test substantiation.

The application of numerical methods for virtual testing (e.g. Finite Element Method) or engineering formulas to complex structures in modern aircraft is considered reliable only when validated by full scale tests (ground and/or flight tests) [44]. Experience relevant to an aircraft or its sub-assembly in the utilization of such methods should be considered. Hence finite element method can be considered adequate.

1.2 Scientific Context

Extensive research around the world has been carried out on composite structures in past three decades, still a complete and validated methodology for predicting the behavior of composite structures including the effects of damage is yet to be achieved, [123]. This is mainly due to the complex nature of these materials, so that damage initiation, propagation and ultimate failure depend upon a lot of deterministic parameters such as: geometry, material constituents, lamination sequence, boundary conditions, load history, loading rate and failure modes and also on not yet deterministically known or quantified parameters such as process induced or assembling induced ones. As far as the aeronautics is concerned, the major effort has been produced to characterize an intrinsic mechanical behavior of standard samples under selected corresponding loads to safely ensure the certification requirements.

1.2.1 Constitutive Modeling

In the framework of continuum mechanics, the constitutive model of a material is the relation used to characterize its physical properties, and to use them as the link between reaction behavior of the system and the loading. In structural mechanics, a constitutive model relates applied *stresses* or *forces* to *strains* or *deformations*. Constitutive models are often classified as (i) explicit, (ii) implicit and (iii) hybrid.

For damage tolerance studies, all the developed, except elastic, constitutive models include failure modes detected by corresponding failure criteria. But even if numerical or analytical models are now able to reproduce the amount of damage on laboratory samples, these models are not completely predictive since limited by hypotheses related to the mechanical characterization domains, and to the numerical models capabilities. Furthermore, these models are difficult to use for a certification approach because each “standard sample” is a particular case of structure not representative of dimensions, shapes, assembling constituents etc. of real industrial parts. In order to introduce the goals and methodology, let us explain the scientific “lock-points” the author is interested in.

1.2.1.1 Explicit Models

These constitutive models are derived from phenomenological observations and used to reproduce it. This is a classical approach to define a material behavior, [123]. They connect the measurable strength properties of a material to its external or in situ behavior using physically based theories. This can be defined at macroscopic or microscopic level. The idea is to define a general behavior based on non dissipative potential energy principle and, often, hypoelastic material behavior. From a material point of view, a constitutive stress-strain relation is normally used, where stress is a function of strain, strain rate, strain history, temperature and material properties.

A macroscopic level is at a range of scales starting from individual plies and laminates and going to structural components and assemblies. At this level a generalized stress-strain relationship is derived from work potential of the system itself considered as conservative. This equation is used to define the stiffness of a single ply or complete laminate using classical laminate plate theory, [62, 120]. The stress and strain fields of material are determined solving this equation together with the strain-displacement, compatibility and equilibrium equations that are complementary assumptions of continuum mechanics theory. This is commonly carried out using finite element analysis.

The major limitation of explicit or phenomenological models is that they are able to reproduce only the observed behavior, so they may not be relevant if all the influencing parameters leading to damage or failure have not been identified a priori.

1.2.1.2 Implicit Models

Implicit models are usually more suited to represent highly complex and nonlinear material behavior at the ply scale. These models characterize the material behavior using mathematical relationships between inputs and outputs of a system and do not attempt to represent all the underlying physics, [123]. In order to identify an implicit model for a material system, a set of input and output data is required. Then identification process is used to find an optimum approximation function.

It is worth noting that these models are only valid within the range they are developed. Hence they may not be suitable across different length scales. Another drawback is the need to characterize the mathematical parameters for each different material.

1.2.1.3 Hybrid Models

Hybrid models combine salient features of both explicit and implicit models, and rely on both physically-based and approximation methods to characterize material behavior. Dissipated Energy Density (DED) approach is an example of hybrid model, [123]. In DED approach an arbitrary polynomial function mathematically defines the energy lost due to nonlinearities. Then DED is expressed in terms of a polynomial equation and incorporated into material constitutive relation. A solution to this equation is retrieved through iterative process, [123].

1.2.1.4 Summary

Since author's intent is to be able to predict numerically the damage behavior of composite under various energies of impact, he has oriented his choice towards hybrid constitutive models. Models based on a safe potential and a damaged potential are also in this category, [72]. These models include failure criteria, derived from phenomenological observations and mathematical functions for damage evolution. Energy release rate models also fall in this category.

1.2.2 Composite Failure

Experimental identification of material failure stresses or strains is vital in definition of failure criteria. Material characterization is often done in accordance with standards organizations e.g. the International Standards Organizations (ISO), American Society for Testing and Materials (ASTM) and European Structural Integrity Society (ESIS) etc. These are generally limited to strength and fracture mechanics parameters. Material strength properties may be determined by relatively simple tensile, compressive and shear tests. Fracture mechanics tests have been classified according to modes of crack propagation. However, these tests are sometimes problematic and all fracture mechanics properties cannot be determined reliably.

Traditionally, uniaxial testing machines are used to characterize one or two material constants per test coupon. The advent of multiaxial test machines will help overcome this issue and allow for the application of loads in various degrees of freedom.

1.2.2.1 Failure Mechanisms

The complex structural and manufacturing processes of composite materials engender a variety of failure mechanisms. These failure mechanisms are well described in textbook by Daniel Gay taught in engineering schools [62]. An extended literature exists on these damages, that are always the same whatever the loading, but in proportion and localization highly depend on it loading/solicitation rate. To represent these damages in a constitutive model, it is necessary to characterize their proportion, their location and their evolution dependence on the loading. Damage mechanisms under each loading of interest are characterized by these three key points, and their effect on the material ruin at the scale of interest through failure criteria giving rise to constitutive models.

- **Fiber failure** is one of the simplest failure mechanisms to identify and quantify due to a high tension along the fiber direction and can be characterized by uniaxial tension tests.

- **Fiber-matrix debonding** is relatively complex failure mode to characterize and strongly depends upon the fabrication processes of unidirectional tapes.

- **Matrix cracks** or intralaminar damage takes birth from cracks or voids between fibers within a single composite layer (ply). These occur due to an overload of tension in a direction perpendicular to the fibers, so their density varies depending on the loading gradients: uniformly distributed in case of a global perpendicular tension, uniformly distributed and branching under a punch load.

- **Fiber buckling** is a structural phenomenon occurring in compression in fiber direction. Though by itself buckling may not cause the composite to fail, but it may promote other types of damages, such as fiber matrix debonding.

- **Delaminations** or interlaminar damage is the separation between internal layers of a laminate having different orientations and is often caused by high level of discontinuous through-thickness stresses. There exist different ways to see and measure delaminations through destructive and nondestructive means of testing. Delaminations can be responsible for the ruin of a structure when it is subjected to an in-plane compression for example.

1.2.2.2 Failure Criteria

Various researchers have pursued development of failure criteria for composite materials, and a countless number of theories exist today. These criteria may be classified according to the theories that are based on: (i) strength or fracture mechanics theories, (ii) failure prediction (general or particular to a damage mode) or (iii) damage planes (in-plane or intralaminar). Our focus shall be on theories for in-plane and interlaminar failure. These theories are largely based on stress components of an individual ply within a laminate. For unidirectional prepreg materials, failure is classified according to fiber direction. Fiber failure occurring in fiber axis and matrix failure occurring in plane and orthogonal (parallel) to fiber axis.

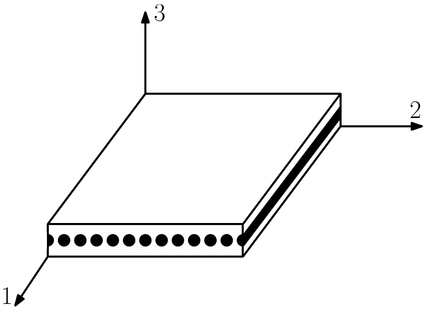

Figure 1.5: Description of unidirectional ply axes

In this manuscript σ and ϵ are used for stress and strain respectively; X, Y, Z and S represent strengths in fiber, matrix, out of plane and shear directions; subscripts 1, 2 and 3 refer to the fiber, transverse and out of plane directions (see Figure 1.5); subscripts T and C denote tension and compression respectively.

When describing choice of failure values important note is to be made for usage of in situ values as suggested by Davila and Camanho [48]. It has been found experimentally that ply embedded within a multi-directional laminate shows an increase in transverse tensile and shear strengths as compared to the strength values for play in a completely unidirectional laminated. This enhancement is due to a positive effect of neighboring plies and implies that values taken from standardized experimental characterization coupons can underestimate ply strengths. It is important to note that although most of authors refer to these limit values as material properties, these are actually structural properties based on orthotropic nature of ply.

Fiber based Failures Tensile fiber failure occurs due to accumulation of individual fiber breakages within plies. These failures become critical when there is no enough number of fibers remaining to support the required load. It is customary among researchers, [37, 71], to apply maximum strength or maximum strain criterion at each ply making use of material limit values taken from experiments. To cumulate fiber breakage and fiber matrix debonding, Hashin [71] has used quadratic interaction criterion involving in-plane shear while Chang and Chang [37] apply Hashin's quadratic interaction criterion and also incorporate nonlinear shear behavior.

- Hashin [71] 3D fiber tensile failure

$$\left(\frac{\sigma_{11}}{X_T}\right)^2 + \frac{(\sigma_{12}^2 + \sigma_{13}^2)}{S_{12}^2} \geq 1 \tag{1.1}$$

- Chang and Chang [37] fiber tensile failure

$$\sqrt{\left(\frac{\sigma_{11}}{X_T}\right)^2 + \frac{\sigma_{12}^2/2G_{12} + \frac{3}{4}\alpha\sigma_{13}^4}{S_{12}^2/2G_{12} + \frac{3}{4}\alpha S_{13}^4}} \geq 1 \tag{1.2}$$

α from nonlinear shear law

Compressive fiber failure is observed to be due to microbuckling and formation of kink bands. There is debate over whether these phenomena can be considered separate failure modes. Generally, microbuckling is considered to be more of a global failure mode while kinking is assumed to be initiated by local microstructural defects, as suggested by Pinho et al. [125]. Gohorianu [65] showed that microbuckling could be the reason for axial reduction of E_{11} modulus when loaded in compression.

Matrix Cracks There are two major orientations of matrix cracks due to the two major sizes of heterogeneities within plies: crossing through thickness cracks and stacking cracks. Through thickness cracks are perpendicular to fibers or at the fiber matrix interfaces, while stacking parallel cracks do not cross the overall width and are generally longer along the fiber direction. Through thickness cracks are considered as a proper damage, stacking parallel cracks are often not taken into account since they are parallel to delamination whose sizes and induced strength reduction are more effective. Matrix cracks are believed to initiate typically at defects or fiber-matrix interfaces, accumulated throughout the laminate and integrate to failure across a critical failure plane.

- Hashin [71] 3D matrix tensile failure

$$\left(\frac{\sigma_{22} + \sigma_{33}}{Y_T}\right)^2 + \frac{(\sigma_{23}^2 - \sigma_{22}\sigma_{33})}{S_{23}^2} + \frac{(\sigma_{12}^2 - \sigma_{13}^2)}{S_{12}^2} \geq 1 \tag{1.3}$$

- Chang and Chang [37] matrix tensile failure

$$\sqrt{\left(\frac{\sigma_{22}}{Y_T}\right)^2 + \frac{\sigma_{12}^2/2G_{12} + \frac{3}{4}\alpha\sigma_{13}^4}{S_{12}^2/2G_{12} + \frac{3}{4}\alpha S_{13}^4}} \geq 1 \tag{1.4}$$

α from nonlinear shear law

A critical fracture plane is assumed in most of matrix failure criteria for transverse tension/compression loading. Generally an interaction between the tensile normal and in plane shear stress is also taken into account.

Delamination Initiation and propagation of delamination are treated separately. Initiation prediction has been proposed by a number of criteria using stress values of individual ply. Individual ply criteria use combinations of the through thickness tensile and transverse shear strengths in linear or quadratic relationships.

- Hashin [71] delamination initiation

$$\left(\frac{\sigma_{33}}{Z_T}\right)^2 + \left(\frac{\sigma_{23}}{S_{23}}\right)^2 + \left(\frac{\sigma_{13}}{S_{13}}\right)^2 \geq 1 \tag{1.5}$$

- Brewer and Lagace [28] delamination initiation

$$\left(\frac{\langle\sigma_{33}\rangle}{Z_T}\right)^2 + \left(\frac{\langle-\sigma_{33}\rangle}{Z_C}\right)^2 + \left(\frac{\sigma_{23}}{S_{23}}\right)^2 + \left(\frac{\sigma_{13}}{S_{13}}\right)^2 \geq 1 \tag{1.6}$$

- Choi and Chang [39] delamination size prediction

$$D_a \left[\left(\frac{{}^{p}\sigma_{23}}{{}^{p}S_i}\right)^2 + \left(\frac{{}^{p+1}\sigma_{13}}{{}^{p+1}S_i}\right)^2 + \left(\frac{\langle{}^{p+1}\sigma_{22}\rangle}{{}^{p+1}Y_T}\right)^2 + \left(\frac{\langle-\,{}^{p+1}\sigma_{22}\rangle}{{}^{p+1}Y_c}\right)^2\right] \geq 1 \tag{1.7}$$

$p+1$: is the adjacent ply above the considered ply

D_a: empirical constant determined from experiments

S_i, Y_T, Y_C: in situ strength values

Delamination growth prediction criteria are based on fracture mechanics concept of strain energy release rate, $\mathcal{G}$, and compare the $\mathcal{G}_{Ic}$, $\mathcal{G}_{IIc}$ and $\mathcal{G}_{IIIc}$ with the threshold $\mathcal{G}_c$. Determination of mode III strain energy release rate is not very straight forward. Therefore some authors ignore the contribution. Another approach is to combine mode II and mode III components into a single $\mathcal{G}$ value.

- Whitney [155] delamination propagation (Power Law)

$$\mathcal{G}_T \geq \left(\frac{\mathcal{G}_I}{\mathcal{G}_{Ic}}\right)^m + \left(\frac{\mathcal{G}_I}{\mathcal{G}_{IIc}}\right)^n + \left(\frac{\mathcal{G}_{III}}{\mathcal{G}_{IIc}}\right)^p \tag{1.8}$$

$m = n = p = 1$: linear; $m = n = p = 2$: quadratic

- Benzeggagh and Kenane [20] delamination propagation

$$\mathcal{G}_T \geq \mathcal{G}_{Ic} + \left(\mathcal{G}_{IIc} - \mathcal{G}_{Ic}\right)\left[\mathcal{G}_{II}/\left(\mathcal{G}_I + \mathcal{G}_{II}\right)\right]^\eta \tag{1.9}$$

η: curve fit parameter

Ply Failure Several authors have proposed criteria which predicted failure of entire ply contrary to separate ply failure modes e.g. Tsai and Wu [151]. In this so-called "fully interactive" criterion, all the strength data is adopted to create a failure surface, usually in stress space. In situations where delamination can be ignored, ply failure criteria are more suited. The interactive criteria lack in phenomenological basis and have origins in theories proposed for metals. However, these criteria are commonly applied in widely available FE codes due to the same level of accuracy demonstrated as theories in which failure modes are considered.

$$\begin{aligned} &\sigma_{11}\left(\frac{1}{X_T} - \frac{1}{X_C}\right) + \left(\sigma_{22} + \sigma_{33}\right)\left(\frac{1}{Y_T} - \frac{1}{Y_C}\right) + \frac{\sigma_{11}^2}{X_T X_C} + \frac{\sigma_{22}^2 + \sigma_{33}^2}{Y_T Y_C} \\ &- \frac{\sigma_{22}\sigma_{33}}{Y_T Y_C} + \frac{\sigma_{12}^2 + \sigma_{23}^2 + \sigma_{13}^2}{S^2} - \frac{2\sigma_{11}\sigma_{22}}{\sqrt{X_T X_C Y_T Y_C}} \geq 1 \end{aligned} \tag{1.10}$$

1.2.3 Impact Induced Rate Effects on Failure Mechanisms

Impact on composites may be defined as a *relatively* sudden application of an impulsive force, to a *limited* volume of material or part of a structure. The terms *relatively* and *limited* can have wide range of interpretations as proposed by Hancox [68]. The force is related either to the impact velocity of to impact energy or to the rate of loading in the structure.

In aeronautical structures, the components have to undergo (i) low energy impacts caused by dropped tools or mishandling during assembly and maintenance, (ii) medium energy impacts caused in-service by foreign objects such as tire debris, stones, hail ice or birds, and (iii) high energy impacts caused by fan blade out (FBO) or uncontained engine shrapnels. In a low energy impact (but high enough to produce damage), a very small indentation is produced on the impact surface. This level of damage is often referred to as barely visible impact damage (BVID).

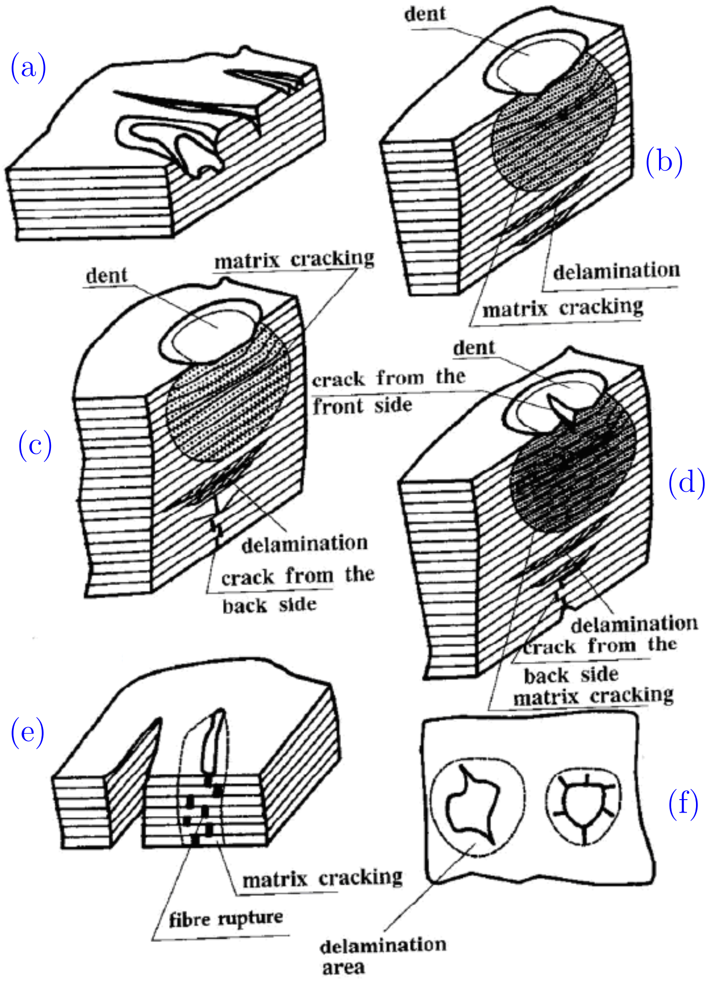

Figure 1.6: Low velocity impact induced damages, Zagainov and Lozino-Lozinski [162].

In terms of projectile/impactor striking velocity Al-Maghribi [6] proposed a classification as follows:

- Low velocity impact: v, between 0 and 50 m/sec
- Medium velocity impact: v, between 50 and 200 m/sec
- High velocity impact: v, between 200 and 1000 m/sec
- Hyper velocity impact: v, greater than 4000 m/sec

The extensive research found in open literature has been mainly focused on standard lab plate specimens and technological samples. And it has been observed that dynamic failure modes of composites are significantly different from traditional metallic materials, [3, 4]. Low velocity impact damage of metal structure starts from the impacted surface and is detectable by visual inspection. As far as composites are concerned, significant amount of permanent damage in the form of subsurface delaminations, matrix cracking and fiber breakage may be present in situ without being detectable by "outside" visual inspection, [5, 35, 132]. Understanding of impact phenomena, damage mechanisms and development of appropriate predictive models is necessary for developing improved materials and design methods.

It has been shown that, for unidirectional laminates under low velocity impact, matrix cracks arise before the delamination, Liu [103], Richarson and Wisheart [132]. Initially these cracks are parallel to fibers and oriented at an angle with interface, after reaching the interface between different ply orientations they propagate parallel to unidirectional ply plane. By now adjacent plies containing matrix cracks have different bending stiffnesses, thus delamination propagation follows. The shock energy is absorbed by failure of the weakest link, i.e. the interface between plies of different orientations, Bonini [21].

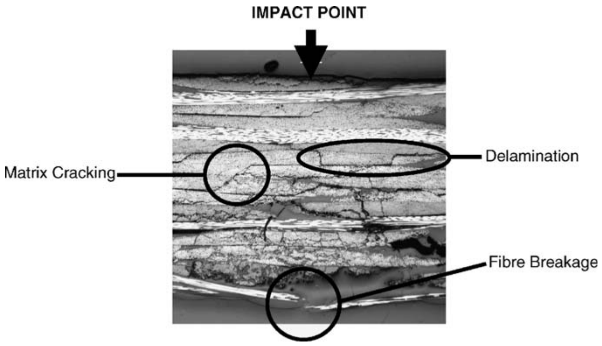

Figure 1.7: Different types of impact damage, Mitrevski et al. [115].

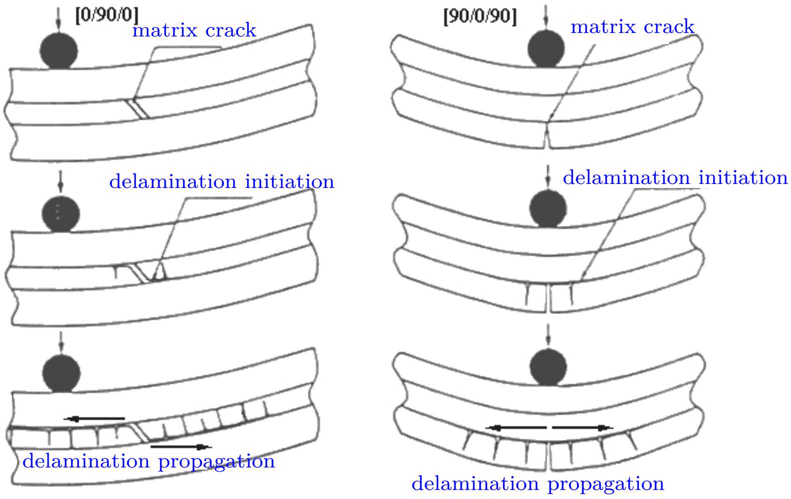

Figure 1.8: Initiation and propagation of low velocity impact induced damage.

Abrate [3; 4], López-Puente et al. [105], Olsson [121] argue that in the case of a low velocity impact, the plate response is dominated by the global bending while at higher velocities plugging, which is a combination of local crush and out of plane shear loading, phenomena dominates. Experimental evidence of the plugging phenomenon has been provided by Gama and Gillespie Jr [60] for glass fiber composites under ballistic impact and by Tennyson and Lamontagne [146] for carbon fiber composites under hypervelocity impacts. Extremely small and fast impactors, thus small impact times, generate dilatation waves Olsson [121]

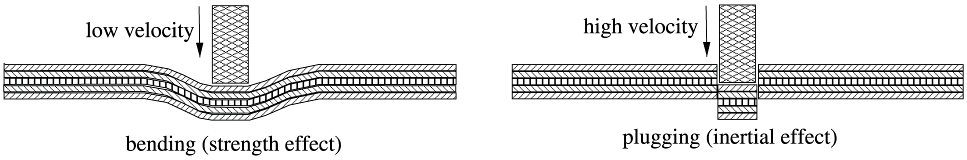

Figure 1.9: Effect of velocity on laminate response, López-Puente et al. [105].

It can be inferred, in a more general consideration, that only velocity is not sufficient to define an impact, in particular when residual damage and strength are to be classified. Indeed, during the impact, inertial phenomena and diameter/plate thickness effects also characterize the loading. Even the loading itself is not enough to characterize global "domains" of behaviors of the target since simultaneously loading rate effects of the constituents and assembly conditions also affect the 3–D structure called the composite plate.

1.2.4 Damage Modeling

Failure criteria are used to represent sudden failure of the ply or to introduce a progressive failure through damage evolution.

Various approaches have been used to experimentally determine onset and progression of damage. Typically, this is done by monitoring one particular type of parameter, for instance the axial Young's modulus of a ply in a simple coupon specimen made of $[\pm\theta]_{2s}$, to predict or follow start and damage growth, related to fiber breakage. Damage characterization approaches can be generally categorized as based on theories of strength or fracture mechanics, [33, 50, 95, 123, 125]. The damage mechanics approach has been applied to both intralaminar and interlaminar damage prediction. One or more damage parameters are introduced into material constitutive law with a primary aim of stiffness reduction.

1.2.4.1 Continuum Damage Mechanics

In damage mechanics framework the effects of damage are represented as part of material definition and generally confine most other damage modeling approaches. This process typically involves development of equations to represent damage initiation and growth. These equations are then incorporated into explicit or hybrid constitutive law. Multiple variables can be used to represent separate damage mechanisms or a single may suffice to capture effects of all the damage types.

Strength based approach is fairly simple, as one or more strength criteria are defined and material being studied is irreversibly damaged once these criteria are verified. The criteria themselves can be defined in terms of single stress limits, linear or quadratic combination(s) of various stress terms or normalized stress terms. A number of other parameters similar to stress can be used to characterize damage e.g. strain, force, displacement and rotation etc. Strength based damage characterization approach is commonly applied to predict damage initiation and not progression of existing damage e.g. the case for delamination predictions.

1.2.4.2 Interface Elements

For delamination and debonding, cohesive elements present a number of advantages over other modeling approaches e.g. capacity to investigate both initiation and growth of damage and incorporate both strength and fracture mechanics theories. An other added advantage is that the use of interface elements does not require the assumption of an initial damage size or propagation direction. Furthermore, computationally expensive remeshing procedures are not required to capture propagating delamination. However, in order to obtain an accurate solution, a fine mesh size is desired. For coarser meshes, cohesive finite elements can be prohibitively inaccurate.

Classical fracture mechanics approach is based on the assumption of an existing crack and therefore, is used to characterize damage progression. This approach is not commonly used for most forms of composite damage but has been successfully applied to study delamination and debonding. Classical fracture mechanics were developed to study single crack propagation at a uniform rate in metals. The growth of this macroscopic defect is controlled by strain energy release rate. The study of a single macrosocpic crack is analogous to delamination propagation in composites. Therefore, the principles of classical fracture mechanics have been applied without exception to investigate delamination growth. Lachaud [92] and Prombut [128] have shown that the strain energy release rate is affected by a number of parameters e.g. loading, crack growth direction, orientation of plies adjacent to delaminations, proportion of different crack propagation modes etc.

1.2.4.3 Meshless Methods

Chen and Medina [38] have applied Smoothed Particle Hydrodynamics (SPH) method in 2D to qualitatively represent the damage mechanisms of a high velocity impact. The method was then applied in 3D by the same authors, Medina and Chen [112].

This method allows a *"natural"* separation of particles thus being a promising compromise between the continuum mechanics and the discrete mechanics.

1.3 Objectives

In order to certify aerospace composite structures, the manufacturer needs to know the behavior of structures during “normal” solicitation environment, and demonstrate the ability of these structures to bear the load for a minimum period, e.g. to the next technical inspection maintenance, even after the onset of damage between two maintenance intervals. Thus the specific aerospace needs selected for this study are: 1) understand to formulate and improve the impact behavior of composite structures for various configurations of characteristic impacts encountered during aircraft service life, 2) determine the extent of damage after an impact for some types of characteristic impacts, 3) relate quantitatively the measured external and unobservable internal impact damage.

From a scientific perspective, the question we have chosen to study is: what physical phenomena are predominating the resistance of the structure and how one should model them to predict the internal expansion of the damage for different configurations of impact: low energy shocks, high energy shocks on the fuselage.

Another key point is about the predictive ability of numerical mechanical models, that is the purpose of this study to avoid à priori choices of numerical tools or numerical parameter testing.

To analyze the effect of inter-ply damage and intra-ply damage on the global behavior of composite samples, we have decided to follow a parallel modeling of these two damages. First we propose to model the delamination using a cohesive method. The counterpart of this model is that it must be defined à priori, thus limiting the predictability of the model. Then we propose to use a Continuous Damage Mechanics (CDM) based modeling for the ply, that also takes into account for delamination effect on the strength reduction. Strain rate effect is taken into account on both the rigidities and strength correlation also related to damage evolution speed. A special analysis and comparison is made between these two models and real impact tests on different composite plates (T700S/M21, T800S/M21, different stacking sequences and thicknesses, different energies and impact velocities).

2

Constitutive Law: Interface

The unidirectional composites often contain a resin rich layer between two plies as shown in Figure 2.1. This resin rich layer or interface has been modeled by interface elements. This chapter primarily focuses on validation of material model developed for interface simulation. Organization of the chapter is as follows: at first static characterization experiments are presented, followed by dynamic tests. Next the finite element modeling techniques will be presented and followed by material law used for cohesive elements. In the last section this developed material model is validated by correlation with characterization experiments.

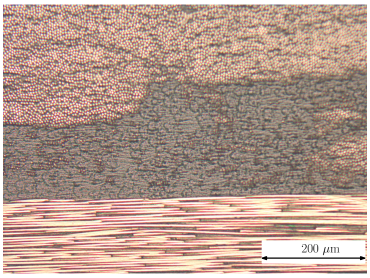

Figure 2.1: Resin rich layer in a T800S/M21 laminate.

2.1 State of the Art

Interlaminar damage in the form of delamination has been an active field of research in the recent past. Stress gradients occurring near geometric discontinuities such as ply drop-offs, flange and stiffener terminations and all types of holes promote delamination initiation, trigger intra-ply damage and may cause significant loss in structural integrity. At certain times a single delamination can exhibit drastic consequences. The flexural stiffness of a homogeneous beam can be reduced to 25% of its original value by splitting it into two halves. If instead the same beam is split into three beams, the stiffness is reduced to 11% of the original value [131].

2.1.1 Experimental Characterization

Fracture mechanics is the branch of science that deals with the study of cracks in a structure. Fracture mechanics is based upon the hypothesis that a structure always contains defects. These defects may be present in the form of surface cracks or internal cracks. Fracture mechanics analysis relates parameters coming from loading, geometry and material. Then it can be inferred under which conditions the cracks may propagate and eventually cause complete failure of the structure.

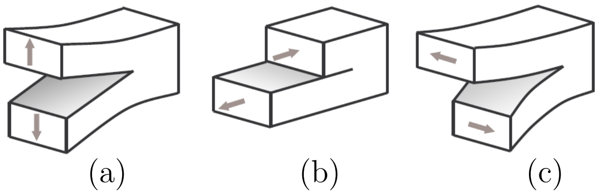
(a) (b) (c)

Figure 2.2: The three modes of delamination (a) Mode I; (b) Mode II and (c) Mode III.

Figure 2.2 illustrates the three elementary modes of failure.

- Mode I (opening mode) corresponds to a tensile stress generated by the displacement perpendicular to the crack plane.
- Mode II (shearing mode) corresponds to a shear stress in the crack plane generated by the displacement perpendicular to crack front.
- Mode III (tearing mode) corresponds to a shear stress generated by a displacement parallel to the crack front.

Originally, fracture mechanics was developed for homogeneous isotropic materials. Soon after introduction it has been used very efficiently to characterize composite materials [92]. The composite materials are very stiff in laminate plane and behave as linear elastic materials under large displacements. Damage is supposed to be confined in a very small zone as compared to the other specimen dimensions. In addition, fracture is “brittle” i.e. the fracture point is found in the linear part of force-displacement curve. Thus analysis by Linear Elastic Fracture Mechanics (LEFM) is a suitable choice.

2.1.1.1 Strain Energy Release Rate

The analysis of crack initiation and propagation is based upon energy balance between initial and final states. This approach considers that extension of a crack requires an addition of energy related to creation of a new surface. This energy is supplied by the loss of potential energy of cracked body. The crack can propagate under the condition that this loss of potential energy should be at least equal to the energy required for creation of new surface. In other words, the work required to extend a crack from initial length a to $a + \Delta a$ will be same as the energy required to close the crack from $a + \Delta a$ to a. For crack propagation the energy balance is written as follows:

$$\mathrm{d}U_{total} = \mathrm{d}W_{ext} - \mathrm{d}U_e - \mathrm{d}U_d - \mathrm{d}U_k - 2\gamma \cdot \mathrm{d}A = 0 \tag{2.1}$$

Where:

U_{total} : Total energy of the system
W_{ext} : External work done for crack propagation
U_e : Elastic strain energy stored in system
U_d : Dissipated energy
U_k : Kinetic energy
γ : Superficial decohesion energy
$\mathrm{d}A = b \cdot \mathrm{d}a$: Crack surface created by extension $\mathrm{d}a$, b is breadth dimension

The dissipated energy by crack propagation is therefore $2\gamma \cdot \mathrm{d}A$ as there are two new surfaces created about crack plane. In context of LEFM, the only energy dissipated is the superficial cohesion energy. Since the dissipated energy $dU_d = 0$.

The crack propagates when the kinetic energy of the system increases. The propagation condition is written as:

$$\frac{\mathrm{d}(W_{ext} - U_e)}{\mathrm{d}A} - 2\gamma = \frac{\mathrm{d}U_k}{\mathrm{d}A} \geq 0 \tag{2.2}$$

Let $\Pi = U_e - W_{ext}$ where Π represents the potential energy stored in the structure, we define:

$$\mathcal{G} = -\frac{\mathrm{d}\Pi}{\mathrm{d}A} \tag{2.3}$$

Where $\mathcal{G}$ is the strain energy release rate, i.e. the surface energy available for crack propagation. The energy required for creation of a unit crack surface is:

$$\mathcal{R} = 2\gamma \tag{2.4}$$

Where $\mathcal{R}$ is called resistance to crack propagation.

The Griffith's propagation criteria implies that:

- Stable Propagation : $\frac{\mathrm{d}U_k}{\mathrm{d}A} = 0$ or $\mathcal{G} = \mathcal{R} \implies$ The available energy, $\mathcal{G}$, is equal to the energy required for new surface creation, $\mathcal{R}$.
- Unstable Propagation : $\frac{\mathrm{d}U_k}{\mathrm{d}A} > 0$ or $\mathcal{G} > \mathcal{R} \implies$ The excessive energy is dissipated as kinetic energy.

2.1.1.2 Quasi-Static Tests

In the following paragraphs introduce the widely accepted methods for mode I, II and mixed-mode strain energy release rate characterization. Details of less popular methods can be found in Lachaud [92], Prombut [128] and Tay [145].

Mode I

The double cantilever beam test has been standardized for mode I strain energy release rate characterization [11, 83]. This test method consists of a composite beam with an initial defect. The initial delamination is made to propagate by pulling the two composite arms in a direction perpendicular to the plane of defect. The two beams are loaded as cantilever beams, therefore the test is named double cantilever beam test. As the two arms separate from each other pure mode I propagation is obtained.

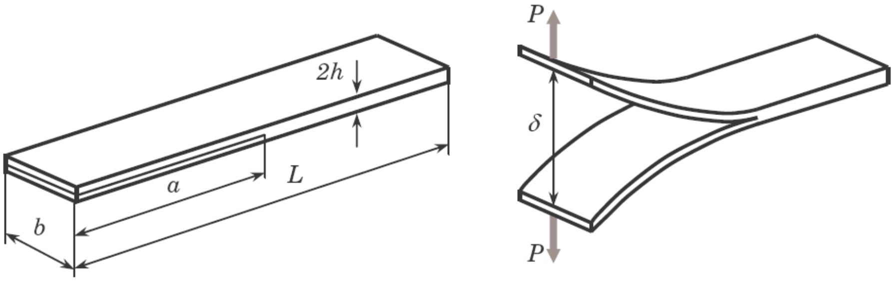

Figure 2.3: Double cantilever beam (DCB) specimen for Mode I testing [152].

A very thin non-stick film is used to induce initial defect (thickness less than $13\mu m$ as recommended by ASTM–D5528–01 [11] and ISO–15024 [83] standards. The resin rich zone found near end of this film may give incorrect values of interlaminar toughness. The specimen over all length L is 120 mm, breadth b is $20 - 25$ mm and thickness $2h$ is $3 - 5$ mm.

If E_f is the flexural modulus of the beam then strain energy release rate in accordance with beam theory is given by:

$$\mathcal{G}_I = \frac{12P^2a^2}{b^2E_fh^3} \tag{2.5}$$

$$C = \frac{8a^3\delta^2}{bE_f h^3} \tag{2.6}$$

Where C is the compliance of the beam. By combining the above two equations, it is possible to obtain strain energy release relationship in terms of displacement

$$\mathcal{G}_I = \frac{3E_f h^3\delta^2}{16a^2} \tag{2.7}$$

Mode II

Mode II delamination, or shearing mode, is produced due to relative sliding movement of opposite crack surfaces. Although Carlsson et al. [36] invented the method in 1986 it is yet to be standardized. One of the difficulties is that mode II crack propagation is accompanied by the formation of a damage zone, matrix microcrack ahead of the crack tip, which finally coalesce. Hence, it is difficult to determine the real crack length. Friction between sliding surfaces is another factor adding to uncertainty. These problems thus generate great variability in results obtained in mode II. As a consequence, a single $\mathcal{G}_{IIc}$ value as material property is hard to obtain [152].

Two popular experimental methods for mode II strain energy release rate determination are: (**a**) end-notched flexure (ENF see Figure 2.4) and (**b**) end-loaded split (ELS see Figure 2.5). In both methods, delamination is propagated by shear loading of specimen and growth is monitored. Specimen preparation and initial defect induction are essentially similar to mode I specimens.

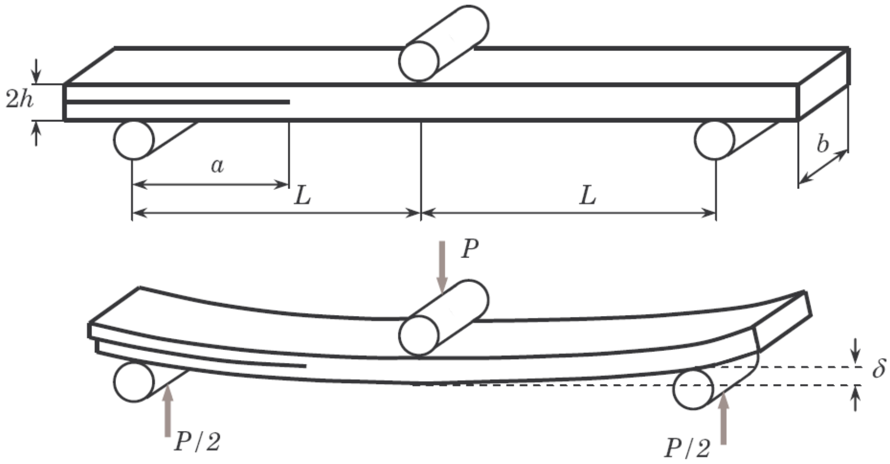

Figure 2.4: End Notch Flexure (ENF) specimen for Mode II testing [152].

As shown in Figure 2.4, ENF is a three point bending, Davies et al. [46], of composite beam containing initial defect. According to beam theory approach, mode II energy release rate as function of applied load and compliance of specimen can be obtained as follows:

$$\mathcal{G}_{II} = \frac{9P^2a^2}{16b^2E_fh^3} \tag{2.8}$$

$$C = \frac{3a^2 + 2L^3}{8bE_fh^3} \tag{2.9}$$

The term $2L^3$ corresponds to compliance of the system without initial defect. Thus the energy release rate as function of displacement can be obtained as:

$$\mathcal{G}_{II} = \frac{36\delta^2E_fh^3a^2}{(3a^3 + 2L^3)^2} \tag{2.10}$$

Another difficulty with this test is the unstable crack growth. Crack growth is only stable for the ratio $a/L > 0.7$. Most studies with ENF use an $a/L = 0.5$, hence instable crack growth. To avoid this problem a new version, 4 point end-notched flexure (4ENF), of the test can be found in Davies et al. [46].

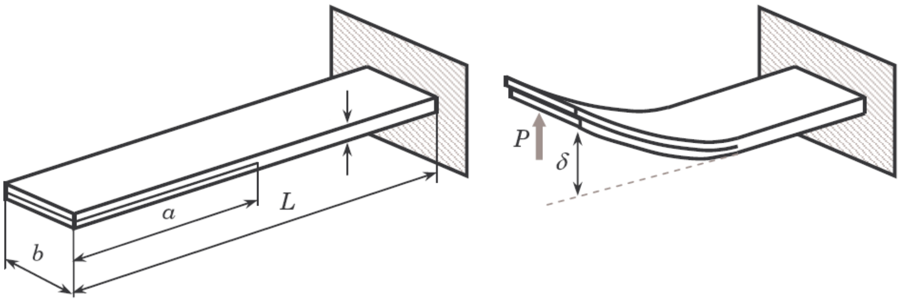

Figure 2.5: End Loaded Split (ELS) specimen for Mode II testing [152].

End loaded split is another method of obtaining pure mode II strain energy release rate. ELS is preferred over ENF for stable delamination propagation. The undamaged portion of specimen is clamped while the end containing delamination is loaded by applying a displacement or force perpendicular to plane of specimen, Davies et al. [47]. Crack propagation is stable if the condition $a/L > 0.55$ is verified. The fixture required is however not straight forward but complicated to provide a perfect boundary conditions.

The beam theory equation of strain energy release rate and compliance for ELS specimen is given by:

$$\mathcal{G}_{II} = \frac{9P^2a^2}{4b^2E_fh^3} \tag{2.11}$$

$$C = \frac{3a^3 + L^3}{2bE_fh^3} \tag{2.12}$$

In terms of displacement the $\mathcal{G}_{II}$ is given as:

$$\mathcal{G}_{II} = \frac{9\delta^2E_fh^3a^2}{(3a^3 + L^3)^2} \tag{2.13}$$

Some other pure mode II test methods exist but are not very commonly used, among these are: the rail shear method, stabilized end notched flexure (SENF), center notched flexure (CNF) [109] and cantilever bend end notched method (CBEN).

Mixed mode I+II

Most commonly used test method for mixed mode delamination propagation characterization is the mixed mode bending (MMB see Figure 2.6) method proposed by Crews, Jr and Reeder [42]. This test method is now part of ASTM standards as ASTM–D6671–06 [12]. This method uses a specimen identical to the DCB specimens and allows determination of interlaminar fracture toughness for mixed mode ratios I/II ranging from pure mode I to pure mode II. Mode participation ratio I/II can be varied by changing the loading point on lever (modifying distance c) or by changing the fulcrum position on the lever arm (varying distance d).

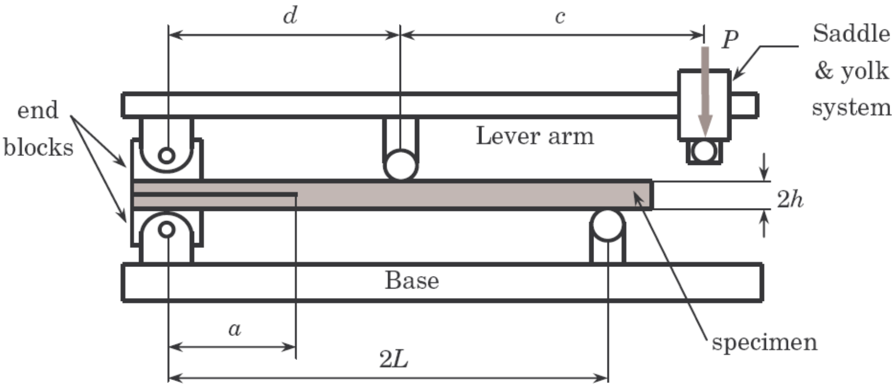

Figure 2.6: Mixed-Mode Bending (MMB) apparatus for Mode I+II testing [152].

When a downward force is applied on lever arm, central portion of specimen experiences a downward force and tensile load is applied through end blocks. To keep lever arm vertical, a saddle and yolk system in combination with rollers is used to reduce friction loads. The final equations for energy release rates are of the form:

$$\mathcal{G}_I = \frac{3\delta^2 E_f h^3}{4a^4\left(\dfrac{c+d}{2L} - 1 + \dfrac{c}{2}\right)^2} \tag{2.14}$$

$$\mathcal{G}_{II} = \frac{9\delta^2 E_f h^3 a^2}{\left(3a^3 + \dfrac{d^2(2L-d)^2}{2L}\right)^2 \left(\dfrac{c+d}{2L} - 1 - \dfrac{c}{2}\right)^2} \tag{2.15}$$

Other mixed mode testing methods include mixed-mode end loaded split (MMLES), cracked lap shear test (CLS), open notched flexure (ONF) etc, [128].

2.1.1.3 Dynamic Tests

Dynamic testing of composites is an active field of research at the moment. The dynamic test methods are yet to be standardized. In the following paragraphs a few of the test methods which seem to give reliable results are presented.

Mode I

Smiley and Pipes [138] used DCB geometry with high cross-head speeds to study rate effects on mode I fracture toughness. They observed a negative rate effect i.e. for graphite epoxy materials the fracture toughness decreased from $180 - 40$ J/m^2 over 4 decades of loading rate.

Kusaka et al. [91] also used DCB specimen, but crack opening in dynamic loading was obtained by placing a wedge mounted on SHPB, see Figure 2.7(a). They were able to identify a transition region for unstable crack propagation. Below and above this transition region crack propagation is stable. As far as the rate effects are concerned, the average fracture toughness value decreased with loading rate. Sun and Han [141] also used wedge insert fracture (WIF) test method, see Figure 2.7(b), to test glass and carbon fiber composites. In their experiments with SHPB, they obtained crack speeds of $1000s^{-1}$. Their experiments showed that dynamic fracture toughness of a crack propagating at a speed up to $1000s^{-1}$ equals the static fracture toughness. Accurate determination of crack location, specimen preparation and initial defect generation are some of major problems for thick WIF tests.

Dong et al. [52] have shown that a Brazillian disk specimen containing a central crack can be used to find dynamic stress intensity factors for brittle materials. Banks-Sills et al. [14; 15] have used the similar specimen geometry to find strain energy release rate equations for 0°/90° and $+45°/-45°$ interface pairs. Theoretically it is possible to test mixed mode behavior by simply orienting the crack at an angle to the bars longitudinal axes. Specimen preparation is the major issue with these tests. Specimens used by Banks-

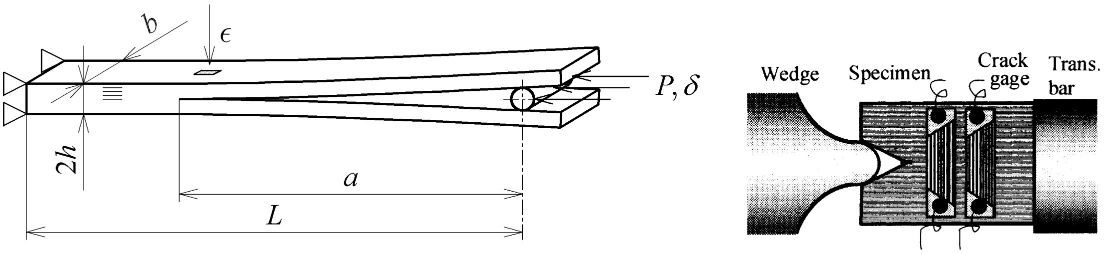

(a) Thin WIF specimen [90]. (b) Thick WIF specimen [141].

Figure 2.7: Two variants of wedge insert fracture (WIF) specimen.

Sills et al. [14; 15] were glued to aluminum, thus adding uncertainties related to interface (**a**) residual stresses and (**b**) strain rate dependent behavior.

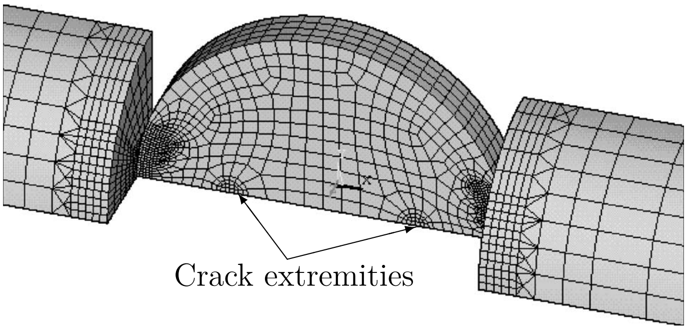

Figure 2.8: FEA simulation of a Brazilian disk specimen [52].

Modified 3-point bending tests of Wu and Dzenis [159] showed a decrease of $10-20\%$ for mode I dynamic fracture toughness while mode II dynamic fracture toughness did not differ from the static value.

Mode II

Maikuma et al. [110] invented CNF specimen for specific purpose of dynamic testing. The specimen is dynamically loaded by drop tower. Their analysis takes into account effects of kinetic energy. They observed a decrease of 20 and 28% for initiation values for AS4/2220-3 and APC-2. Mode II interlaminar propagation toughness was reduced by 24 and 44% for AS4/2220-3 and APC-2 over 5 decades of loading rate. In the case of a CNF specimen the pre-cracking, i.e. cracking of the resin rich areas found near the end of initial delamination film, is not a straight forward job.

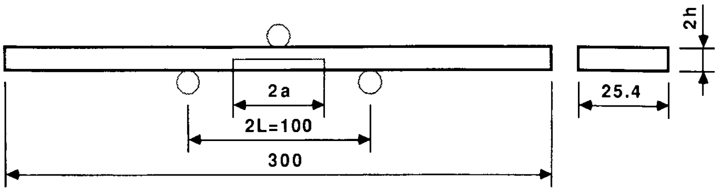

Figure 2.9: CNF specimen for mode II testing [110].

Todo et al. [147] used ENF specimen with drop tower to study $\mathcal{G}_{IIc}$ of carbon fiber and glass fiber composites. They observed a 53% increase in $\mathcal{G}_{IIc}$ for carbon fiber composites while a decrease of 34% was observed for glass fiber composites.

Nwosu et al. [119] used SHPB apparatus for dynamic pure mode II delamination study. CNF and ENF specimen were studied. They concluded that delamination and energy absorbed were increased with loading rate. It was further observed that cracks in CNF contributed more to mode II fracture than edge cracks of ENF. CNF specimens showed a higher compressive strength and sustained higher energy absorption than ENF. Thus one can assume that cracks found near the edge have greater tendency to reduce structural strength than cracks embedded deeper.

Mixed-mode I+II

Widely used dynamic mixed mode specimen is the ONF specimen. Wosu et al. [158] employed this specimen in Hopkinson's bar experiments. They argue that effect of kinetic energy before fragmentation is not significant and can be neglected. At impact energies $E_i \leq 4$ J, dynamic and total strain energy release rates are independent of mixed-mode rotation. While at higher impact energies $4 \geq E_i \leq 9.3$ J, dynamic strain energy release rate decreases with mixed mode ratio, while total strain energy release rate increases rapidly.

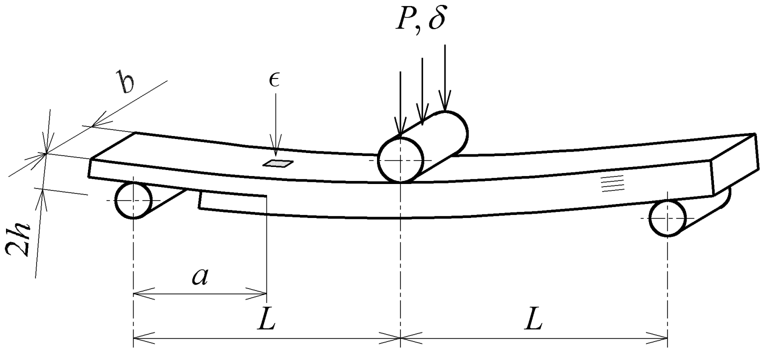

Figure 2.10: ONF specimen for mixed-mode testing [90].

Kusaka [90] also tested ONF specimen with a 3-bar SHPB system. They deduced that pure mode I and II strain energy release rates decreased after reaching a local maximum. Furthermore at higher strain rates the linear fracture criteria was not verified. Thus indicating a positive strain rate dependence. The individual fracture toughnesses may decrease but the mixed mode behavior improves with higher strain rates.

Liu et al. [102] used Brazilian disk specimen to investigate mode I, mode II and crack tip mixed mode fracture toughnesses. They concluded that mode I fracture toughness was unaffected by the loading rate while mode II fracture toughness showed an increase of 50% under impact loading.

2.1.2 Liner Elastic Fracture Mechanics Based Numerical Modeling

The linear elastic fracture mechanics method, for delamination modeling, has been used extensively where the shape of the delamination front can be predicted and a suitably shaped finite element mesh can be provided. However, when irregular shaped delamination fronts are anticipated, this method requires an adaptive mesh approach that is another costly computational process. The cohesive fracture model solves some of the limitation of the linear elastic fracture mechanics method, however a definitive study of its abilities has yet to be found in the literature [54].

2.1.2.1 Different Methods for in Plane Nodal Opening

The use of FE methods is well known and has been developing since the 1970s. The ability to discretized continuum into a collection of regular shapes has provided a powerful analysis tool for many applications, however this ability may be considered a liability when fracture is considered.

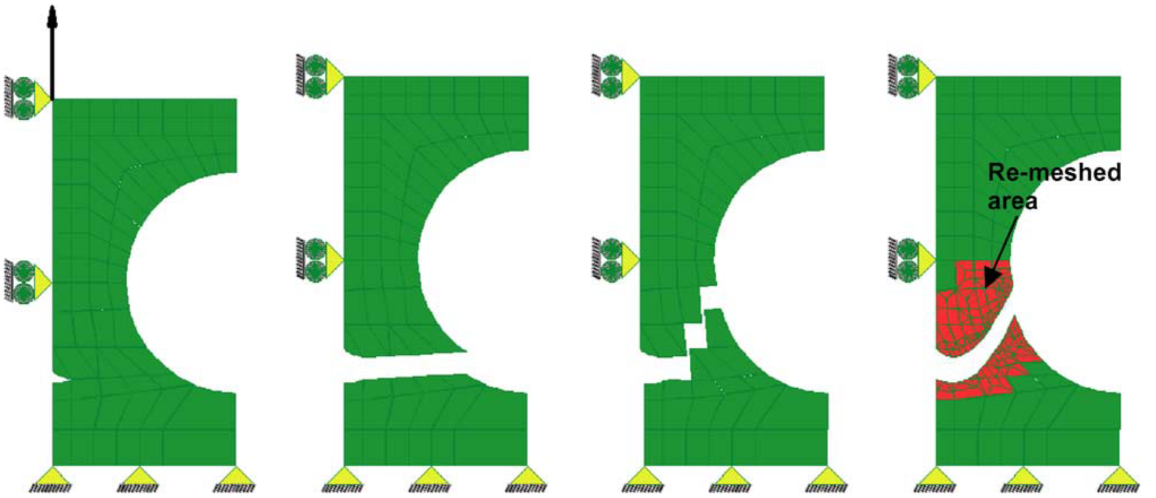

(a) Cracked Structure (b) Plane Fracture (c) Stepped Fracture (d) Re-meshed Fracture

Figure 2.11: Uni-axially loaded structure, note re-meshed crack fracture, [54].

Let us consider a simple structure discretized by finite elements with an initial crack and subjected to a uni-axial tension force as shown in Figure 2.11(a). An admissible solution is obtained if the crack is assumed to propagate along the element boundaries as shown in Figure 2.11(b). However, this may over-predict the fracture load as the solution may not be the minimum energy solution. If the crack is assumed to propagate in steps along element boundaries, as shown in Figure 2.11(c), the solution is inadmissible solution and incompatible with the LEFM. The correct solution is obtained by adaptive remeshing of structure, as shown in Figure 2.11(d).

2.1.2.2 Cohesive Fracture Mechanics

In 3D an interface is a surface of a volume. The problems of: (**a**) curved fronts and (**b**) initial flaws can both be overcome by using hypothetical *"interface elements"* by placing them at potential delamination sites. Progressive delamination is then modeled by introducing a softening traction/relative displacement relationship as a *"material model"* for the interface elements see Figure 2.12. Fracture mechanics is indirectly introduced because the area under the softening curve is equated (as an input parameter) to critical fracture energy ($\mathcal{G}_c$) [113].

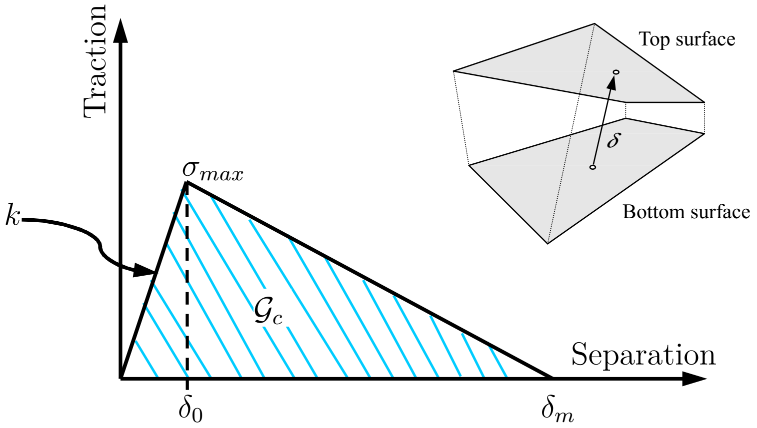

Figure 2.12: Traction-relative displacement law.

$$\mathcal{G}_c = \int_0^{\delta_m} \sigma \, \mathrm{d}\delta \tag{2.16}$$

In implicit Finite Element (FE) codes, decohesion elements have been successfully used to simulate standard delamination toughness tests (Double Cantilever Beam (DCB), Mixed-Mode Bending (MMB) and End Notch Flexure (ENF)) [8, 31, 33, 51, 113].Camanho and Dávila [31] simulated debonding of skin/stiffener specimens. Overlap tests were simulated by Mi et al. [113]. While, De Moura et al. [51] simulated compression after impact (CAI) of composite plates. In explicit analyses, non-linear springs have been used to model the interfaces in layered composites [157]. Some work using a cohesive zone approach is presented by Johnson et al. [86], where the application is penetration impact of a steel ball in a composite plate.

Delamination simulation of laminated composites can be divided in: (**a**) delamination initiation and (**b**) delamination propagation [33]. Delamination initiation analyses are usually based on stresses and use criteria such as the quadratic interaction of the interlaminar stresses in conjunction with a characteristic distance [34]. The characteristic distance is an averaging length that is a function of geometry and material properties, so its determination always require extensive testing [31]. Delamination initiation can be related to interface stiffness (k) [113].

The interface/decohesion elements can be divided into two main groups [33]: (**a**) continuous interface elements and (**b**) point decohesion elements. Different authors have proposed a variety of continuous decohesion elements: (**a**) zero-thickness volumetric elements connecting solid elements [50], (**b**) finite-thickness volumetric elements connecting shell elements [131], and (**c**) line elements [16, 53]. Point decohesion elements are identical to non-linear spring elements connecting nodes [32, 50, 58].

Reedy, Jr et al. [131] implemented an eight node hex constraint element to connect opposing sub-laminate shell elements, this made the two opposing shell elements act as a single shell element until a prescribed failure criterion was satisfied. Once the failure criterion was met, the connection was broken, and a discrete delamination initiated and propagated.

Farley and Jones [58] model delamination by disconnecting "zero length" extensional springs between coincident nodes of adjacent shell elements when the energy release rate reaches a critical value. Their large deformation analysis uses a nonlinear elastic idealization with a maximum strain failure criterion for the in-plane material model. This interface element looks like, and is meshed like a standard hex element, but it is massless. It does not use shape functions, [164]. It shares nodes with two, opposing sub-laminate shell elements and uses these nodal displacements and rotations to determine the nodal forces and moments that are needed to make the opposing shell elements act as single element until the connection is broken.

Li and Sridharan [99] have compared a continuum solid element with a small finite thickness and cohesive element with zero-initial thickness for delamination simulation. They have found that cohesive element was able to predict both crack initiation and large crack growth with sufficient accuracy. The solid element model also consistently predicted crack initiation, but was unable to predict the crack growth accurately. It gave consistently higher loads for given crack extensions and predicted that the crack growth shut off prematurely. Further examination illustrated that in the case of solid elements a "*neck*" developed due to compressive stresses at some distance from the crack tip. Apparently this neck formation "*locked*" the crack from growing and caused the inaccurate results given by the model.

They argued that there are four parameters of the model, viz. initial stiffness (k), maximum stress (σ_{max}), failure strain (ϵ_f) and the thickness of the cohesive layer in the context of a single mode of fracture, say in mode I. They also showed that the thickness of the cohesive layer did not affect the performance of the model provided its value is of the same order of magnitude as the process zone thickness. Alfano and Crisfield [7] have also shown that thickness of cohesive layer does not play any role in the mechanics of layer itself.

In another work, Borg et al. [22] used a discrete cohesive zone approach to model delamination. Coincident nodes were tied together with a penalty formulation before delamination onset. During damage propagation, the nodal forces were reduced to zero as the amount of dissipated work approached a value corresponding to the fracture energy, which was obtained from the fracture toughness using the respective nodal area. Borg et al. [23; 24; 25] then modified the model to use a damage formulation in a penalty contact algorithm for shell elements. When simulating contact between shell elements, there are no coincident nodes as for solid elements. Instead the contact takes place at the surfaces of two adjacent shell elements. The delamination model is made up of two components. The first is an adhesive penalty contact for bonding initially tied shell elements. It accounts for the thickness offset when calculating penalty forces and penalty moments. With this penalty contact formulation it is possible to model composite laminates using multiple layers of shell elements, one for each individual lamina in the laminate. The second part of the delamination model is the cohesive zone model. It is based on a damage formulation which reduces the adhesive forces/stresses as adjacent shell elements debond.

2.1.2.3 Strain Rate Effects

Harding and Li [70] reported that an increase in loading rate of about six orders of magnitude raised the average value of shear stress on the failure plane by ≈ 70%, for the carbon/carbon interfaces. Later on, in a study by Li et al. [98], the influence of through-thickness compressive stress on the Mode II damage evolution was studied. It was shown that the increase of $\mathcal{G}_{IIc}$ is a corresponding result of the increased shear strength. The normal compression can significantly suppress delamination by increasing both the shear strength and fracture energy.

Guedes et al. [67] studied the dynamic response of quasi-isotropic laminates by compression with SHPB. They observed a considerable increase in failure strength when compared to the static values. They also observed that the specimen failed by splitting into sub-laminates. From their point of view, fundamentally the interfaces were excited during these experiments and participation from plies could be neglected. As a consequence it can be further hypothesized that the strain energy release rate increases with high strain rate.

For numerical modeling Guedes et al. [67] and Li et al. [98] considered a similar approach. Under dynamic loading conditions, area under the curve was increased to take into account this positive loading rate effect.

2.1.3 Emerging Discrete Methods/Use of SPH

In a previous study carried out at our laboratory, Jacquet [84] while using SPH method obtained good, qualitative, representation of high speed impact damages. In this study each ply and interface was modeled by a layer of particles. The positive point of the method is the interaction between stress states of interface and plies. As the stress coupling is “natural” due to sphere of influence (to be described: sphere of influence in chapter 1) and therefore no need to define extra contact conditions between plies and interfaces. The method seems to be promising as it allows the crack branching without prior knowledge of damage location [114]. The downside of this method is that, to date, the method has not been stable enough, [82], to distinguish the orientation of fracture surfaces from the deformed views, [84]. This might be due to uncontrolled numerical failures yet to be studied.

2.1.4 Concluding Remarks

The experimental studies found in literature show that the standard test methods exist for determination of pure mode I and mixed mode I+II strain energy release rates under static loading. ENF and ELS type of tests are usually carried out to determine mode II strain energy release rate but a standard test procedure does not exist to this time. Therefore, the DCB, ELS and MMB tests have been studied in this study.

In the case of dynamic strain energy release rate characterization, no standard test method exist for any pure mode or mixed mode loading. Different authors have reported different results depending upon the material, test setup or type of analysis carried out. It is difficult to estimate from the literature survey the dependency of strain energy release rate for materials used for this study. It is proposed that the Hopkinson’s bar apparatus can be a promising technique to investigate the dynamic loading dependent behavior of strain energy release rate.

In the previous paragraphs it is seen that for planar or stepped nodal fracture, a crack can only follow the element boundaries, which might not always be the admissible solution therefore a smaller size of elements or adaptive meshing will be required. Even if the adaptive meshing techniques, the solution might not converge due to anisotropic nature of plies and finite elements themselves. Similarly the SPH method requires some improvements from the numerical point of view to be used as truly predictive method for delamination simulations.

In authors opinion, the cohesive finite elements are a suitable choice for crack opening simulations as they are able to predict the initiation and propagation of the crack when some prior knowledge of the crack surface is available. When loading causes a crack closure, a contact has to be defined between elements adjacent to cohesive finite elements.

2.2 Developed Cohesive Interface Model

In the following paragraphs the mixed-mode cohesive material law that was developed and implemented in commercial FE code LS-DYNA® as a user defined material model is presented. At the start of this project the material law did not exist as a standard material in LS-DYNA®. As a first step the bilinear law is chosen as material model.

In LS-DYNA® decohesion elements are formulated in terms of a *traction vs. relative displacement* relationship instead of the traditional *stress vs. strain* relation [107]. Two surfaces (top and bottom) are considered, as shown in Figure 2.12. Every point in these surfaces has a corresponding point in the other surface, designated as homologous point. These homologous points have same coordinates before the interface is loaded. The relative displacement between each pair of homologous points is projected in a local reference system, which expresses the relative displacement in terms of an opening mode and a sliding mode. Sliding can be due to mode II (*shear*) or III (*tear*) loading (or a combination of both).

Prior to softening/delamination onset, an elastic constitutive law relates the relative displacement of both the top and bottom surfaces with the traction (force per unit area). For pure mode I or pure mode II problems, the interface is considered to have a linear elastic behavior until the respective maximum allowable stress is reached. Then, the stiffness is reduced in such a way that the energy absorbed per unit area is equal to the corresponding critical energy release rate ($\mathcal{G}_{Ic}$ or $\mathcal{G}_{IIc}$, respectively), see Figure 2.13.

Delamination onset relative displacements are defined as $\delta_{I_0} = \dfrac{\sigma_n}{k_I}$ and $\delta_{II_0} = \dfrac{\sigma_s}{k_{II}}$, where σ_n and σ_s are onset tractions in normal and sliding mode. Where k_I and k_{II} are cohesive elements rigidities for normal and sliding modes, respectively. The pure mode failure displacements are defined by $\delta_{I_m} = \dfrac{2\mathcal{G}_{Ic}}{k_I \delta_{I_0}}$ and $\delta_{II_m} = \dfrac{2\mathcal{G}_{IIc}}{k_{II} \delta_{II_0}}$.

The mixed-mode model is based on delamination onset and propagation approach proposed by Camanho et al. [33]. They propose quadratic interaction between the tractions to predict softening onset. The elastic relationship is valid until a stress-based initiation criterion is verified. From this stage onwards, the stiffness reduction occurs for each mode in such a way that a propagation criterion defines the energy absorbed in the mixed-mode situation. A criterion able to capture the mixed-mode fracture toughness under different mode ratios is used to predict delamination propagation. In this particular decohesion element formulation, the sliding mode (δ_{II}) is considered to represent both modes II (δ_{shear}) and III (δ_{tear}) because the distinction between mode II and III depends on the direction of the relative displacement between homologous points with respect to the orientation of the crack front. The relative displacement is defined as:

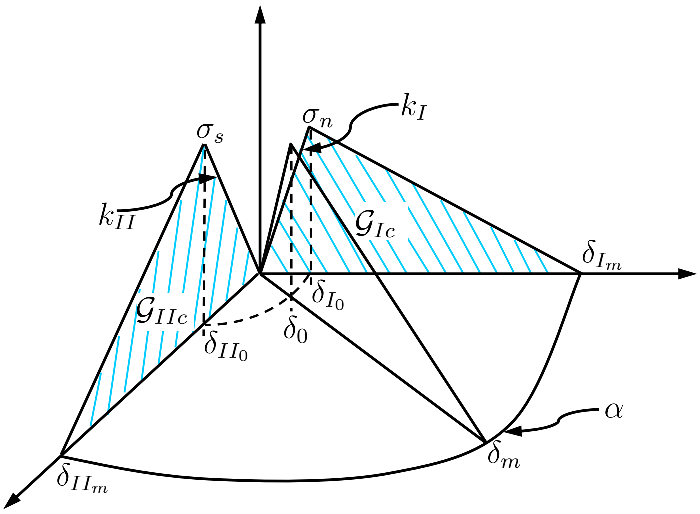

Figure 2.13: Mixed-mode traction separation law.

$$\delta = \sqrt{\langle\delta_I\rangle^2 + \delta_{II}^2} \tag{2.17}$$

where

$$\delta_{II} = \sqrt{\delta_{\text{shear}}^2 + \delta_{\text{tear}}^2} \tag{2.18}$$

For mixed mode behavior

$$\beta = \max\left(0, \frac{\delta_{II}}{\delta_I}\right) \tag{2.19}$$

Mixed-mode onset displacement is:

$$\delta_0 = \delta_{I_0}\delta_{II_0}\sqrt{\frac{1+\beta^2}{(\delta_{II_0})^2 + (\beta\delta_{I_0})^2}} \tag{2.20}$$

Mixed-mode propagation criterion is a power law as used by Mi et al. [113] and Allix et al. [10]:

$$\left(\frac{\mathcal{G}_I}{\mathcal{G}_{Ic}}\right)^\alpha + \left(\frac{\mathcal{G}_{II}}{\mathcal{G}_{IIc}}\right)^\alpha = 1 \tag{2.21}$$

In terms of relative displacement one can write:

$$\delta_m = \begin{cases} \dfrac{1+\beta^2}{\delta_0}\left[\left(\dfrac{k_I}{\mathcal{G}_{Ic}}\right)^{\alpha} + \left(\dfrac{k_{II}\beta^2}{\mathcal{G}_{IIc}}\right)^{\alpha}\right]^{-\frac{1}{\alpha}} & \Longleftarrow \delta_I > 0 \\ \delta_{II_m} & \Longleftarrow \delta_I \leq 0 \end{cases} \tag{2.22}$$

$$d = \frac{\delta_m(\delta - \delta_0)}{\delta(\delta_m - \delta_0)} \tag{2.23}$$

For carbon fiber epoxy composites, one can represent the mixed-mode data typically by using $1 \leq \alpha \leq 2$.

The two discontinuities existing in the bilinear law (at peak stress and complete decohesion) may generate numerical instabilities in an explicit implementation. In certain situations, a stress wave may be generated at those points, and excite high-frequency oscillations that can completely break the decohesion elements in the vicinity. This problem can be overcome by using damping algorithms, higher mesh refinement, lower interface strength, higher fracture toughness or lower load-rate. However, the particular finite element model that is not affected by these shock waves is not always straightforward to define [126].

2.2.1 2D Plane Strain Study

A MATLAB® program is written to better understand the above explained model. This subroutine takes less than ten minutes of CPU time to solve the finite element model with boundary conditions of a half DCB model, as shown in Figure 2.14, by using explicit time integration scheme, [164].

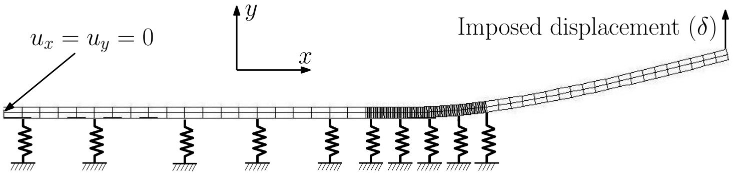

Figure 2.14: Schematic representation of MATLAB® finite element model.

The finite element consists of 2D plane strain elements, with 2 × 2 integration points. The cohesive elements are modeled as simple 1D spring elements. The symmetry of the specimen allows to model only one arm of DCB specimen. Two elements are used for the DCB arm in thickness direction. The location of the springs, as shown in Figure 2.14, is for illustration purpose only, otherwise one spring element is used for each degree of freedom for each element along x-direction where x-coordinate is zero. Total length of the arm is 120 mm, pre-crack length is 40 mm and thickness of the arm is 1.55 mm. A refined mesh with 0.2 mm long elements is used for crack propagation study. The material properties for plane strain elements are: flexural modulus, $E_f = 120$ GPa and Poisson's ratio, $\nu = 0.3$. The 1D spring elements have spring constant, $k_I = 100$ kN/mm^3 and maximum stress, $\sigma_n = 50$ MPa.

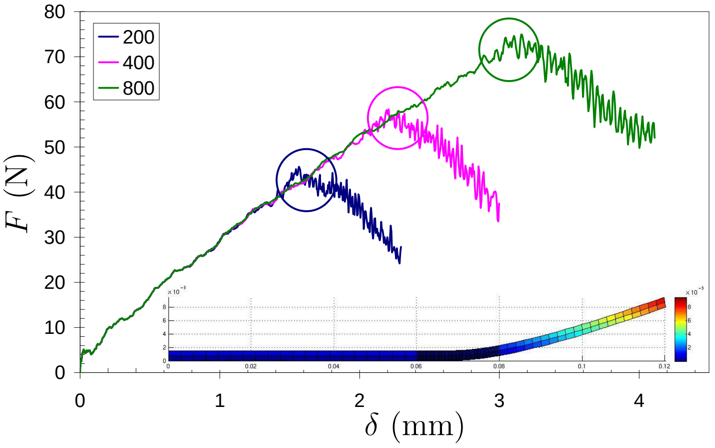

Figure 2.15: Influence of critical strain energy release rate, $\mathcal{G}_{Ic} \in \{200, 400, 800\}$ J/m^2.

Figure 2.15 shows the influence of three different values of $\mathcal{G}_{Ic}$. The higher values of $\mathcal{G}_{Ic}$ cause the crack to propagate after a larger displacement has been reached. The slope of the propagation portion of the curve is governed by the critical strain energy release rate value. With higher value of $\mathcal{G}_{Ic}$ the slope of the crack propagation portion is less steeper (green and pink curves). The circles in Figure 2.15 show the start of propagation portion of curve. The oscillations at this point are attributed to the bilinear cohesive law due to the transition from undamaged ($d = 0$) to partially damaged ($d < 1$) and from partially damaged to fully damaged ($d = 1$) states.

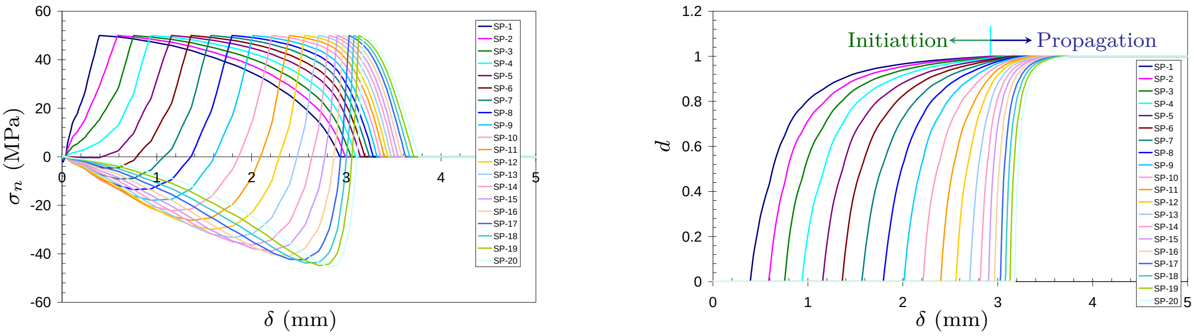

(a) σ_n vs δ

(b) d vs δ

Figure 2.16: (a) Normal stress as a function of opening displacement and (b) damage parameter as a function of opening displacement for $\mathcal{G}_{Ic} = 800$ J/m^2.

The normal stress, in first twenty springs from opening side i.e 4 mm of propagation length, as a function of opening displacement is shown in Figure 2.16(a). It is observed that each spring passes from compressive stress to tensile stress. The damage starts taking place when σ_n becomes 50 MPa, the maximum value allowed. The distance traveled by the opening end is higher for the first spring to pass from undamaged state ($d = 0$) to the fully damaged state ($d = 1$). Once the crack propagation ($\sigma_n = 0$ and $d = 1$ for first spring) occurs, this distance becomes constant. Similarly, the opening end has to travel a smaller distance to break a spring during the propagation phase as shown in Figure 2.16(b). At each instant there are 14 damaged spring elements, which allows for a stable crack propagation.

Allix et al. [9] have proposed a delay damage model to incorporate strain rate effects and as an added advantage to remove mesh dependability problems. It is to be noted that a similar delay damage effect was implemented only for 2D study of the problem, as a proper strain rate dependent interface characterization methods is not at author's disposal. If n is the current and $n-1$ the previous time-step in explicit integration scheme then, the speed of damage $\dot{d}$ at current time step is calculated as follows:

$$\dot{d}^n = \frac{1}{\tau}\left[1 - \mathrm{e}^{-\kappa\left\langle d^n - d^{n-1}\right\rangle}\right] \tag{2.24}$$

Where τ and κ are the parameters to be determined from experiment or inverse analysis as shown by [6]. d^n is calculated for current time-step by using Equation 2.23 and d^{n-1} is the value of damage parameter at previous time-step. Then the damage parameter is updated as:

$$d^n = d^{n-1} + \dot{d}^n \Delta t \tag{2.25}$$

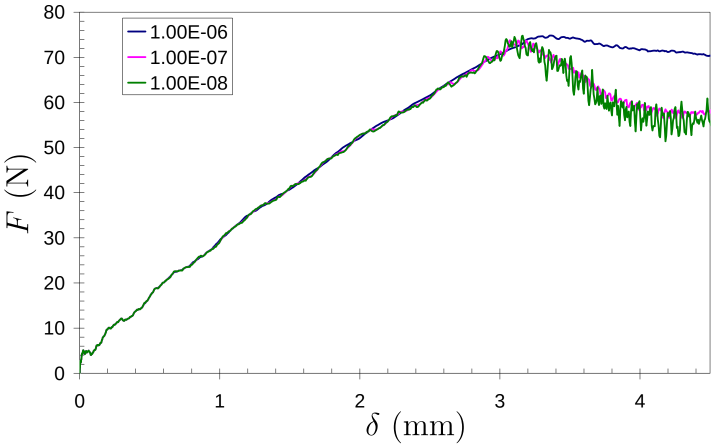

Figure 2.17: Influence of critical time τ for $\kappa = 1$.

Figure 2.17 shows the influence of parameter τ on the crack propagation response. One can see that the higher values of τ tend to diminish the oscillations and a stable crack propagation is achieved. This also modifies the slope of the propagation part of the curve which is an indirect modification in the value of $\mathcal{G}_{Ic}$.

2.3 Numerical Parameter Identification

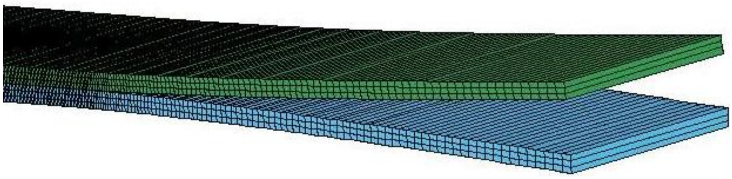

Figure 2.18: A typical finite element mesh for DCB specimen.

In the following paragraphs some of the purely numerical parameters that might influence simulation results are discussed. Then numerical and experimental results of (i) double cantilever beam (DCB), (ii) end-loaded split (ELS) and (iii) mixed-mode bending (MMB) tests are discussed. The finite element models consist of eight node brick elements with one integration point for composite arms and one element in breadth direction. Three elements are placed in thickness direction. A zero thickness layer of four point cohesive elements is placed between the two composite arms. Cohesive elements are deleted from the calculation when δ_m is reached for any integration point in cohesive elements.

2.3.1 Numerical Parameter Sensitivity Study

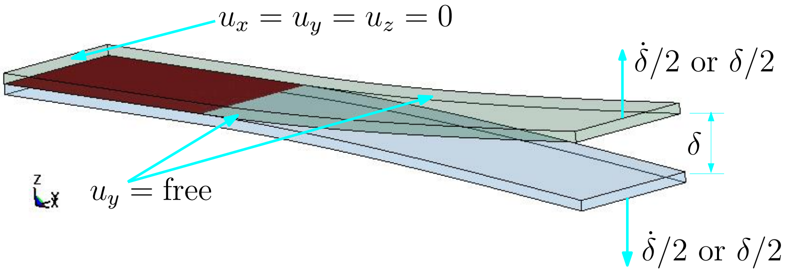

Figure 2.19: Numerical model, load and boundary conditions (DCB).

In order to obtain a numerical model conforming to the hypotheses of mechanics and experimental conditions, a double cantilever beam (DCB) test case from [126] is investigated. The loading and boundary conditions are shown in Figure 2.19. Material data and loading displacement rate are same as Pinho et al. [126]. Specimen dimensions are: $a_0 = 53$ mm, $b = 20$ mm and $h = 3.1$ mm. Composite arms of DCB specimen have flexural modulus, $E_f = 119$ GPa and $\nu = 0.3$. For interface elements: maximum normal stress for mode I, $\sigma_n = 60$ MPa and the interface stiffness, $k_I = 100$ kN/mm^3. The DCB arms opening rate, $\dot{\delta} = 560$ mm/sec.

Influence of Damping: A nodal mass proportional damping algorithm was invoked as proposed by Crisfield et al. [43]:

$$[D] = 2\omega_n [M] \tag{2.26}$$

Where ω_n is the lowest eigenvalue of structure, and D is the damping matrix. In this particular case a global damping constant $(2\omega_n)$ of 3,000 in international system of units (SI) is used.

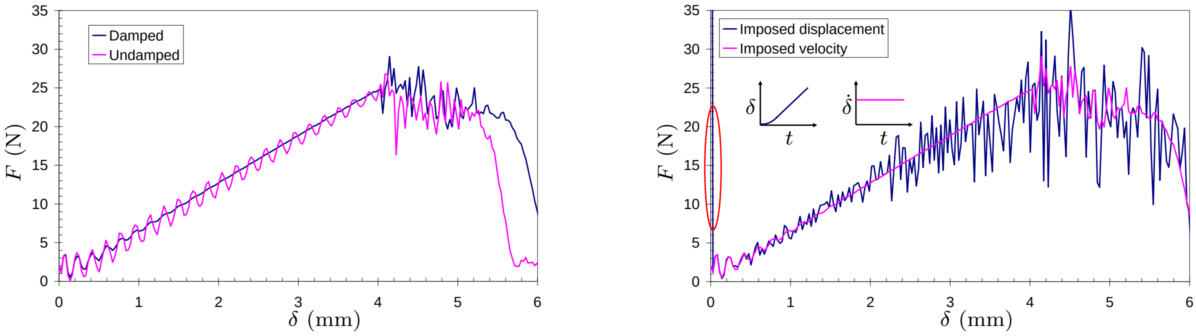

(a) Damped and undamped global response.

(b) Imposed displacement and imposed velocity global response.

Figure 2.20: Effect of damping and type of loading on numerical model.

The effect of damping is shown in Figure 2.20(a). The damped simulation shows a more stable response even after the crack starts to propagate, ($\delta \approx 4$ mm). There is a sudden dip of force as soon as the crack propagates in the case of undamped simulation. The undamped numerical model fails ($\delta \approx 5.2$ mm) before the damped model.

Imposed displacement and imposed velocity: Next the method of loading the DCB specimen, as shown in Figure 2.20(b), is studied. In an actual DCB experiment the specimen is loaded via imposed constant displacement (acceleration=0) of specimen holding ends (Figure 2.26). The finite element code LS-DYNA® proposes various possibilities of loading a specimen i.e (i) imposed displacement, (ii) imposed velocity, (iii) imposed acceleration and (iv) imposed force. The first two possibilities are compared in order to be compatible with the assumption of constant loading rate in an experiment. The respective loading curves as a function of time are shown in Figure 2.20(b). It is observed that for this particular case the imposed displacement generates two numerical shocks in the simulation: (i) at time $t = 0$ sec and (ii) when the slope of the curve changes to give a constant loading rate. The oscillations due to waves propagating in the system cannot be damped out even though a global mass proportional damping is used. On the other hand the imposed velocity response is more stable due to the type of finite difference integration scheme used by the finite element code. The numerical failure of DCB specimen occurs due to hourglass mode perpendicular to xz-plane, as shown in Figure 2.21.

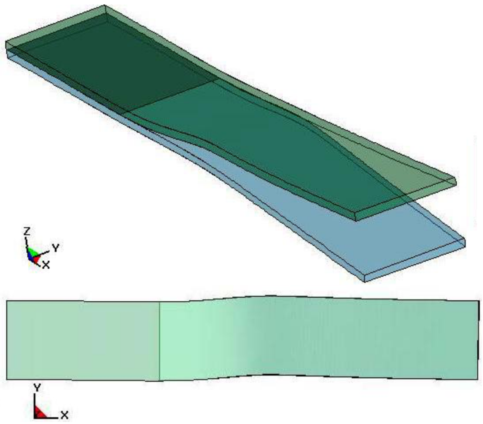

Figure 2.21: DCB specimen numerical failure due to hourglass mode.

Hourglass modes: are zero energy modes which appear due to the use of under-integrated elements (Figure 2.22). These deformation modes can have severe negative effects as explained in the previous paragraph. The finite element code LS-DYNA® proposes different formulations to control these purely numerical effects. The fundamental principal of these formulations is to apply viscous damping or small elastic stiffness capable of stopping the anomalous modes with negligible effects on stable global deformations.

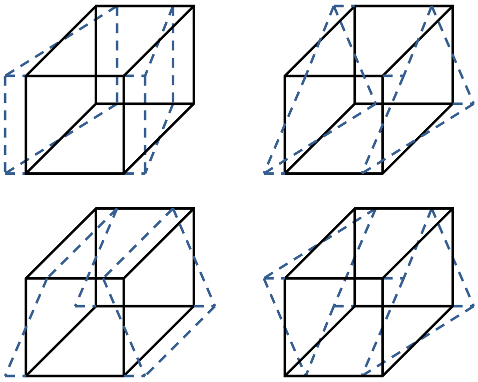

Figure 2.22: Schematic representation of hourglass modes.

Influence of hourglass formulations: In order to obtain pure mode I response and alleviate the hourglass mode perpendicular to xz-plane, displacements of all the nodes on faces parallel to xz-plane are blocked in y-direction, Figure 2.23. The imposed velocity is same as explained above.

Figure 2.24 shows $F-\delta$ curves of a DCB simulation with different hourglass formulations proposed in LS-DYNA®, [107]. None of these formulations allowed to exactly recover ref. [126] results. The author was unable to reproduce the linear elastic portion

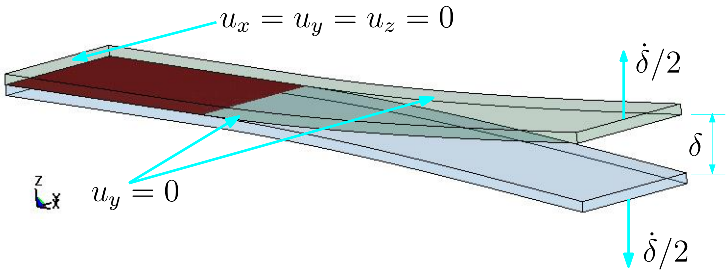

Figure 2.23: Retained numerical model, load and boundary conditions for DCB.

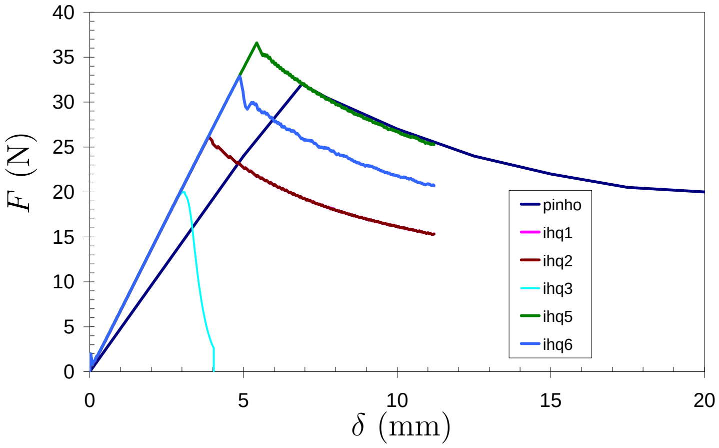

Figure 2.24: Comparison of different hourglass controls with Pinho et al. [126].

of the curve i.e the initial global stiffness of structure (Figure 2.24) the crack propagation portion of the curve was obtained with sufficient accuracy. The force displacement response of hourglass control types ihq=1 and ihq=2 is superimposed and underestimates the peak force as does ihq=6, moreover ihq=3 (a viscous formulation) is not suitable in this particular case, [79]. It can be seen that ihq=5 is best suited to represent the physical model as it reproduces qualitative as well as quantitative results.

Influence of interface element length: Figure 2.25 shows influence of length of cohesive elements, the analyses conducted during the study demonstrated that the element size is a key factor for the development of accurate FE models as highlighted by [7, 63, 113]. In particular, it was observed that the decohesion process zone ahead of the crack tip should be represented by a sufficient number of cohesive elements in order to achieve a smooth crack growth and a structural response unaffected by large oscillations and abrupt jumps or irregularities. Geubelle and Baylor [63] propose that a rough idea of the cohesive zone size R can be obtained from the following static expression:

$$R = \frac{\pi}{2}\frac{E}{1-\nu^2}\frac{\mathcal{G}_{Ic}}{\sigma_{max}^2} \tag{2.27}$$

They further showed that the element size must be chosen at least two or three times smaller than the static estimate of the cohesive zone size to ensure the convergence of the

CVFE scheme [63]. This conclusion is in agreement with that reached by Camacho and Ortiz [30] for their extrinsic CVFE scheme.

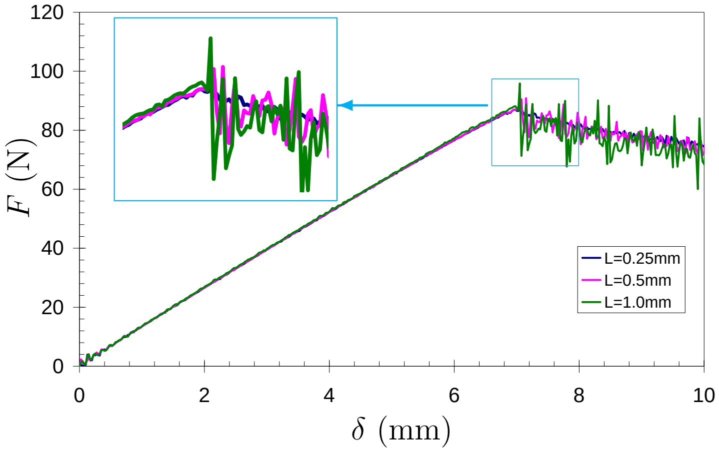

Figure 2.25: Influence of length of cohesive finite elements.

Figure 2.25 shows results of different element lengths of cohesive finite elements on global response of a DCB simulation. The model material properties are, (i) DCB arms: $E_f = 120$ GPa and $\nu = 0.3$ (ii) cohesive elements: $k_I = 100$ kN/mm^3, $\mathcal{G}_{Ic} \approx 800$ J/m^2, $\sigma_n = 60$ MPa and length of cohesive zone is ≈ 0.4 mm. It is observed that smaller the length of a cohesive element, the less oscillatory the response is. As soon as the length of the interface element becomes bigger than the cohesive zone, the response becomes more perturbed.

2.3.2 Identification of Mode I Parameters

Double cantilever beam (DCB) tests of T800S/M21 were conducted with specimen dimensions as 120 mm (L) × 25 mm (b) × 3.1 mm ($2h$). A pre-crack of 40 mm is realized by introducing a 13 μm thick Teflon® film. Tests were carried out on a servo-hydraulic machine under a constant displacement rate of 2 mm/min for quasi-static [83] and 30 m/min (0.5 m/sec) for pseudo-dynamic tests. For dynamic tests the specimen is pre-cracked up to 45^{+1}_{-1} mm to avoid artificial increase in critical strain energy release rate values often observed in the case of dynamic mode II experiments, [110]. Crack length was measured by two methods, (i) a traveling microscope and (ii) KRAK GAGES from RUMUL© see Figure 2.26. Critical strain energy release rate calculations are based on values obtained visually for quasi-static tests. The initiation values of ≈ 450 J/m^2 and propagation values of ≈ 800 J/m^2, for $\mathcal{G}_{Ic}$, have been reported by [128] while using a similar material (T700S/M21). A value of 765 J/m^2 for $\mathcal{G}_{Ic}$ was chosen which gives the admissible values of $50 - 65$ mm for a.

For numerical simulations the DCB arms have isotropic material properties: flexural

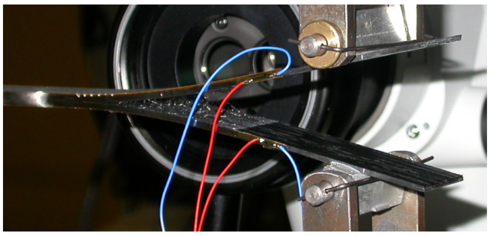

Figure 2.26: DCB specimen loaded in a servo-hydraulic machine.

modulus E_f = 120 GPa and Possion's ratio $\nu = 0.3$, for cohesive element: normal and tangential stiffness were 100 kN/mm^3 each, both normal and tangential maximum stresses were 60 MPa ($\sigma_n = \sigma_{22}^r \approx \sigma_{33}^r$, where superscript r represents the failure stress). Mode I critical energy release rate was 765 J/m^2. Length of interface element was 0.2 mm. Composite arms opening rate of $\dot{\delta} = 0.5$ m/sec is applied as a constant nodal velocity (see Figure 2.23).

For quasi-static and dynamic tests there was no considerable difference in overall form of the force displacement curve, as shown in Figure 2.27, thus it can be said that the strain rate effects are not apparent in this range of loading speeds.

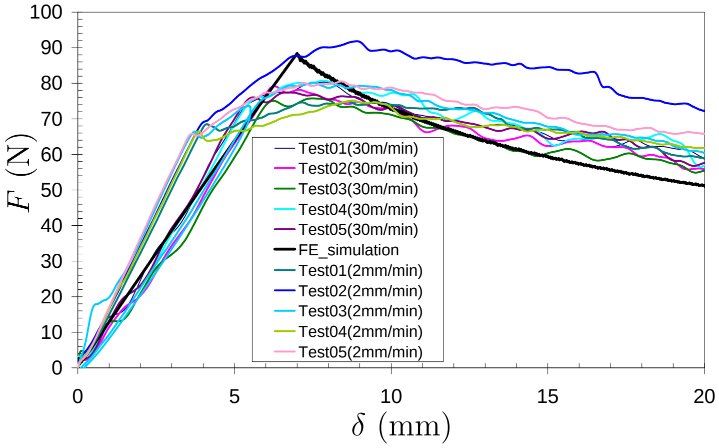

Figure 2.27: DCB: Force displacement curves numerical and experimental results, [78].

It can be seen in Figure 2.27 that results of numerical simulation and experimental force displacement ($F - \delta$) curves are in close comparison. Slightly higher values of peak force and corresponding displacement on numerical curve can be attributed to a stiffer mode I numerical model. Another reason could be the local plasticity of the crack tip zone due to presence of a thicker resin rich layer.

2.3.3 Identification of Mode II Parameters

Experimental results of quasi-static end-loaded split (ELS) tests for pure mode II of T700S/M21 are taken from Prombut [128]. Specimen dimensions are 140 mm (L) × 20 mm (b) × 4.68 mm ($2h$). A pre-crack of 80 mm is introduced by a 13 μm thick

Teflon® film. This crack is propagated by 4 mm in order to break the resin present near the end of Teflon® film. Specimen end with pre-crack is displaced vertically via ADAMEL LHOMARGY DY26 tension-compression machine. A fixture keeps the opposite end of specimen clamped and allows a horizontal displacement.

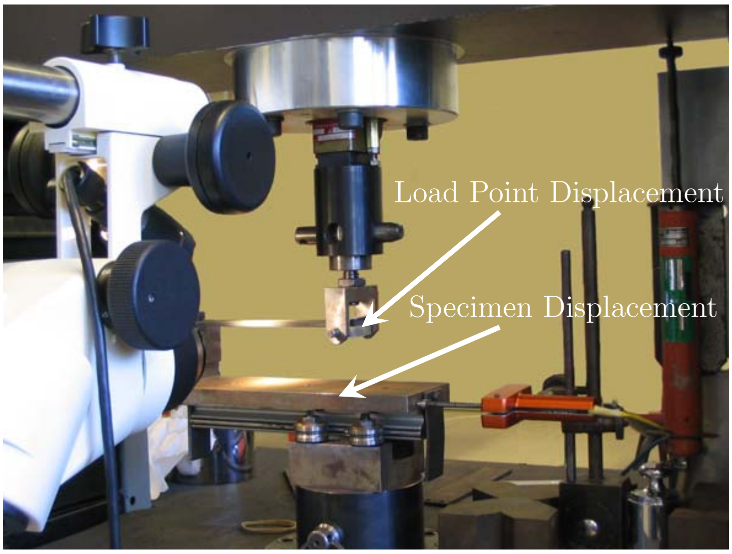

Figure 2.28: ELS specimen loaded by screw driven machine.

Table 2.1: Material properties used for ELS and MMB simulations of T700S/M21

E_f (GPa)	E_{22} (GPa)	E_{33} (GPa)	ν_{12}	ν_{23}	ν_{13}	G_{12} (GPa)	G_{23} (GPa)	G_{13} (GPa)
98.62	7.69	7.69	0.33	0.4	0.33	4.75	2.75	4.75

The corresponding numerical model has a pre-crack of 84 mm. Orthotropic elastic material constants are shown in Table 2.1. Cohesive element properties are same as for mode I simulations. Average mode II fracture toughness ($\mathcal{G}_{IIc}$) value of 1387 J/m^2, from [128], is used for numerical simulation. Loading and boundary conditions are shown in Figure 2.29. A displacement rate ($\dot{\delta}$) of 0.24 m/sec is applied at the pre-cracked end. While, the opposite end of specimen is fixed.

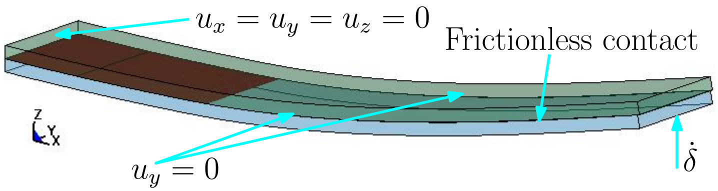

Figure 2.29: Numerical model, load and boundary conditions (ELS).

Contact: The cohesive finite elements are deleted from the simulation as soon as δ_m is attained at any of the integration points in order to remove the elements with zero stiffness. This requires that a contact condition be defined between composite arms to represent the actual test conditions. Therefore, a frictionless penalty based contact has been defined for these simulations.

Comparison of experiments and numerical simulations reveals a small difference in peak force (≈ 8%) and beam end displacement (≈ 4%). This mismatch can be attributed to the dissimilarity of boundary conditions for experimental and finite element results. During the ELS test, only vertical displacement is allowed for the load point. While, in the simulation, the load point can move along x-axis.

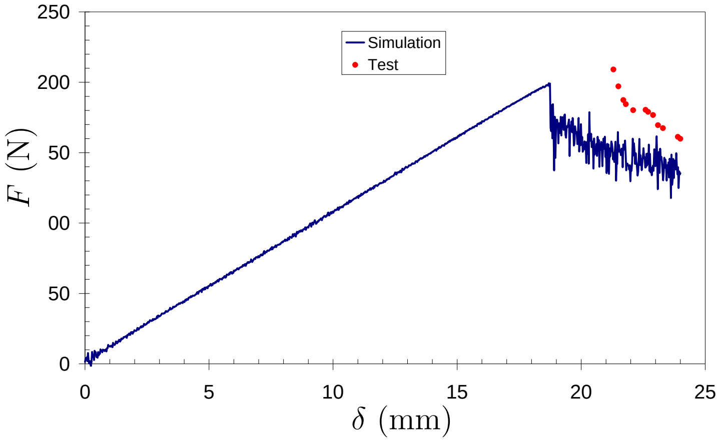

Figure 2.30: ELS: Force displacement curves, numerical and experimental results, [81].

2.3.4 Validation by Mixed-Mode I+II Correlation

In order to test the validity of numerical model in mixed mode loading situation, the mixed mode bending (MMB) test of T700S/M21, with 50% mode I, from Prombut [128] is simulated. Specimen dimensions are 100 mm ($2L$) × 20 mm (b) × 4.68 mm ($2h$). A pre-crack of 25 mm is introduced in a similar method as described above for ELS and DCB specimen.

Table 2.2: Material parameters for interface elements.

k_I (kN/mm^3)	k_{II} (kN/mm^3)	σ_n (MPa)	σ_s (MPa)	$\mathcal{G}_{Ic}$ (J/m^2)	$\mathcal{G}_{IIc}$ (J/m^2)	α
100	100	60	60	545	1387	1.5

For numerical simulations the pre-crack is 29 mm, the value obtained by a small pre-cracking as is done for pure mode I and mode II tests. A somewhat complicated mounting and loading fixture is modeled by using rigid elements and joints, see Figure 2.32. Material properties for composite arms are same as reported earlier in Table 2.1. Average values of $\mathcal{G}_{Ic}$ and $\mathcal{G}_{IIc}$ are 545 J/m^2 and 1387 J/m^2 respectively. Value of constant α defining

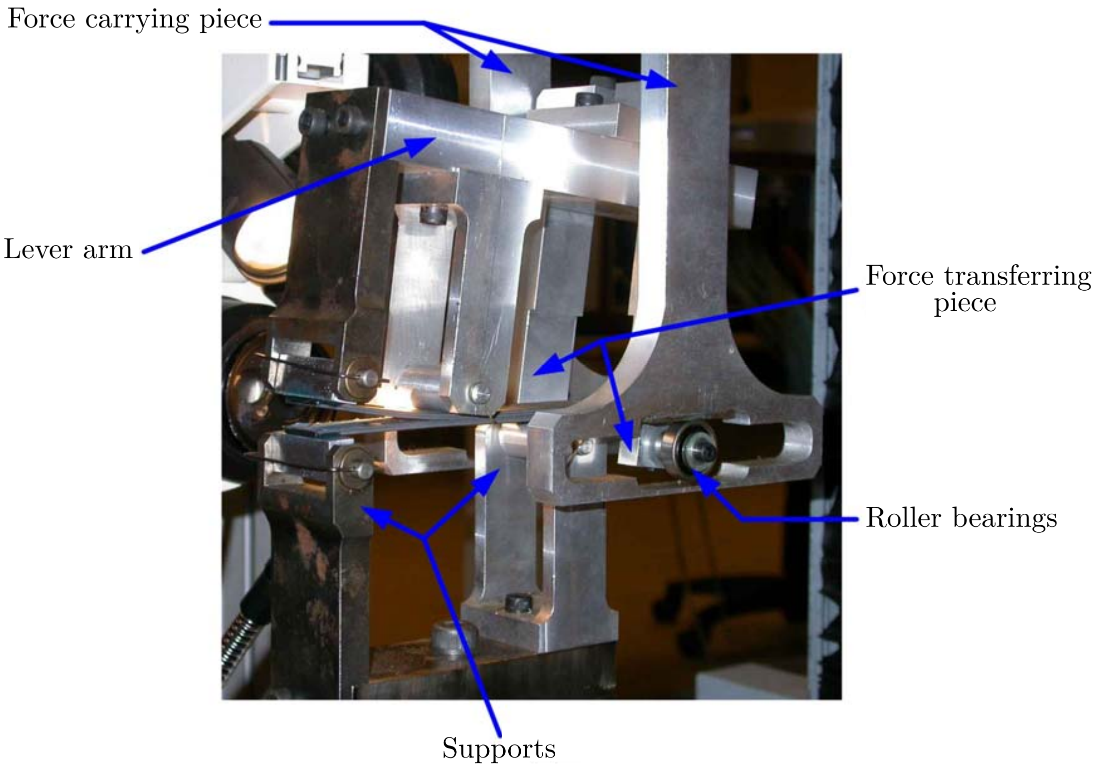

Figure 2.31: Mixed mode bending (MMB) test setup, Prombut [128].

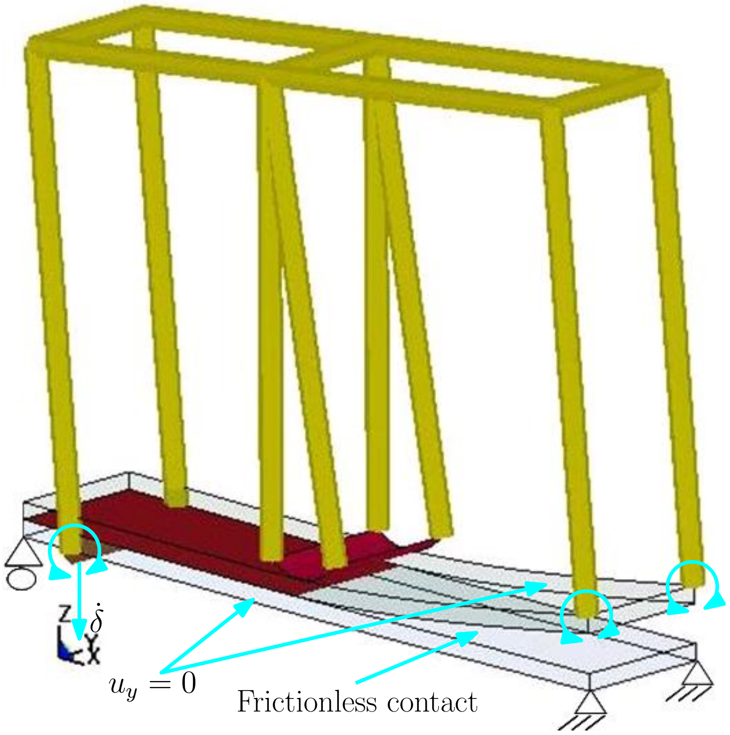

Figure 2.32: MMB: Numerical model, load and boundary conditions.

mixed mode delamination propagation (Eq. 2.22) is 1.5. The rest of cohesive element parameters are given in Table 2.2. A displacement rate ($\dot{\delta}$) of 0.5 m/sec is applied at the joint as shown in Figure 2.32. A penalty type of frictionless contact is also defined as described above for the ELS case.

Results from numerical simulation and tests are traced in Figure 2.33. Numerical model is in close agreement with experimental results for both force and displacement.

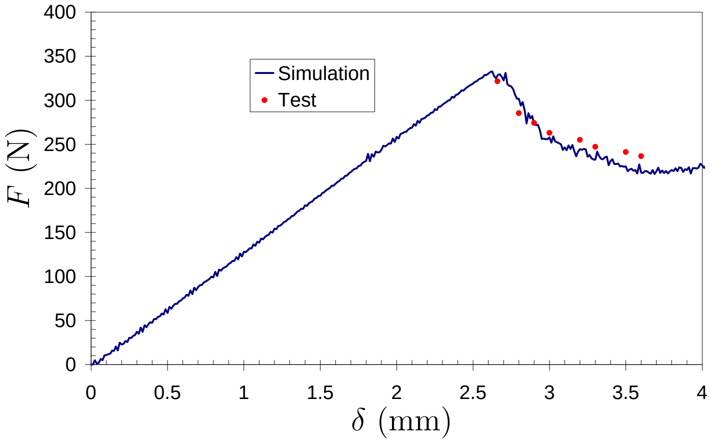

Figure 2.33: MMB: Force displacement curves, numerical and experimental results, [81].

2.4 Conclusions

This chapter has focused on the crack propagation simulation by cohesive finite elements. It has been observed that the cohesive finite elements can be used to represent the crack propagation behavior of unidirectional composite materials when the spatial location of crack is known à priori.

Attained objectives:

A bilinear cohesive material law was developed and implemented in MATLAB® and the commercial finite element code LS-DYNA®. The robust MATLAB® program allows the user to carry out quick numerical parameter study by varying different numerical parameters. This serves as a first step in better understanding of cohesive material model and appropriate choice of numerical parameters, such as σ_n, k_I and $\mathcal{G}_{Ic}$, based on experimental experience.

The commercial finite element code was used to represent the physical model with sufficient accuracy. A numerical simulation methodology was developed to allow the robust implementation of finite element based numerical model to predict the global response of widely used crack propagation experiments. The purely numerical parameters influencing the finite element simulation were identified. The optimized numerical models thus obtained were then used to simulate the response of two types of unidirectional composite materials: T700S/M21 and T800S/M21 during DCB, ELS and MMB types of test setups.

Perspectives:

One of the objectives of this study was to study the strain rate dependent behavior of strain energy release rate. Some tests were conducted by modifying the existing Hopkinson's bar setup at ISAE as shown in Figure 2.34.

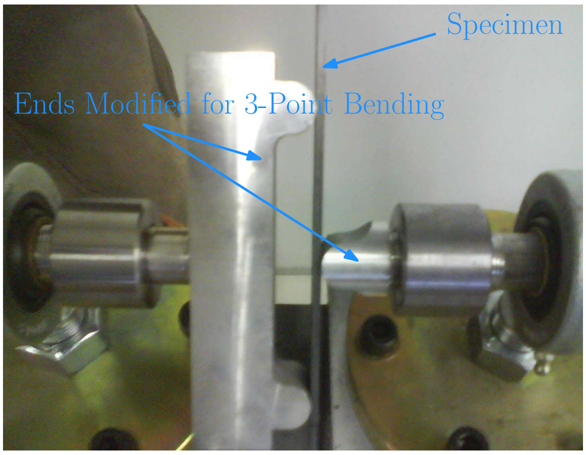

Figure 2.34: Modified Hopkinson's bar setup of 3-point bending test on ENF specimen.

The addition of extra interfaces generates perturbations in wave propagation which render the results completely unexploitable. Figure 2.35 shows a typical signal of a 3-point bending test with Hopkinson's bar setup. The addition of large masses at bar ends causes the undesired shocks, as shown by red dashed ellipses. This pollutes the signals of incident and transmission bars and the amount of applied force cannot be determined.

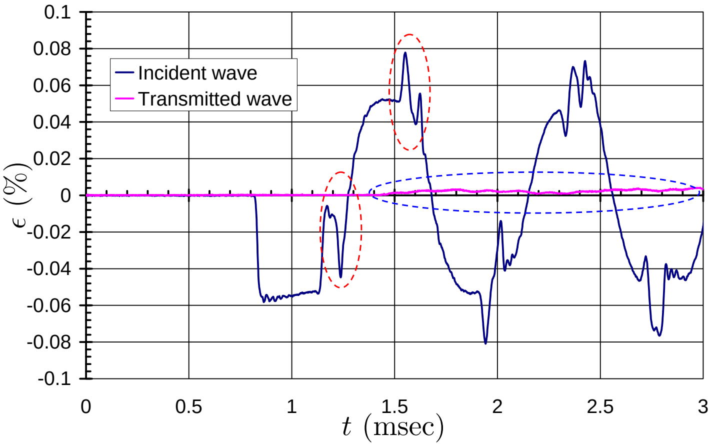

Figure 2.35: A typical signal of 3-point bending test with an SHPB apparatus.

A second problem with this kind of setup is the very weak signal recorded at strain gage on mounted on the transmission bar, as shown by blue dashed ellipse in Figure 2.35. This weak signal is a result of bouncing of elastic waves inside the modified bar ends. Furthermore, the crack propagation does not occur in the first impact, and when the crack propagation occurs, the high speed camera used for filming of the phenomenon does not have adequate image acquisition frequency and resolution. Therefore, the crack propagation speeds cannot be determined accurately.

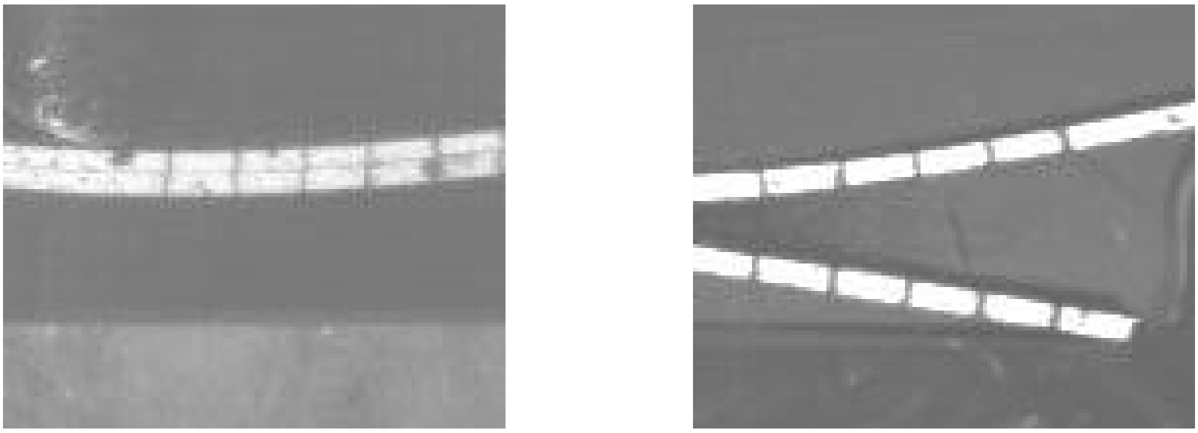

(a)

(b)

Figure 2.36: SHPB 3-point bending (a) ENF specimen and (b) ONF specimen.

A closed form solution for bending tests of concrete beams with Hopkinson's bars setup has been proposed recently by Bailly et al. [13]. As a perspective it is proposed that a 3-bar setup, [13, 90], be used to further investigate strain energy release rate as function of higher strain rates.

3

Constitutive Law: Ply

This chapter presents a damage mechanics model based on Matzenmiller-Lubliner-Taylor (MLT) model [111]. The material characterization tests will also be presented in this chapter. Quasi-static tests and dynamic material characterization tests by using Split Hopkinson's Pressure Bars (SHPB) have been conducted to obtain mechanical properties of unidirectional composite material T800S/M21. Prediction from numerical tests have been compared with the experiments.

The first section of the chapter presents a brief description of strain rate effects and strain rate dependent material characterization methods as found in literature. The numerical material models often used to represent these experimental behaviors are also presented. The second section of this chapter is dedicated to the identification of required mechanical material data by quasi-static and dynamic tests by SHPB. Quasi-static tests have been carried out for both T700S/M21 and T800S/M21 materails. While, the dynamic tests have been carried out for only T800S/M21 material.

In the third section of this chapter the modified MLT continuum damage mechanics based material model is presented. This material model is implemented in the commercial finite element analysis code LS-DYNA® as a user defined material model. At the same time robust MATLAB® functions/programs are written to carry out numerical parameter sensitivity studies for quasi-static and dynamic loadings. The appropriate mechanical and numerical parameters which have been identified are then used to simulate quasi-static and dynamic SHPB tests. The numerical predictions from LS-DYNA® are compared with the experiments in the last section of this chapter. The conclusions are then drawn at the end of the chapter.

3.1 Literature Survey

This section is mainly comprised of two major portions. At first the dynamic mechanical material data characterization studies are presented and then the second portion focuses on numerical material models capable of reproducing the mechanical behavior of these materials by using the material data as an input.

Traditionally, for very low strain rates i.e quasi-static tests servohydraulic or screw driven machines are used. The quasi-static testing of composite materials is generally well known [62]. Therefore, the attention is focused towards the dynamic test methods employed in scientific community to study the dynamic behavior of composite materials.

Few experimental results summarize the T700S/M21 or T800S/M21 composites under impact loading [27]. Al-Maghribi [6] has observed that even the low velocity impacts can generate *"High strain rates"* as categorized by Nemat-Nasser [117], see Figure 3.1. Furthermore, Michel [114] observed that it is important to characterize the material being studied in the strain rate regimes which will be observed under actual (impact) loading. In order to characterize a material for strain rate ($\dot{\epsilon}$) regimes of interest during the impact velocities (< 120m/sec) and mass (< 3 kg) used for this study, the literature survey is limited to dynamic characterization by Hopkinson's bar setup as far as the test methods are concerned. For a wider range of strain rates the reader is invited to see [117] and for a focused study on very high strain rate testing by a two stage gas gun, one can refer to [114].

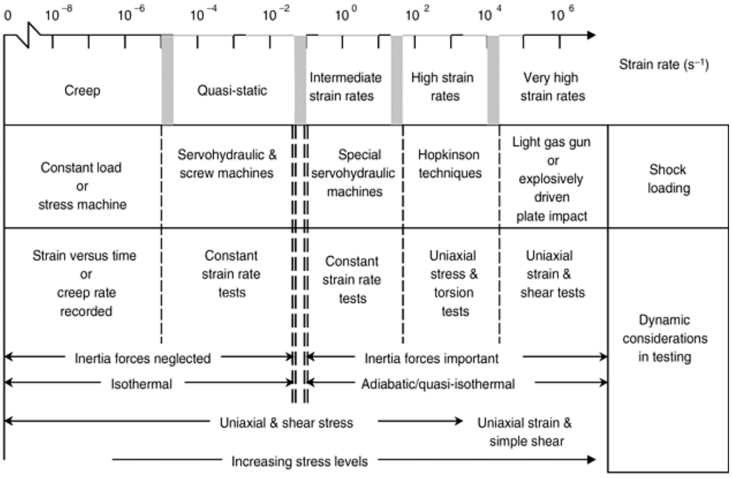

Figure 3.1: Regimes of $\dot{\epsilon}$ and associated experimental setups [117].

3.1.1 Experimental Characterization of Rate Sensitive Behavior

In order to characterize a material in the range of $10^2 - 10^4 s^{-1}$, see Figure 3.1, Split Hopkinson's Pressure Bars (SHPB) are the preferred choice, [64, 117, 118]. Some authors have also used the drop tower (DT) setup to investigate the dynamic tension [17] and compression [75] of unidirectional composites. A major problem with the drop tower is the ringing phenomenon caused by the wave propagation in the impactor and thus polluting the force and deformation measurements.

Here, first of all a small theoretical introduction to SHPB is presented and then some of the experimental studies of interest are presented with respect to the unidirectional carbon/epoxy composites. Various studies on glass/epoxy composites can be found in [56, 69, 100, 140, 144, 149]. A study on impact behavior of SMC composites can be found in [6]. For studies on woven aramid and polyethylene composites one can refer to [134] and [74].

3.1.1.1 Split Hopkinson's Pressure Bar apparatus

A schematic arrangement of compressive split Hopkinson's bar (SHPB) is shown in Figure 3.2. In order to simplify the equations used for physical properties extraction; the striker/impactor, input/incident and output/transmission bars are made of the same material and diameter. The striker bar impacts the incident bar. This impact generates an elastic compressive wave of constant amplitude and finite duration in the input/incident pressure bar. It is possible to adjust incident pulse wavelength by varying length of striker bar, as the pulse in the incident bar is directly proportional to two times the length of the striker bar. The amplitude of the pulse is also directly proportional to the impact velocity of the striker bar [61]. When this compressive loading wave reaches the incident bar-specimen interface, some part of the wave gets reflected from the specimen-incident bar interface, while some part is passed on to the transmitted bar. The physical properties are determined from magnitudes of these reflected and transmitted pulses. High numbers of internal reflections take place in the short specimen during the duration of the loading pulse since the loading pulse is long compared to the wave travel time in the specimen. These reflections are necessary for the uniform stress distribution in specimen.

The overall specimen dimensions are required to be small to minimize the effects of longitudinal and lateral inertia and wave propagation within the specimen [85]. In addition, a frictional constraint exists at the pressure bar-specimen interface due to the transverse expansion of the specimen during loading. The frictional effects are highest when the specimen is at rest and this may produce non-uniform deformation in the specimen. By applying a thin film of lubricant at the interfaces, these frictional constraints can be significantly reduced [88].

One dimensional wave propagation is assumed to be true for analyzing the strain gages' (shown as dark squares in Figure 3.2) signals. If the modulus, cross section area and density of bar are denoted by E_b, A_b and ρ_b and those for specimen are E_s, A_s and ρ_s, the equations for the strain rate $\dot{\epsilon}$, strain ϵ and stress σ of the specimen are given by

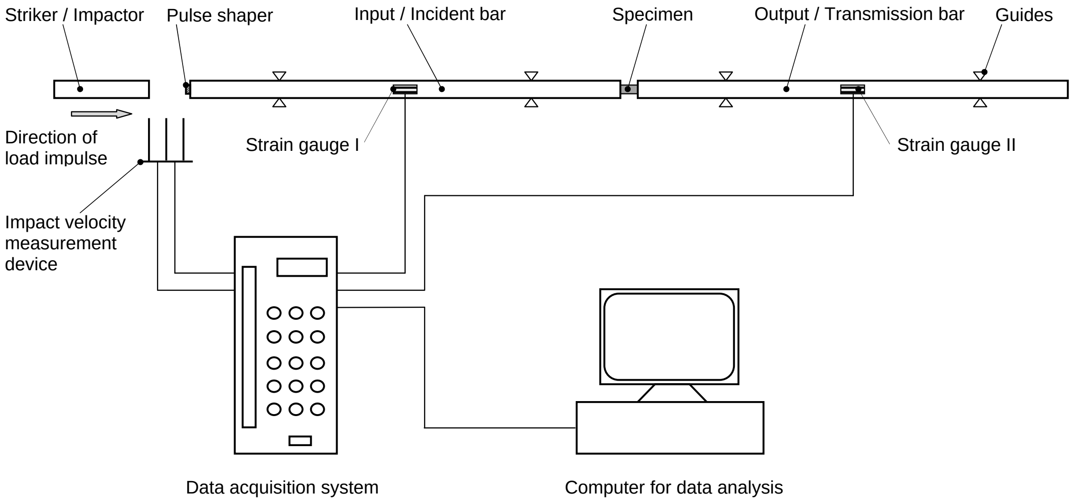

Figure 3.2: Schematic representation of an SHPB.

[64]:

$$\frac{\mathrm{d}\epsilon(t)}{\mathrm{d}t} = \frac{c_o}{L_S}\left[\epsilon_I(t) - \epsilon_R(t) - \epsilon_T(t)\right] \tag{3.1}$$

$$\frac{\mathrm{d}\epsilon(t)}{\mathrm{d}t} = \frac{-2c_o}{L_S}\epsilon_R(t) \tag{3.2}$$

The instantaneous strain value can be calculated by

$$\epsilon(t) = \frac{-2c_o}{L_S}\int_0^t \epsilon_R(t)\mathrm{d}t \tag{3.3}$$

and the stress by

$$\sigma(t) = \frac{E_b A_b}{A_S}\epsilon_T(t) \tag{3.4}$$

$$c_o = \sqrt{\frac{E_b}{\rho_b}} \tag{3.5}$$

where c_o is the speed of sound in bar, L_s is the length of the specimen and $\epsilon_I(t)$, $\epsilon_R(t)$ and $\epsilon_T(t)$ are the strain gage signals of the incident, reflected and transmitted pulses respectively. The above equations are based on the assumption that dynamic forces in both incident and transmitter bar are equal and can be expressed as

$$\epsilon_I(t) + \epsilon_R(t) = \epsilon_T(t) \tag{3.6}$$

It is clear from the above equations that the strain can be obtained by integrating the reflected pulse and the stress in the specimen from the transmitted pulse.

It is a known fact that the waves with narrower frequency bandwidth suffer less from distorting effects of dispersion and this can be obtained by increasing the rise time of the wave [88]. Many authors [118, 139, 148] have used pulse shaping techniques to achieve this. In author's experiments a small piece of paper immersed in grease is used to achieve the increase in rise time.

The results from an SHPB are strongly influenced by the quantity called "acoustic impedence", [88], defined as:

$$\mathcal{Z} = \rho c \tag{3.7}$$

where ρ and c are density and speed of sound in the material. In an ideal case the acoustic impedance of the test sample is desired to be of the same order of magnitude as bars. This is true for T800S/M21 loaded in fiber direction as $\mathcal{Z}_1 \approx 1.55 \times 10^7$ kg/m^2·s^{-2}, but not so true in transverse direction as $\mathcal{Z}_2 \approx 3 \times 10^6$ kg/m^2·s^{-2} (for steel $\mathcal{Z} \approx 4 \times 10^7$ kg/m^2·s^{-2}).

Furthermore, a one dimensional wave propagation is assumed during an SHPB test, the specimen diameter cannot be larger than bar diameter. Cylindrical specimen are preferred over rectangular specimen as geometric considerations conform with the above stated hypothesis. Since the author does not have proper means to prepare cylindrical carbon fiber composite specimen at his disposal, rectangular sheet specimen are used in this study.

3.1.1.2 Dynamic Compression

Hsiao et al. [76] observed that compressive strength increased sharply with strain rate and nearly doubled under dynamic loadings for unidirectional IM6G/3501-6 laminates. Similarly, the modulus was also increased by 37%. The in-plane shear strength showed an increase up to 80%.

Vinson and Woldesenbet [153] also used compression split Hopkinson's bars to study the effect of fiber orientation on the compressive dynamic properties of a unidirectional IM7/8551-7 composite. Their results showed that the ultimate stress: increased with strain rate and decreased with increase in off-axis angle.

Similarly, Hosur et al. [73] tested unidirectional carbon epoxy along 0°, 90° and cross-ply laminates. They observed that the stiffness and dynamic strength exhibit considerable increase as compared to static values.

An intermediate module unidirectional carbon epoxy (IM7/8551-7) was tested by Jadhav et al. [85]. They found that the maximum axial stress and strain increased with increasing strain rate. Strain rate sensitivity of balanced angle-ply laminates was found to be strongly dependent on fiber orientation. Even though fibers are strain rate insensitive, the effect of strain rate on ultimate stress and ultimate strain values was more pronounced with decreasing angle.

3.1.1.3 Dynamic Tension

Gilat et al. [64] used tensile SHPB system to characterize the IM7/977-2 composite in higher strain rate range. A small increase in maximum stress with maximum strain is observed for 90° and 10° specimens. But a more significant effect of strain rate on the maximum stress is observed in the tests with 45° and $[45°]_s$. A test specimen similar to coupon specimen is prepared and cemented in the SHPB. The effect of strain gage on material was also studied and it was found that it strongly influences the results. In all of the configurations tested, higher stiffness was observed with increasing strain rate.

Taniguchi et al. [143] also employed direct tensile Hopkinson's bars to investigate the strain rate dependent behavior of T700S/2500 composite prepreg. They concluded that the tensile properties in longitudinal direction remain unaffected by the strain rate but in transverse and shear direction they are significantly influenced. The strain rate dependence of shear strength is much stronger than that of transverse strength.

3.1.1.4 Dynamic Shear Loading

One of the earliest investigations of strain rate effect in interlaminar shear was carried out by Werner and Dharan [154]. They showed that the strain rate effect in interlaminar shear is small. In transverse shear, however, the strain rate effect is significant due to greater role played by the resin matrix in the deformation process.

Yokoyama and Nakai [161] used double notch shear (DNS) test specimen parallel to fibers in a compressive Hopkinson's bar setup to investigate the interlaminar shear strength of carbon epoxy (T700/2501) materials. They found a little effect on interlaminar shear stress. Previously the same phenomenon was observed by Bouette et al. [26] for unidirectional carbon/epoxy (T300/5208) laminate.

3.1.2 Continuum Damage Models

The key concept in CDM is the assumption that a micromechanical process (microcrack growth) can be treated at a macro level by homogenizing the damage over a representative elementary volume [55]. Where *"micro"* is a scale often defined at fiber and matrix level (μm), *"meso"* at unidirectional ply level (mm) and *"macro"* scale at coupon specimen (cm) and above [95].

From a macroscopic point of view, as defined by Hashin [71], a damage variable, d, is introduced which describes material deterioration. This variable introduced by Kachanov [87] in 1958, is a parameter which operates on tensile stress in a uniaxial loading case and defines effective stress, indeed the effective resistance of the damaged material. The evolution equations for d are defined in framework of irreversible thermodynamics processes and coupled with material constitutive law.

Damage plays an important role in fibrous composite materials. Their behavior is a manifestation of the formation and evolution of microcracks (surface discontinuities) and cavities (volume discontinuities), see paragraph 1.2.2. Furthermore, the formation of cracks is irreversible. Primarily, these defects cause stiffness degradation and small permanent deformations remain in the stress-free body after unloading [156].

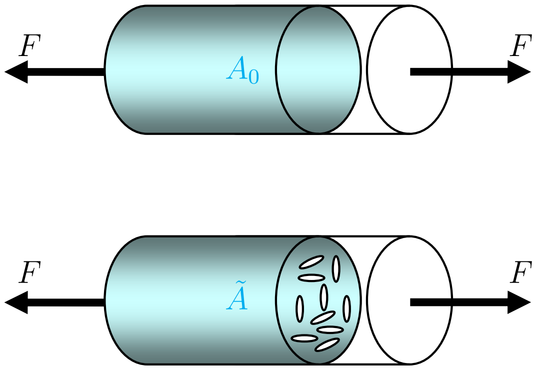

Figure 3.3: Schematic representation of damage by cracking.

Let us consider a bar in tension with initial cross section A_0, Figure 3.3. The damaged state of this bar can be represented by a damage variable d $(0 \leq d \leq 1)$ where $d = 0$ represents the initial *"safe"* state and $d = 1$ represents the complete failure. This variable is often interpreted as reduction of the effective area due to internal damage in the form of internal cracks. Therefore, the effective area resisting the load has reduced form A_0 to $\tilde{A}$, the damaged area, A_d, is then defined as:

$$A_d = A_0 - \tilde{A} \tag{3.8}$$

and then d can be defined as:

$$d = \frac{A_d}{A_0} \tag{3.9}$$

When a force F is applied in a direction normal to A, the effective stress, $\tilde{\sigma}$, related to the effective stress is written as:

$$\tilde{\sigma} = \frac{F}{\tilde{A}} = \frac{F}{A_0(1-d)} = \frac{\sigma}{1-d} \tag{3.10}$$

The deformation of the material is supposed to be a consequence of the effective stress only. Therefore, the uniaxial linear elastic law becomes:

$$\epsilon^e = \frac{\tilde{\sigma}}{E} \tag{3.11}$$

where ϵ^e is the elastic strain and E^0 is the Young's modulus of undamaged material. If $\tilde{E} = E^0(1-d)$ defines the modulus or rigidity of the damaged material, the damage variable can be written as

$$d = 1 - \frac{\tilde{E}}{E^0} \tag{3.12}$$

or in a more general form it is written:

$$E_i = (1-d_i)\,E_i^0 \tag{3.13}$$

One of the first application of continuum damage mechanics (CDM) on composites was carried out by Talreja [142]. The model proposed two damage variables each associated with a principal direction of the material i.e. fiber and matrix. This model was applied to reproduce the macroscopic stiffness reduction of angle-ply composites under quasi-static tensile loading. The model showed good agreement with loss of modulus measured in experiments.

Perhaps, Chang and Chang [37] were the first authors to present a progressive damage model to predict the impact induced damage by finite element analysis. This model assumes that in the post-failure regime a lamina behaves in an ideally brittle manner thus the dominant stiffness and stress components are reduced to zero instantaneously. This assumption is very unrealistic as it does not take into account the constraints that are imposed on the failed lamina by the adjacent laminae and undamaged elements in the neighborhood of the damage site. The net result of these constraints is, from a macroscopic point of view, the stress release and stiffness reduction occur gradually rather than abruptly under quasi-static loading. This behavior can be incorporated in numerical analyses through a homogenized stress-strain model, which exhibits strain softening. Kongshavn and Poursatrip [89] suggest that the damage growth in the vicinity of a crack tip or fracture site in a polymeric composite structure manifests itself in the form of strain softening of the material. Their results suggest that a strain-softening approach is: (**a**) able and (**b**) necessary to accurately model the damage growth observed in composites.

In the next two sections recapitulate some fundamental concepts of two of the CDM models implemented for fiber reinforced composite materials to represent the strain rate dependent behavior under impact loading.

3.1.2.1 Damage Modeling through Energy Computations

Among others, Ladevèze [95] also defines damage as gradual development of micro-voids and microcracks which lead to macro-cracks and then to final rupture. This *"meso"* scale based damage model shows good prediction of bending response but mesh sensitivity is a critical issue as observed by Bayandor et al. [18; 19], while they conducted a comprehensive review of this model implemented in explicit finite element code Pam/Crash.

Although this study has been limited to linear elasticity, it is worth noting that in order to take inelastic strains into account, a plasticity model was proposed by Ladevèze and Le Dantec [96]. The model leads to a laminate failure criterion and takes into account the differences between tension and compression in the fiber direction.

Damage Kinematics of the Elementary Ply The damaged-material strain energy is written by the authors' in the following form:

$$\rho\psi = \frac{1}{2}\left[\frac{\sigma_{11}^2}{E_{11}^0} - 2\frac{\nu_{12}^0}{E_{11}^0}\sigma_{11}\sigma_{22} + \frac{\langle\sigma_{22}\rangle^2}{E_{22}^0(1-d_2)} + \frac{\langle-\sigma_{22}\rangle^2}{E_{22}^0} + \frac{\sigma_{12}^2}{G_{12}^0(1-d_4)}\right] \tag{3.14}$$

where d_2 and d_4 are scalar damage variables that remain constant throughout the ply thickness, ψ is Gibbs specific free enthalpy.

The damage elastic law is:

$$\epsilon^e = C^{-1}\sigma \Leftrightarrow \begin{cases} \epsilon_{11}^e = \dfrac{\sigma_{11}}{E_1^0} - \dfrac{\nu_{12}}{E_1^0}\sigma_{22} \\ \epsilon_{22}^e = \dfrac{\langle\sigma_{22}\rangle}{E_2^0(1-d_2)} + \dfrac{\langle-\sigma_{22}\rangle}{E_2^0} - \dfrac{\nu_{12}}{E_1^0}\sigma_{11} \\ \epsilon_{12}^e = \dfrac{\sigma_{12}}{G_{12}^0(1-d_4)} \end{cases} \tag{3.15}$$

Formulation of Damage Variables Under the assumption that the Gibb's specific free enthalpy (ψ) is related to both (i) the through ply transverse cracking and (ii delamination related specific energies, the scalar variable for damage in transverse direction (d_2) and in plane shear (d_4) are governed by the meso-scale damage quantities Y_{22} and Y_{12}, respectively.

$$Y_{22} = \frac{\partial(\rho\psi)}{\partial d_2} = \frac{\langle\sigma_{22}\rangle^2}{E_{22}^0(1-d_2)^2} \tag{3.16}$$

$$Y_{12} = \frac{\partial(\rho\psi)}{\partial d_4} = \frac{1}{2}\frac{\sigma_{12}^2}{G_{12}^0(1-d_4)^2} \tag{3.17}$$

$$\tilde{Y}_{22} = \sup_{(0,t)}\sqrt{Y_{22}} \tag{3.18}$$

$$\tilde{Y}_{12} = \sup_{(0,t)}\sqrt{Y_{12}+bY_{22}} \tag{3.19}$$

Where b defines the coupling between the damages d_2 and d_4. For unidirectional carbon fiber composites, it is customary to approximate damage evolution by linear laws, even for dynamic applications [41]:

$$d_2 = \frac{\tilde{Y}_{22} - Y_{22}^0}{Y_{22}^c} \tag{3.20}$$

$$d_4 = \frac{\tilde{Y}_{12} - Y_{12}^0}{Y_{12}^c} \tag{3.21}$$

The energy dissipation of each mode is, independently, due to the contribution of stresses and strains involved in the corresponding failure mode. A second point is that in the framework of homogenization theories, it is mandatory to define adequately the representative volume cell, which is same here for both of these specific energies.

The effective stress $\tilde{\sigma}$ is given as follows:

$$\tilde{\sigma} = \begin{bmatrix} \sigma_{11} \\ \dfrac{\langle\sigma_{22}\rangle}{1-d_2} + \langle-\sigma_{22}\rangle \\ \dfrac{\sigma_{12}}{1-d_4} \end{bmatrix} \tag{3.22}$$

Damage Evolution Methodology The assumption is that the shear damage energy release rate Y_{12} is directly proportional to the shear damage d_4, after shear damage initiates and therefore the parameters of the linear fit can be employed to describe the shear damage evolution. Evolution of damage is represented in an irreversible behavior approach that makes it very easy to couple with a plastic-like behavior. Evolution is based on an effective stress and related to a strain potential i.e the undamaged potential minus the dissipations.

Strain Rate Effects Rozycki [136] has proposed to take into account the strain rate effects on material rigidities by using the following function:

$$E^{\max} = E^0 \left(1 + \mathcal{F}\right) \tag{3.23}$$

where $\mathcal{F}$ the viscosity function can have either linear, non-linear or logarithmic form, e.g logarithmic form is as follows:

$$\mathcal{F} = 1 + \mathcal{C} \ln \left(\frac{\dot{\epsilon}}{\dot{\epsilon}_{ref}}\right) + \ln(\eta) \tag{3.24}$$

3.1.2.2 Failure Criteria Based Damage Model

In Matzenmiller-Lubliner-Taylor (MLT) formulation [111], it is assumed that each unidirectional lamina can be represented as a homogenized continuum. Damage is in the form of disk-like cracks (i.e. independent of crack shape) oriented parallel or normal to the fibers. This allows to preserve symmetry of the lamina throughout the damage evolution.

In a two dimensional plane-stress case, two damage variables namely d_1 and d_2, are introduced to represent the relative size of the disk-like cracks. Matzenmiller et al. [111] argue that the effect of damage on shear is different than the effect on the longitudinal or transverse directions so an additional damage parameter, d_4 is required to account for the effect of damage on the shear behavior. The stress strain relationship in 2-D is written as [156]:

$$\epsilon = C^{-1}\sigma \tag{3.25}$$

where

$$C^{-1} = \begin{bmatrix} \dfrac{1}{(1-d_1)E_{11}^0} & \dfrac{-\nu_{12}^0}{E_{11}} & 0 \\ \dfrac{-\nu_{21}^0}{E_{22}} & \dfrac{1}{(1-d_2)E_{22}^0} & 0 \\ 0 & 0 & \dfrac{1}{(1-d_4)G_{12}^0} \end{bmatrix} \tag{3.26}$$

Damage Threshold What is original in the Matzenmiller et al. [111] model is that the anisotropic damage variables d_i up to failure are related to several different failure modes r_i, and to a linear combination of different damaged failure thresholds. The concept of a threshold function is similar to the yield surface in plasticity theory. Within a certain region in stress space (or strain space), the state of damage in the material will not change. This region, the elastic region, is bounded by a series of surfaces $f_i(\sigma, d_i, r_i)$, where d_i is the damage variable of mode i and r_i the corresponding threshold.

$$f\left(\sigma, d_i, r_i\right) = f_j\left(\sigma, d_i\right) - r_j^2 = \sigma^{\mathrm{T}} \cdot F_j \cdot \sigma - r_j^2 = 0 \tag{3.27}$$

The threshold function, r_i, which is analogous to the flow stress in plasticity theory, then becomes a function of σ and d_i thereby defining the size of the elastic region as damage progresses. The loading surfaces' shapes come from the analytical expression of the failure criterion giving the relation between the stress components and the effective strengths. For example, in 2-D [156] used failure based on maximum stress criterion with interactive terms for matrix dominated transverse and shear damage modes. The equations used are similar to the interactive criteria, distinguishing between fiber and matrix failure modes, proposed by Hashin [71].

$$\text{Fiber Failure} \quad \left(\frac{\sigma_1}{X_{c,t}}\right)^2 - r^2 \begin{cases} \geq 0 \text{ failed} \\ \\ < 0 \text{ intact} \end{cases} \tag{3.28}$$

$$\text{Matrix Failure} \quad \left(\frac{\sigma_2}{Y_{c,t}}\right)^2 + \left(\frac{\sigma_{12}}{S}\right)^2 - r^2 \begin{cases} \geq 0 \text{ failed} \\ \\ < 0 \text{ intact} \end{cases} \tag{3.29}$$

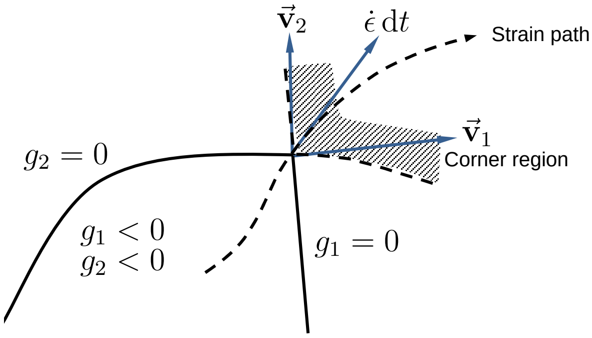

Figure 3.4: Non-smooth loading surfaces in strain space [111].

One can write a condensed quadratic expression, which is rewriten in the strain space using the constitutive tensor. Then damage growth arises only if the strain state and loading rate $\dot{g}_j$ make the boundary of the admissible spaces move outwards the loading surface given by the criterion gradient, what is called by the author the “loading” conditions, see Figure 3.4.

$$g(\epsilon, d_i, r_i) = g_j(\epsilon, d_i) - r_j^2 = \epsilon^{\mathrm{T}} \cdot G_j \cdot \epsilon - r_j^2 = 0 \tag{3.30}$$

$$g_j = 0 \text{ and } \frac{\partial g_i}{\partial \epsilon}\dot{\epsilon} > 0 \tag{3.31}$$

$$\dot{g}_i = \frac{\partial g}{\partial \epsilon}\dot{\epsilon} + \frac{\partial g}{\partial d}\dot{d} - \dot{r}_i = 0 \text{ and } -\frac{\partial g}{\partial d}\dot{d} \leq \frac{\partial g}{\partial \epsilon}\dot{\epsilon} \tag{3.32}$$

These conditions are derived to insure a monotonically increasing threshold r_j for each loading surface $g_j = 0$, and restrict the amount or direction of damage growth.

$$\dot{d}(\sigma, d, \dot{\epsilon}) = \sum_i \phi_i(\sigma, d, \dot{\epsilon}) \cdot q_i(\sigma, d) \tag{3.33}$$

$$\dot{d}(\sigma, d, \dot{\epsilon}) = \phi_1(\sigma, d, \dot{\epsilon}) \cdot 1 = \frac{1}{\mathrm{e}}(1-d)\left(\frac{\epsilon}{\epsilon_f}\right)^{m-1}\frac{\dot{\epsilon}}{\epsilon_f} \tag{3.34}$$

When damage takes place and evolves, the damage variables must monotonically increase through a damage evolution ϕ_j, where ϕ_j are scalar functions that control the amount of growth and q_j functions define an interaction tensor between damage sates and damaged thresholds [107]. Two versions of q_j have been proposed each for woven and unidirectional composite materials in [107]. For unidirectional composites it was found that:

$$q = \begin{bmatrix} 1 & 1 & 1 & 0 & 0 \\ 0 & 0 & 1 & 1 & 0 \\ 0 & 0 & 1 & 0 & 1 \\ 1 & 1 & 1 & 1 & 1 \\ 0 & 0 & 1 & 1 & 0 \\ 1 & 1 & 1 & 0 & 1 \end{bmatrix} \tag{3.35}$$

Damage Evolution Law In their development, Matzenmiller et al. [111] highlight the fact that to this point, no statement has been made about the characteristics of the damage variables. As such, the formulation is fairly general although it does present a rigorous mathematical statement of the problem. In open literature two types of damage growth laws are found. In the examples presented in Matzenmiller et al. [111], a damage variable of the form has been proposed:

$$d = 1 - \exp\left(-\frac{r^m}{me}\right) \text{ with } r \geq 0 \tag{3.36}$$

On the other hand [60, 160] have used:

$$d = 1 - \exp\left(\frac{1}{m}(1-r)^m\right) \text{ with } r \geq 1 \tag{3.37}$$

The difficulty in applying this damage growth law is obtaining the characterization data required for this model as the softening response of fiber-reinforced composites is difficult to obtain. Although Kongshavn and Poursatrip [89] have tried to standardize the test procedure for MLT model. The choice of damage evolution function, ϕ, and stress softening parameter, m, is an open issue.

Strain Rate Effects In paragraph 3.1.1 it is noted that different authors have observed that fiber reinforced composites show an increase in failure strength and rigidity when loaded in matrix dominated modes. Therefore in order to account for enhancement in failure strength and rigidity, logarithmic functions are defined as shown in Equations 3.38 and 3.39, [60, 107, 160]:

$$S^{\max} = S^0 \left\{1 + \mathcal{C}_1 \ln\left(\frac{\dot{\epsilon}}{\dot{\epsilon}_{ref}}\right)\right\} \tag{3.38}$$

$$E^{\max} = E^0 \left\{1 + \mathcal{C}_2 \ln\left(\frac{\dot{\epsilon}}{\dot{\epsilon}_{ref}}\right)\right\} \tag{3.39}$$

where $\mathcal{C}_1$ and $\mathcal{C}_2$ are experimentally determined coefficients.

3.1.3 Numerical Models

The continuous damage models are very useful in Finite Element based numerical models as finite elements are often themselves considered as elementary volumes in which the behavior is somehow homogenized. Furthermore, energy or potential base models are coherent with finite elements which also use the energy conservation hypothesis, and derive local strength and elementary rigidities from energy considerations. A major drawback of finite elements is that the size and shape of representative volume cell are also size and shape of the finite element mesh. The size of the finite element can induce a numerical dissipation in the energy release gradients evolution. The shape of the finite element can also induce a numerical anisotropy in addition to or in conflict with the material model anisotropy in a local finite element approach. Thus meshfree methods can be thought about as emerging solutions. In particular the SPH method has a spherical and non-local interpolation as discussed in paragraph 2.1.3.

3.1.4 Concluding Remarks

The above discussion is by no means an exhaustive study of finite element modeling and strain rate testing of unidirectional carbon epoxy laminates. However, in paragraph 3.1.1 cited studies show that fiber reinforced materials are sensitive to strain rate loading. The carbon fibers are less sensitive to the loading rate but the matrix dominated modes show notable deviation from quasi-static results. The amount of published work on the strain rate dependency of shear damage evolution of composites is limited. While using thermoplastic resin systems, Lataillade et al. [97] and Papadakis et al. [124] were able to measure the changes in shear damage evolution for varying strain rates.

As far as the dynamic testing is concerned, it is preferable that Hopkinson's bar be used and direct measurements be taken from incident and transmission bars. The addition of interfaces always generates uncertainties. The drop towers show the ringing phenomena due to wave propagation inside the impactor and this may pollute the results. The usage of strain gages is not advised as the adhesive of the strain gages may also need to be characterized prior to testing. The inertial effects during high strain rate testing may also suggest that the mass of strain gage and especially connections may no more be negligible.

In finite element model the continuum damage approach is well suited to represent mechanical behavior of fiber reinforced composite materials. On the other hand one has to keep in mind that numerical models that use the shape and size of the mesh to support the damage shape and evolution strongly depend on spatial discretization. If it is aimed to propose predictive numerical models, numerical tools should not interfere with the material damage model. Therefore, the MLT based model, in author's opinion, is more suited especially if it has to be coupled with an SPH spatial discretization.

The rigidity and strength values required for finite element modeling can be characterized using quasi-static and dynamic laboratory tests.

3.2 Physical Properties Characterization

In the following paragraphs characterization of the material data to be used in the MLT model is presented. The quasi-static testing for shear behavior is described at first, followed by the dynamic compression using Split Hopkinson pressure bar system.

3.2.1 Quasi-static Tension Tests

The specimen from T700S/M21 and T800S/M21 unidirectional tapes were fabricated with following dimensions, Length $L = 150$ mm, breadth $b = 20$ mm and thickness $h = 2$ mm.

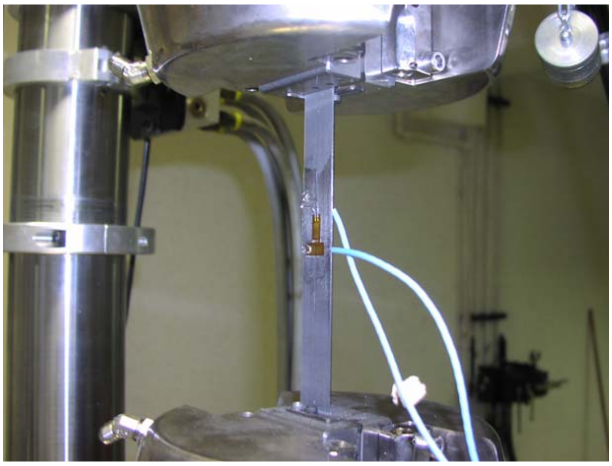

Figure 3.5: Displacement controlled quasi-static test.

Specimen were prepared as detailed in Appendix A and contained ≈ 65% of fibers by volume. A pair of strain gages is placed on the specimen to measure the strains along specimen longitudinal and transverse directions as shown in Figure 3.5. For quasi-static characterization, an INSTRON® 8862 machine is used. Specimen is loaded in tension by applying a displacement rate is 2 mm/min i.e. $\dot{\epsilon} \approx 2 \times 10^{-4} s^{-1}$.

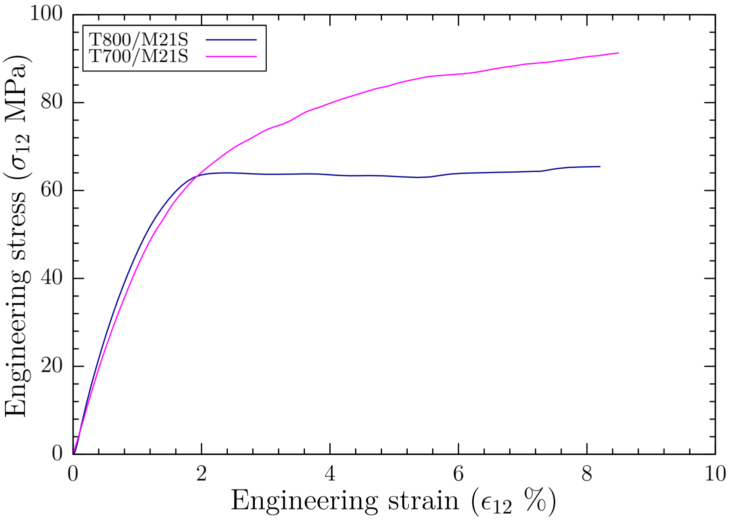

Figure 3.6: Typical response of T700S/M21 [65] and T800S/M21 $[\pm 45]_{2s}$ laminates.

Figure 3.6 shows typical responses of T700S/M21 and T800S/M21 specimen loaded in quasi-static conditions. In spite of the fact that matrix material being used in both composite systems is the same, the shear behavior exhibits a saturated stress-strain curve after 2% deformation for T800/21S. Response of T700S/M21 material system shows a continuous growing stress vs. elongation. Both materials have almost the same linear rigidity before 1.2% elongation (50 MPa).

To understand the stress saturation a microscopic analysis of the two material systems is presented in Figure 3.7. It is observed that matrix (and therefore thermoplas-

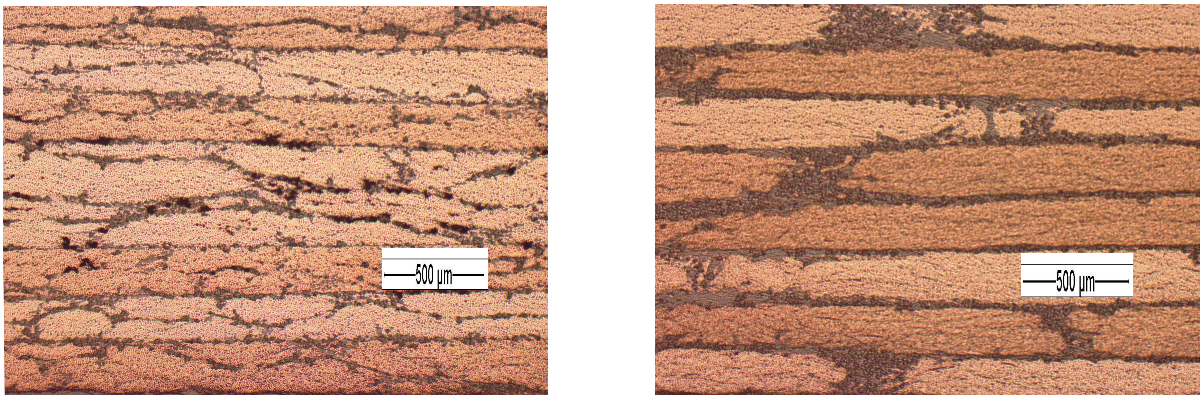

(a) Undamaged T700S/M21

(b) Undamaged T800S/M21

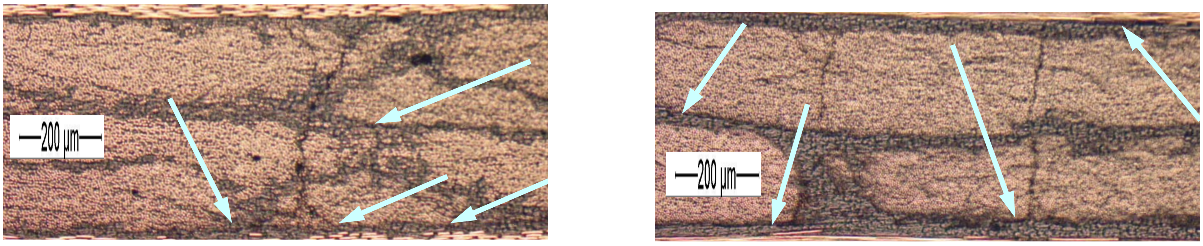

(c) Damaged T700S/M21

(d) Damaged T800S/M21

Figure 3.7: T700S/M21 and T800S/M21 $[\pm 45]_{2s}$ laminates cross-section along 45° plies.

tic grains) are well absorbed in T700 fiber bundles, see Figure 3.7(a), which is not the case for T800S/M21 (Figure 3.7(b)). Therefore, a thicker resin rich layer is observed for T800S/M21. Interface thicknesses are 66^{+2}_{-4} μm and 25^{+5}_{-1} μm for T800S/M21 and T700S/M21, respectively. This may be due to difference in processing of pre-impregnated tapes at HEXCEL® (details are not supplied by manufacturer). In author's opinion, presence of high proportions of thermoplastic resins in a thicker interface layer is the reason for the stress saturation for T800S/M21. Furthermore, one can see that the matrix cracks and interface cracks are coupled and more pronounced for T800S/M21.

On the basis of the observations, it is supposed here that the general elastic behavior of the ply is defined by the first part of the curves of Figure 3.6. The undamaged shear modulus G_{12} is the slope of the curves up to $45-50$ MPa for T800S/M21 and T700S/M21. This stress value is a yield point, σ^y, for the deformation to become irreversible due to ply damage. After these yields, and using the Figure 3.7 it is supposed that the global reaction of the coupons exhibits a coupling between the intra-ply and ±45 interface damage, thicker in T800S/M21 than T700S/M21. As a consequence it is decided to take into account the effect of the interface resistance in the mechanical model.

3.2.2 Dynamic Compression Tests

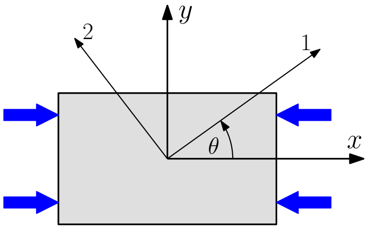

Figure 3.8: Schematic of a loaded $\pm\theta$ laminate in global reference frame.

The SHPB apparatus has been used to characterize the strain rate effect on the mechanical behavior of T800S/M21 samples. The laminate configurations tests are: $[0]_{16}$, $[\pm 15]_{3s}$, $[\pm 30]_{3s}$, $[\pm 45]_{3s}$, $[\pm 60]_{3s}$, $[\pm 75]_{3s}$ and $[90]_{16}$. Figure 3.8 shows schematic representation of a laminated loading in global XY-plane. θ is the angle between ply 1-axis and global x-axis. For SHPB tests global x-axis coincides with the incident and reflected bars. Stresses and strains are calculated using the incident and transmission bar signals using the formulas of paragraph 3.1.1.1. $[0]_{16}$, $[\pm 15]_{3s}$, $[\pm 30]_{3s}$ were tested to see the influence of fibers on laminates, $[\pm 45]_{3s}$ laminate was tested to study the laminate shear behavior, $[\pm 60]_{3s}$, $[\pm 75]_{3s}$ were tested to study matrix shear and transverse compressive behavior and $[90]_{16}$ was tested for pure transverse compressive behavior. Specimen dimensions for $[\pm\theta]_{3s}$, where $\theta \in \{15, 30, 45, 60, 75\}$, tests at strain rate less $500s^{-1}$ were surface area $A_s = 8 \times 3$ mm^2 and $L_s = 8$ mm and for tests above $500s^{-1}$ were $A_s = 6 \times 3$ mm^2 and $L_s = 6$ mm. For $[\theta]_{16}$, where $\theta \in \{0, 90\}$, the specimen dimensions were $A_s = 9 \times 4$ mm^2 and $L_s = 9$ mm for $\dot{\epsilon} < 500s^{-1}$ and $A_s = 14 \times 4$ mm^2 and $L_s = 14$ mm for $\dot{\epsilon} < 500s^{-1}$. For dynamic tests the author has limited himself to extract Nominal stress vs Nominal strain behavior as the material under consideration is orthotropic material with square cross section.

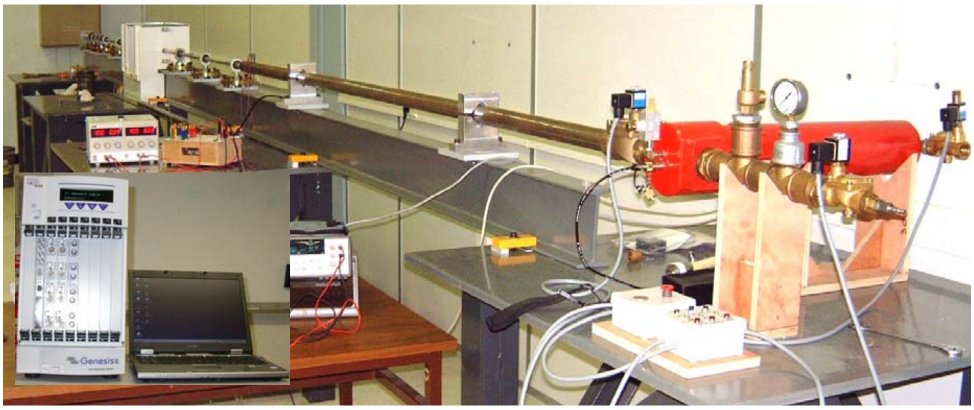

Figure 3.9: Hopkinson's bars setup at ISAE.

A brief description of a classical Hopkinson bar system is given in paragraph 3.1.1.1.

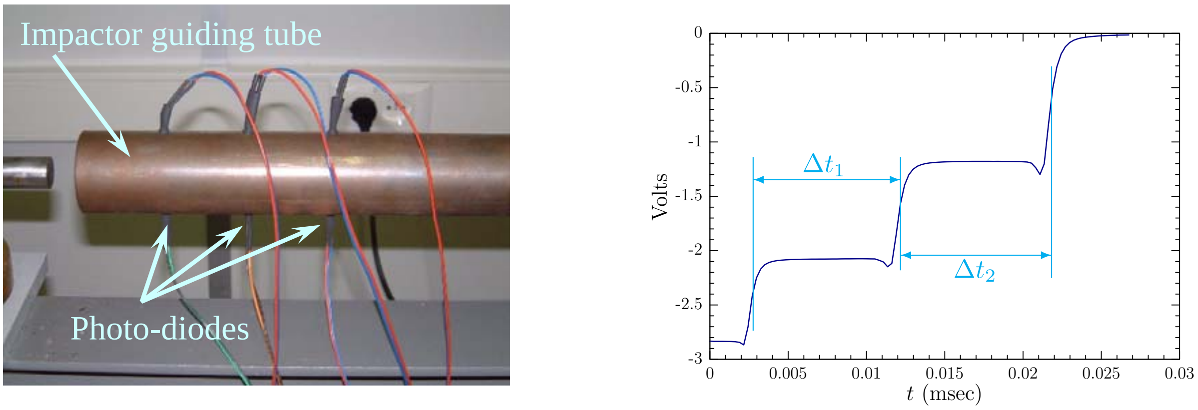

(a) Velocity measurement by photo diodes. (b) Velocity calculation principle.

Figure 3.10: Impactor speed measuring system and a typical signal.

The Hopkinson bar system available at ISAE is a compression type apparatus. The characteristics of this SHPB apparatus are summarized in Table 3.1. The impactor is launched by a compressed air canon system, (red reservoir in Figure 3.9). It travels in a tube equipped with velocity measurement system attached 50 mm before impact. The speed measurement system comprises of 6 photo diodes (3 emitters and 3 receivers), see Figure 3.10(a). Distance between each emitter-receiver pair is 50 mm. As the impactor bar passes in front of photo diodes, the change in signal is recoded by a high speed data acquisition system. A typical Volt-time signal is shown in Figure 3.10(b). The mid point for the stable (i.e horizontal) voltage signal is calculated to find the corresponding time intervals Δt_1 and Δt_2. Impactor velocity is then calculated for these two time intervals. An average of the two velocities is then retained for further test data analysis.

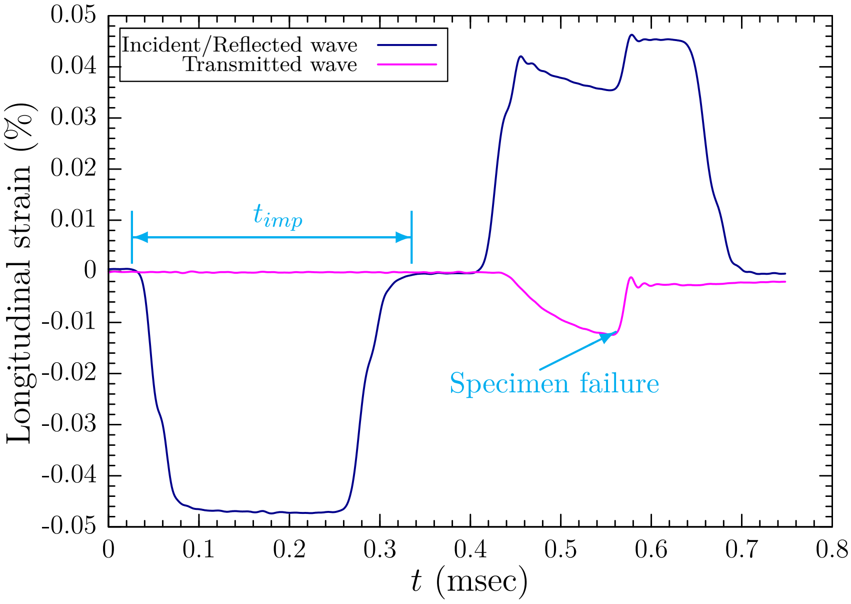

Figure 3.11: Compression of $[\pm 60]_{3s}$ laminate at $\dot{\epsilon} = 380 s^{-1}$.

The data has been acquired by using GEN7t system from LDS-Nicolet© . Data acquisition frequency is 1 MHz during all the tests as recommended in DAVID (**D**épouillement **A**utomatique et **VI**sulaisation pour compression/traction **D**ynamique) user manual [45]. DAVID is a post-processing computer program for SHPB apparatus developed by Laboratoire de Mécanique des Solides at Ecole Polytechnique Palaiseau. This program is dedicated to facilitate extraction of stress-strain curves from data acquired during an SHPB test.

Figure 3.12: Schematic representation of incident bar and specimen interface.

A typical compression response of $[\pm 60]_{3s}$ laminate made of T800S/M21 material is shown in Figure 3.11. The impacting bar generates a compressive wave (with a -ve sign) in the incident bar, which becomes a tensile wave (with a +ve sign) upon reflection from the incident bar/specimen interface, see Figure 3.12. The transmitted part of the wave keeps on traveling in the transmission bar as a compressive wave (again with a -ve sign). The impact time t_{imp} is 280^{+12}_{-8} μsec, which is higher than the analytical prediction. For incident and impactor bars made of same material, time of impact is given as [93]:

$$t_{imp} = \frac{2L_{imp}}{\sqrt{E_b/\rho_b}} \tag{3.40}$$

Table 3.1: Material properties of SHPB test apparatus at ISAE.

Young's modulus of bars, E_b	212.5 GPa
Poisson's coefficient, ν_b	0.3
Impactor/striker length, L_{imp}	0.6 m
Incident bar length, L_{inc}	2 m
Transmission bar length, L_{tra}	2 m
Diameter of bars, D_b	0.02 m
Distance strain gages and specimen	0.997 m

Analytically $t_{imp} \approx 230$ μsec is obtained. This difference between analytical and experimental impact times is attributed to pulse shaping technique. It is strongly recommended by Ninan et al. [118], Ramirez and Rubio-Gonzalez [130], Song and Chen [139], Tsai and Sun [150] to use a pulse shaper during SHPB tests. A simple approach was adopted during these tests by using a piece of paper immersed in grease to replace pulse shaper between impactor and incident bar, see Figure 3.2, and good test repeatability was obtained as far as time of impact is concerned.

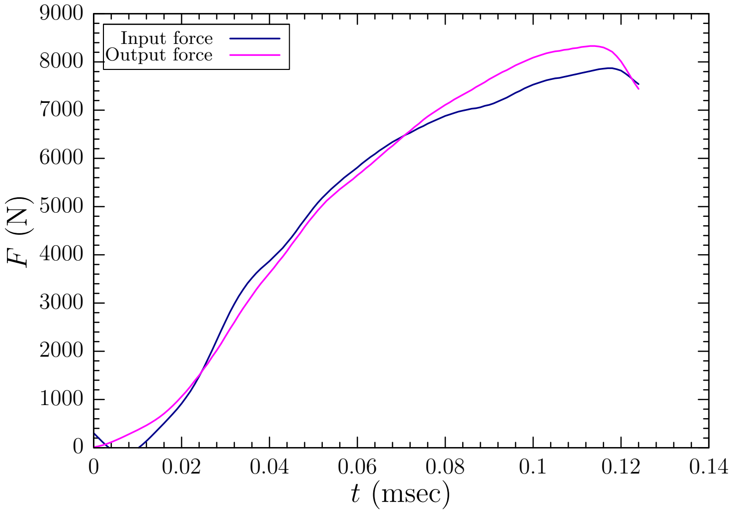

Figure 3.13: Equilibrium verification of input and output forces for a $[\pm 60]_{3s}$.

Before proceeding any further with acquired data, the dynamic equilibrium is verified at first, the fundamental hypothesis during an SHPB test often supposed to be valid. The computer program, DAVID, proposes the following solution. The basic principal of this software is to do a Fast Fourier Transform (FFT) of the incident and reflected wave in incident bar and transmitted wave in transmission bar. The incident wave is forwarded in time while transmitted and reflected waves are brought back in time and energy balance is checked at incident-specimen bar interface assuming an elastic specimen. The software is capable of taking into account the dispersion due to wave propagation phenomenon in cylindrical bars and apply the appropriate corrections proposed by Pochhammer [127] and Chree [40].

In Figure 3.13 a typical equilibrium verification for a $[\pm 60]_{3s}$ laminate is shown. In this study, only those tests were considered valid where input force and output force were considered to be within ±10% of each other.

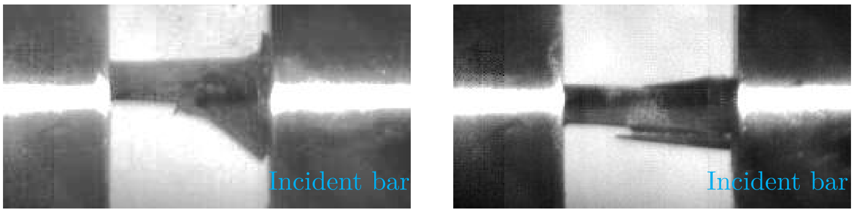

Figure 3.14: Asymmetric failure (on left) and symmetric failure (on right).

A high speed camera was also used to film some of the SHPB experiments. It was observed that for studied strain rates the catastrophic failure of specimen started from the incident bar. Figure 3.14 shows the comparison of symmetric and asymmetric failure of a $[\pm 60]_{3s}$ laminate filmed at 50,000 images/sec. Which means that $\approx$ 13 images are available for complete duration of a compressive incident wave, and even lesser for laminate failure (transmitted wave), see Figure 3.11. This low number of images limits further detailed image analysis. Still the author is able to verify the coherence between DAVID equilibrium prediction and visual image comparison i.e a symmetric failure is observed for those experiments where DAVID also verifies equilibrium of forces.

3.2.2.1 Compression $[0]_{16}$

Figure 3.15: Schematic representation of incident/transmission bar and discs.

In a previous study Rivallant [133] had observed that higher modulus of carbon fibers when loaded in fiber directions causes the local indentation of steel bars thus damaging the bars' ends. For compression along fiber tests two stainless steel discs were used having the same diameters as bars and a length of 10 mm each. These discs were water tempered to increase the surface hardness and thus serve as a protection for bar end, a schematic representation is shown in Figure 3.15. The computer program DAVID also takes into account for wave dispersion effects due to use these kind of extra interfaces.

Figure 3.16 shows traces of dynamic compression at average strain rates of $277 s^{-1}$ and $826 s^{-1}$. There is a slight increase in failure stress, σ^r_{11}, and failure strain, ϵ^r_{11}, while the compressive modulus decreases from 86 GPa to 76 GPa.

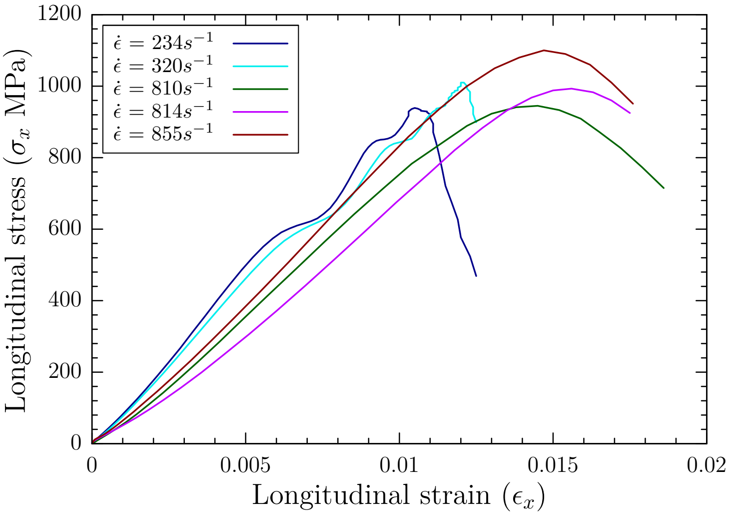

Figure 3.16: Compression along fibers $[0]_{16}$ laminate, nominal stress vs nominal strain.

The compressive failure of carbon fiber plies is usually attributed to micro-buckling of fibers, [123, 125]. This may explain the reduction in modulus and increase in failure strain, as the failure is no more pure compression of fibers but a mixed mode failure of fibers and matrix.

3.2.2.2 Compression $[90]_{16}$

For transverse compression of a $[0]_{16}$ laminated, the observed average dynamic modulus for strain rates below $490s^{-1}$ is 9.7 GPa while the static modulus is 7.64 GPa. The highest strain rate achieved for these tests is $\approx 730s^{-1}$. There is an increase in the compressive modulus at this strain rate. In order to determine true influence of strain rate some more experiments are required at higher strain rates.

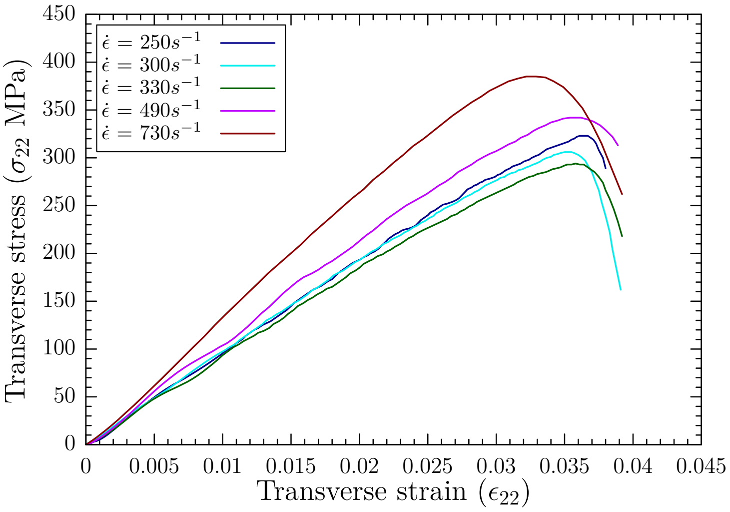

Figure 3.17: Transverse compression $[90]_{16}$ laminate, nominal stress vs nominal strain.

3.2.2.3 Compression $[\pm 45]_{3s}$

Table 3.2: T800S/M21 in plane material properties.

E_{11} (GPa)	E_{22} (GPa)	ν_{12}	G_{12} (GPa)
165	7.64	0.35	5.61

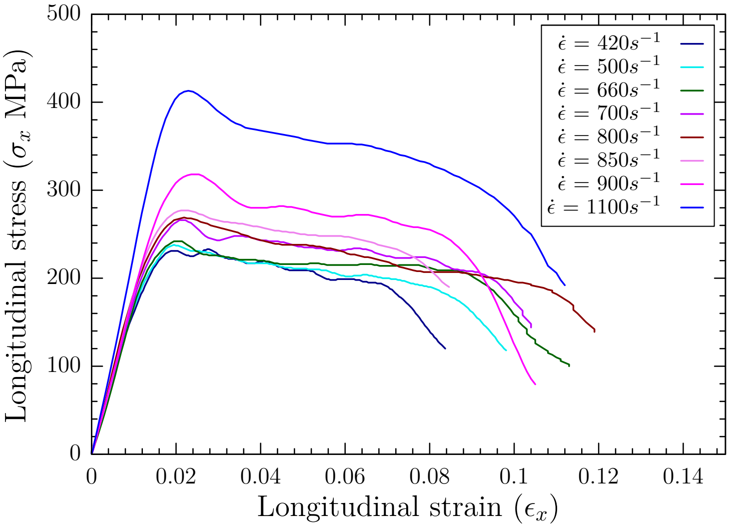

Figure 3.18: Compression of $[\pm 45]_{3s}$ laminate, nominal stress vs nominal strain.

In this paragraph the results of strain rate effect on shear behavior of $[\pm 45]_{3s}$ laminate are presented. An important assumption has been made based on classical laminate theory [62] and previous experimental investigations carried out at our laboratory [65, 92]. It is hypothesized that the global behavior of a $[\pm 45]_{3s}$ loaded in tension and compression is identical for small strains, *"quasi-pure"* shear as defined by Coutellier and Rozycki [41]. Therefore, $\sigma_{12} = 0.5\sigma_x$ and $\epsilon_{12} = 0.5\epsilon_x$. This allows to compare the yield stress, σ^y, in tension and compression for a $[\pm 45]_{3s}$ laminate. Material constants used for calculation of global modulus E_x for this paragraph and remaining $\pm\theta$ laminates by using classical laminate theory [62] are shown in Table 3.2. E_{11}, E_{22} and ν_{12} are taken from [129], while G_{12} was characterized in paragraph 3.2.1.

Classical laminate theory predicts the global modulus E_x for laminate as 19.8 GPa. The dynamic compression results show a minor increase in global modulus of the laminate. The modulus varies from 18.8 GPa to 22.8 GPa. Similarly, the failure stress increases from 190 MPa to 295 MPa and failure strain increases from 7% to 9.5%, see Figure 3.18. The overall behavior of dynamic nominal stress vs nominal strain curves is similar to the quasi-static one. A curve comprising 4 parts can be identified. First a linear elastic region is observed followed by a small nonlinear portion, showing the start of damage (irresponsibility) and then a horizontal plateau for damage accumulation and then comes the complete failure when stress starts to diminish.

In these tests it is seen that the shear yield strength is highly sensitive to strain rate loading. In quasi-static case a σ^y_{12} of $\approx$ 50 MPa, shown by a circle in Figure 3.19 is observed. This value has almost doubled in the case of strain rates above $420s^{-1}$. The second circle shows the point after which the σ^y_{12} follows a logarithmic law. For $420s^{-1} < \dot{\epsilon} < 750s^{-1}$ one observes a plateau region where the σ^y_{12} is constant $\approx$ 120 MPa.

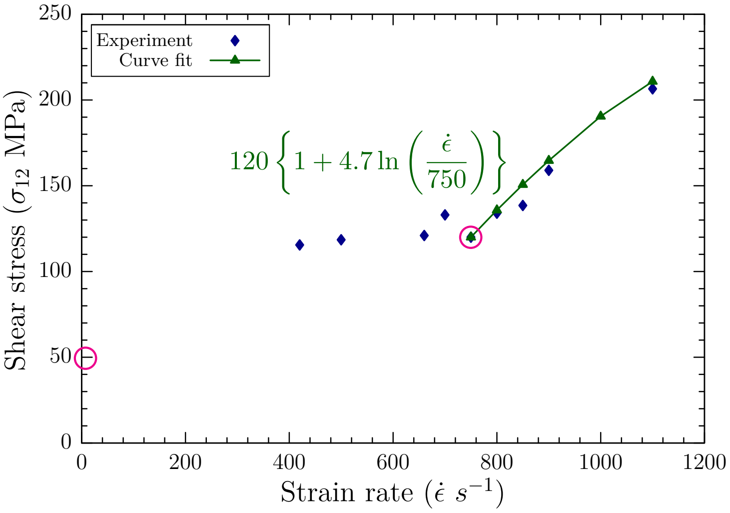

Figure 3.19: Yield stress (σ^y) versus strain rate for $[\pm45]_{3s}$ laminate.

It is difficult to give a solid conclusion, at this point, for this plateau region as the number of tests is limited for $400s^{-1} < \dot{\epsilon} < 750s^{-1}$. Furthermore, we do not have results for $1s^{-1} < \dot{\epsilon} < 400s^{-1}$ hence the evolution of failure strength between this interval is not well know at this point.

3.2.2.4 Compression $[\pm\theta]_{3s}$

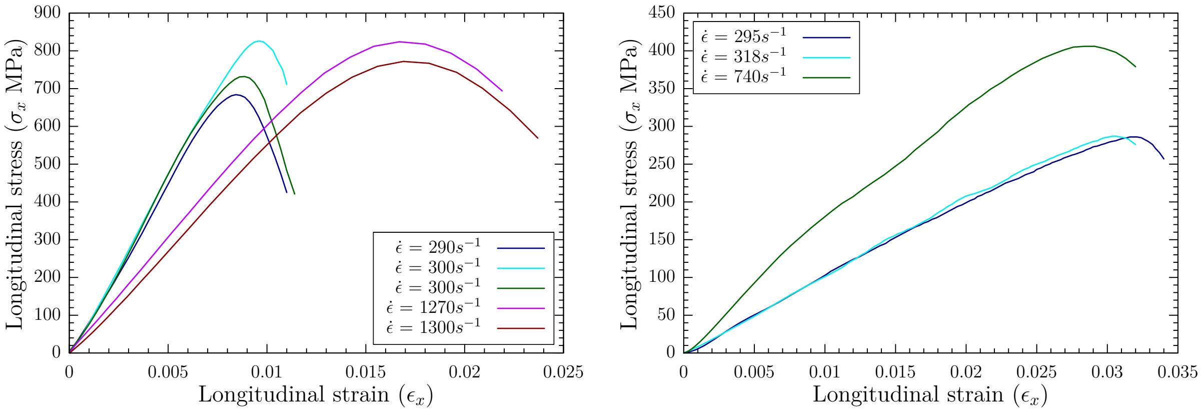

(a) Nominal stress vs Nominal strain.

(b) Nominal stress vs Nominal strain.

Figure 3.20: Dynamic compression of (a): $[\pm15]_{3s}$ and (b): $[\pm75]_{3s}$ laminates.

The Figure 3.20(a) shows curves for dynamic compression of $[\pm15]_{3s}$ laminate. Compressive modulus of $\approx$ 127 GPa is calculated for laminate by using classical laminate theory, which is higher than experimentally found compressive modulus for laminate at $\dot{\epsilon} \approx 300s^{-1}$. If we take $E^c_{11} = 0.75 \times E^t_{11}$, [65], we find global modulus $E_x = 100$ GPa laminate in compression, which is in close agreement with the observed laminate modulus of 95 GPa for average $\dot{\epsilon} \approx 300s^{-1}$. This modulus is reduced to 58 GPa for $\dot{\epsilon} = 1285s^{-1}$ while, failure strain has doubled from 0.9% to 1.8%. The failure stress does not show a significant change, varying from 750 MPa to 800 MPa.

Table 3.3: Dynamic compression of $[\pm15]_{3s}$ laminate.

$\dot{\epsilon}$ (s^{-1})	ϵ^{el} (%)	σ^{y} (MPa)	E_x (GPa)	ϵ^{r} (%)	σ^{r} (MPa)
300	0.6	560	93	0.9	740
1285	1.2	680	57	1.7	790

Table 3.4: Dynamic compression of $[\pm75]_{3s}$ laminate.

$\dot{\epsilon}$ (s^{-1})	ϵ^{el} (%)	σ^{y} (MPa)	E_x (GPa)	ϵ^{r} (%)	σ^{r} (MPa)
310	1.95	200	10	3.1	280
740	2.1	320	15	2.7	400

Only three valid tests are available for $[\pm75]_{3s}$, Figure 3.20(b). Therefore, the general tendency of global behavior is compared which is similar to the results observed in the above paragraph. As compared to the static compressive modulus of 7.64 GPa the dynamic moduli are botained as 10.3 GPa for $\dot{\epsilon} = 310s^{-1}$ and 15.3 GPa for $\dot{\epsilon} = 740s^{-1}$. The failure stress, σ_x^r, shows a considerable increase from ≈ 290 MPa to ≈ 410 MPa.

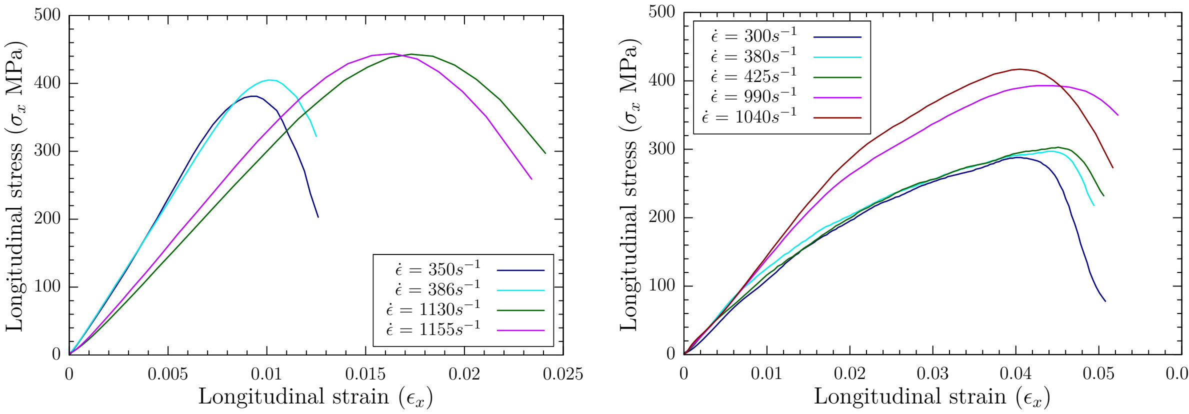

(a) Nominal stress vs Nominal strain.

(b) Nominal stress vs Nominal strain.

Figure 3.21: Dynamic compression of (a): $[\pm30]_{3s}$ and (b): $[\pm60]_{3s}$ laminates.

Table 3.5: Dynamic compression of $[\pm30]_{3s}$ laminate.

$\dot{\epsilon}$ (s^{-1})	ϵ^{el} (%)	σ^{y} (MPa)	E_x (GPa)	ϵ^{r} (%)	σ^{r} (MPa)
370	0.06	280	47	1.0	390
1140	1.2	380	32	1.7	440

Table 3.6: Dynamic compression of $[\pm 60]_{3s}$ laminate.

$\dot{\epsilon}$ (s^{-1})	ϵ^{el} (%)	σ^{y} (MPa)	E_x (GPa)	ϵ^{r} (%)	σ^{r} (MPa)
370	1.2	145	12	4.6	280
1115	1.7	240	14	4.2	400

Global tensile modulus for a $[\pm 30]_{3s}$ laminate is 54 GPa. Figure 3.21(a) shows results of dynamic compression of such a laminate. The dynamic modulus for an average strain rate of $370s^{-1}$ is, 46 GPa, close to the calculated static value. This modulus is reduced by 30% and becomes 32 GPa at average strain rate of $1140s^{-1}$. The failure stress increases from 390 MPa to 440 MPa. Accordingly the failure strain increases from 1.02% to 1.74%.

For a $[\pm 60]_{3s}$ laminate, Figure 3.21(b), it is observed that two average strain rates $370s^{-1}$ and $1115s^{-1}$. For these strain rates dynamic compressive moduli for laminate are 12 GPa and 14 GPa, respectively. The calculated static modulus is 10.8 GPa. Furthermore, the failure stress is increased by $\approx 36\%$.

3.2.2.5 Summary of Dynamic Compression Results

In the above paragraphs it has been observed that the T800S/M21 is strain rate sensitive. It is chosen to plot hereafter tendency curves of three effective global mechanical behavior properties on fiber angle and strain rate using the values identified in the previous tables. The purpose is to identify whether it is necessary or not to take into account strain rate effects in material damage model to be defined later on, and if so in what manner.

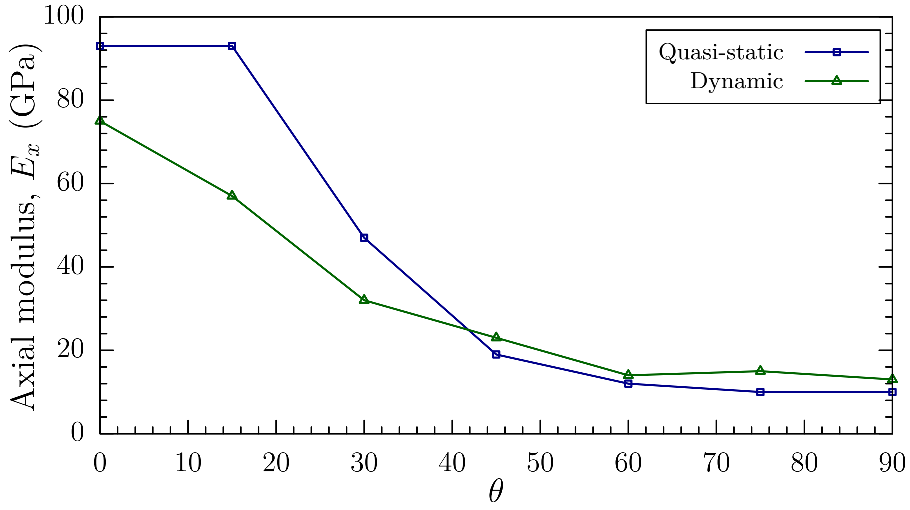

Figure 3.22: Tendency of effective Young's modulus as a function of specimen angle and strain rate.

For fiber oriented samples (0°, 15°, 30°), the compressive dynamic elastic modulus decreases with the strain rate by $20\% - 40\%$ (see Figure 3.22). In all three cases the limit elastic deformation is 0.6% in quasi-static and 1.2% in dynamics. Typical deformations at rupture are about 1% in quasi-static and 1.5% – 1.7% in dynamics. At this moment it is not known whether this effect comes from the resin inside the ply or at interfaces. It is possible that local effects due to dynamic compression of 0° plies generate unexplainable results, Figure 3.22.

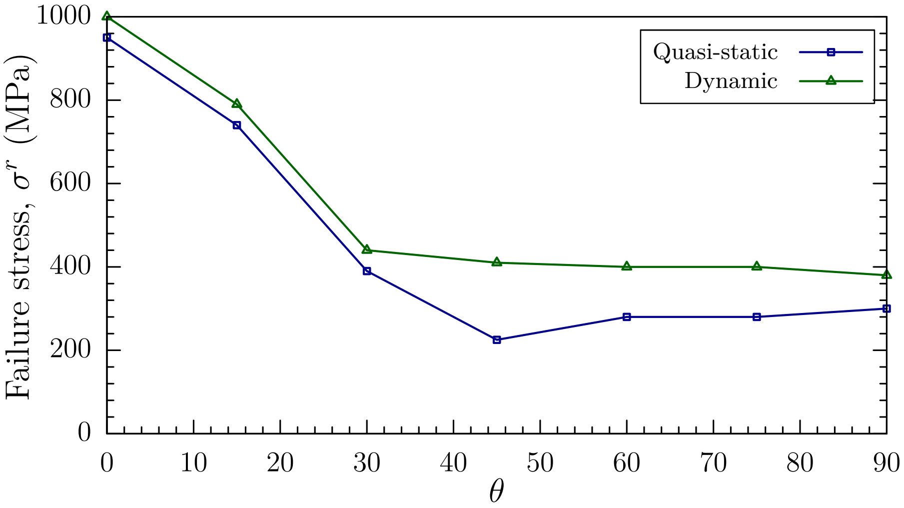

Figure 3.23: Tendency of longitudinal failure stress as a function of specimen angle and strain rate.

For fibers de-oriented samples (60°, 75°, 90°) the compressive elastic modulus increases by the 17% – 30% (see Figure 3.22). The limit elastic strain both in quasi-static and dynamic compression grow with growing angles from 1.2% – 1.7% to 2.4% – 2.7%. This effect is attributed to the viscoelastic behavior of epoxy resins or interfaces.

One can notice that whatever the angle after 45°, 1.2% of deformation is a limit at which curves of longitudinal failure stresses and effective moduli show a slope variation. The reader is reminded that 1.2% was identified previously as the elastic limit of deformation after which the behaviors of T700S/M21 and T800S/M21 change in quasi-static tension and quasi-static compression. Thus it is suggested that the matrix effect for angles greater than 45° it is suggested that a saturation effect appears due to the resin rich layer at interfaces as described in above paragraph.

In all cases, the failure stress increases with strain rate. For fiber oriented samples failure stresses decrease with the growing angle both in quasi-static and dynamic compression of about 25% for $\theta = 15°$ and 60% for $\theta = 30°$ with respect to $\theta = 0°$. The dynamic/quasi-static ratio of failure stresses grows with growing angle up to 1.1 at 30° (see Figure 3.23).

For fiber disoriented samples failure stresses remain approximately constant with growing angle in quasi-static and dynamic with a dynamic/quasi-static ratio of about 1.3 (see Figure 3.23).

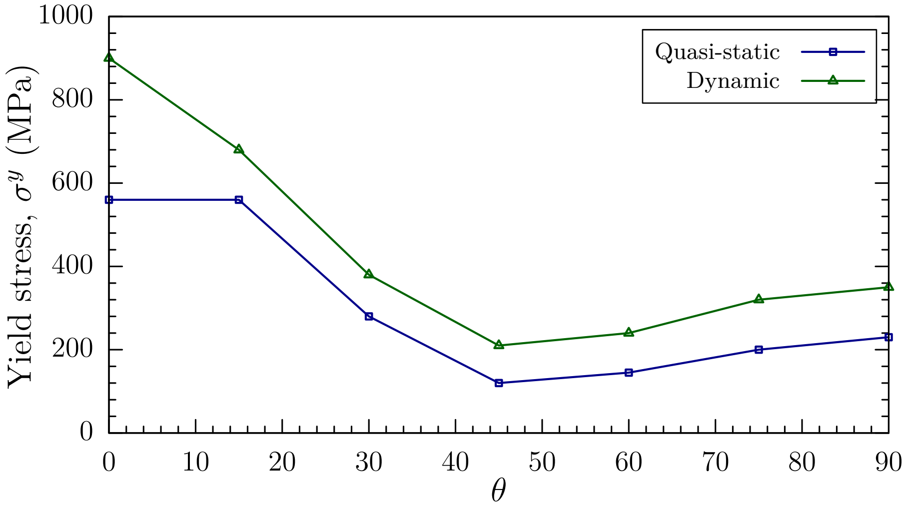

Figure 3.24: Tendency of longitudinal yield stress as a function of specimen angle and strain rate.

These two curves, in author's opinion, show the predominant effect of the ply behavior on the elastic limit and global failure of the samples. Thus it is decided to include strain rate effects on strengths and to use these values to initiate and propagate damages up to failure in modified continuum damage mechanics law. Strain rate effects have been identified on 45° samples.

Since the effect of the matrix depends both on angles and strain rate in an indirect way and with no rigorously identified physical meaning, It is decided that any variation of the elastic moduli in the material damage law is not taken into account. On the contrary, failure stresses exhibit a continuous dependency on the strain rate, as does the apparent yield stresses.

3.3 Constitutive Law

This section is dedicated to the modified material model used for Hopkinson bar experiment simulations and the impact simulations to be presented later on. The modifications and enhancements in the basic MLT model are presented at first. Then a parametric study for 1-D finite element model is presented. Comparison with the basic material model is then conducted. And in the last paragraphs the correlation with the Hopkinson's bar experiments is presented.

3.3.1 Proposed/Modified MLT Model

In paragraph 3.1.2.2 the failure criteria based MLT model as found in open literature is presented. The model identifies 6 damage modes d_i, $i = 1 \cdots 6$, which operate on 6 moduli of an orthotropic material (Equation 3.44), and 5 ruin modes r_i, $i = 1 \cdots 5$ based on 5 corresponding failure modes. Four modifications are proposed in: (i) failure criteria to incorporate compression in transverse direction (ii) calculation of test stress σ^* (iii) damage coupling matrix to couple d_5 with delamination ruin mode and (iv) damage saturation to introduce failure. These modifications are discussed in the following paragraphs.

For damage calculation it is proposed that:

$$d_i = q_{ij}\phi_j, j = 1 \cdots 5 \text{ and } \phi_j = 1 - \mathrm{e}^{\frac{1}{m_j}\left(1 - r_j^{m_j}\right)}, r_j \geq 1 \tag{3.41}$$

Damage evolution function ϕ is unchanged from [160]. For d_1:

$$d_1 = (1 - \phi_1) + (1 - \phi_2) + (1 - \phi_3) \tag{3.42}$$

Lachaud [92] has shown that the damage parameter d for unidirectional composite materials never reaches a value of 1, but there is a damage saturation limit for these materials especially in transverse direction. Once this damage saturation has been reached, failure can occur at any instant without further detectable increase in damage. This observation has been implemented particularly for damage parameter d_2, i.e whenever $d_2 > d_{max}$, d_2 is set equal to 1, so the material does not support the load in ply transverse direction anymore. As a consequence of this the coupling matrix dictates that d_4 and d_5 are also set to a value of 1.

Based on experimental observations in paragraph 3.2.1 and literature survey [57, 115] (e.g see Figure 1.7) it is proposed to couple d_5 with the ruin mode r_5 as the cracks inside unidirectional ply are not always perpendicular to the ply 1-2 plane especially for low velocity impact loading. Therefore the coupling matrix q becomes:

$$q = \begin{bmatrix} 1 & 1 & 1 & 0 & 0 \\ 0 & 0 & 1 & 1 & 0 \\ 0 & 0 & 1 & 0 & 1 \\ 1 & 1 & 1 & 1 & 1 \\ 0 & 0 & 1 & 1 & \underline{\boldsymbol{1}} \\ 1 & 1 & 1 & 0 & 1 \end{bmatrix} \tag{3.43}$$

The flexibility matrix in 3D is given by Equation 3.44, in order to take into account the out of plane normal and shear associated damages.

$$C^{-1} = \begin{bmatrix} \frac{1}{(1-d_1)E_{11}^0} & \frac{-\nu_{21}}{E_{22}} & \frac{-\nu_{31}}{E_{33}} & & & \\ \frac{-\nu_{12}}{E_{11}} & \frac{1}{(1-d_2)E_{22}^0} & \frac{-\nu_{32}}{E_{33}} & & & \\ \frac{-\nu_{13}}{E_{11}} & \frac{-\nu_{23}}{E_{22}} & \frac{1}{(1-d_3)E_{33}^0} & & & \\ & & & \frac{1}{(1-d_4)G_{12}^0} & & \\ & & & & \frac{1}{(1-d_5)G_{23}^0} & \\ & & & & & \frac{1}{(1-d_6)G_{13}^0} \end{bmatrix} \tag{3.44}$$

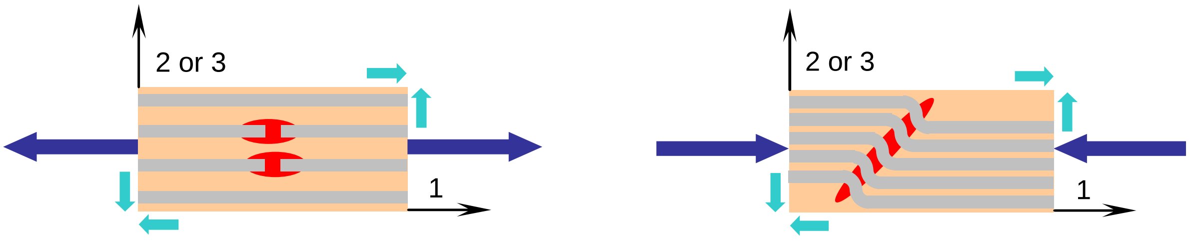

(a) Tensile failure in fiber direction.

(b) Compressive failure in fiber direction.

Figure 3.25: Tension and compression failure in fiber direction.

$$f_1(\sigma, d, r) = \left(\frac{\langle\sigma_{11}\rangle}{X_T}\right)^2 + \frac{\sigma_{12}^2 + \sigma_{13}^2}{S_{fs}^2} - r_1^2 = 0 \tag{3.45}$$

The tensile failure criteria is presented in Equation 3.45. The effect of shear loadings is taken into consideration, since the material strength S_{fs}, the debonding strength of fiber matrix interface, is not characterized, an appropriate value is chosen based on experience. X_T is the tensile failure stress in fiber direction.

Equation 3.46 describes the fiber failure due to compression. This failure criteria takes into account the average of the eventual loading by the adjacent material exerting compressive normal stresses in transverse and out of plane direction.

$$f_2(\sigma, d, r) = \left[\frac{\left\langle -\sigma_{11} + \frac{\langle -\sigma_{22} - \sigma_{33}\rangle}{2}\right\rangle}{X_C}\right]^2 - r_2^2 = 0 \tag{3.46}$$

where X_C is the compressive failure stress in fiber direction.

The third failure mode represents the crushing of material as describe in Equation 3.47. This failure criteria is utilized to represent the crushing of material due to high stresses in the material below the impactor in an impact event.

$$f_3(\sigma, d, r) = \left[\frac{\langle -(\sigma_{11} + \sigma_{22} + \sigma_{33}) \rangle}{3Z_C} \right]^2 - r_3^2 = 0 \tag{3.47}$$

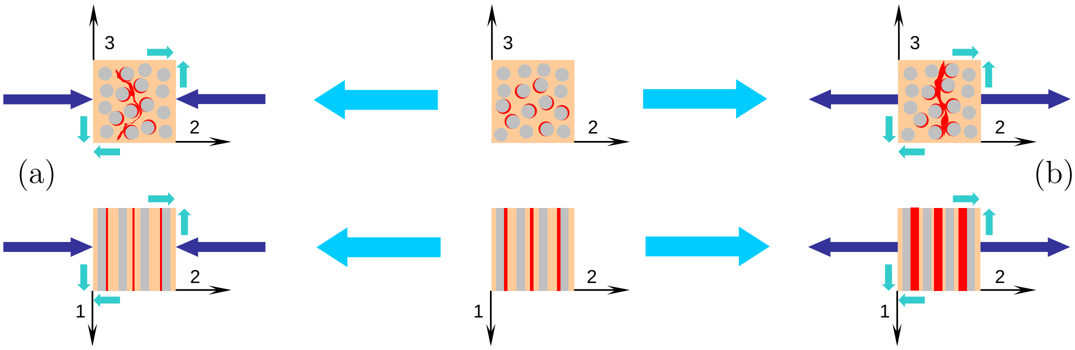

Figure 3.26: (a) Compression and (b) tension in transverse direction.

$$\begin{aligned} f_4(\sigma, d, r) = \Bigg[& \left(\frac{\langle \sigma_{22} \rangle}{Y_T} \right)^2 + \left(\frac{\langle -\sigma_{22} \rangle}{Y_C} \right)^2 \\ & + \left(\frac{\sigma_{12}}{S_{12} + \langle -\sigma_{22} \rangle \tan\varphi} \right)^2 + \left(\frac{\sigma_{23}}{S_{23} + \langle -\sigma_{22} \rangle \tan\varphi} \right)^2 \Bigg]^2 - r_4^2 = 0 \end{aligned} \tag{3.48}$$

The transverse cracking due to σ_{22} is coupled with in plane shear due to σ_{12} and out of plane (perpendicular to fiber direction) shear due to σ_{23} as shown in Figure 3.26. Equation 3.48 has been modified to take into account the failure due to pure compression in transverse (2-)direction as well. Y_T and Y_C are failure stresses in tensile and compressive loading along the transverse direction. S_{12} and S_{23} are the shear failure stresses in $1-2$ and $2-3$ planes. The failure criteria takes into account the difference in mechanical behavior due to opening or closing of the cracks. The parameter $\tan\varphi$ can be considered as a coefficient of friction for material and only intervenes when the material is loaded in compression. Therefore, this parameter has an effect of material shear strength enhancement proportional to the compressive load.

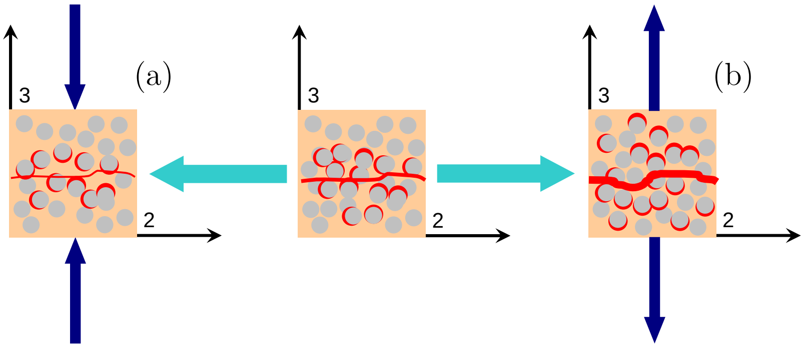

Figure 3.27: (a) Compression and (b) tension in out of plane direction.

$$\begin{aligned} f_5(\sigma, d, r) =& S_{del} \left[\left(\frac{\langle \sigma_{33} \rangle}{Z_T} \right)^2 + \left(\frac{\sigma_{13}}{S_{13} + \langle -\sigma_{33} \rangle \tan\varphi} \right)^2 \right. \\ & \left. + \left(\frac{\sigma_{23}}{S_{23} + \langle -\sigma_{33} \rangle \tan\varphi} \right)^2 \right]^2 - r_5^2 = 0 \end{aligned} \tag{3.49}$$

The out of plane normal stress σ_{33} is coupled with out of plane (parallel with fiber direction) shear σ_{13} and out of plane (perpendicular to fiber direction) shear σ_{23}, see Equation 3.49. Z_T is the tensile failure stress in out of plane (3-)direction and S_{13} is the shear failure stress in $1-3$ plane. This failure criteria represents the delamination failure. The parameter S_{del} gives the possibility to include a non local approach i.e depending on the stresses of adjacent elements, one can modify the delaminated area. At this moment, this parameter has not been used.

3.3.2 Modified and Reference MLT Models: 1–D Comparison

A MATLAB® program was written to solve a 1-D bar element with following material properties, $A_s = 20 \times 2$ mm^2, $L_s = 20$ mm, $E = 20$ GPa, $X_T = 60$ MPa and $d_{max} = 0.99$, by using implicit-time integration scheme, [164]. This allows to test different material model combinations and influence of different model parameters, e.g ϕ the damage evolution function and m the material softening parameter, in less than 1 sec of CPU time.

An illustration of numerical integration schemes for modified MLT, Figure 3.28(a), and reference MLT, Figure 3.28(b), models, respectively. The solution methods consist of calculation of a test stress, σ^*, which is then modified to find admissible stress at particular time-step of interest. For the modified model the damaged modulus for loading and unloading stress calculations is used whereas for reference model loading stress is calculated by undamaged modulus and unloading stress by damaged modulus. It is worth

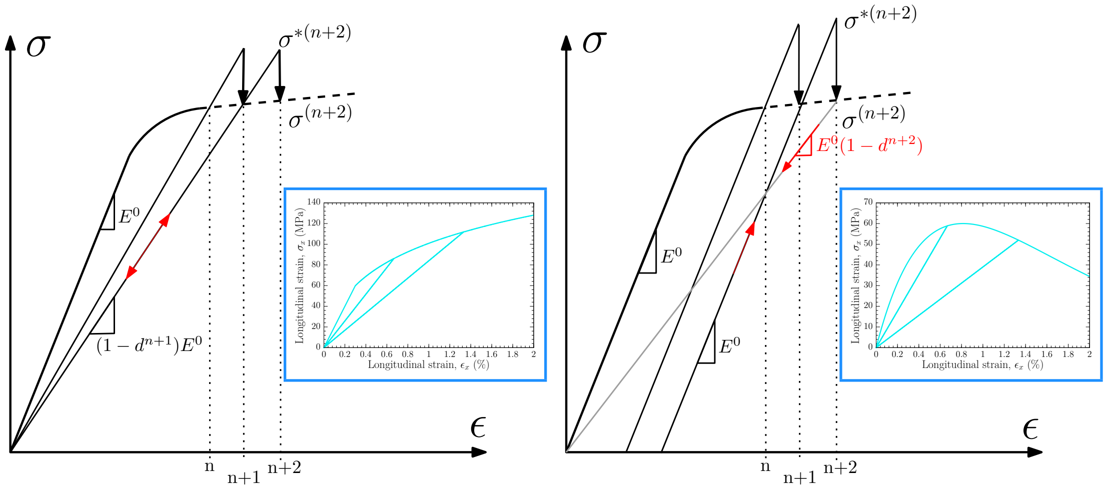

(a) Diffused damage (modified) model [77]. (b) Rupture modeled by softening, [111].

Figure 3.28: Illustration of numerical integration schemes for the two models.

noting that the modified material model at the moment and reference model do not incorporate plasticity. Therefore, no residual strains remain after unloading, as shown on the respective inner frames. For the evaluation of the failure criteria the reference model verifies:

$$\frac{\sigma^*}{\sigma^r} - r \geq 0 \tag{3.50}$$

for damage to take place, where σ^r is the failure stress. On the other hand the proposed diffused damage model verifies that:

$$\frac{\sigma^*}{(1-d)\sigma^y} - r \geq 0 \tag{3.51}$$

where σ^y is the stress value for the damage of material to start. Furthermore, in the above examples, as soon as the damage parameter attains a values superior or equal to d_{max} it is set equal to one i.e the rigidity of material disappears and failure takes place.

As described earlier in paragraph 3.1.2.2, two types of choices for damage evolution are found in literature. Matzenmiller et al. [111], Williams and Vaziri [156] use $\phi = \exp\left(\frac{-r^m}{me}\right)$, while Xiao et al. [160] has proposed $\phi = \exp\left(\frac{(1-r)^m}{m}\right)$. The four possible combinations of the damage evolution functions and material models (modified and reference) are presented in Figure 3.29. Figures 3.29(c) and 3.29(d) show that there exists a limit for these cases to recapture the material rigidity above $m = 4$, below this value of m the model predicts a very soft response.

Figures 3.29(a) and 3.29(b) show that the material response is linear-elastic to the threshold value X_T. In Figure 3.29(b), it can be seen that the stress as a function of strain is always decreasing thus unable to represent the stress saturation behavior of T800S/M21. In author's opinion the modified material model with damage evolution law shown in Figure 3.29(a) is more suited to represent the quasi-static experimental behavior as observed in paragraph 3.2.1. Therefore, the combination shown in Figure 3.29(a) is retained for further investigations.

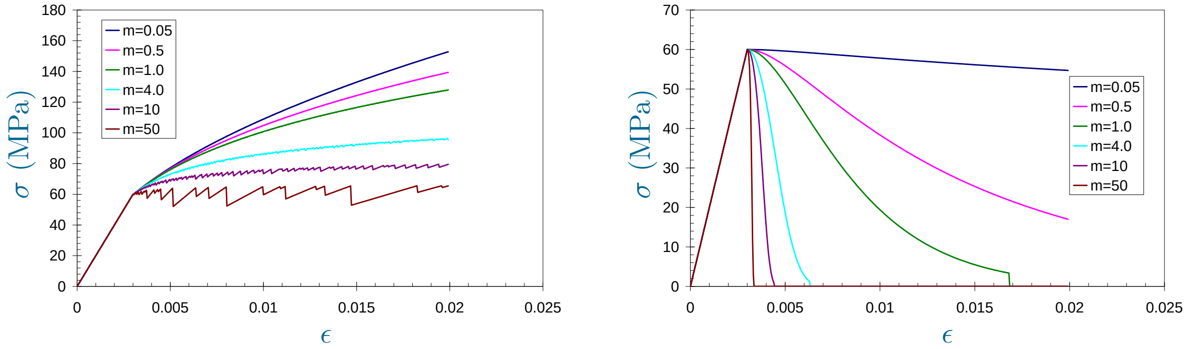

(a) $\phi = \exp\left(\frac{(1-r)^m}{m}\right)$, $\sigma^* = (1-d)E^0\epsilon$ (b) $\phi = \exp\left(\frac{(1-r)^m}{m}\right)$, $\sigma^* = E^0\epsilon$

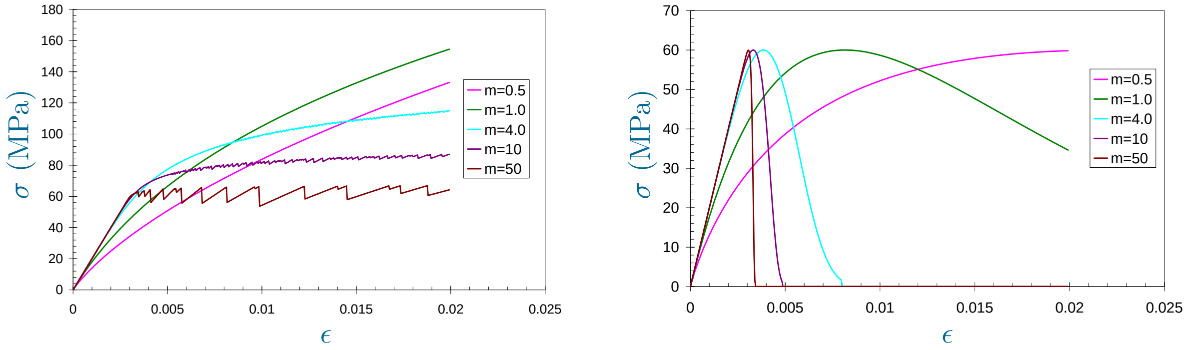

(c) $\phi = \exp\left(\frac{-r^m}{me}\right)$, $\sigma^* = (1-d)E^0\epsilon$ (d) $\phi = \exp\left(\frac{-r^m}{me}\right)$, $\sigma^* = E^0\epsilon$

Figure 3.29: Four variant models based on MLT continuum damage mechanics model.

3.3.3 Quasi-static Tension Simulation

Until now the material model has been selected and modified in an attempt to predict the quasi-static tensile behavior. So this particular section is dedicated to correlation of numerical material and finite element model with the quasi-static experiments of T700S/M21 and T800S/M21. Finite element code LS-DYNA® is used to solve the quasi-static problem. Figure 3.30 shows the boundary conditions of the LS-DYNA® finite element model. The laminate symmetry allows to construct one half of the model. Symmetry boundary conditions about xy-plane, to represent symmetric laminate, and yz-plane, to represent clamping in INSTRON® machine, are applied. This numerical model contains 300 under-

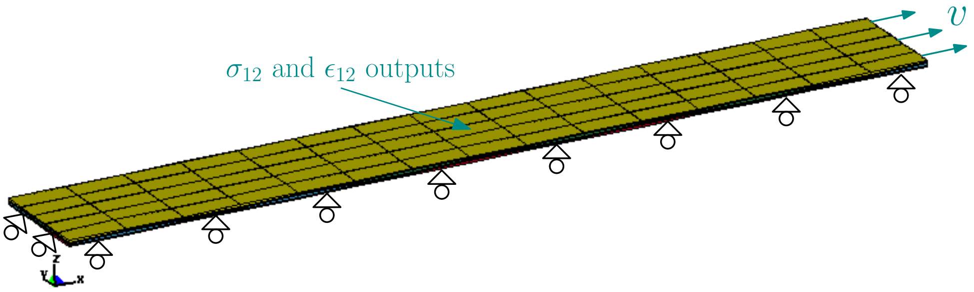

Figure 3.30: Quasi-static tension FEA model.

integrated (1 integration point 8 nodes) solid elements. In order to have a finite element model which takes less 10 minutes to be solved by using the explicit-time integration scheme [164], it is chosen to apply a velocity $v = 1$ m/sec. This choice of applied velocity is purely based on a compromise between solution time and dynamic effects to be damped out as a damping algorithm same as section 2.3.1 of Chapter 2 has been used.

Table 3.7: Material model data for T700S/M21 simulation.

E_{11} (GPa)	E_{22} (GPa)	E_{33} (GPa)	ν_{12}	ν_{23}	ν_{13}	G_{12} (GPa)	G_{23} (GPa)	G_{13} (GPa)
135	7.69	7.69	0.34	0.4	0.34	4.75	2.75	4.75
X_T (GPa)	X_C (GPa)	Y_T (GPa)	Y_C (GPa)	Z_T (GPa)	Z_C (GPa)	S_{12} (GPa)	S_{23} (GPa)	S_{13} (GPa)
2.2	1.2	0.04	0.25	0.04	0.7	0.045	0.045	0.045
-	S_{fs} (GPa)	S_{del}	m_i	φ	d_{max}	$\mathcal{C}_1$	$\dot{\epsilon}_{ref}$ (s^{-1})	-
–	1.5	1.0	1.75	10	0.87	–	–	–

Table 3.8: Material model data for T800S/M21 simulation.

E_{11} (GPa)	E_{22} (GPa)	E_{33} (GPa)	ν_{12}	ν_{23}	ν_{13}	G_{12} (GPa)	G_{23} (GPa)	G_{13} (GPa)
165	7.64	7.64	0.35	0.4	0.35	5.61	2.75	5.61
X_T (GPa)	X_C (GPa)	Y_T (GPa)	Y_C (GPa)	Z_T (GPa)	Z_C (GPa)	S_{12} (GPa)	S_{23} (GPa)	S_{13} (GPa)
2.2	1.2	0.045	0.28	0.045	0.7	0.05	0.05	0.05
-	S_{fs} (GPa)	S_{del}	m_i	φ	d_{max}	$\mathcal{C}_1$	$\dot{\epsilon}_{ref}$ (s^{-1})	-
–	1.5	1.0	10	10	0.87	4.7	750	–

Material data sets used for T700S/M21 and T800S/M21 are shown in Tables 3.7 and 3.8, respectively. The moduli and strength values are of the same order of magnitude for both materials. The failure strength Y_C for T800S/M21 was determined from the transverse compression tests with SHPB, while for T700S/M21 an estimated value has

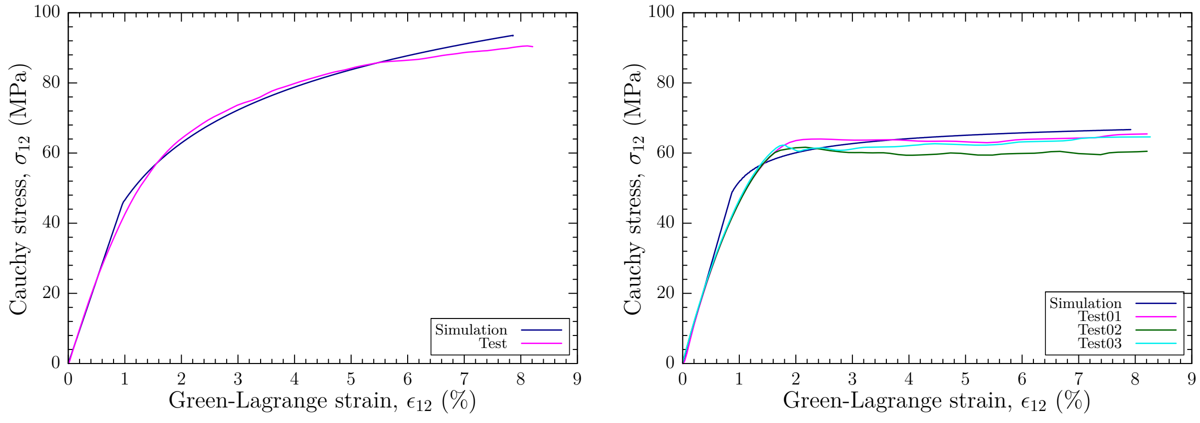

(a) T700S/M21 (b) T800S/M21

Figure 3.31: Comparison between test and numerical prediction of tensile behavior of T700S/M21 and T800S/M21, $[\pm 45]_{2s}$ laminates.

been used. Similarly, Z_C for both materials was chosen based upon the tests conducted by Briche [29].

Figure 3.31 shows the results of experimental and numerical correlation of T700S/M21 and T800S/M21 material systems. The numerically obtained values of stress and strain are measured within an element located in the middle specimen as shown in Figure 3.30. While the experimental results are same as described earlier. It is clear from the comparison of Figure 3.31(a) and 3.31(b), that the damaged behavior of both materials is defined by the damage softening parameter m. For T700S/M21 and T800S/M21 the corresponding values of $m_2 = 1.75$ and $m_2 = 10$, respectively, are suitable for prediction of quasi-static behavior. Another important point to be noted here is the damage saturation incorporated by setting $d = 0.87$ for both materials. Once this value has been reached the material moduli E_{22}, G_{12} and G_{23} are instantly reduced to zero.

3.3.4 1-D Parametric Study of SHPB

In this section a robust MATLAB® program developed to simulate an SHPB test is presented. This small program takes less than 5 sec to do a linear elastic simulation of SHPB test, by using explicit-time integration, [164]. This program was developed to help in selection of (i) impactor length (ii) impactor velocity (v_{imp}) and (iii) specimen dimensions (L_s, A_s) for a desired strain rate ($\dot{\epsilon}$) before an SHPB test.

3.3.4.1 Mesh and Boundary Conditions

The SHPB apparatus is modeled by using 1-D bar elements. 200 elements are used to represent each (Incident and Transmission) bar. The specimen is also modeled with the same type of elements, 16 in number, but with a different cross section. These choices for spatial discretization are to take into account the wave propagation effects and at the same time to keep the solution time to a minimum. Since the author is interested in only the first compressive wave propagating in the SHPB system, the contact between the bars and specimen is not modeled and the ends of specimen and bars share a common node. Material properties and dimension of SHPB system are same as in Table 3.1.

Analytical formulas are used to introduce the amplitude and duration of the compressive stress wave in the incident bar. For illustration purpose, the compressive waves in this section are shown with a positive sign. The time of impact can be found using Equation 3.40, and the amplitude of the force due to compressive wave observed by the bars made of same material and having same cross section is given as [93]:

$$F = \frac{1}{2} \rho_b \, A_b \, c_o \, v_{imp} \tag{3.52}$$

Where ρ_b and A_b are density and area of the bars, respectively. c_o is the speed of sound in the bars and v_{imp} is velocity of impactor bar.

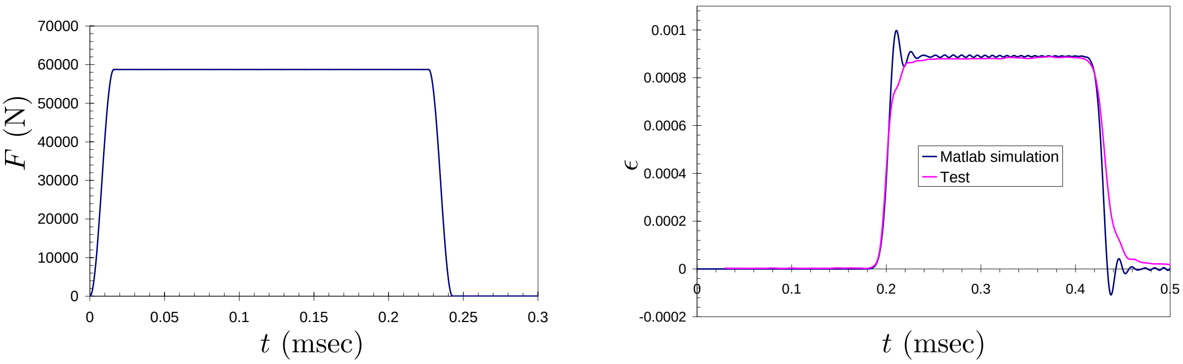

(a) Force applied at incident bar end.

(b) Strain in incident bar.

Figure 3.32: Comparison experiment and MATLAB® results, $v_{imp} = 9.13$ m/sec.

Figure 3.32 shows the applied force and the observed longitudinal strain in the incident bar. The rise time i.e time for stress (or strain) to attain the maximum value is $\approx 1/50$ of impact time. The comparison with a test at v_{imp} is shown in figure in Figure 3.32(b). A good correlation is obtained for the rise time of strain in the incident bar and time of impact, t_{imp}. Al-Maghribi [6] has compared this MATLAB® function with commerical codes MECANO (implicit code) and EUROPLEXUS (explicit code) using similar 1-D finite elements and a good correlation is obtained, it is also shown that the oscillations experienced by the numerical model can be damped by introducing a damping algorithm. For the purpose of this study the error generated by these oscillations is accepted, and damping has not been incorporated.

3.3.4.2 Influence of Impactor Length (L_{imp})

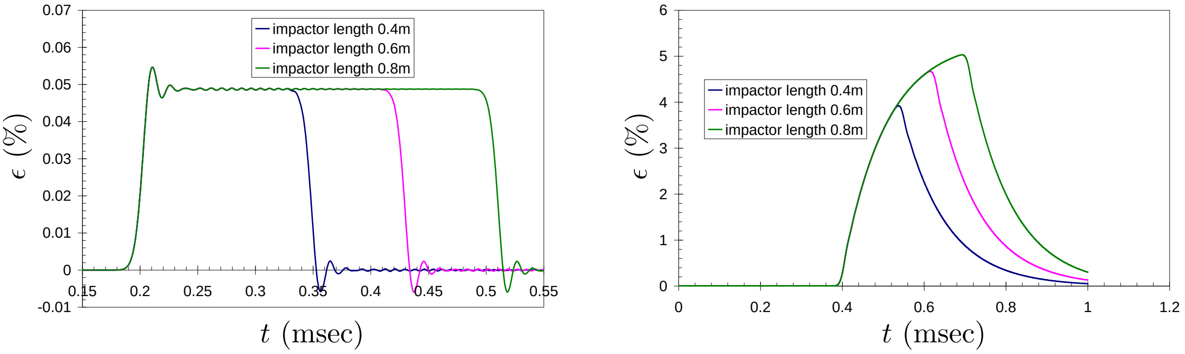

(a) Strain in incident bar. (b) Strain in specimen.

Figure 3.33: Influence of impactor length, $v_{imp} = 5$ m/sec.

As it is seen that time of impact is directly proportional to impactor length as $t_{imp} = 2L_{imp}/c_o$. Figure 3.33 shows results for three different impactor lengths, $L_{imp} \in \{0.4, 0.6, 0.8\}$. For the same impact velocity it can be seen that the maximum strain in specimen increases with increase in impactor length as the specimen is solicited for a longer duration of time. Thus, one can estimate the suitable impactor length depending on material to be tested (ductile or brittle materials).

3.3.4.3 Influence of Impactor Velocity (v_{imp})

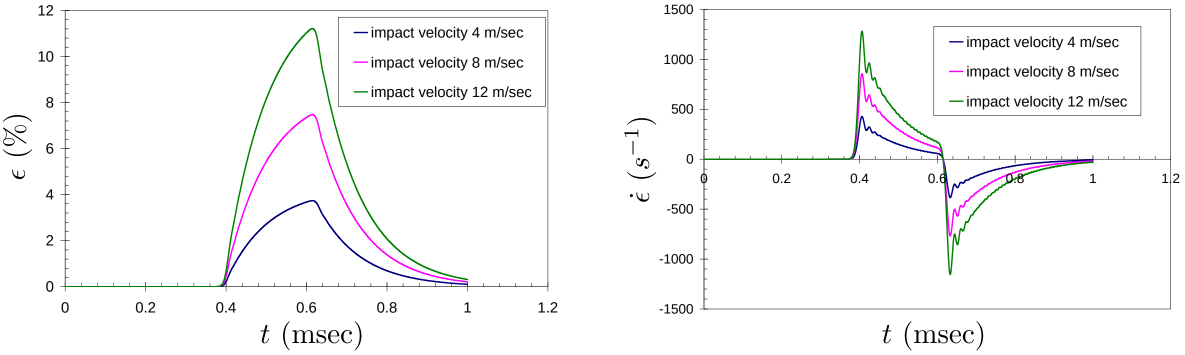

(a) Strain in specimen. (b) Strain rate in specimen.

Figure 3.34: Influence of impact velocity, $L_{imp} = 0.6$ m.

The impact velocity is related to the amplitude of force as $F = 0.5\rho_b A_b c_o v_{imp}$. Increase in applied force manifests as an increase of strain experienced by the specimen. As a consequence the strain rate also increases as $\dot{\epsilon} = \partial\epsilon/\partial\text{t}$. Figure 3.34 shows the results for three different impact velocities, $v_{imp} =\in \{4, 8, 12\}$ m/sec. Therefore, one can have a good estimation of the maximum strain rate to be expected.

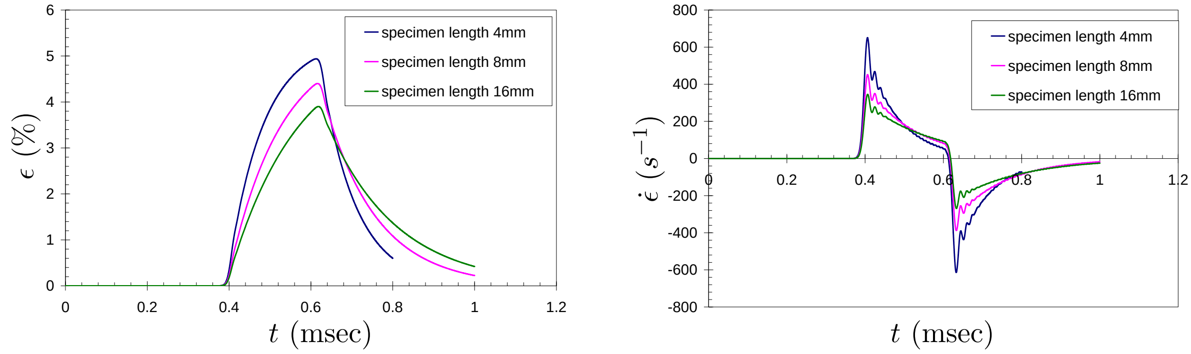

(a) Strain in specimen.

(b) Strain rate in specimen.

Figure 3.35: Influence of specimen length $v_{imp} = 5$ m/sec, $L_{imp} = 0.6$ m.

3.3.4.4 Influence of Specimen Length (L_s)

Figure 3.35 shows the results for a specimen with initial length, $L_s \in \{4, 8, 12\}$ mm. The results shown here are for instantaneous strain rates in specimen. To illustrate the author's point let us consider the equation DAVID uses for strain rate calculation:

$$\dot{\epsilon} = \frac{v_{inc} - v_{tra}}{L_s} \tag{3.53}$$

Where v_{inc} and v_{tra} are incident and transmission bar-end velocities, respectively. Therefore, to obtain higher strain rates one can keep the length of specimen small for same impact velocity and impactor length.

3.3.4.5 Strain Rate Effects

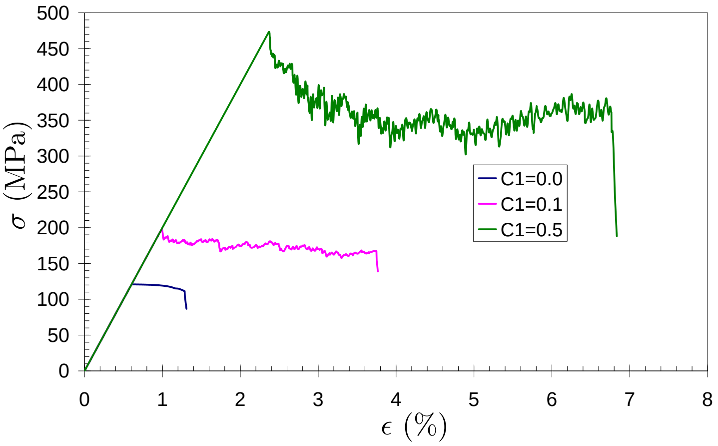

Figure 3.36: Influence of constant $\mathcal{C}_1$.

In section 3.2.2 an improvement in yield strength for T800S/M21 laminates is observed. We do a parameter sensitivity study using the developed MATLAB® program. The material model does not incorporate the change in modulus due to compression loading and neither does it incorporate the enhancement in modulus depending upon strain rate at the moment. Therefore, only the effect of strength enhancement due to increase in strain rate is compared.

The specimen dimensions are $L_s = 8$ mm and $A_s = 10 \times 3$ mm^2. Impact velocity is 5 m/sec and quasi-static yield strength $S^0 = 120$ MPa. To incorporate yield strength enhancement the expression $S^{max} = S^0\{1 + \mathcal{C}_1 \ln(\dot{\epsilon}/\dot{\epsilon}_{ref})\}$ is implemented. It is observed that the quasi-static strength value ($\mathcal{C}_1 = 0$) is not adequate for dynamic simulations giving small failure strain of $\approx 1.4\%$. The higher values of $\mathcal{C}_1$ tend to make specimen resist more as yield stress and failure strain increase as shown in Figure 3.36.

3.3.5 Dynamic Compression Simulation

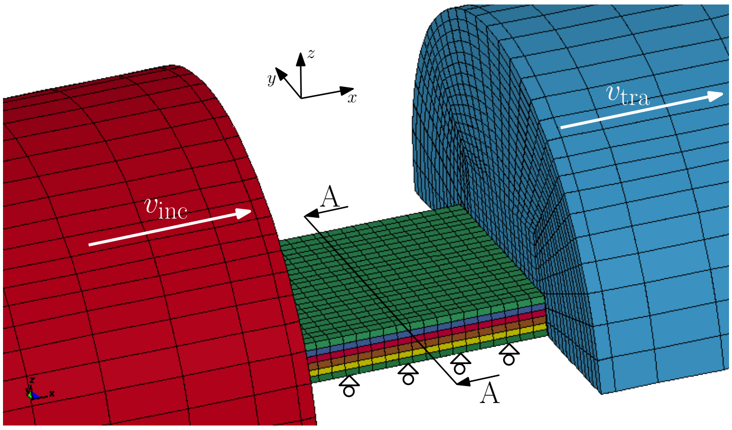

Figure 3.37: Dynamic compression model and boundary conditions.

This section describes the dynamic compression test simulations of SHPB by using the finite element code LS-DYNA® in order to take into account the experimentally determined parameters. The finite element model for these simulations is shown in Figure 3.37. The symmetry of laminates justifies the half model. Symmetry of the specimen is modeled by restraining the z-displacement of nodes in xy-plane as shown in the above figure. The under-integrated 8 node solid elements with 1 integration point are used. The incident and transmission bars are modeled by rigid (non-deformable) elements. Contact between specimen and rigid bars is modeled by the penalty formulation, [107]. The end velocities for incident bar (v_{inc}) and transmitted bar (v_{tra}) calculated by DAVID are used as an input for the finite element model. The finite element model takes less 8 minutes for the calculation to be completed. For experimental setup we have limited ourselves to the nominal stress vs nominal strain behavior, so the stresses are measured across the section A-A as shown in Figure 3.37. The material data set used for the following simulations is same as shown in Table 3.8.

3.3.5.1 Compression $[\pm 45]_{3s}$

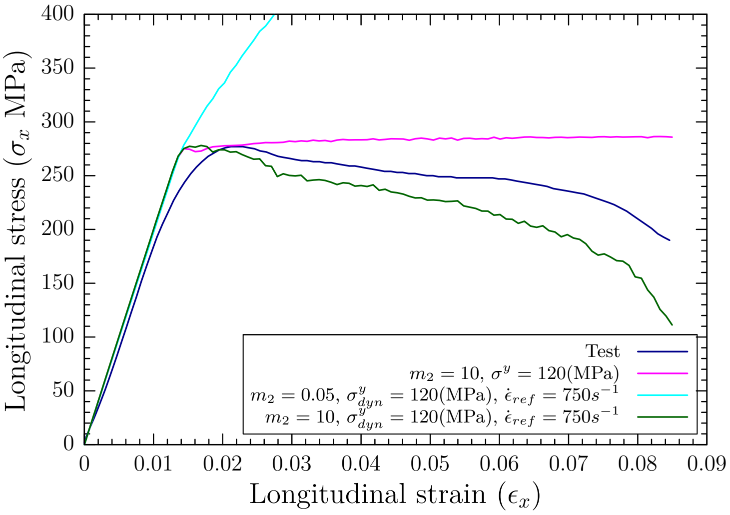

Figure 3.38: 3-D SHPB simulation of $[\pm 45]_{3s}$ laminate at $\dot{\epsilon} = 850s^{-1}$

Figure 3.38 shows the results of simulations carried out for a test at $\dot{\epsilon} = 850s^{-1}$. The curve shown in magenta is for a simulation where σ^y_{12} is kept constant at a fixed value of 120 MPa. It can be seen that the failure, as in test (curve in navy blue color), is never attained but simulation shows an increase in strain with $\approx$ constant stress. From here it is concluded that it is not sufficient to use only a fixed value of σ^y_{12} to capture the experimental response. The curve in dark green color shows the simulation with a softening parameter m_2 from quasi-static tests. The higher difference between a simulation and tests after $\epsilon_x > 7\%$ suggests that this parameter may also depend upon strain rate. At the moment it is chosen to keep the value of m_2 determined from static tests as the failure strain is well reproduced and the difference for failure stress in experimental and simulation results is $< 20\%$.

3.3.5.2 Compression $[\pm\theta]_{3s}$

Material properties used for $[\pm\theta]_{3s}$, where $\theta \in \{15, 30, 60, 75\}$, laminates are same as described in Table 3.8. There is only one exception i.e for a $[\pm 15]_{3s}$ laminate $E_{11} = 0.75 \times 165 = 124$ GPa is used. The elastic modulus of the laminate calculated in simulation is then in close agreement with the experimentally found modulus, see Figure 3.39(a). Simulation results show that predicted σ^y, σ^r and ϵ^r are higher than the experimental values.

Similarly for the remaining laminates, the predicted elastic moduli are slightly lower than the experimental values. The reason being that the material model at the moment does not take into account the strain rate related changes in moduli. The numerical model does predict well the σ^y for the $[\pm 75]_{3s}$ laminated, but σ^r and ϵ^r are not well

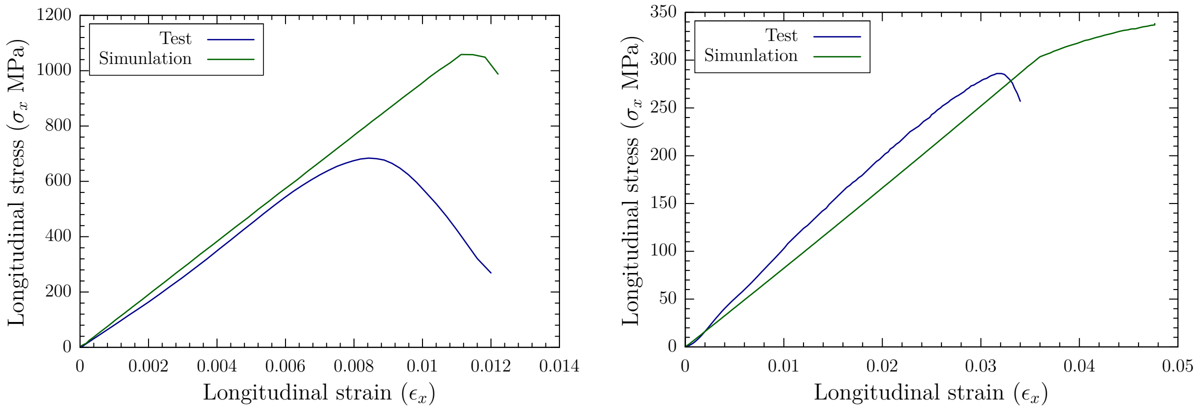

(a) Comparison test and simulation.

(b) Comparison test and simulation.

Figure 3.39: (a) $[\pm 15]_{3s}$ laminate at $\dot{\epsilon} = 290s^{-1}$ and (b) $[\pm 75]_{3s}$ laminate at $\dot{\epsilon} = 295s^{-1}$.

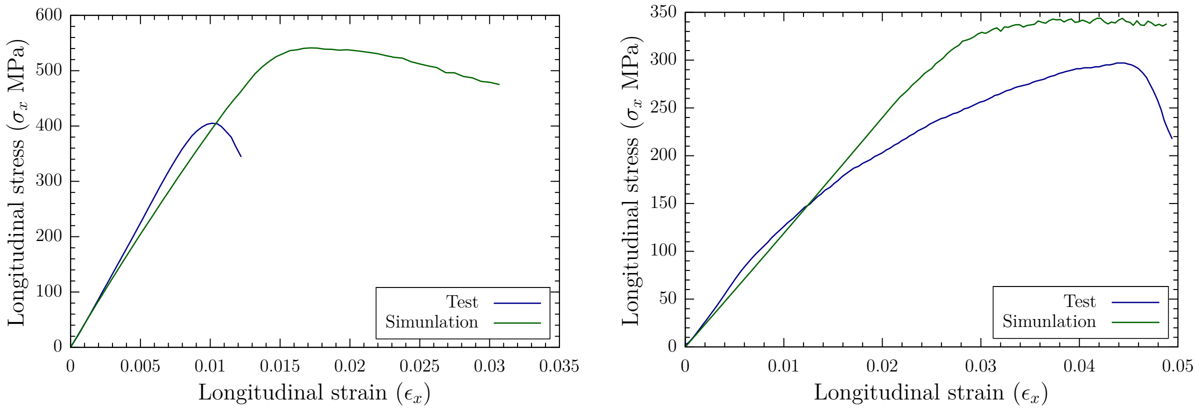

(a) Comparison test and simulation.

(b) Comparison test and simulation.

Figure 3.40: (a) $[\pm 30]_{3s}$ laminate at $\dot{\epsilon} = 386s^{-1}$ and (b) $[\pm 60]_{3s}$ laminate at $\dot{\epsilon} = 380s^{-1}$.

reproduced. In the case of $[\pm 30]_{3s}$ and $[\pm 60]_{3s}$ laminates, considerable deviation is shown by simulation from experimental results. The exact cause of these differences remains to be investigated. In the first time, the evolution of shear moduli has to be included in the material model. The second point for further investigation is the coupling matrix (Equation 3.43), as it is considered that participation from all the damage modes is of the same order of magnitude which might not be the case for $[\pm\theta]_{3s}$ laminates.

3.4 Conclusions

This chapter has focused on presentation of a material model developed and calibrated using experiments. Experiments were presented in the first place to explain the damage saturation and strain rate effects observed during quasi-static and dynamic testing, respectively.

Quasi-static and dynamic tests where conducted. The quasi-static tests allowed to determined the material constants required for material mode e.g different moduli and pure mode failure stress values. The dynamic tests done with SHPB allowed to conclude that strain rate effects for matrix dominated modes in T800S/M21 are more and more visible when the strain rate becomes more than $700s^{-1}$. For the strain rates in the order of $200 - 500s^{-1}$ the material behavior is quasi-identical but different from quasi-static tests. The yield stress for a $[\pm 45]_3 s$ laminate was found to be double for $200s^{-1} < \dot{\epsilon} < 750s^{-1}$ as compared to quasi-static value. The higher strain rates above $1500s^{-1}$ could not be tested as the specimen preparation procedure has to be improved. In this study the experiments were carried out on as cut specimen. A considerable improvement can be obtained by machining the both ends of specimen at the same time.

The material model developed in this study uses a failure criteria based damage modeling approach. Based on experimental evidence damage saturation has been introduced into the model. Strain rate effects on strength enhancement of composite materials and interaction between different failure modes has been presented. The material model was then used to predict the SHPB experiments. A good correlation was obtained for $[\pm 45]_{3s}$ laminate response. For the case of $[\pm\theta]_{3s}$ more tests are required. For material model some more investigations into shear moduli enhancement and damage coupling matrix have to be carried out.

The developed material model has shown promising results for dynamic mechanical behavior modeling of unidirectional composite materials. This material model is tested for prediction of response of an impact event in Chapter 5. Before passing on to impact simulations, the results of an experimental study to understand the impact behavior and observe the impact induced damage of composite coupon specimen is presented in Chapter 4.

4

Impact Tests on Coupon Specimen

This chapter presents the experimental results of impact tests carried out on unidirectional composite plates. In open literature one can find that the impact response of a plate is different in the case of large mass impact and small mass impact, [3–5, 105, 122].

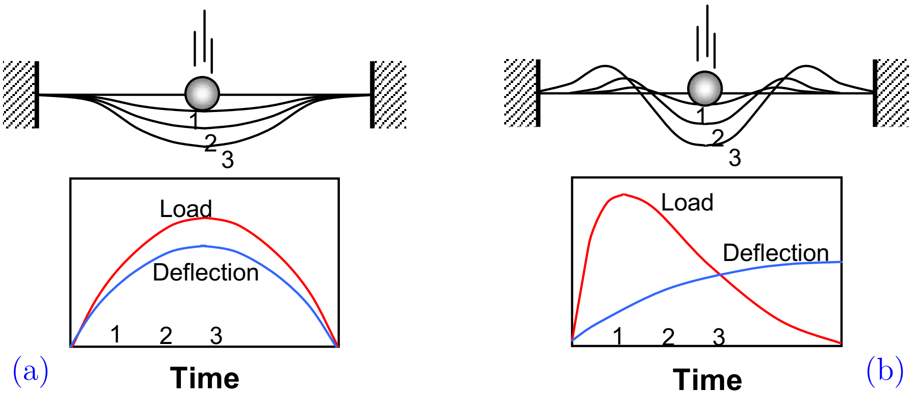

Figure 4.1: Typical (a) large mass and (b) small mass impact response, [122]

Small mass impact on plates is a common response type caused by hailstones and runway debris. The response in such cases is wave controlled and the load and deflection are out of phase and independent of plate size and boundary conditions [122]. The large mass impact is often due to tool drop or freight carriage trolleys collision. A clear classification of velocity to define high or low velocity impact does not exist in literature, Abrate [3]. In this study the behavior of composite plates under different type of solicitations in terms of mass and velocity is investigated. In this study the author refers to large mass and low velocity tests as drop tower (impact) tests and medium velocity small mass tests as canon (impact) tests. Mass of composite plates used in this study is ≈ 10 g or less. For drop tower tests, the impactor has a mass $M \in \{1.213, 2.369\}$ kg and for canon tests the impactor mass $M \in \{0.016, 0.017\}$ kg.

4.1 Specimen Preparation

The specimen are prepared by hand lay–up of unidirectional material as explained in detail in Appendix A. The specimen dimensions for impact tests are $L = 150^{+0.5}_{-0} \times b = 100^{+0.5}_{-0} \times h$. The length and breadth directions are same for all specimen whereas the thickness varied according to the number of plies for each specimen. The stacking (lay–up) sequences are shown in Table 4.1. Average thickness of T700S/M21 plies is 0.125 mm while T800S/M21 plies are 0.25 mm thick.

Table 4.1: Stacking/Lay-up sequences.

Material	lay–up sequence
T700S/M21	$[0_2, 90_2, 0_2, 90_2]_s$
T700S/M21	$[0_2, 45_2, 90_2, -45_2]_s$
T800S/M21	$[-45, 45, 90, 90, 0]_s$
T800S/M21	$[-45, 45, 0, 90, 0, 0, -45, 45, 0]_s$
T800S/M21	$[45, -45, 90, 0, 90, 90, 45, -45, 90]_s$

Since, it was not possible to measure the force and displacement results for some of the experiments, strain gages were pasted on the side opposite to impacted face. Three gages were pasted at a distance of 20 mm from expected impact point.

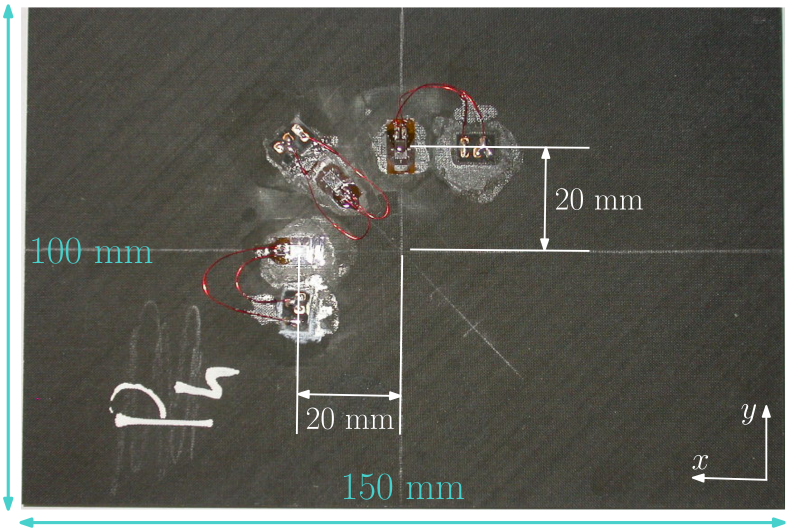

Figure 4.2: Strain gages pasted on test specimen (opposite to impact side).

4.2 Drop Tower Tests (Large Mass Low Velocity)

The drop tower setup used for impact tests is shown in Figure 4.3. The impactor consists of a movable trolley equipped with a load cell and an impactor head diameter of 16 mm. The specimen is placed on a 300×200 mm^2 and 20 mm thick steel support plate bolted to a rigid frame. The steel plate serves as support to the specimen and contains a 125×75 mm^2 pocket, Figure 4.4. Three steel pins (*"pion"*) of 3 mm diameter are screwed to the support plate in order to facilitate the composite plate specimen positioning.

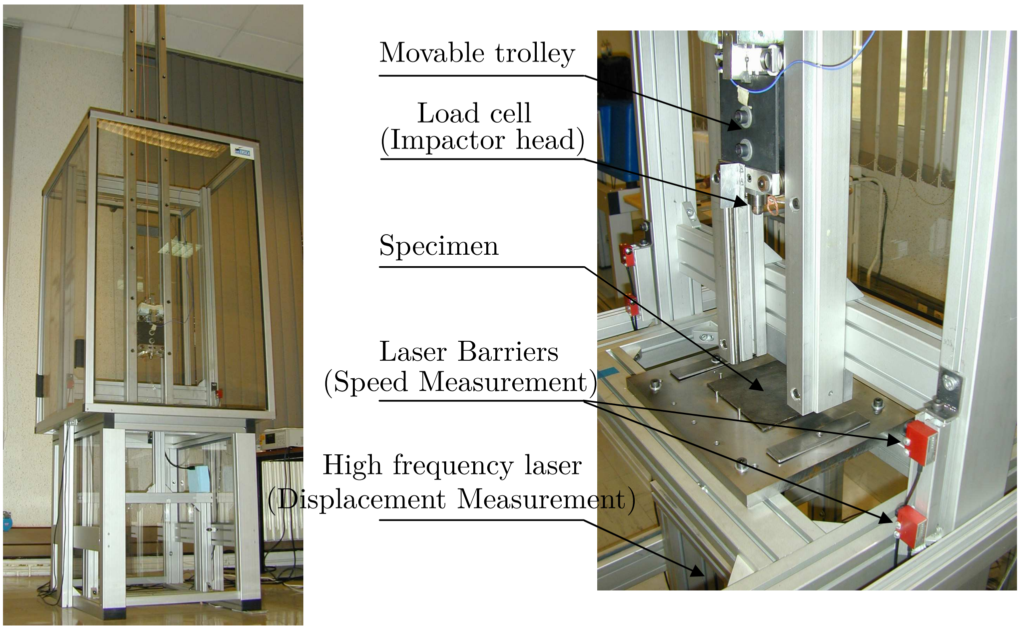

Figure 4.3: Large mass, low velocity Drop Tower impact setup.

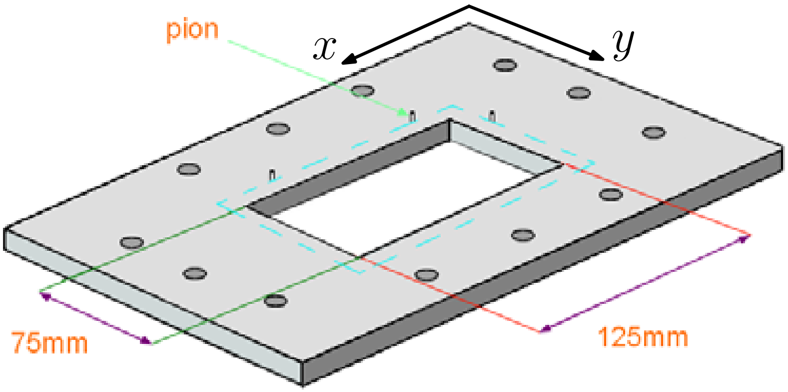

Figure 4.4: Specimen support plate with rectangular pocket.

The kinetic energy before impact,

$$E_{imp} = \frac{1}{2} M v_{imp}^2 \tag{4.1}$$

where, M is mass of the impactor and v_{imp} is the impactor velocity.

Based on the required energy before impact E_{imp}, the drop height, h', of impactor is calculated by a simple hand calculation as $h' = v_{imp}^2/(2g')$, where g' is the constant standard gravity.

The impactor is then dropped from the above determined height. The data is acquired by the same data acquisition system (GEN7t) at data acquisition frequency of 1 MHz as used for SHPB experiments in Chapter 3. Distance between the velocity measuring lasers is 50 mm. The time taken to travel this distance is registered by the data acquisition system, velocity calculation is then trivial. The force of impact is measured by the load cell mounted on the trolley and displacement of specimen side opposite to impact point is measured by the high frequency laser situated below the specimen. The impactor trolley is equipped by an anti-rebound mechanism to stop any subsequent impacts.

4.2.1 Global Force/Displacement Transitory Behavior

Figure 4.5 shows results for six tests carried out at ≈ 20 J of impact energy on a 4.5 mm thick T800S/M21 laminate with $[-45, 45, 0, 90, 0, 0, -45, 45, 0]_s$ lay–up. The force measured by impactor increases as time increases and then decreases after reading a maximum point. The displacement of the opposite face to impact side shows the similar behavior. The average maximum force for these tests is 8854 N. The dispersion in maximum force is not significant Figure 4.5(a), which is not the case for the displacement, as a function of time, curve, Figure 4.5(b).

The blue circle in Figure 4.5(a) illustrates the time (0.5 msec after contact takes place) which can be attributed to the delamination propagation as observed by various authors [137, 163]. After this point in time, the global response of the laminate is different from the undamaged one as the vibrating frequencies change and small amplitude vibrations are observed. These small amplitude vibrations are attributed to the delamination propagation, [66, 137, 163]. The blue circles in Figure 4.5(b) highlight two particular curves, which show an irregular displacement as the last ply opposite to impact face has separated from the rest of the laminate and displacement is being measured at this end, in an ideal case the displacement should be measured at the impacted face also.

The force as a function of displacement is plotted in Figure 4.5(c). A small peak of force at displacement equal to 0 mm is observed. In order to further explore the force and displacement as a function of time, the first 0.25 msec of a typical curve in Figure 4.5(d) have been plotted. The load cell signal is more smooth as compared with the displacement signal which shows a stepped response. The high frequency laser used for displacement measurement is limited at 50 kHz. Therefore each step corresponds to 0.02 msec (about 20) points when data is acquired at 1 MHz. The time required for the force to attain the

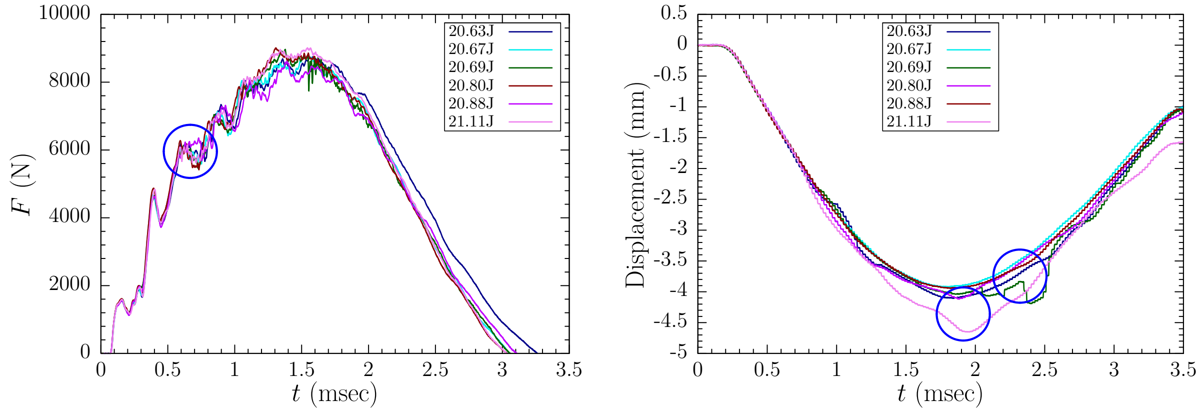

(a) Force–time response.

(b) Displacement–time response.

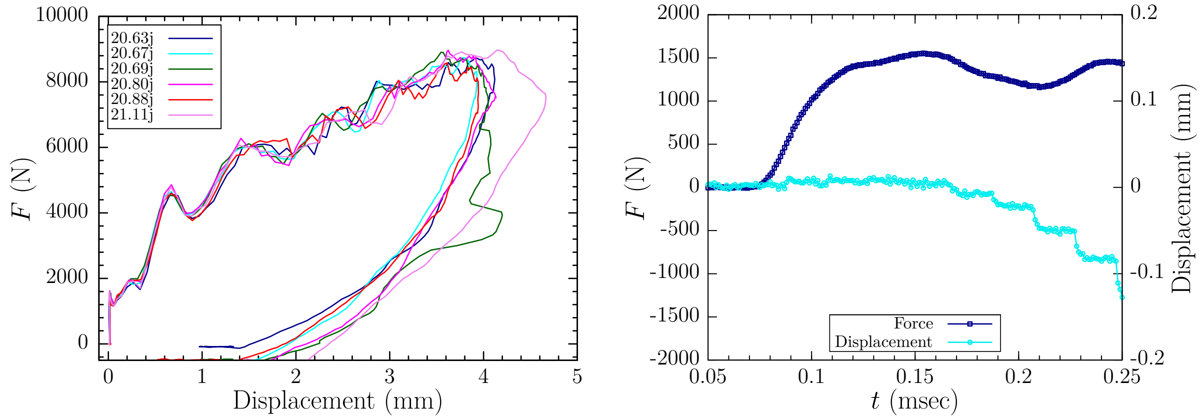

(c) Force–displacement

(d) Start of force/displacement–time curves

Figure 4.5: Force and displacement curves, $E_{imp} \approx 20$ J on 4.5 mm thick T800S/M21.

first peak of ≈ 16 kN starting from 0 N is 0.045 msec. Therefore, enough time for data acquisition system to capture any variation in displacement. Thus it is assumed that this first peak of force is associated with the instant local indentation of the specimen before the start of specimen bending.

4.2.1.1 Influence of Impact Energy

Increase of impact energy manifests itself as an increase in peak force registered by load cell as shown in Figure 4.6(a). Similarly the maximum displacement of the face opposite to impact increases, Figure 4.6(b). The force–time signal falls back to zero after a peak force has been achieved, this is not same in the case of displacement–time curve. This difference can be attributed to the permanent deformation of the specimen.

4.2.1.2 Influence of lay–up Sequence

Force–time impact response of 2 mm thick T700S/M21 specimen is shown in Figure 4.7. Two different lay–up sequences are tested at approximately iso–impact energies. The quasi–isotropic specimen, $[0_2, 45_2, 90_2, -45_2]_s$, is more stiff as compared with the bal-

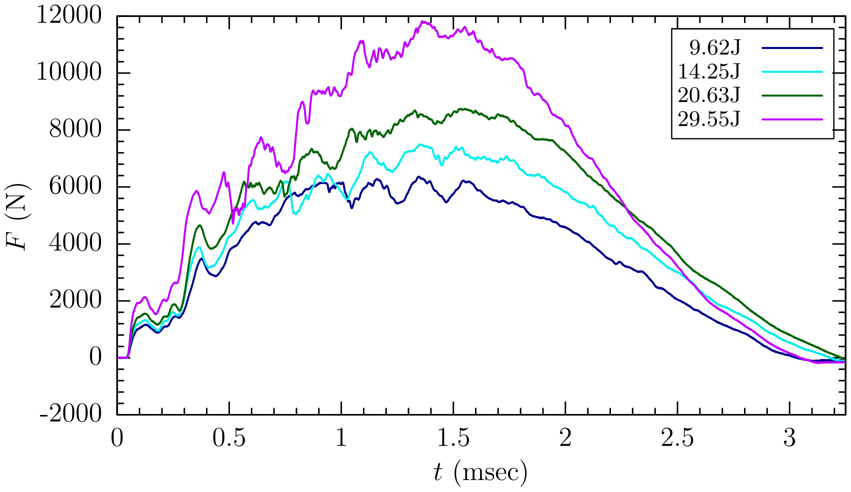

(a) Force–time response.

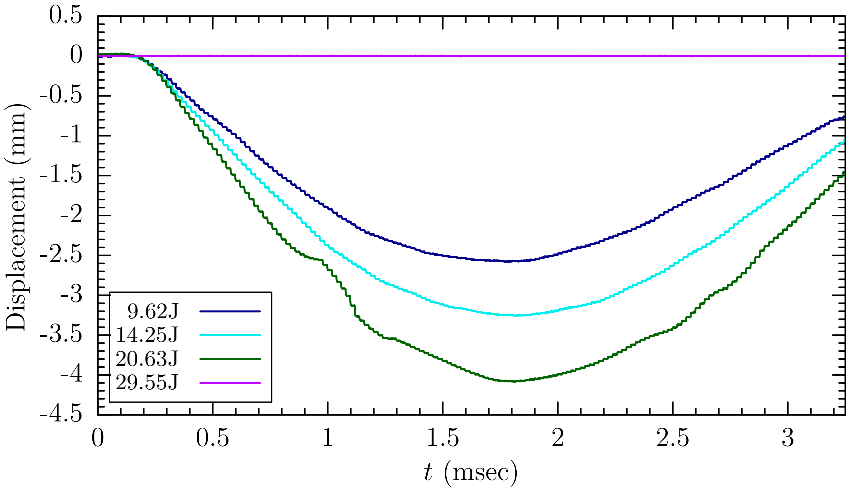

(b) Displacement–time response.

Figure 4.6: Drop tower tests for T800S/M21 $[-45, 45, 0, 90, 0, 0, -45, 45, 0]_s$ laminate.

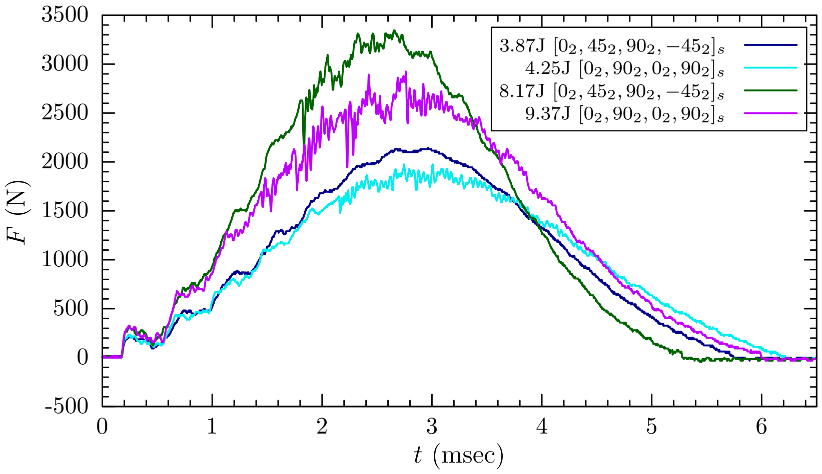

Figure 4.7: Force–time response of T700S/M21, 2 mm thick laminate.

anced ply specimen, $[0_2, 90_2, 0_2, 90_2]_s$, specimen. Therefore, the peak forces are higher for quasi–isotropic specimen and the duration of impact time is smaller. On time scale the oscillations in force–time curve associated with damage arrive later for quasi–isotropic specimen as compared to the balanced ply specimen.

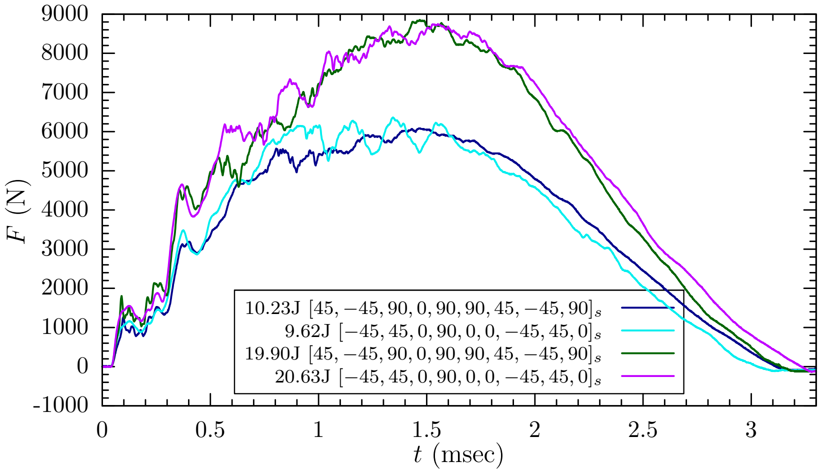

Figure 4.8: Force–time response of T800S/M21, 4.5 mm thick laminate.

In Figure 4.8 force–time response of a relatively thick plate of 4.5 mm made of T800S/M21 is shown for approximately same impact energies and different lay–up sequences. The $[-45, 45, 0, 90, 0, 0, -45, 45, 0]_s$ specimen is slightly more stiff in bending (along x-direction, Figure 4.4) as compared with $[45, -45, 90, 0, 90, 90, 45, -45, 90]_s$ specimen. Therefore, the impact duration is lower and peak force is slightly higher for $[-45, 45, 0, 90, 0, 0, -45, 45, 0]_s$ specimen.

4.2.1.3 Conclusions

The duration of impact depends upon various factors like the impact energy, lay–up sequence and final thickness of the specimen. The specimen with higher bending stiffness show a smaller impact duration independent of the thickness of the plates used in present study. In the case of thinner plates (2 mm) the higher impact energy gives a smaller impact time while the reverse is observed for (4 mm) thick plates. It is also observed that higher impact energies generate a higher permanent deformation in the specimen of same thickness.

4.2.2 Post–impact Defects Examination

Several post–impact examinations were done to study the impact induced defects. In start, the profiles of indentation marks (Barely Visible Impact Damage) are investigated as described in [2]. Then the ultrasonic examinations (C–Scan) and X–ray images were obtained to study the orientations and sizes of delamination which cannot be seen by the naked eye. And finally a microscopic examination was carried out to study the matrix cracks and delamination interaction. All of the results for C–Scan, X–Ray and microscopic examinations will not be shown in order to keep the document as brief as possible.

4.2.2.1 Profile of Impacted Zone

The two dimensional measurement of crater generated by the impactor was carried out by a profilometer. A surface area of 15×25 mm^2 was chosen based on the visual inspection of the impacted specimen, Figure 4.9. The profile measuring sensor moved in y-direction of the specimen and registered the depth of the profile in z-direction (in and out of paper). The increment in x-direction was chosen to be 0.5 mm in order to reduce the acquisition time.

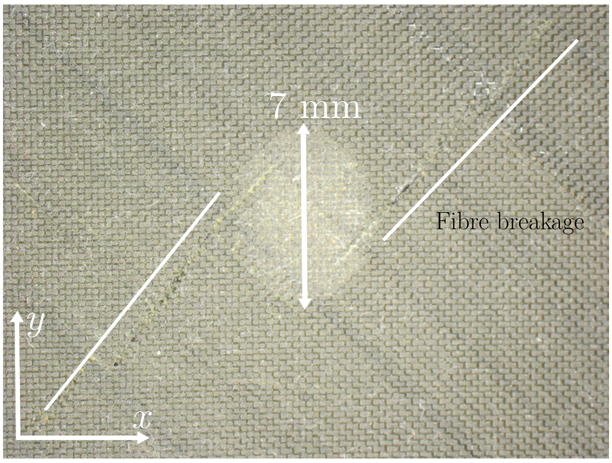

Figure 4.9: A typical indentation mark on T800S/M21, $[-45, 45, 0, 90, 0, 0, -45, 45, 0]_s$, laminate, $E_{imp} \approx 20$ J.

Some typical results of the surfaces generated by using these measured profiles for a $[-45, 45, 0, 90, 0, 0, -45, 45, 0]_s$ laminate are shown in Figure 4.10. Although visually one gets an impression that the elliptic crater formed due to impact is oriented in y-direction, a precise measurement indicates that this ellipse is oriented along x-direction of the specimen. This is attributed to a lower number of 90° layers in this particular lay-up sequence. The dent diameter is calculated by identify the three adjacent measurements giving the biggest depth of dent and averaging the corresponding diameters.

The fiber breakage is observed to start from the brink of the elliptical dent. The eccentricity of the lines representing fiber breakage in Figure 4.11 is higher for lower impact energies. These fiber breakage lines become collinear as the impact energy increases.

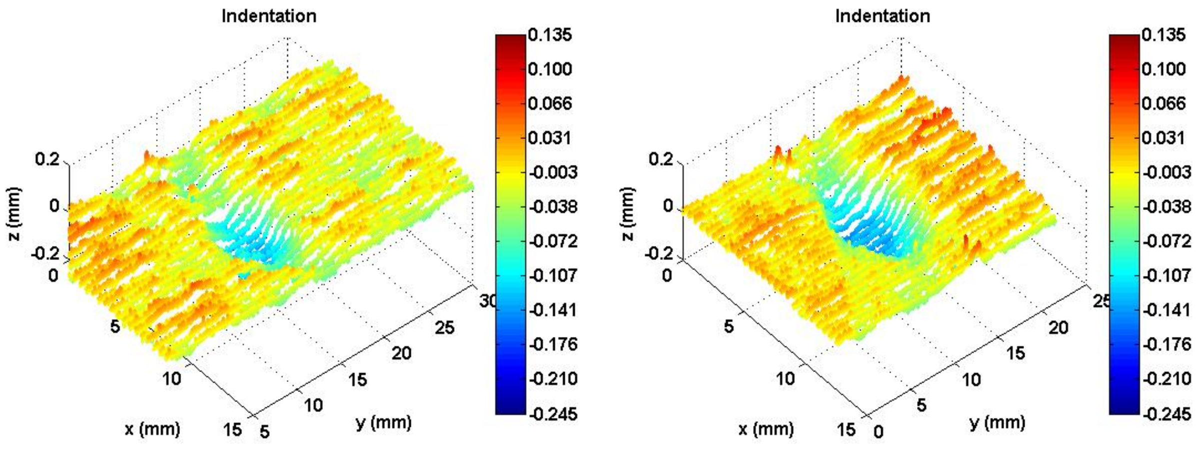

(a) $E_{imp} \approx 10$ J (b) $E_{imp} \approx 15$ J

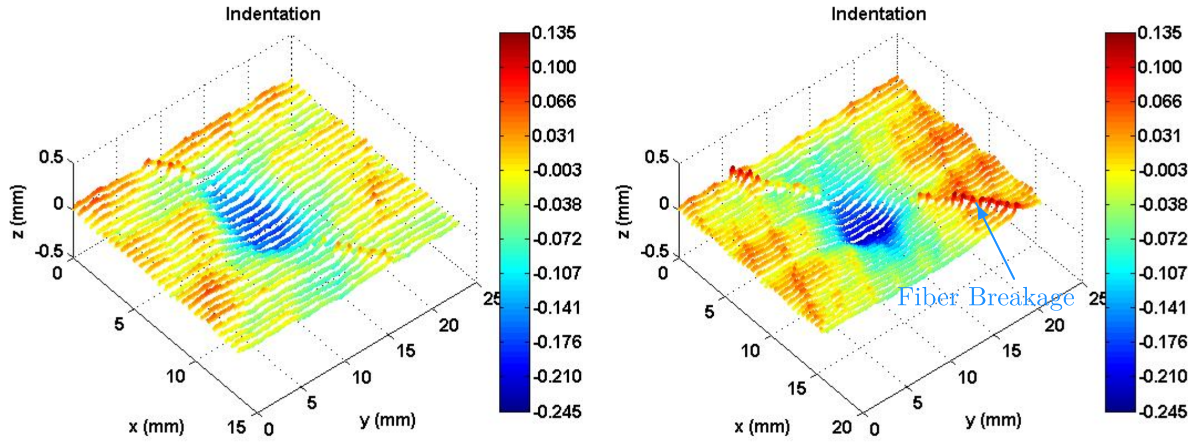

(c) $E_{imp} \approx 20$ J (d) $E_{imp} \approx 30$ J

Figure 4.10: Measurement of indentation for drop tower tests.

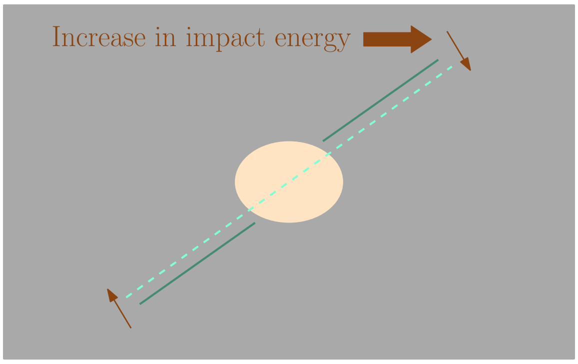

Figure 4.11: Fiber breakage and impact energy.

Table 4.2: Indentation profiles for Drop Tower Tests

Impact Energy (J)	Dent Depth (μm)	Dent Diameter (mm)
9.62	110	9.5
14.25	144	11.8
20.67	182	14.9
20.69	184	14.5
20.88	189	14.8
29.55	219	19.8

4.2.2.2 C–Scan Examination

The ultrasonic examination is a reliable method for obtaining the impact induced delamination [2]. An ultrasonic wave is sent perpendicular to the specimen and the reflections from the internal defects permit to generate a color coded image. This image is reliable for determination of a rectangular box bounding the defects as shown in Figure 4.12. The size of delaminated surfaces is directly proportional to the impact energy.

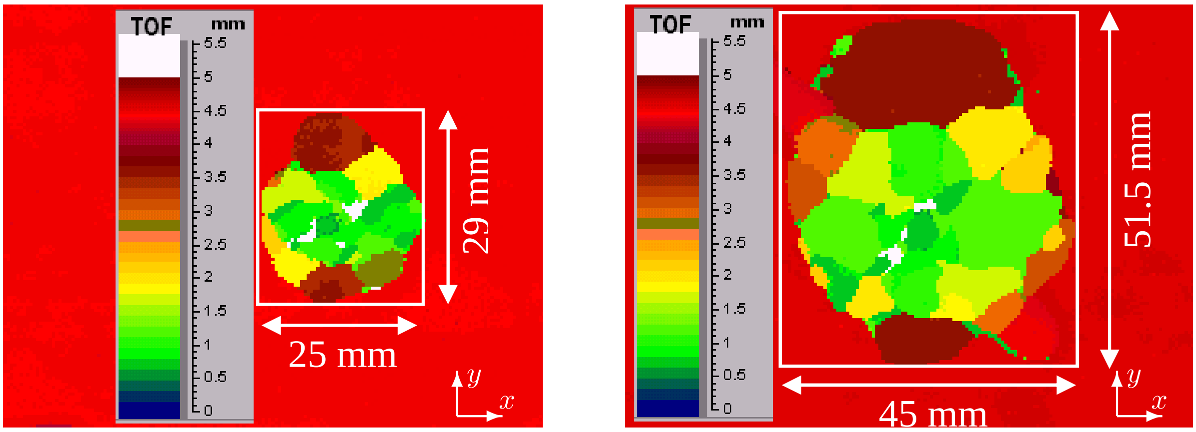

(a) $E_{imp} = 15$ J (b) $E_{imp} = 30$ J

Figure 4.12: Ultrasonic C–Scan images for different impact energies.

4.2.2.3 X–ray Examination

X–rays are another type of examination technique, which provide the information sometimes absent after a C–scan. Usually C–scan images are more suited to determine location and extent of the delamination defect while X–rays are not capable of providing location of delamination with sufficient accuracy. Presence of transverse cracks, perpendicular to ply plane, is easily determined by the X–rays.

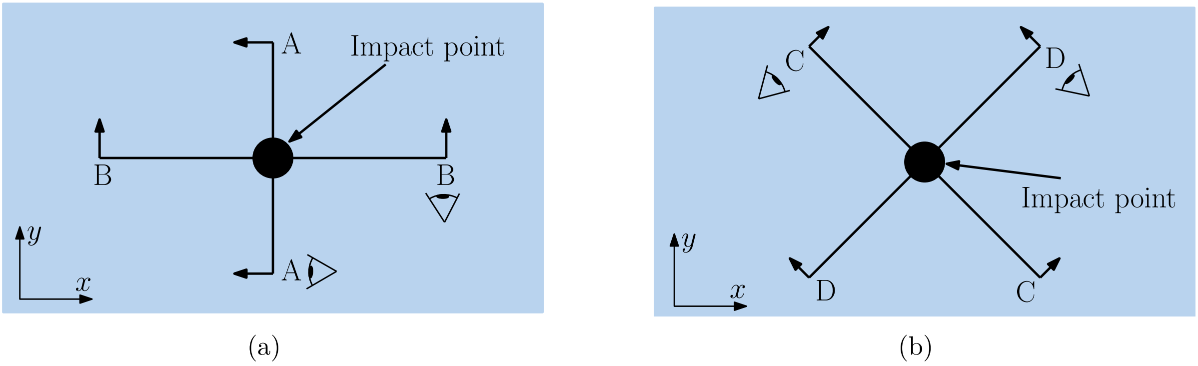

(a)

(b)

Figure 4.13: Cutting plans for microscopic examinations.

The cutting planes for any subsequent microscopic images are shown in Figure 4.13. Section A–A is along global y-direction and section B–B is along global x-direction of specimen. Similarly the sections oriented at $-45°$ and $45°$ with global x-direction are shown in Figure 4.13(b).

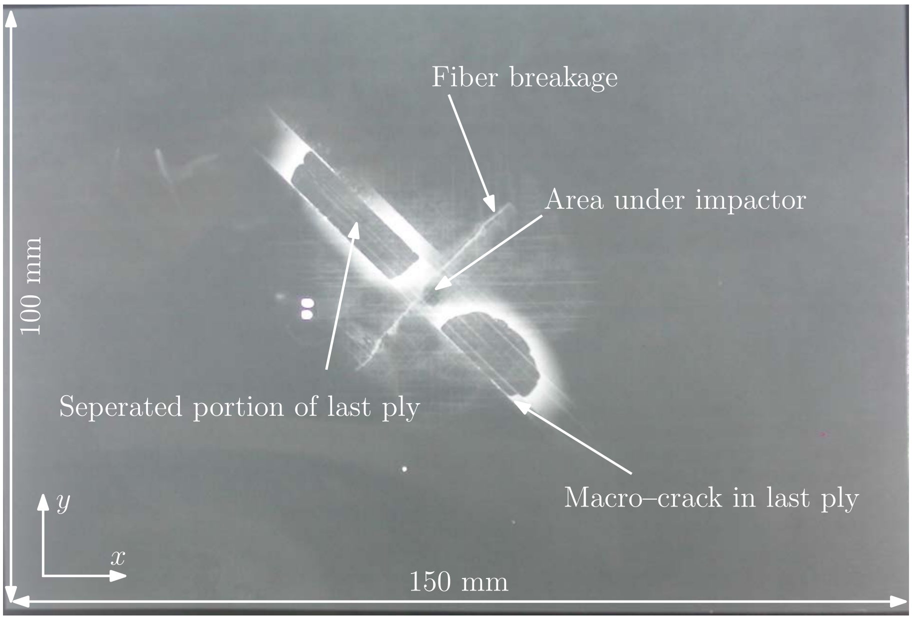

Figure 4.14: X–ray image of $[-45, 45, 0, 90, 0, 0, -45, 45, 0]_s$ laminate, $E_{imp} = 30$ J.

Figure 4.14 show an X–Ray image of an impact test at 30 J. In this study it is observed that for thicker laminates (4.5 mm) there is always a compacted zone below the impactor. On the other hand the fiber breakage as observed in Figure 4.14 is typical of laminates with $-45°$ or $45°$ ply on impacted side. The separation of the last ply opposite to impacted face was observed for impact energies above 15 J.

4.2.2.4 Microscopic Examination

The Scanning Electron Microscope (SEM) was used to analyze the matrix cracks in T700S/M21 specimen of 2 mm thickness. Figure 4.15 shows images of tests conducted at 4 J and 8 J impact energy. The plate is cut into half along the direction of 0° ply. The quasi-isotropic laminates, $[0_2, 45_2, 90_2, -45_2]_s$, show only matrix cracking for impact energy of 4 J, Figure 4.15(a). At slightly higher impact energy of 8 J it is observed that the delamination to start between layers of different orientations. This particular lay-up sequence was studied to investigate the existence of delamination in plies of the same orientation. It is worth noting that delamination does not exist between plies of same orientation. In this lay-up configuration the delamination propagates on both sides away from the zone under the impactor.

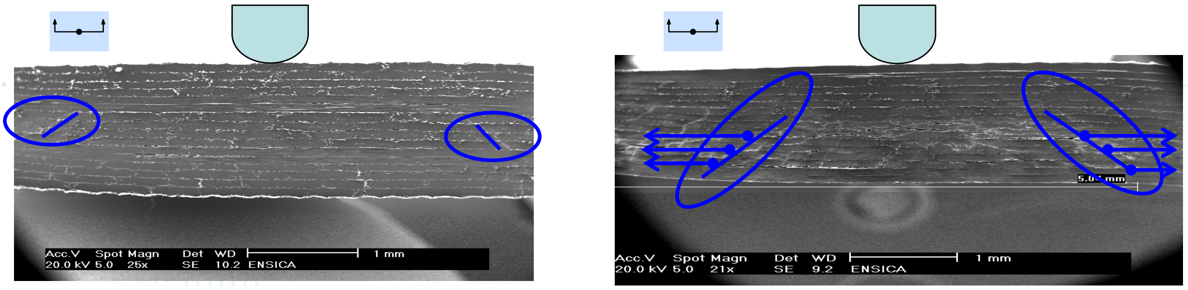

(a) $E_{imp} = 4$ J (b) $E_{imp} = 8$ J

Figure 4.15: Scanning Electron Microscope (SEM) images of T700S/M21 quasi-isotropic, $[0_2, 45_2, 90_2, -45_2]_s$, laminate, [80].

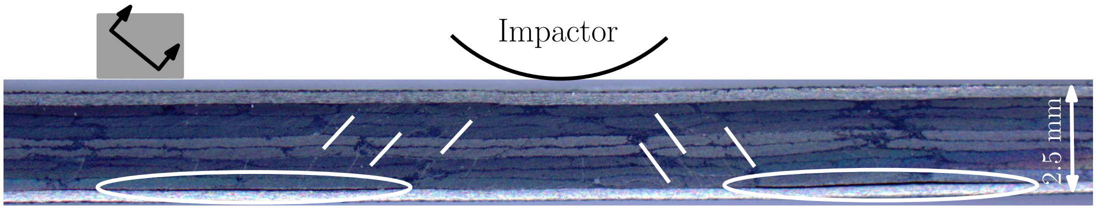

Figure 4.16: Optical microscope image of T800S/M21 specimen impacted at 10 J with lay-up sequence as $[-45, 45, 90, 90, 0]_s$.

An optical microscope is used to investigate the damage in T800S/M21, in order to generate images for larger cross sectional areas in lesser amount of time. The damages in a thinner laminate, 2.5 mm impacted at 10 J, are shown in Figure 4.17. In addition to the matrix cracks, delamination is observed between the last two plies opposite to impact side.

Figure 4.17 show a microscopic image of T800S/M21 specimen with lay-up sequence as $[45, -45, 90, 0, 90, 90, 45, -45, 90]_s$. The impact energy is same as in the above paragraph. It can be observed that in the case of a thicker laminate, 4.5 mm, at the same impact

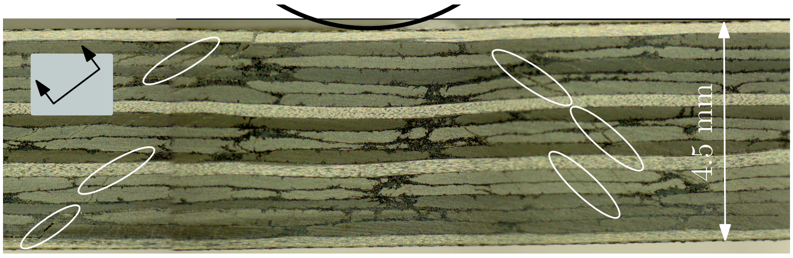

Figure 4.17: Optical microscope image of T800S/M21 specimen impacted at 10 J with lay-up sequence as $[45, -45, 90, 0, 90, 90, 45, -45, 90]_s$.

energy the damages consist primarily of matrix cracking and the delamination in the last two plies is not present. This surely is due to the thickness of the specimen.

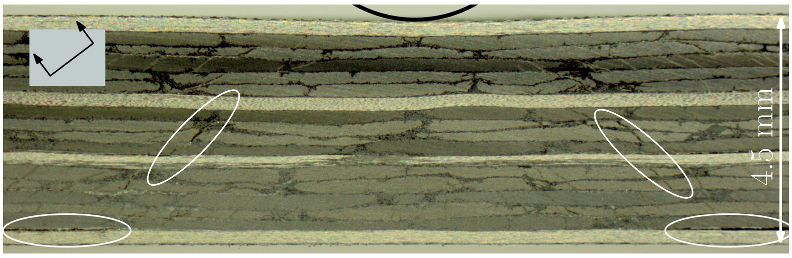

Figure 4.18: Optical microscope image of T800S/M21 specimen impacted at 20 J with lay-up sequence as $[45, -45, 90, 0, 90, 90, 45, -45, 90]_s$.

Finally the Figures 4.17 and 4.18 are compared. The lay-up sequence is same for these 4.5 mm thick plates. The difference in impact energy manifests itself as larger delamination area overall. There is a large delamination present at the last interface, $-45/45$, from the impact side. The matrix cracks are also more open and easier to visualize. The particular behavior may be associated with the larger impact force and global bending experienced by the specimen.

4.3 Canon Tests (Small Mass Medium Velocity)

From the bibliographic studies it is known that the damage phenomena of composite specimen submitted to impact loading are different for different impact energies, [3–5, 105, 122]. Furthermore, these authors have shown that only impact energy is not sufficient to characterize the impact behavior of composite materials. Therefore, the impact behavior of composite materials depends not only the impact energy but also on the combination of impact mass, M, and impact velocity, v_{imp}.

As a preliminary study, some impact tests were carried out on a medium velocity canon (gas gun) setup, Figure 4.19(a). A schematic of this gas gun apparatus is shown in Figure 4.19(b). The projectile/impactor is shown in Figure 4.19(c). The impactor is a stain less steel ball of 16 mm diameter. Since it is not possible to launch this ball alone in

(a) Canon test apparatus at ISAE.

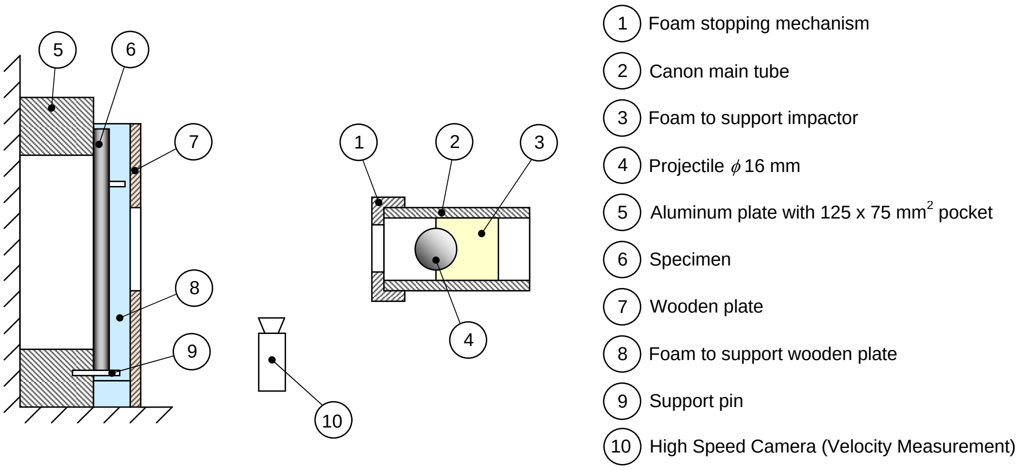

(b) Schematic representation of canon test (dimensions not to scale).

(c) Impactor used for canon tests.

Figure 4.19: Small mass, medium velocity impact test setup.

the canon tube, a foam support is used to place the ball in impactor tube. The downsides of use of this support are: (i) once the support and ball exit the canon main tube, the ball and support may separate from each other and there exists a possibility of the support striking the specimen after impactor ball or (ii) when both of them do travel joined to each other the crash of foam can also cause damage to plate. Since, it is not envisaged to numerically model the foam, canon was equipped with a support arrest mechanism, shown as part 1 in Figure 4.19(b).

A high speed camera, part 10 in Figure 4.19(b), was placed 100 mm before the specimen to measure the velocity of impactor as accurately possible. Finally, to stop the specimen from falling down on the ground a wooden plate with hole, part 7, was used. The support plate dimensions are same as in Figure 4.4. The support plate is bolted on a heavy block of iron (> 300 kg), which itself is bolted to the ground. The support plate can, therefore, be considered as a rigid support.

4.3.1 Transitory Strain Gage Signals

The support mechanism for canon test setups is not equipped with an impact force or displacement measuring device. Therefore, the strain gages were pasted on the face opposite to impact in order to obtain least possible information at particular points regarding the impact induced strains. Figure 4.20 shows results of some of the canon tests.

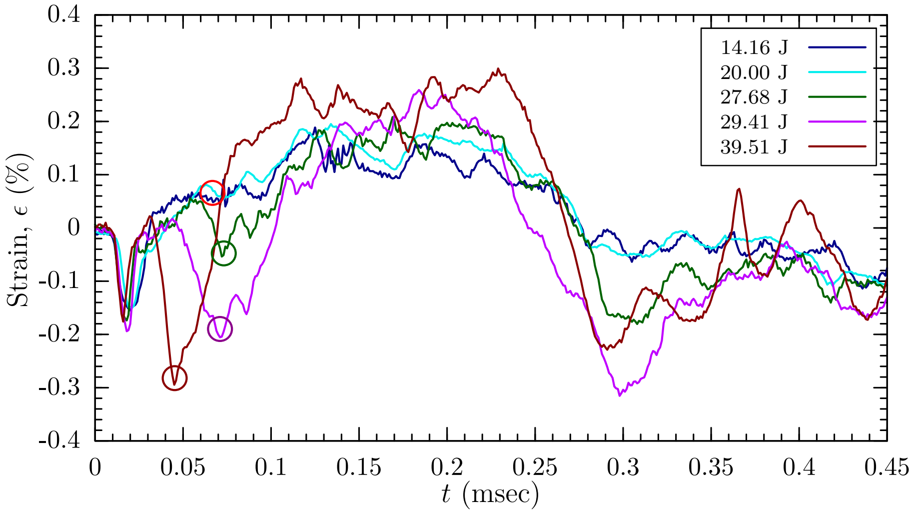

Figure 4.20: Strain (ϵ_x) in T800S/M21, $[-45, 45, 0, 90, 0, 0, -45, 45, 0]_s$, laminate at different impact energies.

The strain gages signals are for the gages pasted along the global x-direction, Figure 4.2, to measure the tensile strain due to bending of the specimen. For tests at impact energy above 25 J, it is observed that there are two compressive waves which pass through the strain gage, as shown by green, magenta and dark-red circles in Figure 4.20. The second compressive wave is not observed for tests at ≈ 15 J and 20 J, as shown by red circle

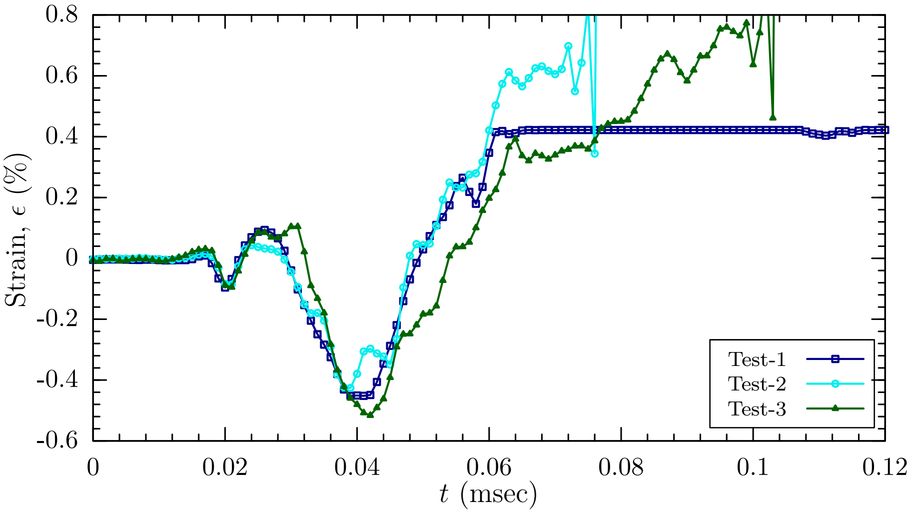

Figure 4.21: Strain (ϵ_x) in T800S/M21, $[-45, 45, 0, 90, 0, 0, -45, 45, 0]_s$, laminate ($E_{imp}$ = 100 J).

in Figure 4.20. The amplitude of these compressive waves is directly proportional to the specimen and global bending is then followed. The time of impact is ≈ 0.3 msec.

Three canon impact tests were conducted at E_{imp} = 100 J. The strain gages signals are shown in Figure 4.21. The overall form of the curves is similar to the ones shown in Figure 4.20 with two compressive waves before global bending of the plate. The saturation of the strain gage signals occurs as the strain gages mounted on the specimen are damaged due to extensive bending of specimen and cracking of the last ply opposite to impact face. The first compressive wave differs significantly in shape as compared with the Figure 4.20. The order of magnitude is same for the strains observed in Figures 4.20 and 4.21. In case of 100 J tests, this can be attributed to the shape of the impactor. As the foam arrest mechanism was incorporated afterwards.

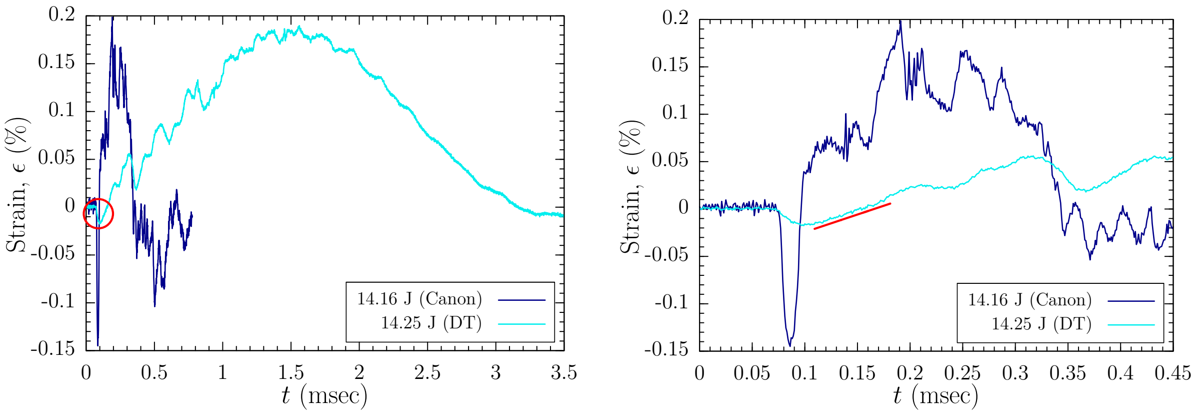

(a) Time of impact, drop tower and canon test.

(b) Time of impact, zoom on $0 - 0.45$ msec.

Figure 4.22: Comparison of ϵ_x registered in drop tower and canon tests, E_{imp} = 15 J.

In Figure 4.22 a comparison of strains measured in global x-direction during canon and drop tower tests at approximately same level of impact energy for T800S/M21, $[-45, 45, 0, 90, 0, 0, -45, 45, 0]_s$, laminate is shown. A difference of 10 times for duration of impact is observed, Figures 4.22(a) and 4.22(b). It is worth noting that there is a compressive wave in both tests before the global bending of the plate as shown by a red circle in Figure 4.22(a). Based on analytical studies of SHPB one can hypothesize that this compressive wave has a magnitude directly proportional to the impact velocity of the impactor. For canon test impact velocity is 50.0 m/sec ($M = 0.017$ kg) and for drop tower it is 3.47 m/sec ($M = 2.368$ kg). The duration of this compressive wave is then proportional to the length (size) of impactor. For canon test, the impactor is a steel ball with diameter 16 mm and for drop tower tests the impactor is a hemispherical head with a ≈ 200 mm long trolley behind it. Therefore, before the compressive wave in drop tower tests is completed, the global bending of the specimen starts, as shown by the red line in Figure 4.22(b).

4.3.2 Post–impact Defects Examination

Similar to the drop tower tests, the post–impact defects were examined for the canon tests. The same order for nondestructive and destructive examination methods is followed here as in above paragraphs. The results of canon tests will be compared at the same time with the drop tower tests.

4.3.2.1 Profile of Impacted Zone

In Figure 4.23, it is observed that for approximately same level of impact energy the indentation mark produced by the drop tower is more severe as compared with the canon test. The elliptical shaped indentation mark is oriented along the global x-direction of the specimen for both tests. The major and minor axes for this indentation mark have a higher value for the drop tower tests. Furthermore, it is observed that the fiber failure present in drop tower tests is absent for the canon tests. Table 4.3 recapitulates the measurements of dent depth for both tests. The test $34++$ in Table 4.3 corresponds to a test where exact speed of impactor could not be measured, but pre–impact drop height show that the impact energy is above 34 J. It is worth noting that the dent depth produced by canon tests is less than the drop tower tests, for the same level of impact energy.

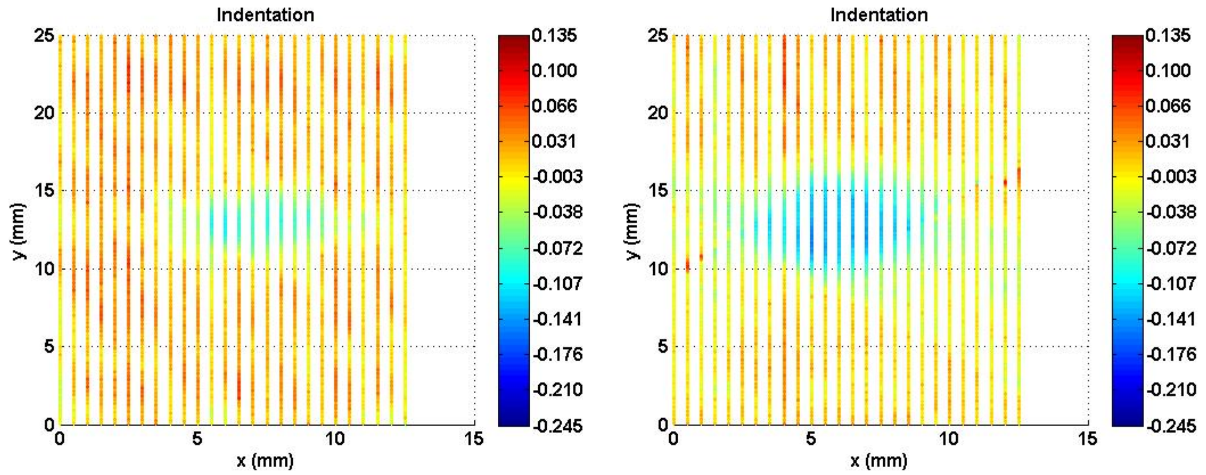

(a) Canon test, $E_{imp} \approx 15$ J.

(b) Drop Tower test, $E_{imp} \approx 15$ J.

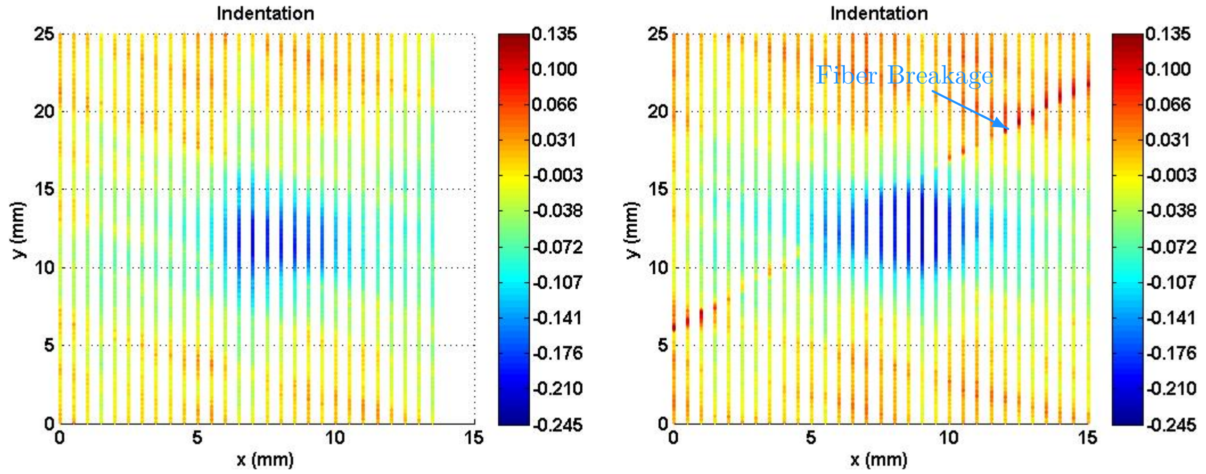

(c) Canon test, $E_{imp} \approx 30$ J.

(d) Drop Tower test, $E_{imp} \approx 30$ J.

Figure 4.23: Comparison indentation after Drop Tower and Canon tests.

Table 4.3: Comparison of indentation profiles for Drop Tower and Canon tests

Drop Tower		Canon	
Impact Energy (J)	Dent Depth (μm)	Impact Energy (J)	Dent Depth (μm)
9.62	110	×	×
14.25	144	14.16	130
20.67	182	20.00	150
20.69	184	×	×
20.88	189	×	×
29.55	219	29.41	171
34++	237	×	×
×	×	39.51	185

4.3.2.2 C–Scan Examinations

Canon impact test specimen were also passed through C–Scan imaging. Figure 4.24 compares the C–Scan images generated for canon tests and drop tower tests. It can be observed that the size of the bounding box for delamination surfaces is higher for the drop tower tests. It was further observed that for $[-45, 45, 0, 90, 0, 0, -45, 45, 0]_s$ laminate, the larger size of the bounding box was along the global y-direction of the specimen for all the drop tower tests and canon tests below 20 J. In case of canon tests with impact energy above 20 J, the larger size of the bounding box was along global x-direction of the specimen.

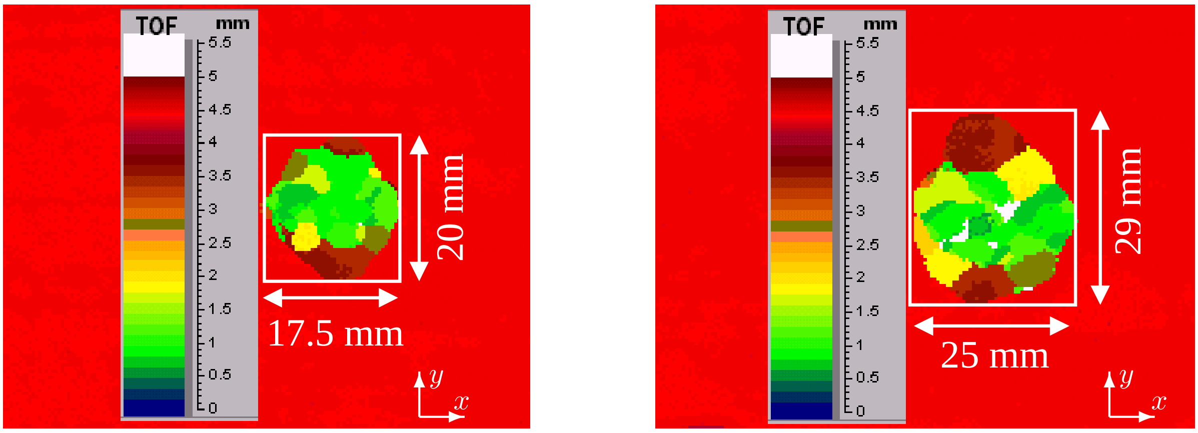

(a) Canon test, $E_{imp} = 15$ J (b) Drop tower test, $E_{imp} = 15$ J

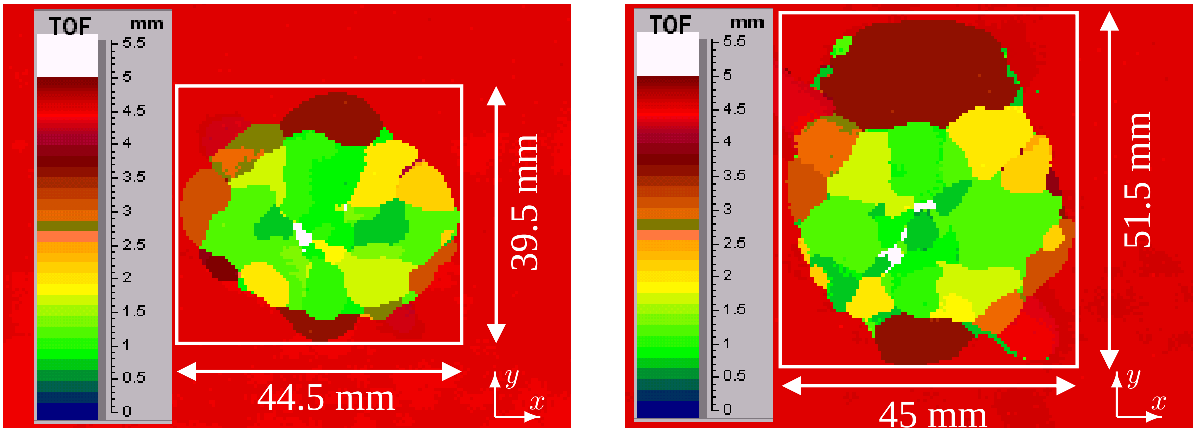

(c) Canon test, $E_{imp} = 30$ J (d) Drop tower test, $E_{imp} = 30$ J

Figure 4.24: Comparison C–Scan images for different Canon and Drop Tower tests.

4.3.2.3 X–ray Examinations

The X–ray examinations conducted on the canon test specimen further confirmed that there were no fiber breaking on the impacted face of the specimen. In case of the drop tower tests, some macro-cracks (visible by naked eye) in ply opposite to impact face were observed. In case of canon tests conducted at the same impact energy these macro-cracks were not visible, but nevertheless a large delamination along matrix cracks was present above this ply and confirmed by the X–ray images.

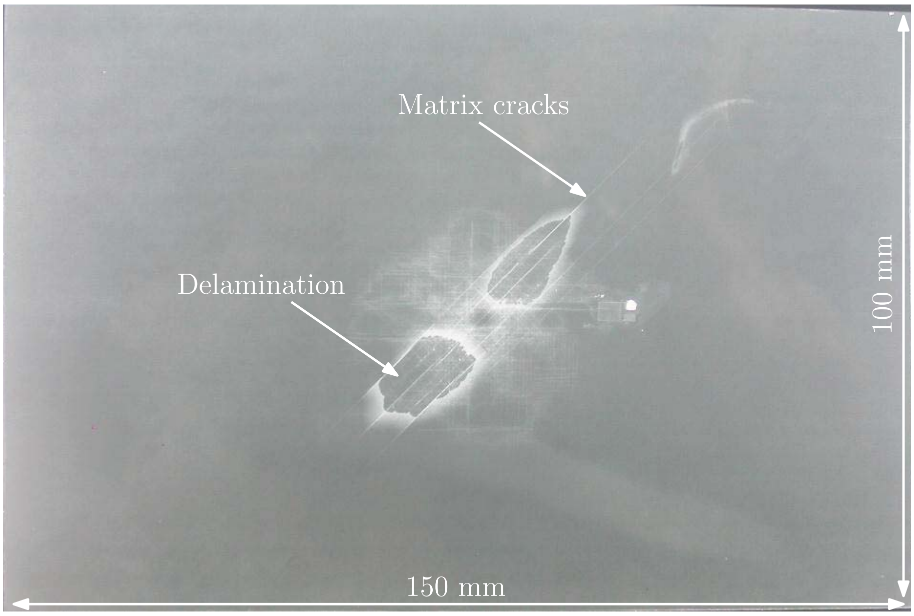

Figure 4.25: X–ray image of $[-45, 45, 0, 90, 0, 0, -45, 45, 0]_s$ laminate, $E_{imp} = 30$ J.

4.3.2.4 Microscopic Examination

The microscopic examination of T800S/M21, $[-45, 45, 0, 90, 0, 0, -45, 45, 0]_s$, laminated specimen tested by a canon were also conducted. Figure 4.26(a) shows a half cross section view of a specimen cut along global y-direction of specimen. The delamination and matrix cracking are the primary damage modes observed in this view. A comparison of Figures 4.26(a) and 4.26(b) reveals that delamination and matrix cracks are more open for a drop tower impact case (Figure 4.26(b)).

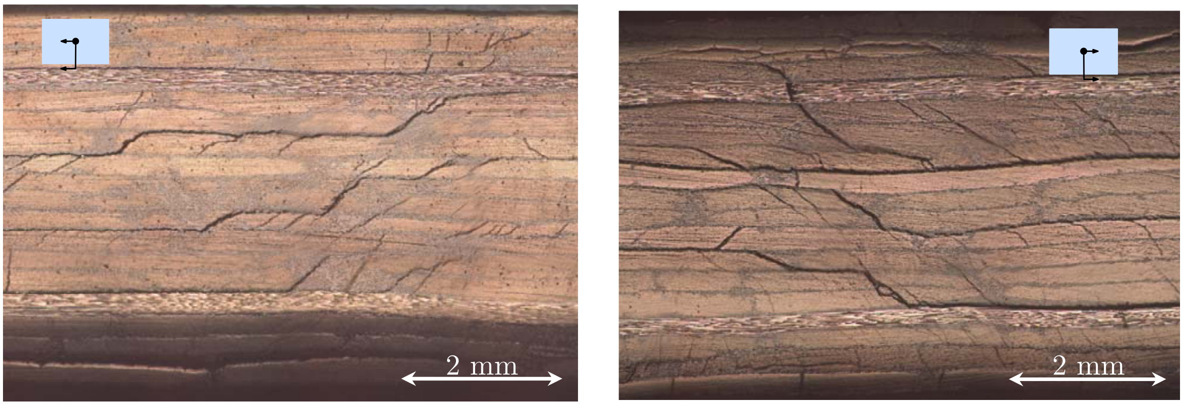

(a) Canon test, $E_{imp} = 30$ J

(b) Drop tower test, $E_{imp} = 30$ J

Figure 4.26: Optical microscope image of T800S/M21 laminate.

This is attributed to the larger bending and higher permanent deformation in the case of drop tower impacted specimen. It appears that the ratio of matrix cracks to delamination under the impacted zone is higher in the case of a canon impacted test than the drop tower impacted tests. This remains to be confirmed by a dedicated statistical study.

These microscopic examinations have also allowed to locate and measure accurately the position and size of delamination. The detailed microscopic examination of 15 J and 30 J impacted specimen each tested for canon and drop tower setup was carried out. It was confirmed that the largest delamination existed between 0°/90° interface for 15 J canon and drop tower tests (15 J and 30 J). On the other hand for 30 J canon test, the largest delamination existed between $-45°/0°$ interface.

4.4 Conclusions

The objective of this experimental study was to determine the damages generated by the low and medium velocities with the help of two of the experimental methods (Impact by a Drop Tower and Impact by a compressed air gas gun), in order to show the loading rate effects on the kinetics of damage onset. The impact energies are 4, 8, 10, 15, 20, 30 and 100 J and the impact velocities vary from 4 m/sec to 100 m/sec.

Two materials are studied: the first is a high resistance fiber (T700S/M21) with improved matrix toughness and fabricated by solvent process, the second is an intermediate modulus (T800S/M21) where the interface between the layers is charged by the thermoplastic nodules (Hot melt fabrication) for fuselage applications. Two types of stacking sequences are used, one classically called the quasi-isotropic (T700S/M21) and the other less classical $[\pm 45, 0, 0, 90, 90, 0, 0, \pm 45]$ not respecting the stacking rules but developed for the airplane fuselage applications.

The defects are analyzed by the ultrasonic, X–Ray, profilometer and postmortem microscopic examinations.

Concerning the kinetics of defect onset for the quasi-isotropic stacking, the post impact defect is globally in the form of a cone inside the thickness and elliptic in plane. It is observed that the first damages at (low energies and low velocities) are cracks inside the ply thickness due to shearing. These micro-cracks entail thereafter the delamination between the layers of different orientations. The orientation of delamination is guided by the relative angle between plies on both sides of the delamination. For these types of laminates, the presence of macro-cracks on the opposite side to impact favors the delamination propagation.

In case of stacking sequence $[\pm 45, 0, 0, 90, 90, 0, 0, \pm 45]$, the form of damage is different and is rather cylindrical in thickness direction and circular in plane. We again observe the matrix cracks at the origins of delamination between plies of different orientations, but the size of the delamination is minimized by the fact that for the same energy, there are lesser macro-cracks on side opposite to impact. The presence of sub-laminate $[\pm 45]$ delays the onset of these macro-cracks.

As far as the loading rates are concerned, it appears that the defects (delamination) found after canon impact for the same energy, have smaller sizes as compared with the damages found after low velocity impact (Drop Tower). It appears that the global bending of the impacted plates is more important during the Drop Tower tests, therefore increasing the size of the damage as well. These observations are also found on the dent depth which is low after impact at a higher loading rate. The next chapter is therefore dedicated to modeling (by different numerical methods) of the post impact damage onset for different types of loadings and different stacking sequences with the help of material models developed in the previous chapters.

5

Impact Modeling of Coupon Specimen

In this chapter the two developed models, bilinear cohesive damage model (Chapter 2) and the deterministic continuum damage model (Chapter 3), are applied to simulate impact of coupon test specimen. The results from simulation with the experiments, of drop tower and canon tests, obtained in Chapter 4 are compared.

The cohesive damage law simulations are presented first and then the ply damage simulations. The results used for comparison with experiments are global transitory force/displacement and local damages from damage variables in simulations with C–Scan and microscopic images.

The last section of this chapter presents an initial investigation to show the prospects of Smoothed particle Hydrodynamics one of the new meshless methods, [104], to model the linear elastic behavior of a low velocity impact. The results for this calculation will be compared with results from finite element calculation and experimental results.

5.1 Impact Modeling: Cohesive Damage Law

This section focuses on the impact damage modeling by using damageable cohesive finite elements. The numerical model is based on the parameter calibration studies already presented in Chapter 2. The numerical model is presented first and then the globally measure quantities, impact force and specimen displacement are compared with the numerically predicted results. Then the following paragraphs focus on the damaged cohesive element areas (interfaces). The size of damaged cohesive elements is compared with the experimental measurements by C–Scan and X–ray imaging.

5.1.1 Finite Element Model

The numerical finite element model is constructed by using solid finite elements with 3 degrees of freedom (DOF) and 1 integration point per element. Each layer of laminated composite material is modeled by one layer of solid elements. A penalty based frictionless contact is defined between: (i) composite specimen and impactor, and (ii) composite specimen and metallic support. In order to better illustrate the Figure 5.1(a) shows a quarter of the finite element model. The boundary conditions are also shown in the same figure. The support and impactor are considered rigid (i.e undeformable), [6]. Support is constrained in all directions while impactor is also constrained in x- and y-direction. An initial velocity v_{imp} is applied to the impactor as measured during experiments in paragraph 4.2. The effects of gravity are not taken into account.

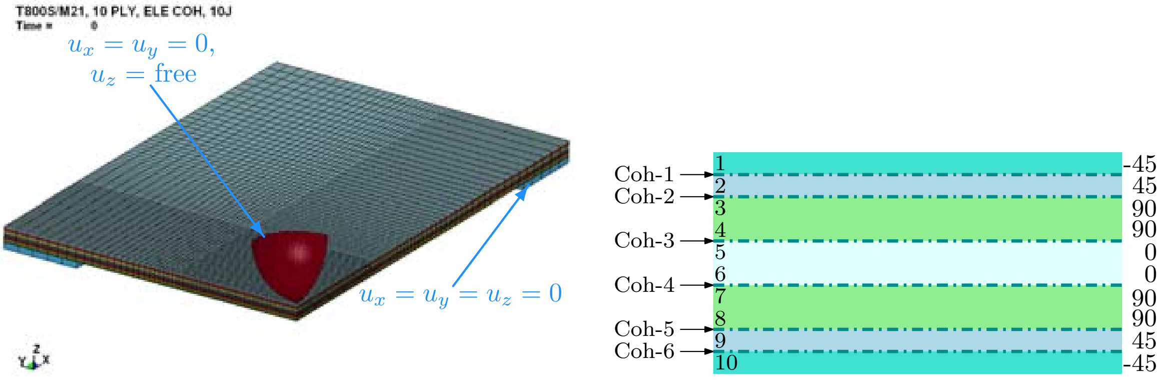

(a) (b)

Figure 5.1: (a) Quarter Finite Element Model, (b) Location of cohesive elements

A layer of 4 point cohesive finite elements, [107], is placed between the plies of different orientations as shown in Figure 5.1(b). These cohesive finite elements share nodes with the solid elements and have zero thickness as presented in Chapter 2. These cohesive elements are deleted from the simulation as described in the above referenced Chapter. A frictionless contact is defined between plies, which becomes active when a cohesive element is deleted. In order to capture strain gradients properly, size of finite elements has been chosen smaller in the impacted zone.

Table 5.1: Elastic orthotropic material properties for plies (T800S/M21).

E_{11} (GPa)	E_{22} (GPa)	E_{33} (GPa)	ν_{12}	ν_{23}	ν_{13}	G_{12} (GPa)	G_{23} (GPa)	G_{13} (GPa)
157	8.5	8.5	0.35	0.53	0.35	4.2	2.2	4.2

The elastic orthotropic material properties are shown in Table 5.1 and the interface material properties are given in Table 5.2.

Table 5.2: Material parameters for interface elements (T800S/M21 simulation).

k_I (kN/mm^3)	k_{II} (kN/mm^3)	σ_n (MPa)	σ_s (MPa)	$\mathcal{G}_{Ic}$ (J/m^2)	$\mathcal{G}_{IIc}$ (J/m^2)	α
100	100	60	60	765	1250	1.0

5.1.2 Comparison: Test and Simulation

5.1.2.1 Specimen Global Behavior

Force measured by the impactor mounted on the trolley and displacement measurement by laser on the face opposite to impacted side during an experiment is compared with numerical simulation results to compare the global stiffness and global bending of specimen, Figure 4.3.

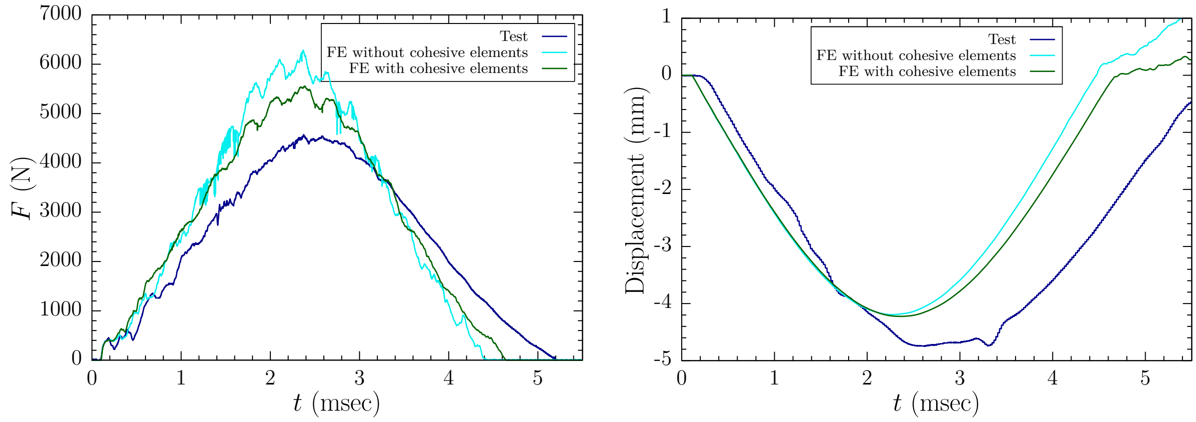

(a) Force–time response.

(b) Displacement–time response.

Figure 5.2: Comparison of experiment and simulation results, $E_{imp} \approx 10$ J

Figure 5.2 shows comparison of transitory force and displacement for (*i*) completely elastic (without cohesive elements), (*ii*) damageable cohesive elements and (*iii*) experimental results. The experimentally obtained peak force is lower than the numerical predictions, Figure 5.2(a), and experimentally obtained displacement is higher than simulation results, Figure 5.2(b). It is obvious that the introduction of damageable cohesive elements allow to dissipate energy (energy dissipated due to delamination) and as a consequence the numerical specimen becomes less stiff. Therefore the time of impact increases and the experimental behavior is being approximated in a better way.

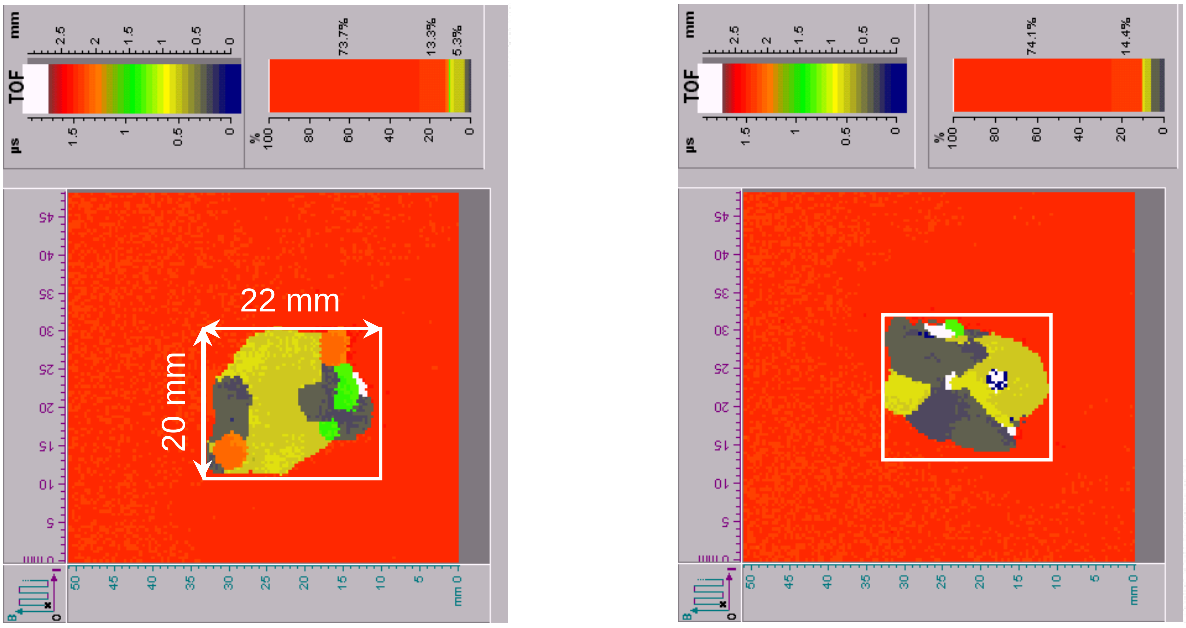

(a) (b)

Figure 5.3: C–Scan images (a) impacted face (b) opposite to impacted face.

5.1.2.2 Comparison of Delamination Area

By plotting the cohesive elements with damage variable d between 0.9 and 1.0 ($0.9 < d < 1.0$) a bounding box representing the delamination area of 27×30 mm^2, Figure 5.4, is obtained. This area is higher than the experimentally obtained value for corresponding area, Figure 5.3. One reason of this could be the absence of micro matrix cracking and macro ply cracking in numerical model. The macro cracks have the tendency to cause delamination arrests. Nevertheless, the orientation of the delamination is well reproduced as the major axis of the elliptical delamination is oriented along the fiber direction of the lower plies e.g the 45/90 interface (second interface from impacted side) labeled as Coh-2 in Figure 5.4 is oriented along 90°.

A cross-section along an angle $-45°$ with global x-direction of specimen is shown in Figure 5.4. The orientation and location of the delamination was further confirmed by the microscopic imaging.

Another cross-section along global y-direction at time, $t = 2.5$ msec is shown in Figure 5.5. It can bee seen that the biggest delamination is oriented along the global y-direction. The diameter of the contact area between the impactor and plate has been measured in the simulations to be around 5 mm. This dimension is a typical length that can be measured in the center of Coh-1, Coh-2 and Coh-3 delamination zones. As can be seen in Figure 5.4, the cohesive elements have been damaged in these zones under the impactor, but the contact is closed between adjacent layers. Even though the size

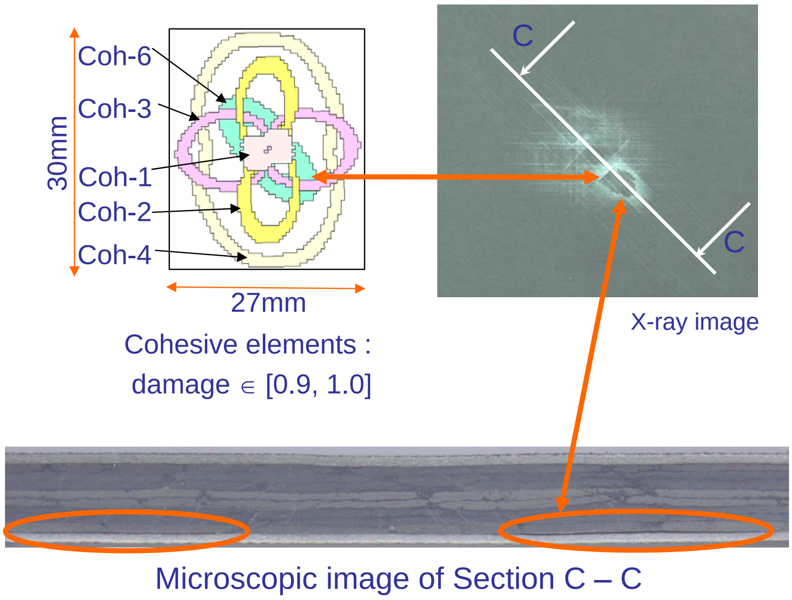

Figure 5.4: Damage variable d $(0.9 < d < 1.0)$ for finite elements, [78].

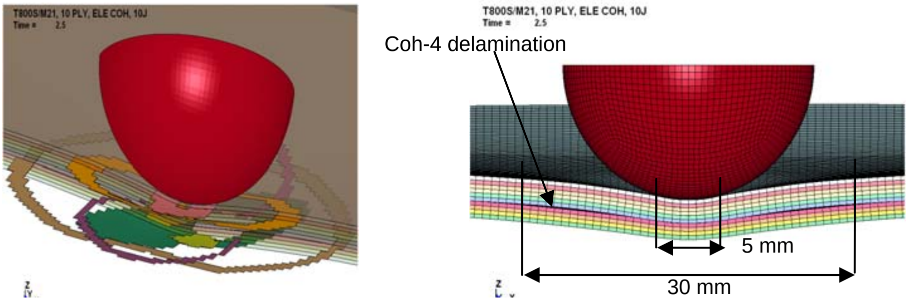

Figure 5.5: Visualization of delamination at 2.5 msec

of the delaminated area is higher than the experimental measure in the central 90/0 and 0/90 interfaces, these have dimensions similar to the experiment in the external interfaces (around 20 mm length), and the physics of local punch and global bending is well reproduced.

In Figure 5.6, the curves of mode II and mode I stresses are presented in a *"correctly"* approximated and another *"less correctly"* approximated interface. These stresses show a global round shape corresponding to the global bending of the plate and local oscillations during the loading of the plate. These oscillations are related to the wave propagation along length, breadth and thickness direction of plate. In Coh-6 (last interface from impacted side) where the delamination length is not consistent with the experiment. It is worth noting that in order to have correct orientation of delamination in $45/-45$ or $-45/45$ interfaces, value of σ_s was reduced to a value of 40 MPa. It is clear from the Figure 5.6 that the stress signal has not been truncated by the maximal tangential stress of 40 MPa as in the case of $45/-45$ (Coh-6) interface.

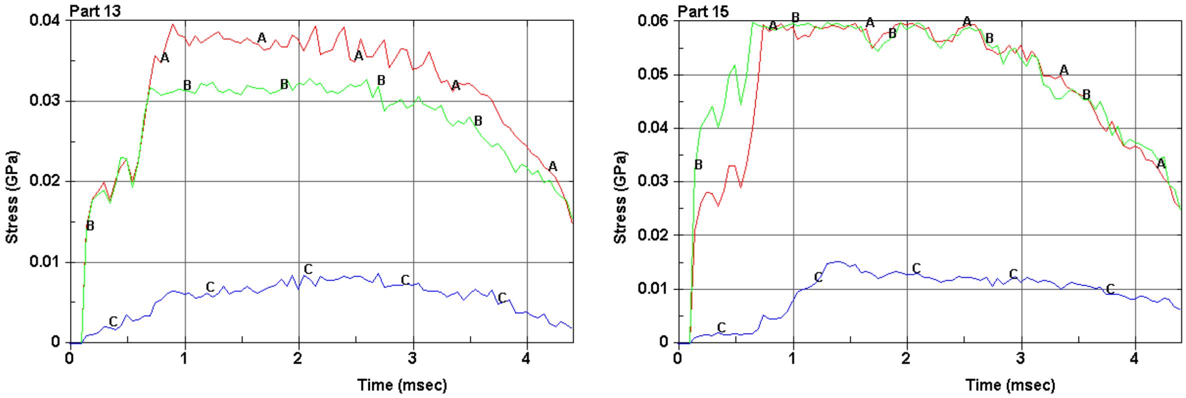

(a) Shear stresses (A & B) and normal stress (C). (b) Shear stresses (A & B) and normal stress (C).

Figure 5.6: Transitory evolution of shear and normal stresses in (a) interface $[+45/-45]$ (Coh-6) and (b) the interface $[90/0]$ (Coh-4), [78].

5.1.3 Conclusions

The results of impact simulations using the bilinear cohesive model have been compared with global transitory force/displacement and delamination damage for an impact specimen. It is shown that the computed delamination areas have the same orientations (shapes) and dimensions in outer layers, while an over-estimate is predicted for inner interfaces. This over-estimate can be attributed to absence of: (*i*) matrix damage, (*ii*) strain rate effects for interfaces and (*iii*) wave propagation effects in the existing finite element and cohesive material model. Since, the composite plies are assumed to be elastic, contact force is higher and the contact duration is lower than the experimental values. The next section of this chapter focuses on impact damage modeling by using the deterministic damage material model taking into account fiber damage, matrix damage, delamination and interaction of the above cited damage modes.

5.2 Impact Modeling: Continuum Damage Law

In Chapter 4, a number of tests have been presented using different combination of mass and velocity in order to understand the effect of strain rate dependent behavior of composite plate specimen. The results presented in the following paragraphs are for a typical lay-up/stacking sequence, $[-45, 45, 0, 90, 0, 0, -45, 45, 0]_s$, where results exist for both large mass and small mass impact configurations.

5.2.1 Finite Element Models

The corresponding numerical finite element models for large mass and small mass impact configurations are shown in Figures 5.7(a) and 5.7(b), respectively. The location of cohesive finite element layers is shown in Figure 5.7(c). It is worth noting that interface

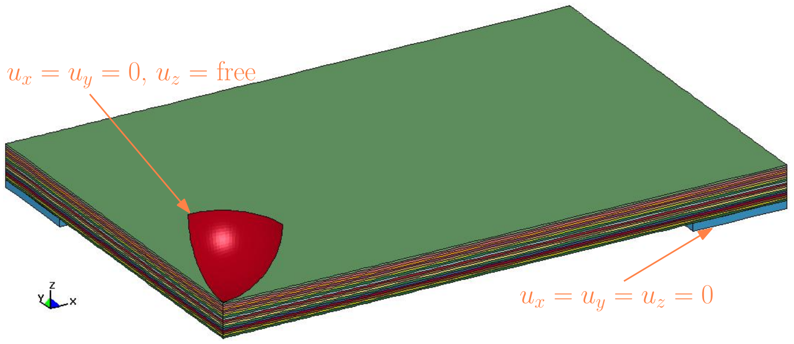

(a) Drop tower impact finite element model.

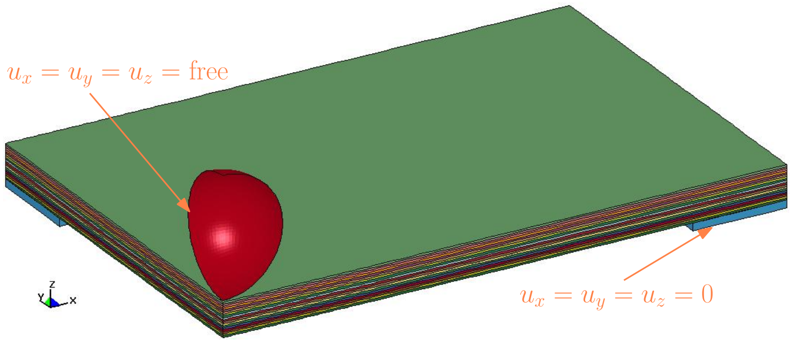

(b) Canon impact finite element model.

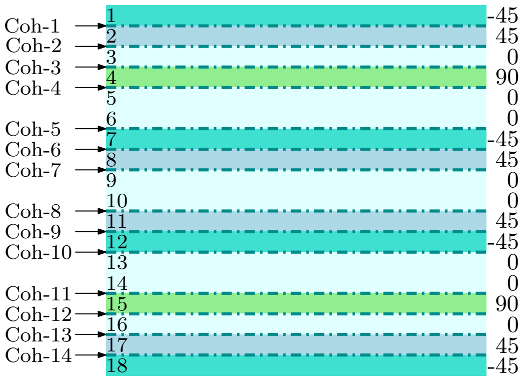

(c) Stacking sequence.

Figure 5.7: Impact finite element models and stacking sequence.

elements were used only when orthotropic elastic material was used for plies and comparison with continuum damage model was done or in other words when ply damage material model is used the interface elements are not used.

For drop tower simulations, the boundary conditions and contact definition are same as defined in the previous section. The impact velocity, $v_{imp} = 3.47$ m/sec. In order to conform with the physical model, the impactor/projectile is free in all three directions for canon impact simulations. The mass of the impactor is 0.017 kg and impact velocity is 40.82 m/sec as measured by the high speed camera. Number of deformable elements in case of continuum damage model is 374,400 and for numerical model containing cohesive interfaces is 665,600. The mesh refinement for coupon specimen in xy-plane is same as in Figure 5.1(a).

Table 5.3: Material model data for T800S/M21 impact simulations.

E_{11} (GPa)	E_{22} (GPa)	E_{33} (GPa)	ν_{12}	ν_{23}	ν_{13}
165	7.64	7.64	0.35	0.4	0.35
G_{12} (GPa)	G_{23} (GPa)	G_{13} (GPa)	X_T (GPa)	X_C (GPa)	Y_T (GPa)
5.61	2.75	5.61	2.2	1.2	0.045
Y_C (GPa)	Z_T (GPa)	Z_C (GPa)	S_{12} (GPa)	S_{23} (GPa)	S_{13} (GPa)
0.28	0.045	0.7	0.05	0.05	0.05
S_{fs} (GPa)	S_{del}	m_i	φ	d_{max}	$\mathcal{C}_1$
1.5	1.0	10	10	0.87	4.7
$\dot{\epsilon}_{ref}$ (s^{-1})	$S_{12}^{dyn} = S_{23}^{dyn} = S_{13}^{dyn}$ (GPa)				
750	0.12				

The material model data constants used for continuum damage model impact simulations are shown in Table 5.3. These material constants are essentially same as identified in Chapter 3.

5.2.2 Comparison: Test and Simulation

5.2.2.1 Specimen Global Behavior

The experimental values available for global specimen comparison are force/displacement results as a function of time for drop tower tests and transitory strain gage signals for the canon tests. The drop tower tests are analyzed first.

Figure 5.8 presents impact force and non-impacted face displacement results as a function of time. It can be seen that the Elastic Simulation gives the highest peak force and lowest impact time, thus a very stiff finite element model. Next come the quasi-static yield stress (Sigma Yield Quasi-static) and dynamic yield stress (Sigma Yield Dynamic) simulation results. In quasi-static yield stress simulation, the shear yield stresses S_{12}, S_{23} and S_{13} have a fixed value of 50 MPa. And for dynamic yield stress simulation, these shear strengths have dynamic value of 120 MPa and evolve according to strain rate dependent logarithmic law as identified in paragraph 3.2.2.3 of Chapter 3.

It is observed that the quasi-static yield stress simulation is more stiffer as compared with the dynamic yield stress simulation, Figures 5.8(a) and 5.8(c). It is noted that all of the numerically predicted results exhibit a higher initial stiffness, Figure 5.8(a). In author's opinion, the drop tower impact test is essentially a plate bending problem. At

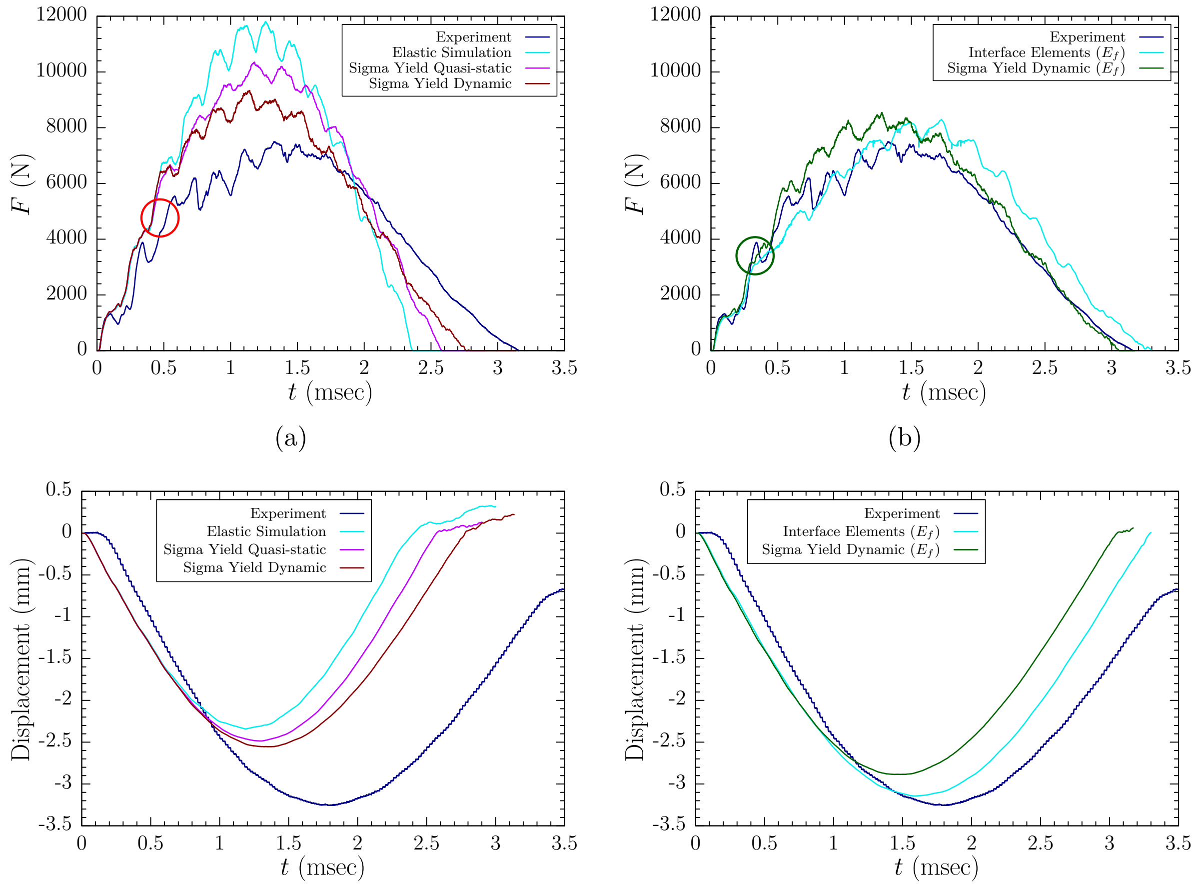

(a) (b)

(c) (d)

Figure 5.8: Force/displacement as a function of time.

this point the continuum damage model does not distinguish between different tensile and compressive moduli. Therefore, as an initial approximation flexural modulus, E_f, of 112 GPa is used for simulations shown in Figures 5.8(b) and 5.8(d).

Table 5.4: Force (N) versus time (msec) results.

	Maximum Force (N) / time (msec)	Contact time (msec)
Elastic Simulation	12,000 / 1.25	2.35
Sigma Yield Quasi-static	10,400 / 1.2	2.58
Sigma Yield Dynamic	9,400 / 1.15	2.75
Interface elements (E_f)	8,200 / 1.75	3.3
Sigma Yield Dynamic (E_f)	8,300 / 1.3	3.05
Experiment	7,800 / 1.32	3.15

In Figures 5.8(a), it can be seen that simulations show a stiff response right from the start of simulation, as highlighted by a red circle. On the other hand by using E_f instead of E_{11}, the initial global stiffness of impacted specimen as highlighted by a dark-green circle in Figure 5.8(b) is better computed. The change in plate stiffness due to damage occurs at 0.7 msec, which is well approximated by the ply damage model, dark-green curve in Figure 5.8(b). The damage in finite element model containing cohesive elements arrives earlier, at around 0.4 msec. As compared with all the simulations, the continuum damage model produces the global frequencies of plate most accurately. At 1.5 msec the continuum damage model and the experimental curve have the same behavior with a small plateau upto 1.75 msec and then an almost linear decrease upto 3 msec.

Displacement of the plate face opposite to impact point is better approached by the simulation with interface elements. The difference of experimental and dynamic yield stress impact simulation can be attributed to the absence of permanent deformation in numerical model.

5.2.2.2 Strain Rate Dependent Local Damage

The damage variable d_4 can be considered as a variable representing both the delamination and matrix cracking. Figures 5.9 and 5.10 compare this damage variable with the experimental results of drop tower and canon experiments, respectively. The impact energy is $\approx$ 15 J for drop tower and canon simulations. The elements where damage saturation has occurred, i.e $d_4 > d_{max}$, are shown in these two figures.

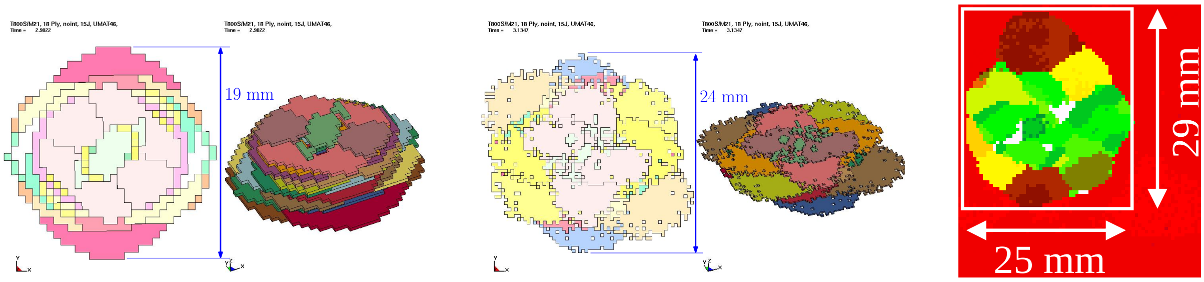

(a) Quasi-static yield stress. (b) Dynamic yield stress. (c) C–Scan image.

Figure 5.9: Elements with damage variable $d_4 \in \{0.87, 1.0\}$, Drop Tower impact at 15 J.

It can be observed that the quasi-static yield stress simulation results of Figures 5.9(a) and 5.10(a) show the damaged elements in the form of a cone. The sizes and orientations are not well computed these elements are compared with C–Scan image. On the other hand when the corresponding impact events are simulated by using the dynamic yield stress in material model, the orientation and overall size of the damaged elements is coherent with the experimental values. The difference between the overall damage size is also lesser in the case of dynamic yield stress simulations.

The values of failure criteria f_4 and f_5 have main contributions in damage variable d_4 and are shown in Figures 5.11 and 5.12. It can be seen that by using the dynamic

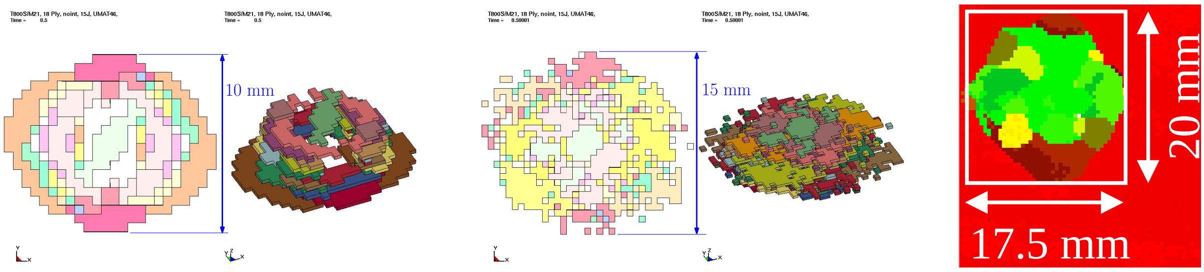

(a) Quasi-static yield stress. (b) Dynamic yield stress. (c) C–Scan image.

Figure 5.10: Elements with damage variable $d_4 \in \{0.87, 1.0\}$, Canon impact at 15 J.

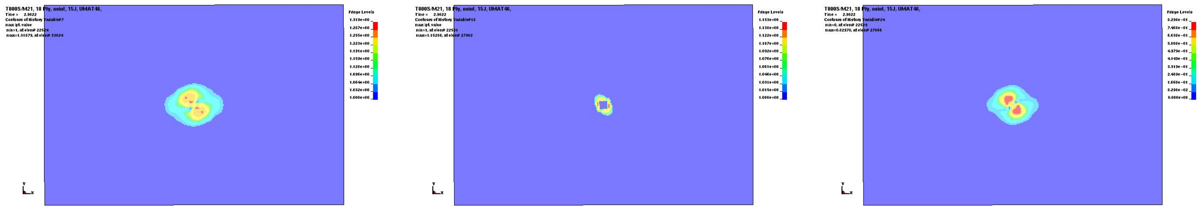

(a) f_4 (Quasi-static yield stress). (b) f_5 (Quasi-static yield stress). (c) d_4 (Quasi-static yield stress).

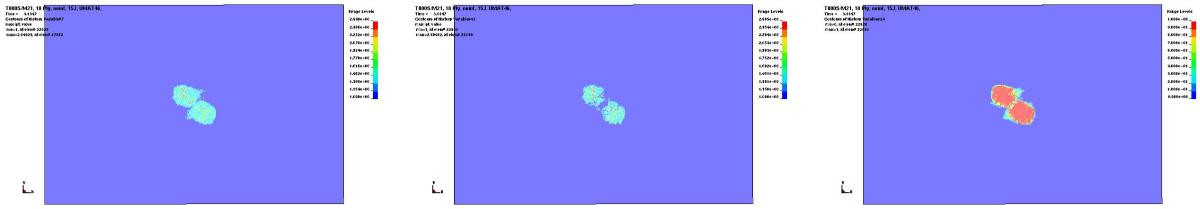

(d) f_4 (Dynamic yield stress). (e) f_5 (Dynamic yield stress). (f) d_4 (Dynamic yield stress).

Figure 5.11: Failure criteria, f_4 and f_5, and damage variable, d_4, for Drop Tower simulation $E_{imp} \approx 15$ J.

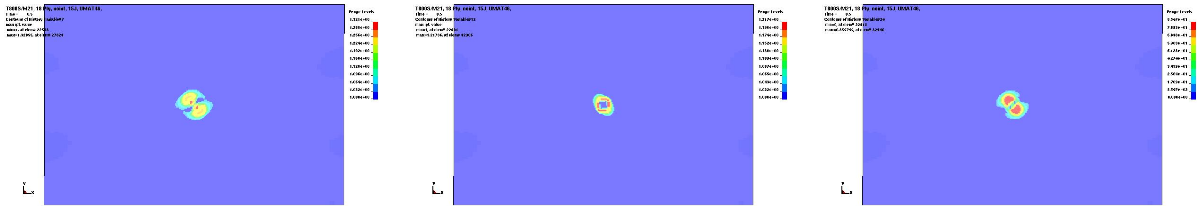

(a) f_4 (Quasi-static yield stress). (b) f_5 (Quasi-static yield stress). (c) d_4 (Quasi-static yield stress).

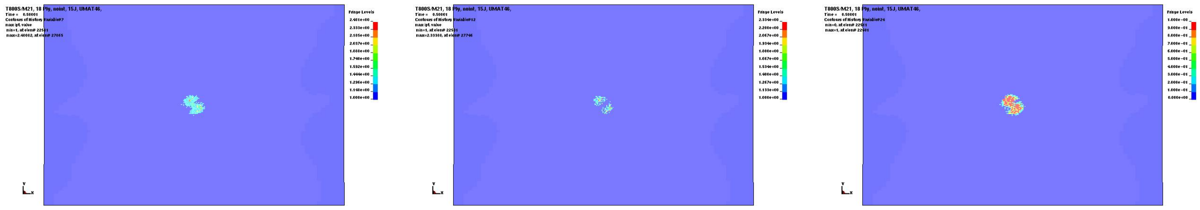

(d) f_4 (Dynamic yield stress). (e) f_5 (Dynamic yield stress). (f) d_4 (Dynamic yield stress).

Figure 5.12: Failure criteria, f_4 and f_5, and damage variable, d_4, for Canon simulation $E_{imp} \approx 15$ J.

yield stress in material model the damage has been localized, Figures 5.11(f) and 5.12(f). In case of quasi-static yield stress simulations diffusive behavior of damage is observed, Figures 5.11(c) and 5.12(c).

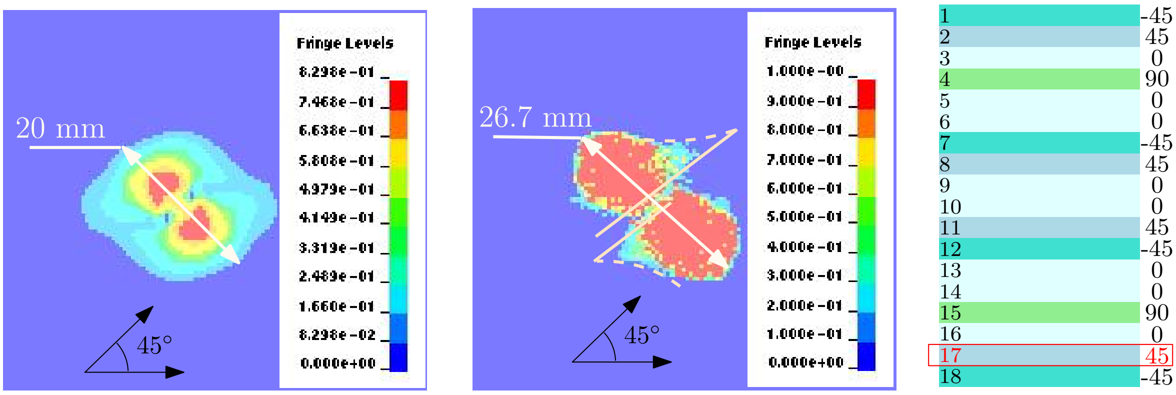

(a) d_4 (Quasi-static yield stress). (b) d_4 (Dynamic yield stress). (c) Lay-up sequence.

Figure 5.13: Damage variable d_4 for second last ply from impact side.

In order to further illustrate this point a zoom on Figures 5.11(c) and 5.11(f) is plotted in Figures 5.13(a) and 5.13(b). This is the second last ply from the impact side and its location is shown in red color in Figure 5.13(c). The ply itself is oriented at 45° with global x-direction of specimen and there below is a ply oriented at $-45°$. For both simulations the orientation of damage variable is along the lower ply. For the quasi-static yield stress case it can be seen that the damage saturation has not occurred. The maximum damage is in the center with a length of 10 mm, half of the over all damaged zone length. On the other hand, the dynamic yield stress simulation has the damaged length of ≈ 27 mm. It is also observed that the delamination arrest is being predicted along the 45° ply.

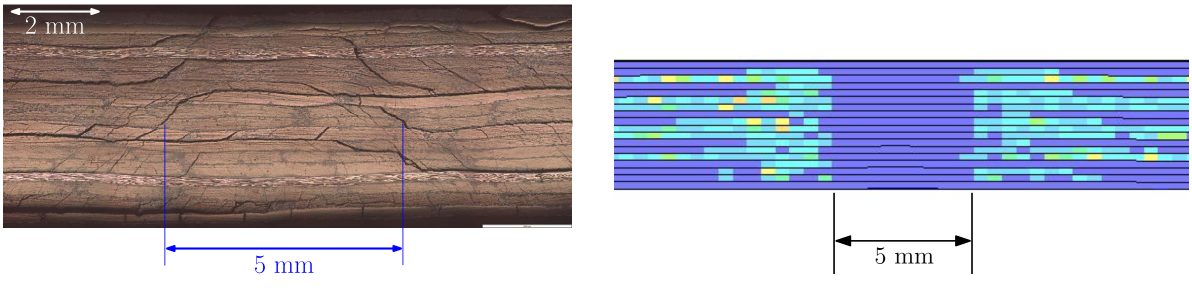

(a) Microscopic image. (b) Failure criteria f_5.

Figure 5.14: Damage from microscopic image compared with failure criteria f_5 in simulation of $E_{imp} = 30$ J.

A cross section of T800S/M21 laminate, $[-45, 45, 0, 90, 0, 0, -45, 45, 0]_s$, impacted at $E_{imp} = 30$ J is shown in Figure 5.14. The cross section shown is along global y-direction (section A–A of Figure 4.13). The comparison of the experimental and numerical results show that the size of the undamaged volume under the impactor in the simulation has the dimensions as in the of microscopic image. The delamination locations predicted by simulation can be identified in the microscopic image. The results are very promising.

A summary of delamination prediction from numerical methods is summarized in Table 5.5. The percentage difference is calculated as follows:

$$\%\text{ age difference} = \frac{\text{Value}_{simu} - \text{Value}_{exp}}{\text{Value}_{exp}} \tag{5.1}$$

where Value_{simu} is the measurement from simulation and Value_{exp} is the experimental measurement.

This comparison reveals that the delamination damage prediction by continuum damage model is in close comparison with the experimental values. The cohesive law over predicts the damage bounding box. In case of higher velocity impacts in canon tests, the difference of experimental and numerical values is also on higher side. This is attributed to the numerical parameter identification for strain rates. It is hypothesized that a dedicated study on identification of strain rate dependent parameters will decrease this difference.

Table 5.5: Delamination bounding box comparison test results and simulation predictions.

Stratification	Impact Energy (J)	Bounding Box (mm×mm)			Diff Int[1]		Diff Umat[2]		Diff overall	
		Interface[1]	Umat[2]	Test	L_x	L_y	L_x	L_y	Umat	Interface
$[45, -45, 90, 0, 90, 90, 45, -45, 90]_s$	10.23[3]	30×32	24×26.5	26×20	15.4%	60%	-7.7%	32.5%	22.3%	84.6%
$[45, -45, 90, 0, 90, 90, 45, -45, 90]_s$	19.90[3]	48.8×67.6	32.5×39	38×31	28.4%	118%	-14.5%	25.8%	7.6%	180%
$[-45, 45, 0, 90, 0, 0, -45, 45, 0]_s$	9.62[3]	28×31	25×22	22×22	27.2%	4.1%	13.6%	0%	13.6%	79.3%
$[-45, 45, 0, 90, 0, 0, -45, 45, 0]_s$	14.25[3]	33.5×39	26.5×24.1	25.5×29	31.4%	34.5%	3.9%	-16.7%	-13.6%	76.7%
$[-45, 45, 0, 90, 0, 0, -45, 45, 0]_s$	20.63[3]	45.6×52	37.5×36	38×36	20%	44.4%	-1.3%	0%	-1.3%	73.3%
$[-45, 45, 0, 90, 0, 0, -45, 45, 0]_s$	29.55[3]	76.8×83	47×43	45.5×51.5	68.8%	61.2%	3.3%	-16.5%	-13.8%	172%
$[-45, 45, 0, 90, 0, 0, -45, 45, 0]_s$	14.16[4]	32.6×33.5	17.5×15	17.5×20	86.3%	67.5%	0%	-25%	-25%	67.4%
$[-45, 45, 0, 90, 0, 0, -45, 45, 0]_s$	20.00[4]	44.1×46.9	19.6×17.6	37.5×30.5	17.6%	53.8%	-47.7%	-42.3%	-69.8%	80.8%
$[-45, 45, 0, 90, 0, 0, -45, 45, 0]_s$	29.41[4]	61.3×71.8	23×19.5[5]	44.5×39.5	37.8%	81.8%	-48.3%	-50.6%	-74.5%	150%
$[-45, 45, 0, 90, 0, 0, -45, 45, 0]_s$	39.51[4]	82.2×88.3	37×25[5]	55.5×39.5	48.1%	124%	-33.3%	-36.7%	-57.8%	67.4 %
$[-45, 45, 0, 90, 0, 0, -45, 45, 0]_s$	100.0[4]	150×100[6]	114.6×82.1	145.2×83.7	×	×	-21.1%	-1.9%	-22.5%	×

---

[1] Bilinear cohesive law
[2] Continuum damage model
[3] Drop Tower
[4] Canon
[5] Conservative values
[6] Separation into two sublaminates

5.2.2.3 Impacted Face Dent Depth Prediction

In order to measure the predicted dent depth, the numerical model is cut along global y-direction (section A–A of Figure 4.13) as shown in Figure 5.15. The maximum displacement of nodes along impacted side and opposite side is extracted and a difference of displacement on bottom side and top side is used for comparison with experimental measurements.

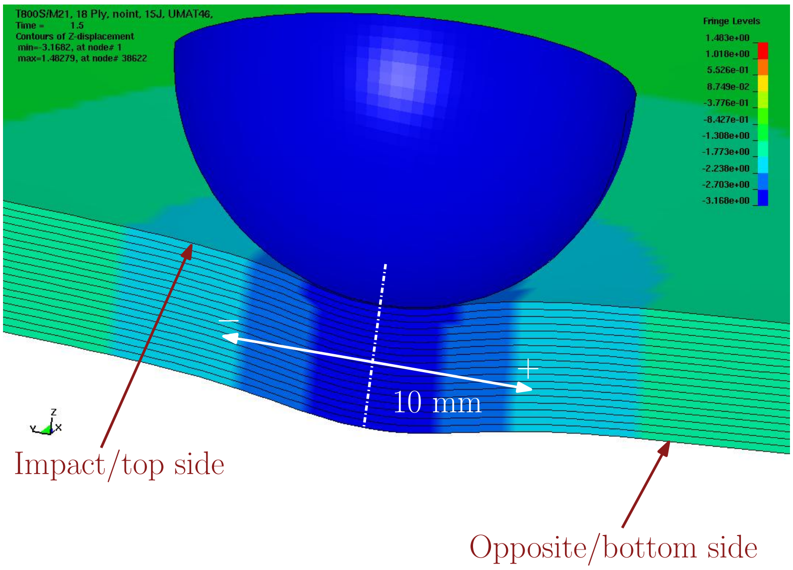

Figure 5.15: Illustration of impact dent prediction.

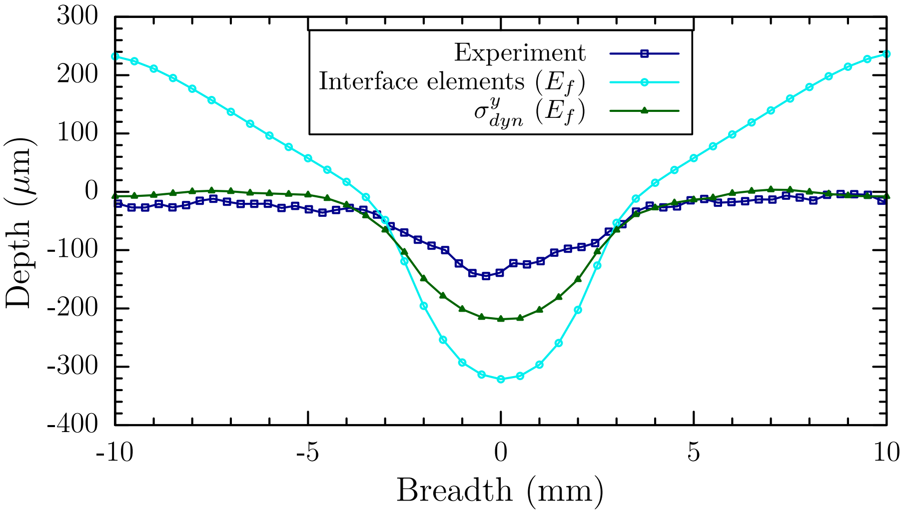

Figure 5.16: Dent depth, numerical models predictions compared with experimental value, $E_{imp} = 15J$.

Figure 5.16 shows the comparison of the dent depth around the impact zone for $E_{imp} =$ 15 J between experimental and numerical measurements. Depth in numerical simulations is defined as the relative displacement of plate nodes below impactor and corresponding nodes on the opposite side in thickness direction, Figure 5.15. As a comparison the numerical depth computed by the numerical simulations using: (i) cohesive elements and (ii) dynamic yield stress damage material model is reported. For this typical impact case dent depth is found -0.16 mm by experimental, -0.22 mm for σ^{y}_{dyn} continuum damage model and -0.32 mm for cohesive model. It can be seen that continuum damage model predicts quite well the crater upto a distance of 10 mm around the impact point.

5.3 Conclusions

The bilinear cohesive material law used for impact simulations produced good qualitative results. Quantitatively, as far as the global results are concerned, the maximum force during simulation is higher than that during a test on the other hand the damaged area is also higher for this numerical model. Another important point is that the maximum shear stress, σ_s, in ±45 interfaces has to be two thirds (40 MPa) of the normal stress (60 MPa), σ_n, in order to initiate and propagate damage in these interfaces.

Another reason for the higher damage area was thought to be due to a highly conservative value of $\alpha = 1$. Due to lack of available time and absence of test data for mixed-mode strain energy release rate for T800S/M21, this minimum value was used. A calculation was then done by taking $\alpha = 1.5$ (as for unidirectional composite materials $1.0 \leq \alpha \leq 2.0$, [126]) showed quasi-identical results as $\alpha = 1$. The variation in the value of α did not affect the delamination surface. It is, therefore, proposed that strain rate dependent behavior is to be taken into account, along with the incorporation of damage in plies.

The continuum damage model simulations carried out with flexural modulus, E_f, instead of tensile modulus, E_{11}, compared quite well with the global response. The initial stiffness of plate is well captured by the simulation and the time of damage to commence is also satisfactory. The time of impact is quasi-identical as compared with an experiment and lower than one predicted by the cohesive finite element model. It is also important to take the strain rate effects into account via evolution of σ^y_{dyn}. This allows to better predict the orientation and size of delamination surface. The localization of damage by using σ^y_{dyn} dissipates energy in right areas and prohibits the diffusive behavior observed when using quasi-static yield stress values.

The cohesive finite element model predicted a higher damage surface as compared with the experiment of large mass small velocity or small mass medium velocity, on the other hand continuum damage model predicted large mass low velocity impact with a difference around -20% as compared with experiment. The continuum damage model underestimates the damage surface. In case of canon tests this difference is slightly on a higher side. The canon impact tests had shown that there is a difference in global behavior of plates when impact energy, E_{imp}, is above 20 J. The experimental and numerical model also show the same trend as at $E_{imp} = 15$ J the difference is -25% and at $E_{imp} = 30$ J this difference is -74.5%. A possible explanation of this behavior is that the material strain rate dependent properties have been identified for strain rates around $1000 s^{-1}$ and this might not be valid in the case of higher energy canon tests. The dent depth predicted by the numerical simulation compares well with experimental values.

In order to further explore the models capabilities with regard to impacts at higher speeds, the canon test system requires to be better equipped in order to obtain the global response of the specimen. Furthermore, the strain rate dependence of moduli is also to be investigated as the global response of canon impact specimen seems to be different that the drop tower impact response.

The dent depth predicted by the model compares well with experimental values. The model does not take into account the plastic deformations, this could be an interesting future development to better correlate with the permanent deformations of specimen.

The time of impact for cohesive finite element impact models was slightly (15%) higher as compared with continuum damage models e.g a drop tower simulation by using continuum damage model of $E_{imp} = 30$ J took 26 hours by using 2 CPUs the similar model containing cohesive element layers took 30 hours.

In order to investigate the prospects of SPH method towards anisotropic material modeling a preliminary investigation is carried out and presented in the following section.

5.4 Low Velocity Impact Modeling using SPH

This study aims to assess the ability of a stabilized Smoothed Particle Hydrodynamics (SPH) method to model the macroscopic and local mesoscopic behavior of composite plates subjected to low velocity impact. The global transitory force and displacement results are compared. The SPH method has proved its capacity to model the fracture [101, 114]. The author is interested in investigating the ability of this method to model laminated composite material under impact. In the first time the method is modified to be compatible with: material anisotropy, stacking, low velocity impact behavior and a finite element mesh around the impact point. The salient features of the method are respectively: (*i*) introduction of anisotropy,(*ii*) stabilization of the method for small deformations and strain rates and (*iii*) SPH–FE coupling. The detailed explanations of developments carried out to stabilize the method and render compatible with finite elements are given in [94].

Here, at the first the results of a feasibility study are presented which show the coherence of flexural behavior of a laminated plate comprising of SPH with a finite element model. In the later paragraphs the results of 4 J low velocity impact elastic finite element simulation and coupled elastic SPH–FE simulation, [82], are presented.

5.4.1 Feasibility Study

The SPH method is a numerical method which discretizes a domain by the particles which possess their own material characteristics and are displaced by interaction and interdependence of neighboring particles inside a sphere of influence. The state of the matter is described by the velocity of the particles, their density, stresses and the flux of forces and the conservation of energy inside the sphere of influence. This method has evolved since its creation [108], notably well suited to the large dynamic deformations. The *"standard"* SPH methods are based on an Eulerian kernel, [104]. In this case the integration support stays the same and the neighboring particles are determined at each cycle of calculation. This technique permits to calculate the large deformations observed by the matter, but is known to exhibit the instabilities of tension which limit the application of the method to large deformations, [116]. A Lagrangian kernel can be chosen. In this case the neighboring particles are same during a calculation which permits to reduce calculation time, and support of kernel evolves. This approach permits to eliminate the majority of tensile instabilities. The method chosen is the total Lagrangian formulation, coherent with the deformations observed during the low energy impact tests and coherent with simplifying hypothesis of elastic behavior which shall be used in numerical models. The reader is invited to refer to the above cited references for additional details.

5.4.1.1 Anisotropy and SPH

In this study, a situation is presented where anisotropy of plies is preponderant during whole phase of loading by the impactor (damage initiation) and then plate deformation following the structural modes (propagation and extension of damage zones). It is therefore necessary to take into account the anisotropy via the constitutive law, here a 3D orthotropic elastic model for each ply. The possibility of damage was not taken into account in the following models. Each ply is modeled by a layer of SPH particles. The reference plane is followed in each particle as a function of time. The material data is show in Table 5.6.

Table 5.6: Elastic orthotropic material properties for plies, T700S/M21.

E_{11} (GPa)	E_{22} (GPa)	E_{33} (GPa)	ν_{12}	ν_{23}	ν_{13}	G_{12} (GPa)	G_{23} (GPa)	G_{13} (GPa)
135	8.5	8.5	0.3	0.4	0.3	4.8	3.2	4.8

5.4.1.2 Bending of a Laminate: Comparison SPH and FE

The stability of the method was tested for a beam bending problem, essentially large displacements are taken into account. The numerical test specimen is a plate with dimensions as $10 \times 32 \times 2$ mm^3 fixed at one end and loaded by a vertical force on the other. The structure contains 8 plies of T700S/M21 at 0°. This is modeled by 8 layers of 8 node solid elements (3 DOF per node) with 1 integration point for FE model and 8 layers of particles for SPH model. The axial stresses are compared for both models. The large displacements undergone by the SPH plate do no provoke the numerical fracture and the method remains stable. The amplitude of the axial stresses is identical and their distribution is similar between two models both in plan and in thickness direction. The SPH plate shows a slightly higher Poisson ratio effect near the edges, which is coherent as the stiffness of FE model is higher due to absence of nodal rotations. The deformed shapes are almost identical. This not only validates the stability of the method but also its capacity to model the orthotropic behavior in large displacements.

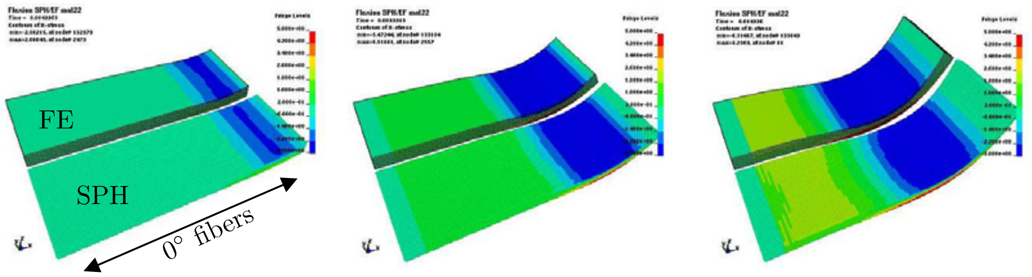

Figure 5.17: Stress distribution in FE and SPH models for a bending case.

5.4.2 Application to impact

5.4.2.1 FE and Coupled FE–SPH Models

The numerical models used for impact simulation are shown in Figure 5.18. A progressive meshing is used for FE only model to have shorter CPU run times. In case of coupled FE-SPH model, the central zone having dimensions 32 mm × 32 mm is discretized by 12,000 particles. These particles are kinematically constrained to finite elements at frontiers of both discretizations. Only one finite element and similarly one particle is used per ply. The stacking sequence is also shown in the same figure.

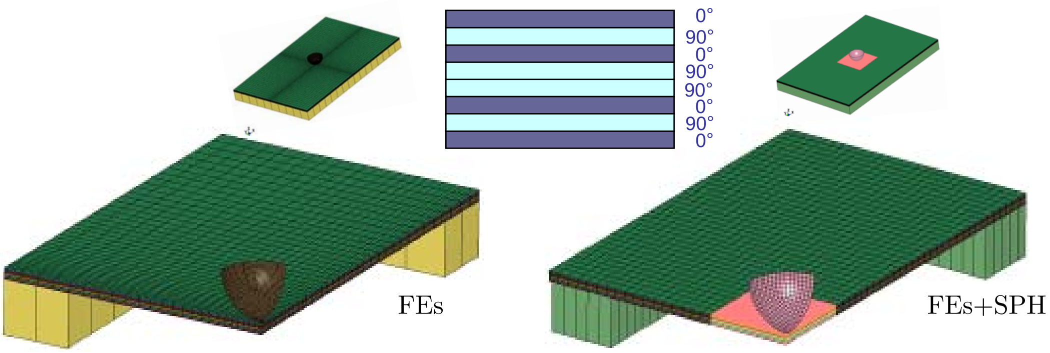

Figure 5.18: Models of laminated plate FE on left and EF–SPH on right hand side.

The plate and suport are modeled by finite elements with 8 nodes (3 DOF per node) and 1 integration point. Each ply has orthotropic elastic material properties. The material properties are same as already defined in Table 5.6. A total number of 30,500 solid elements constitute all FE model. The support and impactor are modeled by rigid elements. Mass of the projectile is 1.369 kg and impact velocity is 2.42 m/sec. The frictionless penalty based contact algorithms are introduced between (*i*) projectile and plate, and (*ii*) plate and support. The dimensions of projectile and support are same as described previously for all impact simulations.

5.4.2.2 Comparison Tests and Simulations

The damage has not been taken into account in numerical simulations. The results are compared for transitory force between plate and projectile, displacement of plate center opposite to impact face and significant stress distribution.

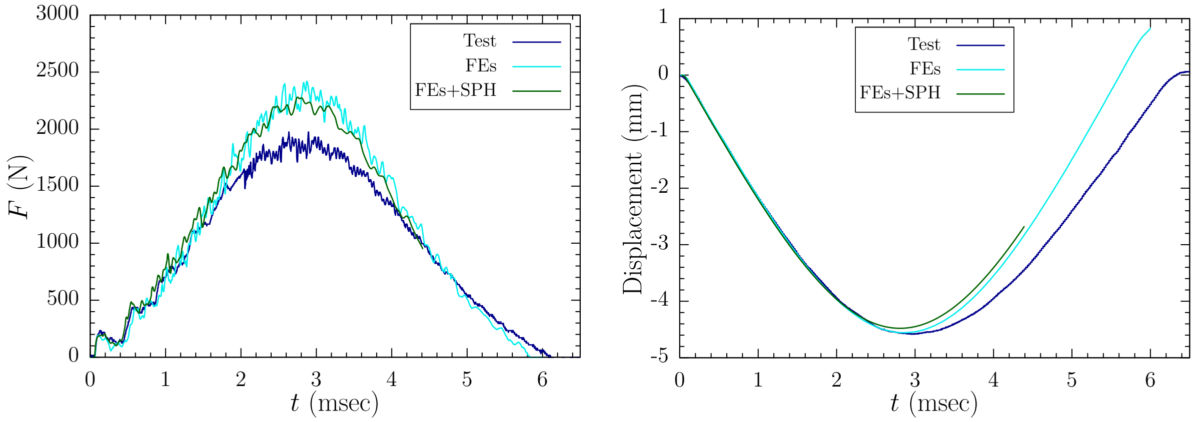

(a) Force versus time. (b) Displacement versus time.

Figure 5.19: Transitory force and displacement, FE and FE–SPH impact simulation.

The force-time curves, Figure 5.19(a), show that the first peak and rising plateau region are well captured by the numerical model. The contact duration is also close to the experimental value. The time corresponding to maximum displacement is same for test and simulation. The difference between maximum experimental and maximum numerical displacement is explained by absence of damage in numerical model and therefore numerical responses are more rigid. Except the elastic stiffness, the numerical results are in close comparison with experimental results.

Table 5.7: Comparison of experiments, FE and FE–SPH numerical models

	Displacement (mm)	Peak Force (N)
Test	4.58 at 2.9 msec (ref)	1900 (ref.)
Simulation FE only	4.62 at 3 msec (+0.8%)	2350 (+23%)
Simulation FE–SPH	4.41 at 2.8 msec (−3.1%)	2250 (+18%)

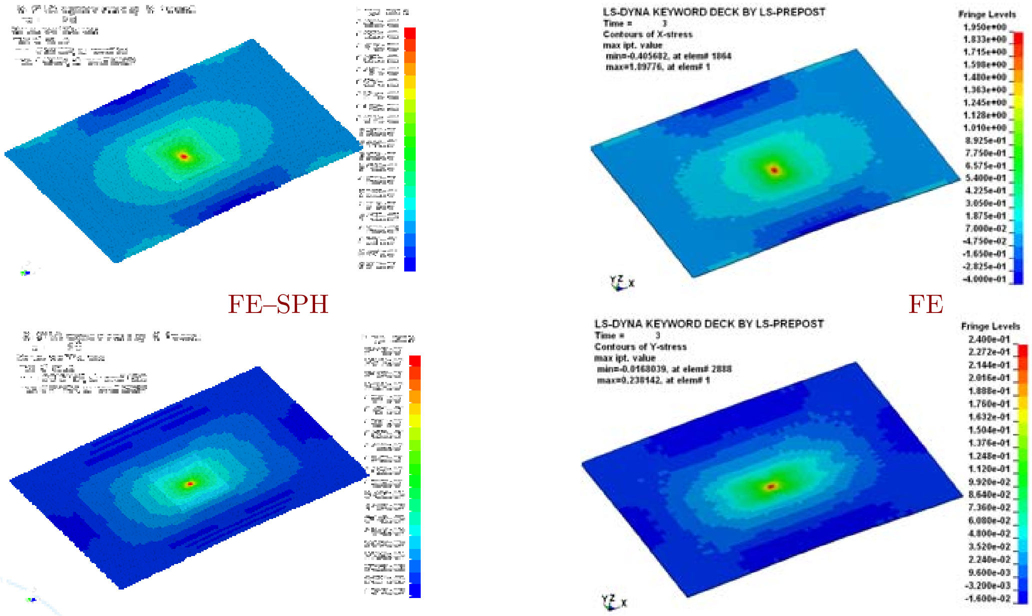

Figure 5.20: σ_x in last ply (0°) for FE–SPH and FE $[-400, 1950]$ above and σ_y in second last ply (90°) for FE–SPH and FE $[-16, 240]$ below.

The highest stresses in the last ply from top (oriented at 0°) and second last ply from top (oriented at 90°) are summarized in Table 5.8. The coherence of both numerical model results evident in this table.

Table 5.8: Stresses σ_x, σ_y, σ_{yz} and σ_{zx} in last two plies.

	σ_{xx} (MPa)	σ_{yy} (MPa)	σ_{yz} (MPa)	σ_{zx} (MPa)
Last ply at 0° (FE)	−405 to 1900	−17 to 240	−23 to 23	−114 to 114
Last ply at 0° (FE–SPH)	−395 to 1950	−16 to 245	−16 to 16	−105 to 105
Last ply at 90° (FE)	−22 to 91	−230 to 2050	−173 to 173	−118 to 118
Last ply at 90° (FE–SPH)	−22 to 97	−220 to 2060	−173 to 173	−118 to 118

To further illustrate above point a cross section view along global y-direction (section B–B of Figure 4.13) of the numerical model is shown in Figure 5.21 at maximum displacement ($t = 2.8$ msec). The contact surface from both numerical models is in close agreement.

In both numerical models, the extent of each delamination ellipse (in Figure 5.22(a)) between the last two plies (5 mm long) corresponds to the last ply zone where tensile stresses along x-direction, transverse shear (xz-plane) stresses of $40 - 95$ MPa and tensile stresses along y-direction of the order of $40 - 95$ MPa are superposed. Similarly in the second last ply, oriented at 90°, there is a zone where the normal stresses in x-

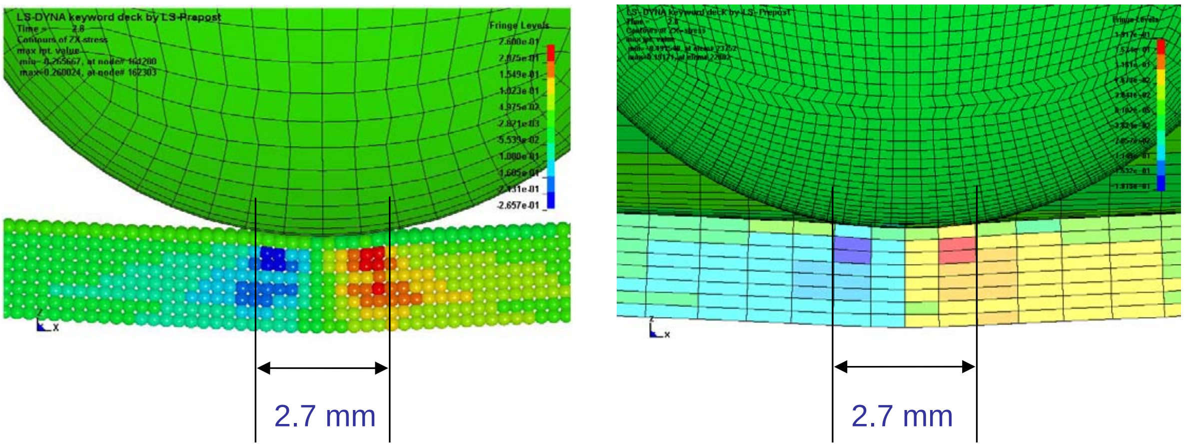

(a) Coupled finite element and SPH.
(b) Finite elements without SPH.

Figure 5.21: Contact surface from FE–SPH and FE numerical models.

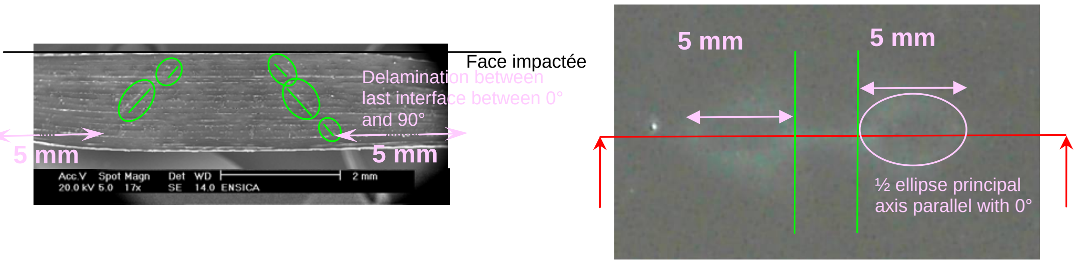

(a) Microsocpic image, section parallel with global x-direction.

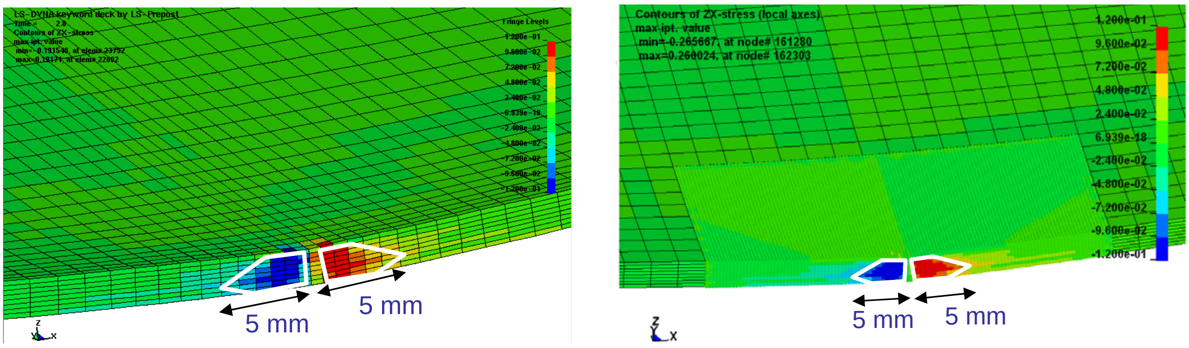

(b) FE.
(c) FE–SPH.

Figure 5.22: Qualitative prediction of damage initiation along global xz-plane.

and y-direction of the order of $40 - 95$ MPa and 115 MPa, respectively, are superposed (Figures 5.22(b) and 5.22(c)). The shear stress levels envelope is oriented in the direction of delamination observed in last two plies and has the same ellipsoidal shape. The spacing between the ellipses is symmetric in calculations and is of the same order of magnitude as delamination ellipses observed in tests.

5.4.3 Conclusions

This study has shown the capability of SPH method to model the linear orthotropic elastic behavior of laminated composites, the method is stable and FE–SPH coupling is continuous. The feasibility study shows that the finite elements show a higher stiffness on the other hand, the SPH permits to take Poisson's ratio effects into account. The low velocity impact results show that both the numerical models exhibit almost same levels of peak force and non impacted side displacement. The analysis of stresses along a cross section allows qualitative prediction of crack onset. The promising results are being shown by the SPH method. The present state of contract between ISAE and LSTC, the proprieters of LS-DYNA® , does not allow our laboratory access to some portions of this commerical code. Therefore, in future the incoroporation of damage material model in SPH simulations is envisaged.

Conclusions and Perspectives

In order to certify aerospace composite structures, the manufacturer needs to know the behavior of structures during “normal” solicitation environment of an aircraft service life, and demonstrate the ability of these structures to bear the load for a minimum period, e.g. to the next technical inspection maintenance, even after the onset of damage between two maintenance intervals. In the particular case of impacts, it is necessary to understand the behavior of composite structures for various loading characteristics. To determine the extent of damage in case of impact and quantitatively relate the external and internal measures of damage is a key issue.

From a scientific perspective the question addressed in this study is: is it possible to predict internal damage extent and localization based on external dent measure and the knowledge of loading rate and intensity?

In this frame it was aimed in this study to propose a robust predictive damage material model capable of representing effects of loading and strain rates on impact induced damage in thin composite structures typical of aeronautical components. Two numerical approaches have been investigated on laboratory samples: discontinuous openings or continuous damage material modeling.

The followed methodology was first to experimentally characterize the behavior of T700S/M21 and T800S/M21 samples at different loading rates. Then numerical models were proposed for continuous or discontinuous damages. Finally, numerically predicted impact damages are compared with real test impact experiments. A special attention is focused on the influence of loading mass and velocity on damage extent. The significant conclusions of each part of this study are detailed hereafter.

The main objective of the experimental characterization was to highlight effects of loading rate and intensity on stress limits and delamination propagation speeds. A deliberate choice had been made à priori to characterize separately the interface behavior and ply behavior as usually done by most of researchers in the composite community.

Indeed the interface behavior is well known to be related to delamination when crack branching is not taken into account and is the most catastrophic damage for the post impact residual strength. Since delamination is a structural effect, the choice was made to use Linear Elastic Fracture Mechanics to derive a cohesive law. The protocol for dynamic measurements of strain energy release rates requires first a quasi-static identification. DCB, ENF and MMB tests have been completed for each mode. Bilinear limit stress–relative displacement laws have been successfully characterized. On the other hand, dynamic tests that have been realized did not give satisfactory results. It could not be concluded whether or not delamination propagation speeds were influenced by loading rate. Nevertheless, in author's opinion the cohesive method is a suitable choice for crack propagation modeling as it is capable of representing both initiation and propagation of delamination. A numerical cohesive model was developed and implemented in the commercial code LS-DYNA®. A parametric study had been made to determine the best choice of numerical options that less influence the mechanical behavior. For both T700 and T800 based samples, the same type of law was used, with different appropriates values for each material. In all cases, finally, it was found that, since the tension and compression moduli of the carbon fibers are different, it was necessary to introduce a "flexural" modulus to get the right flexural rigidity of the plies for the numerical virtual tests to be comparable with real tests experiments. It is highlighted that this modulus is the only explicitly determined mechanical parameter of the plies behavior that directly influences the fit of the cohesive law used for the interface behavior modeling. The $\mathcal{G}_c$ indeed includes also an influence of the plies on the interface modeling but this effect is not explicitly formulated and thus cannot be controlled. Finally it is concluded that despite their simplicity and fair structure assembling representation, cohesive models are neither really predictive nor robust.

To evaluate the effects of the plies behavior on the global damage, quasi-static and dynamic tests on balanced angle ply laminates were conducted. In quasi-static $[\pm 45°]_{3s}$ tension tests, T700 and T800 based composites exhibit different behaviors: 50 MPa represent a saturation stress level for T800 samples only. It is suggested that this phenomenon is an effect of the resin rich interface that is thicker for T800 based samples than for T700 ones.

In dynamic tests, three global values are proposed to characterize the behavior up to rupture: an elastic modulus, an elastic yield stress and a maximum rupture stress. Whatever the angle, the global yield stress and dynamic rupture stress are always 30% to 50% greater

than quasi-static values. It is hypothesized that these two stresses are ply's properties. Dynamic values of the global elastic modulus on the contrary are lower than quasi-static ones for angles lower than 45°, in the same proportion. Above this critical angle, dynamic and quasi-static elastic moduli are of the same order of magnitude and remain almost constant. It is hypothesized that this global elastic modulus is a parameter that directly reflects the matrix contribution in the global laminate behavior: strain rate softening in the plies for angles below 45° and predominant effect of the resin rich interface above 45°. The global elastic modulus is therefore a structural property.
To investigate the effect of strain rates on the ply behavior in T800S/M21, dynamic tests have been done on $[\pm 45]_{3s}$ with SHPB. The presented results allowed the author to conclude that strain rate effects on the yield stress were more pronounced when the strain rate became more than $750s^{-1}$, following an exponential law. For strain rates $200s^{-1} < \dot{\epsilon} < 750s^{-1}$ the yield stress was found to be constant and twice the quasi-static value.
The synthesis of the experimental study on $[\pm 45]_{3s}$ laminates gives the following conclusions for the T800S/M21 laminate behavior : rupture of plies arises in tension and compression for the same deformation limit whatever the strain rate, yield stresses and maximum failure stresses are strain rate dependent with the previous derived law, yield stresses and maximum failure stresses dependence on angles is related to matrix or fiber failure modes, the global elastic modulus of each ply is chosen to be independent of strain rate, saturation of stresses is the reflect of matrix trough ply softening and resin rich layer coupling. In order to represent these phenomena, a damage continuum mechanics material model is proposed and developed.

The continuum damage mechanics model proposed to model the quasi-static and dynamic behavior of unidirectional composite materials is based on failure criteria. The failure criteria were identified from bibliographic studies and important modifications have been proposed based on experimental observations to characterize the material in various desired loading directions and solicitation ranges. Conforming with experimental evidence, damage saturation has been introduced into the model. Strain rate effects on strength enhancement of composite materials and interaction between different failure modes has been implemented. At the moment the variation in moduli as a function of strain rate has not been taken into account. The material model was then used to predict the SHPB experiments. A good correlation was obtained for $[\pm 45]_{3s}$ laminate response. For the case of $[\pm\theta]_{3s}$ laminates more investigations are required both in terms of experiments and numerical studies to identify shear moduli enhancement and damage couplings. The quasi-static tests allowed to determine the material constants and failure values.

Two types of impact test setups were used for experimental investigation of impact event on composite coupon specimen. The objective of this experimental study was to determine the damages generated by the low (large mass) and medium (small mass) velocities with the help of impact by a Drop Tower and impact by a compressed air gas gun, respectively, in order to show the loading rate effects on the kinetics of damage onset. The impact energies were 4 J to 100 J and the impact velocities varied from 4 m/sec to 100 m/sec. As far as the loading rates were concerned, it was observed that the defects (delamination and dent depth) found after canon impact for the same energy, have smaller sizes as compared with the damages found after low velocity impact (Drop Tower).

Two types of impact induced damage modeling approaches were studied. The first approach was the cohesive damage law where the damage was considered to be localized in the interface and the second approach was by the proposed continuum damage mechanics material law where damage was considered to be continuously distributed in the ply and interface. In case of impact simulations with cohesive damage model, the qualitative results were satisfactory. It was observed that the bilinear cohesive parameters required to initiate damage in [±45] interfaces had to be different than [0/90] interfaces in order to achieve these qualitative results. Quantitatively, the difference, as compared with experimental values, is on a higher side i.e. above 50%. The cohesive damage model over predicts the delamination sizes. In author's opinion it is important to take into account the strain rate effects and damage inside ply plane.

The impact experiments simulated with damage mechanics material model gave highly satisfactory results, difference of ±25% for overall bounding box, for delamination prediction of low velocity impact tests. The continuum damage model has also shown promising results in terms of dent depth prediction. It was also demonstrated that the effects of strain rate dependent parameters are important for a better correlation of delamination surfaces with experiments for both types of impact experiments. In case of higher velocity impacts, the difference of predicted delamination surfaces with respect to experiments was on a higher side. The continuum damage model has to be further refined in terms of strain rate dependent parameter identification and damage coupling in order to better predict higher velocity (Canon) impacts. The dent depth prediction can be further improved by taking plastic–like behavior into account in the continuum damage mechanics.

In order to investigate the low velocity impact simulation of composite materials by SPH, a meshless method, a preliminary study was undertaken. The stabilized SPH method showed promising results for low velocity impact simulations where material orthotropy played an important role in global behavior of specimen. The analysis of stresses along a cross section allowed qualitative prediction of crack onset. The administrative constraints had limited the author from exploring the coupling of the damage mechanics material model with the SPH method. Therefore, the seemingly *"natural"* coupling between SPH method and damage mechanics material remains to be achieved.

Perspectives:

Various possibilities can be envisaged to continue this study.

The experimental portion of this study has shown that a new dedicated Hopkinson's bar (3-bar) set up is required to identify loading rate dependent behavior of strain energy release rate. Furthermore, intensive instrumentation and more powerful high speed and high resolution cameras are required to conduct quality tests for strain energy release rate experiments. For the cohesive damage law has to be modified to take into account the strain rate effects.

Similarly a dedicated tensile Hopkinson's bar setup is required for identifying strain rate dependent parameters for continuum damage mechanics law. A detailed study is then to be carried out to improve the understanding and correlation of $[\pm\theta]$ laminates. The damage material model parameters have to be characterized in higher strain rate regimes. The incorporation of plastic like permanent deformation in damage mechanics model will permit to better predict the size of dent depth.

In case of loading rate influence on coupon impact specimen, the canon setup requires better instrumentation to record global specimen behavior. In order to better correlate numerical impact simulations with experiments sophisticated observation equipment is required, e.g equipment for tomography.

The coupling of damage mechanics model with SPH method will be able to shed more insight to the impact events where material anisotropy plays an important role as continuum damage model will be able to become discontinuous as required to represent fracture.

Bibliography

[1] Abdi, F., Surdenas, J., Munir, N., Housner, J., and Keshavanrayana, R. (2009). *Virtual Testing Predictive Modeling For Fatigue and Fracture Mechanics Allowables*, chapter 6, pages 137–185. Springer Science+Business Media.

[2] Aboissiere, J. (2003). *Propagation de dommages d'impact dans un materiau compoiste stratifié a fibres de carbonne et résine époxyde*. PhD thesis, Ecole Nationale Supérieure d'Ingénieurs de Constructions Aéronautiques, Département Génie Mécanique, 1, Place Emile Blouin - 31056 Toulouse Cedex 5.

[3] Abrate, S. (1991). Impact on laminated composite materials. *Applied Mechanics Reviews*, 44:155–190.

[4] Abrate, S. (1994). Impact on laminated composites: Recent advances. *Applied Mechanics Reviews*, 47:517–544.

[5] Abrate, S. (2001). Modeling of impacts on composite structures. *Composite Structures*, 51:129–138.

[6] Al-Maghribi, A. (2008). *Comportement des matériaux composites à fibres courtes: Application à l'impact basse vitesse*. PhD thesis, Institut Supérieure de l'Aéronautique et de l'Espace, Département de Mécanique des Structures et Matériaux, 10 Avenue Edouard Belin, 31055 Toulouse Cedex 04.

[7] Alfano, G. and Crisfield, M. A. (2001). Finite element interface models for the delamination analysis of laminated composites: mechanical and computational issues. *International Journal for Numerical Methods in Engineering*, 50:1701–1736.

[8] Allix, O. and Corigliano, A. (1999). Geometrical and interfacial nonlinearities in the analysis of delamination in composites. *International Journal of Solids and Structures*, 25:2189–2216.

[9] Allix, O., Feissel, P., and Thévenet, P. (2003). A delay damage mesomodel of laminates under dynamic loading: basic aspects and identification issues. *Computers and Structures*, 81:1177–1191.

[10] Allix, O., Ladevèze, P., and Corigliano, A. (1995). Damage analysis of interlaminar

fracture specimens. *Composite Structures*, 31:61–74.

[11] ASTM–D5528–01 (2001). *Standard Test Method for Mode-I Interlaminar Fracture Toughness of Unidirectinal Fiber-Reinforced Polymer Matrix Composites.* American Society for Testing of Materials.

[12] ASTM–D6671–06 (2006). *Standard Test Method for Mixed Mode I-Mode II Interlaminar Fracture Toughness of Unidirectional Fiber Reinforced Polymer Matrix Composites.* American Society for Testing of Materials.

[13] Bailly, P., Delvare, F., and Richomme, S. (2007). Essai dynamique de rupture en flexion de matériaux quasi-fragiles obtenue à l'aide d'un dispositif de barres de Hopkinson. 18$^{\text{ème}}$ Congrès Français de Mécanique.

[14] Banks-Sills, L., Boniface, V., and Eliasi, R. (2005). Development of a methodology for determination of interface fracture toughness of laminate composites – the 0°/90° pair. *International Journal of Solids and Structures*, 42:663–680.

[15] Banks-Sills, L., Freed, Y., Eliasi, R., and Fourman, V. (2006). Fracture toughness of the $+45°/-45°$ interface of a laminate composite. *International Journal of Fracture*, 141:195–210.

[16] Barenblatt, G. I. (1962). Mathematical theory of equilibrium cracks in brittle failure. *Advances in Applied Mechanics*, 7:55–129.

[17] Barre, S., Chotard, T., and Benzeggagh, M. L. (1996). Comparative study of strain rate effects on mechanical properties of glass fibre reinforced thermoset matrix composites. *Composites Part A*, 27A:1169–1181.

[18] Bayandor, J., Thomson, R. S., and Scott, M. L. (2004a). An investigation into an advanced composite finte elemetn explicit Bihpase model: Part I - Elastic Parameters. *Journal of Composite Materials*, 38(23):2119–2132.

[19] Bayandor, J., Thomson, R. S., and Scott, M. L. (2004b). An investigation into an advanced composite finte elemetn explicit Bihpase model: Part II - Damage Parameters. *Journal of Composite Materials*, 38(23):2133–2142.

[20] Benzeggagh, M. L. and Kenane, M. (1996). Measurement of mixed-mode delamination fracture toughness of unidirectional glass/epoxy composites with mixed-mode bending apparatus. *Composites Science and Technology*, 86:439–449.

[21] Bonini, J. (1995). *Contribution à la prédiction numérique de l'endommagement de stratifiés composites sous impact basse vitesse.* PhD thesis, ENSAM, Bordeaux.

[22] Borg, R., Nilsson, L., and Simonsson, K. (2001). Simulation of delamination in fiber composites with a discrete cohesive failure model. *Composites Science and Technology*, 61:667–677.

[23] Borg, R., Nilsson, L., and Simonsson, K. (2002). Modeling of delamination using a discretized cohesive zone and damage formulation. *Composites Science and Technology*, 62:1299–12314.

[24] Borg, R., Nilsson, L., and Simonsson, K. (2004a). Simulating DCB, ENF and MMB experiments using shell elements and a cohesive zone model. *Composites Science and*

Technology, 64:269–278.

[25] Borg, R., Nilsson, L., and Simonsson, K. (2004b). Simulation of low velocity impact on fiber laminates using a cohesive zone based delamination model. *Composites Science and Technology*, 64:279–288.

[26] Bouette, B., Cazeneuve, C., and Oytana, C. (1992). Effect of strain rate on interlaminar shear properties of carbon/epoxy composites. *Composites Science and Technology*, pages 313–321.

[27] Bouvet, C., Castanié, B., Bizeul, M., and Barrau, J.-J. (2009). Low velocity impact modelling in laminate composite panels with discrete interface elements. *International Journal of Solids and Structures*, 46:2809–2821.

[28] Brewer, J. C. and Lagace, P. A. (1988). Quadratic stress criterion for initiation of delamination. *Journal of Composite Materials*, 22:1141–1155.

[29] Briche, F. (2009). Etude du comportement mécanique de matériaux composites stratifiés sous impact basse vitesse - Application au fuselage de l'A350. Master's thesis, Ecole des Mines.

[30] Camacho, G. T. and Ortiz, M. (1996). Computational modeling of impact damage in brittle materials. *International Journal of Solids and Structures*, 33:2899–2938.

[31] Camanho, P. P. and Dávila, C. G. (2002). Mixed-mode decohesion finite elements for the simulation of delamination in composite materials. TM-2002-211737, NASA Langley Research Center.

[32] Camanho, P. P., Dávila, C. G., and Ambur, D. R. (2001). Numerical simulation of delamination growth in composite materials. TP-2001-211041, NASA Langley Research Center.

[33] Camanho, P. P., Dávila, C. G., and De Moura, M. F. (2003). Numerical simulation of mixed-mode progressive delamination in composite materials. *Journal of Composite Materials*, 37:1415–1438.

[34] Camanho, P. P. and Matthews, F. L. (1999). Delamination onset prediction in mechanically fastened joints in composite laminates. *Journal of Composite Materials*, 33(10):906–927.

[35] Cantwell, W. J. and Morton, J. (1991). Impact response of composites - A review. *Composites*, 22:347–362.

[36] Carlsson, L. A., Gillespie, Jr, J. W., and Pipes, R. B. (1986). On the analysis and design of the end notched flexure (ENF) specimen for Mode II testing. *Journal of Composite Materials*, 20:594–604.

[37] Chang, F.-K. and Chang, K.-Y. (1987). A progressive damage model for laminated composites containing stress concentrations. *Journal of Composite Materials*, 21:834–855.

[38] Chen, J. K. and Medina, D. F. (1998). The effect of projectile shape on laminated composite perforation. *Composites Science and Technology*, 58:1629–1639.

[39] Choi, H. Y. and Chang, F.-K. (1992). A model for predicting damage in

graphite/epoxy laminated composites resulting from low-velocity point impact. *Journal of Composite Materials*, 26(14):2134–2169.

[40] Chree, C. (1889). The equations of an isotropic solid in polar and cylindrical coordinates, their solutions and applications. *Trans. Cambridge Philos. Soc.*, 14:250–369.

[41] Coutellier, D. and Rozycki, P. (2000). Multi-layered multi-material finite element for crashworthiness studies. *Composites: Part A*, 31:841–851.

[42] Crews, Jr, J. H. and Reeder, J. R. (1988). A mixed-mode bending apparatus for delamination testing. TM-1988-100662, NASA Langley Research Center.

[43] Crisfield, M. A., Jelenic, G., Mi, Y., Zhong, H. G., and Fan, Z. (1997). Some aspects of the non-linear finite element method. *Finite Elements in Analysis and Design*, 27:19–40.

[44] CS-25 (2007). *Certification Specifications for Large Aeroplanes.* EASA.

[45] DAVID (2009). *David Instruction Manual.* Laboratoire de Mécanique des Solides, Ecole Polytechnique 91128 Palaiseau Cedex.

[46] Davies, P., Blackman, B. R. K., and Brunner, A. J. (1998). Standard test methods for delamiantion resistance of composite materials: Current status. *Applied Composite Materials*, 5:345–364.

[47] Davies, P., Blackman, B. R. K., and Brunner, A. J. (2001). Mode II delamination. In Moore, D. R., Pavan, A., and Williams, J. G., editors, *Fracture mechanics testing methods for polymers, adhesives, and composites*, chapter 4 - Delamination Fracture Mechanics, pages 307–337. Elsevier Science Ltd and ESIS.

[48] Davila, C. G. and Camanho, P. P. (2003). Failure criteria for FRP laminates in plane stress. TM-2003-212663, NASA Langley Research Center.

[49] De Florio, F. (2006). *Airworthiness An Introduction to Aircraft Certification.* Butterworth-Heinemann, 1st edition.

[50] De Moura, M. F. S. F., Gonçalves, J. P. M., Marques, A. T., and De Castro, P. M. S. T. (1997). Modeling compression failure after low velocity impact on laminated composites using interface elements. *Journal of Composite Materials*, 31(15):1462–1479.

[51] De Moura, M. F. S. F., Gonçalves, J. P. M., Marques, A. T., and De Castro, P. M. S. T. (2000). Prediction of compressive strength of carbon-epoxy laminates containing delamination by using a mixed-mode damage model. *Composite Structures*, 50:151–157.

[52] Dong, S., Wang, Y., and Xia, Y. (2006). Test method: A finite element analysis for using Brazilian disk in split Hopkinson pressure bar to investigate dynamic fracture behavior of brittle polymer materials. *Polymer Testing*, 25:943–952.

[53] Dugdale, D. S. (1960). Yielding of steel sheets containing slits. *Journal of Mechanics and Physics of Solids*, 8:100–104.

[54] Elder, D. J., Thomson, R. S., Nguyen, M. Q., and Scott, M. L. (2004). Review of delamination predictive methods for low speed impact of composite laminates. *Composite Structures*, 66:677–683.

[55] Eshelby, J. D. (1961). Elastic inclusions and inhomogeneities. In Sneddon, I. N.

and Hill, R., editors, *Progress in solid mechanics*, pages 89–140. Amsterdam: North-Holland.

[56] Eskandari, H. and Nemes, J. A. (2000). Dynamic testing of composite laminates with a tensile Split Hopkinson Bar. *Journal of Composite Materials*, 34(4):260–273.

[57] Espinosa, C. and Collombet, F. (1991). Impact de plaques composites : caractérisation et modèles. *Journal de Physique III*, pages 1953–1968.

[58] Farley, G. L. and Jones, R. M. (1992). Prediction of the energy-absoprtion capability of composite tubes. *Journal of Composite Materials*, 26:388–404.

[59] Fonta, P. (2009). The airbus approach to Eco-efficiency.

[60] Gama, B. A. and Gillespie Jr, J. W. (2008). Punch shear based penetration model of ballistic impact of thick-section composites. *Composite Structures*, 86:356–369.

[61] Gama, B. A., Lopatnikov, S. L., and Gillespie, Jr, J. W. (2004). Hopkinson bar experimetal technique: A critical review. *Appllied Mechanics Reviews*, 57(4):223–250.

[62] Gay, D. (1997). *Matériaux composites*. Hermès, 4$^{\text{ème}}$ edition.

[63] Geubelle, P. H. and Baylor, J. S. (1998). Impact-induced delamination of composites: a 2D simulation. *Composites Part B*, 29B:589–602.

[64] Gilat, A., Goldberg, R. K., and Roberts, G. D. (2002). Experimental study of strain rate sensitivity of carbon/epoxy composite. *Composite Science and Technology*, 62:1469–1476.

[65] Gohorianu, G. (2008). *Influence des défauts de perçage sur la tenue en matage des stratifiés carbone/epoxy*. PhD thesis, Institut Supérieur de l'Aéronautique et de l'Espace, 1, Place Emile Blouin - 31056 TOULOUSE Cedex.

[66] Guan, Z. and Yang, C. (2002). Low-velocity impact and damage process of composite laminates. *Journal of Composite Materials*, 36(07):851–871.

[67] Guedes, R. M., De Moura, M. F. S. F., and Ferreira, F. J. (2008). Failure analysis of quasi-isotropic CFRP laminates under high strain rate compression loading. *Composite Structures*, 84:362–368.

[68] Hancox, N. L. (2000). *Impact Behavior of Fibre-reinforced Composite Materials and Structures*, chapter An overview of the impact behaviour of fibre-reinforced composites, pages 1–32. Woodhead Publishing.

[69] Haque, A. and Ali, M. (2005). High strain rate responses and failure analysis in polymer matrix composites - an experimental and finite element study. *Journal of Composite Materials*, 39(5):423–450.

[70] Harding, J. and Li, Y. L. (1992). Determination of interlaminar shear strength for glass/epoxy and carbon/epoxy laminates at impact retes of strain. *Composites Science and Technology*, 45:161–171.

[71] Hashin, Z. (1980). Failure criteria for unidirectional fiber composites. *Journal of Applied Mechanics*, 47:329–334.

[72] Holmquist, T. J., Johnson, G. R., and Cook, W. H. (1993). A computational con-

stitutive model for concrete subjected to large strains, High strain rates, and High pressures. In *The 14th International Symposium on Ballistics*, pages 591–600.

[73] Hosur, M. V., Alexander, J., Vaidya, U. K., and Jeelnai, S. (2001). High strain rate compression reponse of carbon/epoxy laminate composites. *Composite Structures*, 52:405–417.

[74] Hosur, M. V., Islam, S. M. W., Vaidya, U. K., Kumar, A., Dutta, P. K., and Jeelani, S. (2005). Dynamic punch shear characterization of plain weave graphite/epoxy composites at room and elevated temperatures. *Composite Structures*, 70:295–307.

[75] Hsiao, H. M. and Daniel, I. M. (1998). Strain rate behavior of composite materials. *Composites Part B*, 29:521–533.

[76] Hsiao, H. M., Daniel, I. M., and Cordes, R. D. (1999). Strain rate effects on the transverse compressive and shear behavior of unidirectional composites. *Journal of Composite Materials*, 33(17):1620–1642.

[77] Ilyas, M., Espinosa, C., Lachaud, F., Michel, L., and Salaün, M. (2010). Modelling aeronautical composite laminates behaviour under impact using a saturation damage and delamination continuous material model. In *9th International Conference on Fracture and Damage Mechanics*. Nagasaki, Japan.

[78] Ilyas, M., Espinosa, C., Lachaud, F., and Salaün, M. (2009a). Dynamic delamination modeling using cohesive finite elements. In *9th International Conference on the Mechanical and Physical Behaviour of Matrerials under Dynamic Loading*, pages 1567–1573. DYMAT2009, EDP Sciences.

[79] Ilyas, M., Espinosa, C., Lachaud, F., and Salaün, M. (2009b). Simulation of dynamic delamination and Mode I energy dissipation. In *7th European LS-DYNA Conference*. Dynamore.

[80] Ilyas, M., Lachaud, F., Espinosa, C., Michel, L., and Salaün, M. (2009c). Modélisation en dynamique rapide du délaminage des composites à l'aide d'éléments finis cohésifs. In *16ème Journées Nationale des Composites*. JNC-16.

[81] Ilyas, M., Lachaud, F., Espinosa, C., and Salaün, M. (2009d). Dynamic delamination of aeronautic structural composites by using cohesive finite elements. In *17th International Conference on Composite Materials*. ICCM-17, IOM3.

[82] Ilyas, M., Limido, J., Lachaud, F., Espinosa, C., and Salaün, M. (2009e). Modélisation SPH 3D de l'impact basse vitesse sur plaque composite. In *19ème Congrès Français de Mécanique*. CFM-19.

[83] ISO–15024 (2001). *Fiber-reinforced plastic composites - Determination of Mode I interlaminar fracture toughness, G_{IC}, for unidirectionally reinforced materails*. International Organization for Standardization.

[84] Jacquet, E. (2003). Etude numérique de l'endommagement induit par l'impact de débris sur des structures composites. Master's thesis, Ecole Nationale Supérieure d'Ingénieurs de Constructions Aéronautiques.

[85] Jadhav, A., Woldesenbet, E., and Pang, S.-S. (2003). High strain rate properties of balanced angle-ply graphite/epoxy composites. *Composites: Part B*, 34:339–346.

[86] Johnson, A. F., Pickett, A. K., and Rozycki, P. (2001). Computational methods for predicting impact damage in composite structures. *Composites Science and Technology*, 91:2183–2192.

[87] Kachanov, L. (1958). *On the Creep Fracture Time*, volume 8. Akad Nauk, USSR Otd.

[88] Kaiser, M. A. (1998). Advancements in the Split Hopkinson Bar Test. Master's thesis, Virginia Polytechnic Institute and State University, Blacksburg Virginia.

[89] Kongshavn, I. and Poursatrip, A. (1999). Experimental investigation of a strain softening approadh to predicting failure in notched fiber reinfoced composite laminates. *Composite Science and Technology*, 59(1):29–40.

[90] Kusaka, T. (2009). Experimental method for estimating dynamic fracture toughness of polymer matrix composite laminates. In *International Conference on Composite Materials ICCM-17*. IOM3.

[91] Kusaka, T., Hojo, M., Mai, Y.-W., Kurokawa, T., Nojima, T., and Ochiai, S. (1998). Rate dependence of Mode I fracture behaviour in carbon-fibre/epoxy composite laminates. *Composites Science and Technology*, 58:591–602.

[92] Lachaud, F. (1997). *Délaminage de matériaux composites à fibres de carbonne et à matrice organiques : étude numérique et expérimental, suivi par emission acoustique.* PhD thesis, Ecole Nationale Supérieur d'Ingénieurs de Constructions Aéronautique, 1, Place Emile Blouin - 31056 TOULOUSE Cedex.

[93] Lachaud, F. (2009). Introduction aux chocs mécaniques. Master's Course Work.

[94] Lacome, J.-L., Limido, J., and Espinosa, C. (2009). SPH formulation with lagrangian eulerian adaptive kernel. In *4^{th} SPHERIC Workshop*.

[95] Ladevèze, P. (1992). A damage computational method for composite structures. *Computers and Structures*, 44(1-2):79–87.

[96] Ladevèze, P. and Le Dantec, E. (1992). Damage modelling of the elmentary ply for lamintaed composites. *Composites Science and Technology*, 43:257–267.

[97] Lataillade, J. L., Delaet, M., Collombet, F., and Wolff, C. (1996). Effects of the intralaminar shear loading rate on the damage of multi-ply composites. *International Journal of Impact Engineering*, 18(6):679–699.

[98] Li, X., Hallett, S. R., and Wisnom, M. R. (2008). Predicting the effect of through-thickness compressive stress on delamination using interface elements. *Composites Part A*, 39:218–230.

[99] Li, Y. and Sridharan, S. (2005). Performance of two distinct cohesive layer models for tracking composite delamination. *International Journal of Fracture*, 136:99–131.

[100] Lifshitz, J. M. and Leber, H. (1998). Response of fiber-reinforced polymers to high strain-rate loading in interlaminar tension and combined tension/shear. *Composites Science and Technology*, 58:987–996.

[101] Limido, J. (2008). *Etude de l'effet d'usinage grande vitesse sur la tenue en fatigue de pièces aéronautique.* PhD thesis, Institut Supérieur de l'Aéronautique et de l'Espace,

1, Place Emile Blouin - 31056 TOULOUSE Cedex.

[102] Liu, C., Huang, Y., Lovato, M. L., and Stout, M. G. (1997). Measurement of the fracture toughness of a fiber reinforced composite using the Brazilian disk geometry. *International Journal of Fracture*, 87:241–263.

[103] Liu, D. (1988). Impact-induced delamination - A view of bending stiffness mismatching. *Journal of Composite Materials*, 22:647–692.

[104] Liu, G. R. and Liu, M. B. (2003). *Smoothed Particle Hydrodynamics – A Meshfree Particle Method*. World Scientific Publishing Co.

[105] López-Puente, J., Zaera, R., and Navarro, C. (2002). The effect of low temperatures on the intermediate and high velocity impact response of CFRPs. *Composites: Part B*, 33:559–566.

[106] LSTC (2006). *LS-Dyna Theory Manual*. Livermore Software Technology Corporation.

[107] LSTC (2007). *LS-Dyna Keyword Manual*. Livermore Software Technology Corporation.

[108] Lucy, L. B. (1977). A numerical approach to testing of the fission hypothesis. *Astronomical Journal*, 82:1013–1024.

[109] Maikuma, H., Gillespie, Jr, J. W., and Whitney, J. M. (1989). Analysis and experimental characterization of the center notch flexural test specimen for Mode ii interlaminar fracture. *Journal of Composite Materials*, 23:756–86.

[110] Maikuma, H., Gillespie, Jr, J. W., and Wilkins, D. J. (1990). Mode II interlaminar fracture of the center notch flexural specimen under impact loading. *Journal of Composite Materials*, 24:124–149.

[111] Matzenmiller, A., Lubliner, J., and Taylor, R. L. (1995). A constitutive model for anisotropic damage in fiber-composites. *Mechanics of Materials*, 20(2):125–152.

[112] Medina, D. F. and Chen, J. K. (2000). Three-dimensional simulations of impact induced damage in composite structures using the parallelized SPH method. *Composites: Part A*, 31:853–860.

[113] Mi, Y., Crisfield, M., and Davies, G. (1998). Progressive delamination using interface elements. *Journal of Composite Materials*, 32:1246–1272.

[114] Michel, Y. (2007). *Phenomene d'impact à haute vitesse sur cibles minces fragiles - Application au projet de laser megajoule et à la problematique des debris spatiaux*. PhD thesis, Université de Toulouse III - Paul Sabatier.

[115] Mitrevski, T., Marshall, I. H., and Thomson, R. (2006). The influence of impactor shape on the damage to composite laminates. *Composite Structures*, 76:116–122.

[116] Monaghan, J. J. (2002). SPH method without a tensile instability. *Journal of Computational Physics*, 159:290–311.

[117] Nemat-Nasser, S. (2000). Introduction to high strain rate testing. In *ASM Handbook*, volume 8. ASM International.

[118] Ninan, L., Tsai, J., and Sun, C. T. (2001). Use of split Hopkinson pressure bar for testing off-axis composites. *International Journal of Impact Engineering*, 25:291–313.

[119] Nwosu, S. N., Hui, D., and Dutta, P. K. (2003). Dynamic Mode II delamination fracture of unidirectional graphite/epoxy composites. *Composites: Part B*, 34:303–316.

[120] Ochoa, O. O. and Reddy, J. N. (1992). *Finite element analysis of composite laminates*. Kluwer Academic Publishers.

[121] Olsson, R. (2001). Analytical prediction of large mass impact damage in composite laminates. *Composites: Part A*, 32:1207–1215.

[122] Olsson, R. (2003). Closed form prediction of peak load and delamination onset under small mass impact. *Composite Structures*, 59:341–349.

[123] Orifici, A. C., Herszberg, I., and Thomson, R. S. (2008). Review of methodologies for composite material modelling incorporating failure. *Composite Structures*, 86:194–210.

[124] Papadakis, N., Reynolds, N., Pharaoh, M. W., Wood, P. K. C., and Smith, G. F. (2004). Strain rate effects on the shear mechanical properties of a highly oriented thermoplastic composite material using a contacting displacement measurement mehodology - Part B: shear damage evolution. *Composites Science and Technology*, 64:739–748.

[125] Pinho, S. T., Davila, C. G., Camanho, P. P., Iannucci, L., and Robinson, P. (2005). Failure models and criteria for FRP under in-plane or three dimensional stress states including shear non-linearity. TM-2005-213530, NASA Langley Rsearch Center.

[126] Pinho, S. T., Iannucci, L., and Robinson, P. (2006). Formulation and implementation of decohesion elements in an explicite finite element code. *Composites: Part A*, 37:778–789.

[127] Pochhammer, L. (1876). Über die fortplanzungsgeschwindigkeiten schwingungen in einemunbegrentzten isotropen kreiscylinder. *Journal für die reine angewandte Mathematik*, 81:324–336.

[128] Prombut, P. (2007). *Caracterisation de la propagation de delaminage des stratifiés composites multidirectionnels*. PhD thesis, Ecole Nationale Supérieur d'Ingénieurs de Constructions Aéronautique, 1, Place Emile Blouin - 31056 TOULOUSE Cedex.

[129] Rahmé, P. (2008). *Contribution à l'étude de l'effet des procédés Perçage - Alésage sur l'apparition du délaminage dans les structures composites épaisses*. PhD thesis.

[130] Ramirez, H. and Rubio-Gonzalez, C. (2006). Finite-element simulation of wave propagation and dispersion in Hopkinson bar test. *Materials and Design*, 27:36–44.

[131] Reedy, Jr, E. D., Mello, F. J., and Guess, T. R. (1997). Modeling the initiation and growth of delmainations in composite strucutres. *Journal of Composite Materials*, 31(8):812–831.

[132] Richarson, M. O. W. and Wisheart, M. J. (1996). Review of low-velocity impact properties of composite materials. *Composites: Part A*, 27:1123–1131.

[133] Rivallant, S. (2003). *Modélisation à l'impact de pales d'hélicoptères*. PhD thesis, l'École Nationale Supérieure de l'Aéronautique et de l'Espace.

[134] Rodriguez, V., Chocron, I. S., Martinez, M. A., and Sanchez-Galvez, V. (1996). High strain rate properties of aramid and polyethyelene woven fabric composites. *Composites: Part B*, 27B:147–154.

[135] Rouchon, J. (2006). Certification of aircraft composite structures. EUROSAE Formation Continue.

[136] Rozycki, P. (2000). *Contribution au développement de lois de comportement pour matériaux composites soumis à l'impact*. PhD thesis, University of Valenciennes.

[137] Sjöblom, P. O., Hartness, J. T., and Cordell, T. M. (1988). On low-velocity impact testing of composite materials. *Journal of Composite Materials*, 22(1):30–52.

[138] Smiley, A. J. and Pipes, R. B. (1987). Rate effects on Mode I interlaminar fracture toughness in composite materials. *Journal of Composite Materials*, 21:670–687.

[139] Song, B. and Chen, W. (2004). Loading and unloading split Hopkinson pressure bar pulse-shaping techniques for dynamic hysteretic loops. *Experimental Mechanics*, 44(6):622–627.

[140] Staab, G. H. and Gilat, A. (1995). High strain rate characterization of angle-ply glass/epoxy laminates. *Jounral of composite Materails*, 29(10):278–285.

[141] Sun, C. T. and Han, C. (2004). A method for testing interlaminar dynamic fracture toughness of polymeric composites. *Composites: Part B*, 35:647–655.

[142] Talreja, R. (1985). Transverse cracking and stiffness reduction in composite laminates. *Journal of Composite Materials*, 19:355–375.

[143] Taniguchi, N., Nishiwaki, T., and Kawada, H. (2007). Tensile strength of unidirectional CFRP laminate under high strain rate. *Advanced Composite Materials*, 16(2):167–180.

[144] Tasdemirci, A. and Hall, I. W. (2006). Numerical and experimental studies of damage generation in a polymer composite material at high strain rates. *Polymer Testing*, 25:797–806.

[145] Tay, T. E. (2001). Characterization and analysis of delamination fracture in composites: An overview of developments from 1990 to 2001. *Applied Mechanics Reviews*, 56(1):1–32.

[146] Tennyson, R. C. and Lamontagne, C. (2000). Hypervelocity impact damage to composites. *Composites: Part A*, 31:785–794.

[147] Todo, M., Nakamura, T., and Takahashi, K. (1999). Mode II interlaminar fracture behavior of fiber reinforced polyamide composites under static and dynamic loading conditions. *Journal of Reinforced Plastics and Composites*, 18:1415–1427.

[148] Tsai, J. and Sun, C. T. (2002). Constitutive model for high strain rate response of polymeric composites. *Composites Science and Technology*, 62:1289–1297.

[149] Tsai, J. and Sun, C. T. (2004). Dynamic compressive strengths of polymeric composites. *International Journal of Solids and Structures*, 41:3211–3224.

[150] Tsai, J.-L. and Sun, C. T. (2005). Strain rate effect on in-plane shear strength of unidirectional polymeric composites. *Composites Science and Technology*, 65:1941–

1947.

[151] Tsai, S. W. and Wu, E. M. (1971). A general theory of strength for anisotropic materials. *Journal of Composite Materials*, 5:58–80.

[152] Villaverde, N. B. (2004). *Variable mix-mode delamination in composite laminate under fatigue conditions: Testing and Analysis*. PhD thesis, University of Girona.

[153] Vinson, J. R. and Woldesenbet, E. (2001). Fiber orientation effects on high strain rate properties of graphite/epoxy composites. *Journal of Composite Materials*, 35(6):509–521.

[154] Werner, S. M. and Dharan, C. K. H. (1986). The dynamic response of graphite fiber-epoxy laminates at high shear strain rates. *Journal of Composite Materials*, 20:365–374.

[155] Whitney, J. D. (1984). Analysis of instability-related growth of a through-width delamination. TM-86301, NASA.

[156] Williams, K. V. and Vaziri, R. (2001). Application of a damage mechanics model for predicting the impact response of composite materials. *Computers and Structures*, 79:997–1011.

[157] Wisnom, M. R. (1996). Modelling the effect of cracks on interlaminar shear strength. *Composites: Part A*, 27:17–24.

[158] Wosu, S. N., Hui, D., and Dutta, P. K. (2005). Dynamic mixed-mode I/II delamination fracture and energy release rate of unidirectional graphite/epoxy composites. *Engineering Fracture Mechanics*, 72:1531–1558.

[159] Wu, X.-F. and Dzenis, Y. A. (2005). Determination of dynamic delamination tougness of a graphite-fibre/epoxy composite using hopinson pressure bar. *Polymer Composites*, pages 165–180.

[160] Xiao, J. R., Gama, B. A., and Gillespie Jr, J. W. (2007). Progressive damage and delamination in plain weave S-2 glass/SC-15 composites under quasi-static punch-shear loading. *Composite Structures*, 78:182–196.

[161] Yokoyama, T. and Nakai, K. (2006). Evaluation of interlaminar shear strength of a unidirectional carbon/epoxy laminated composite under impact loading. *Jounal de Physique IV*, 134:797–804.

[162] Zagainov, G. I. and Lozino-Lozinski, G. E. (1996). *Composite materials in aerospace design*. Soviet Advanced Composite Technologies Series. Chappman & Hall.

[163] Zhang, Y., Zhu, P., and Lai, X. (2006). Finite element analysis of low-velocity impact damage in composite laminated plates. *Materials and Design*, 27:513–519.

[164] Zienkiewicz, O. C., Taylor, R. L., and Zhu, Z. J. (2005). *The Finite Element Method Its Basis and Fundamentals*, volume 1. Butterworth-Heinmann, 6th edition.

Appendices

A

Material Fabrication, Mechanical Tests.

In this appendix we present the material fabrication procedure followed for composite plate manufacturing followed by the material characterization curves for mechanical parameter identification.

A.1 Laminate Fabrication

The material fabrication was divided into mainly 10 steps which are presented as follows:

Phase 10: Preparation

Material to be prepared:

- Pre-impregnated roller carbon/epoxy (reference UD/M21/35%/268/T800S/300 ply breadth 300 mm with one protected face) taken out of freezer at least 12 hours in advance and suspended in its packing in clean room at ambient temperature
- Cutting table for composite materials
- Compaction table
- Roll support
- Cutting template (300×240 mm^2) made of aluminum alloy
- Metallic square
- Cutter
- Adhesive tape
- Template to help in lay-up/stacking (metallic square to fix the borders of reference during stacking of plies)

- Metallic roller
- Scissors
- White pencil
- Indelible white marker
- Ruler
- Silicon frame 1453D (300 × 240 mm^2 inside)
- Teflon–glass sheet (protection for press plates)
- Flexible polyamide film CAPRAN 518
- Drainage polyester sheet
- Perforated separating film
- Unperforated separating film
- Peeling cloth
- High temperature pressure press with programmable curing cycle
- Garbage can

Figure defining carbon/epoxy plate:

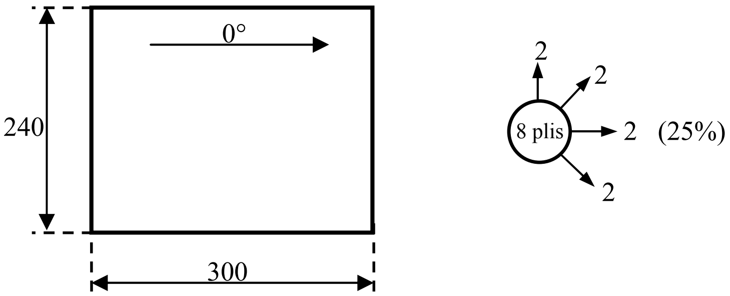

Figure A.1: Definition of an eight ply laminate.

List of stacking/lay-up sequence:

Table A.1: Stacking/Lay-up list.

Plate T800S/M21	
Number of ply	Direction
1	90°
2	45°
3	0°
4	−45°
5	−45°
6	0°
7	45°
8	90°

Phase 20: Cutting of pre-impregnated T800S/M21

- Cover the cutting table with a non perforated separable film which will be changed from time to time
- Take out roll from the packing and place in support in such manner that the unprotected face of the pre-impregnated ply is oriented towards bottom as we unroll the ply, FigureA.2

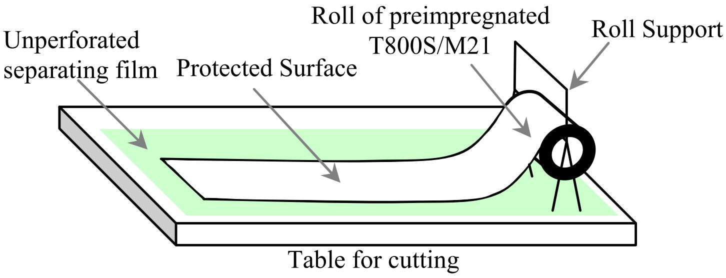

Figure A.2: Preparation for cutting of pre-impregnated plies.

- Place the cutting template (300 × 240 mm^2) according to the desired angle of ply and use the cutter to cut (Figure A.3)
- For the oriented at 45°, when the surface to be cut is not sufficient, ad a band of pre-impregnated ply and join by using the adhesive tape and without superposing the two bans of pre-impregnated ply (Figure A.4)
- Place the template opposite to square.
- Cut the ply with the help of cutter (pay attention to the slipping of template over the protected surface of pre-impregnated ply)
- Remove the template and square

- With the white indelible marker note on the protected face
    - ◇ Number of ply
    - ◇ Orientation
    - ◇ Fibers direction
    - ◇ local and global reference frames
- Remove the cut ply
- Validate the cutting paper
- Put the scrap in garbage can

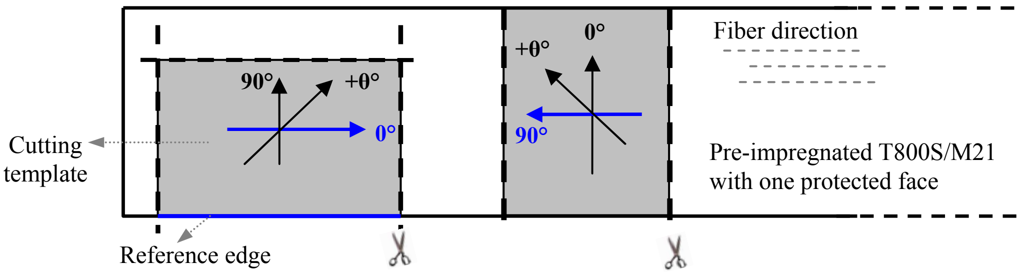

Figure A.3: Cutting of plies at 0 and 90.

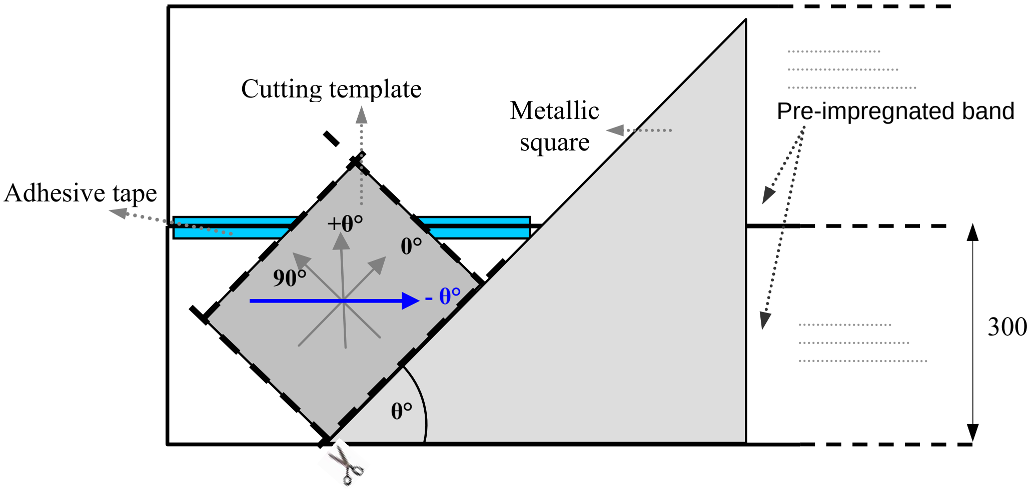

Figure A.4: Cutting of plies at 45.

Phase 30: Stacking/Compaction

- Place a unperforated separating film of 500 × 450 mm^2 (approximate dimensions) on a compaction table
- Position the for stacking
- Conforming to the stacking list:

  - ◇ Place the first ply on protection, unprotected side facing downwards and taking support against the stacking square, Figure A.5.
  - ◇ Remove the upper protection
  - ◇ Put the protection in garbage can
  - ◇ Validate the stacking list
  - ◇ Proceed in the same manner for the remaining plies

- Ensure the compaction of plies with metallic roller (before removing the protection!)

Remark: If the plate comprises of successive plies at $\pm\theta°$, orient them in a fashion that the joined zones do are not situated at same location, Figure A.5, to avoid creation of a weak zone.

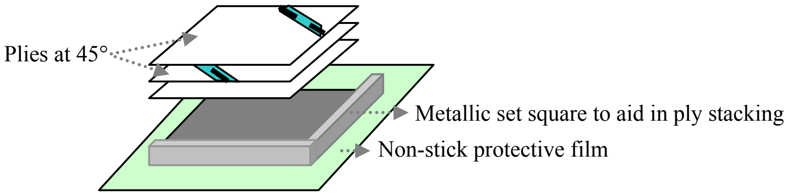

Figure A.5: Stacking/lay-up of plies.

- Conforming with the lay-up list compact the plies after stacking every 4 or 5 plies, Figure A.6, to save pre-impregnated from dust leave the protections on.

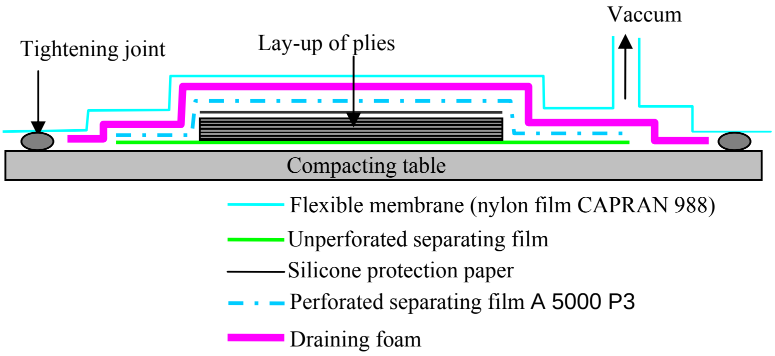

Figure A.6: Compaction of plies.

Phase 40: Press preparation

- Verify the cleanliness of heating press plates
- Place the Teflon–glass film on lower plate

Phase 50: Pressing

- Cut the following products

  - ◇ 2 peeling clothes 350 × 250 mm^2 (ref. B.44444)
  - ◇ 1 perforated separating film 350 × 250 mm^2 (ref. A.5000P3)
  - ◇ 1 absorbing ply 300 × 200 mm^2 (glass cloth satin S5 300 g/m^2)
  - ◇ 2 unperforated separating film 500 × 450 mm^2 (ref. A.5000RNP)

- Place the unperforated separating film (ref. A.5000RNP) on the Teflon–glass already placed on the lower plate of press

- Place in the center of unperforated film a peeling cloth

- Place the stacked plies over the peeling cloth

- Put in place the silicon frame, protecting from the scrap of the peeling cloth, around the stacked plies. The thickness of the silicon frame should be less or equal to the theoretical thickness of plate to be polymerized, Figure A.7.

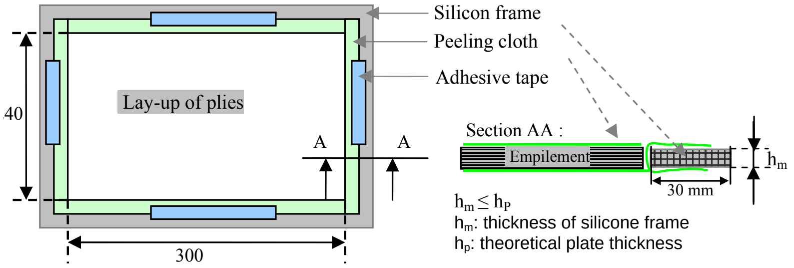

Figure A.7: Placement in silicon frame.

- Place in order (on the stacked plies), Figure A.8:
  - ◇ the second peeling cloth
  - ◇ the perforated separating film
  - ◇ the absorbing film
  - ◇ the second unperforated film
  - ◇ the second Teflon–glass film

- Verify that all the components of mold are in place

- Close the heating plates of press

Phase 60: Polymerization

Machine: Press SATIM with programmable curing cycle

- Introduce the following data:
  - ◇ the surface area of plate and pressure to be applied

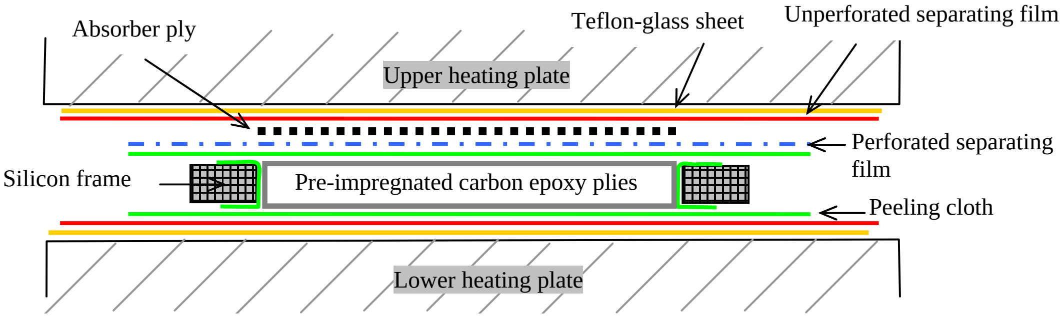

Figure A.8: Plate preparation in the high temperature, high pressure press.

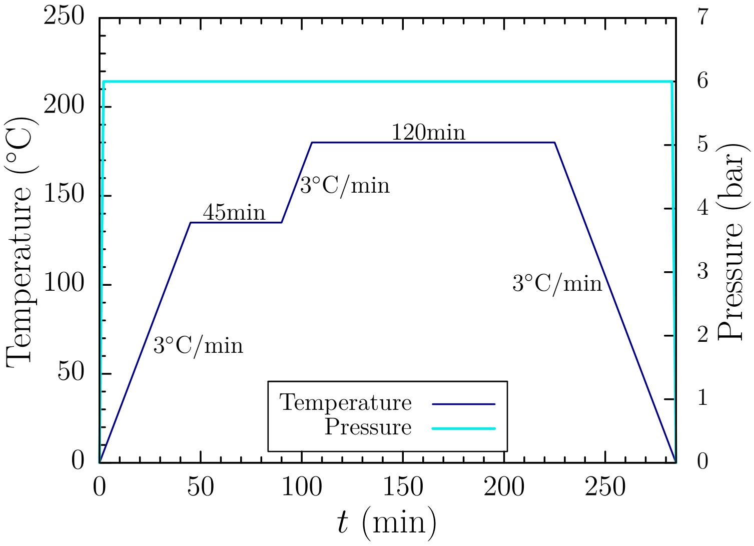

Figure A.9: Temperature and pressure cycle used for plate preparation.

  - ◇ the polymerization cycle, Figure A.9
- Verify whether all the data has been entered properly

Phase 70: Check polymerization

- Verify during the polymerization that the measured temperatures are same as applied ones
- Check for any defects and alarms

Phase 80: Removal from mold

- Take out the plate from the press with the mold, remove the following products
  - ◇ the Teflon–glass film
  - ◇ the unperforated separating film
  - ◇ the absorbing ply

  - ◇ the perforated separating film
  - ◇ the silicon frame

- Keep the peeling cloths which will protect the plate from eventual dust

- Conserve the silicon frame and Teflon–glass films, throw away the other products in garbage can

Phase 90: Marking

- Define the plate reference plane

- With a white indelible marker note:
  - ◇ the direction 0°
  - ◇ the stacking sequence

Phase 100: Check the plate

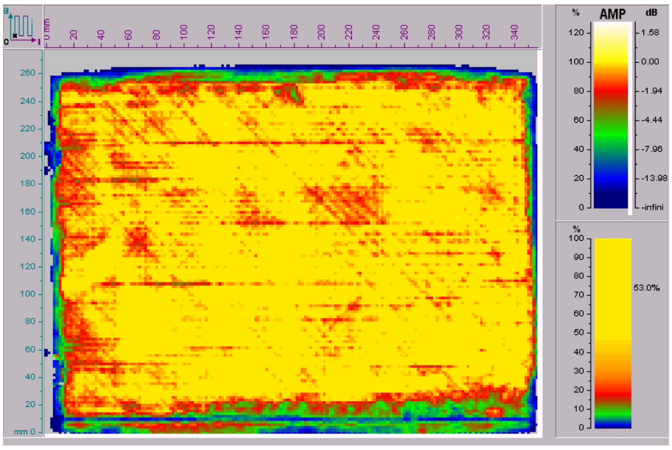

Figure A.10: Typical A-Scan of a plate for impact test specimen.

- Do non destructive (ultrasonic scan) tests to verify the uniform thickness of plate and excess of matrix at different locations. Ultrasonic image for a typical properly fabricated plate, surface area 340 × 200 mm^2, is shown in Figure A.10.

A.2 Mechanical Characterization

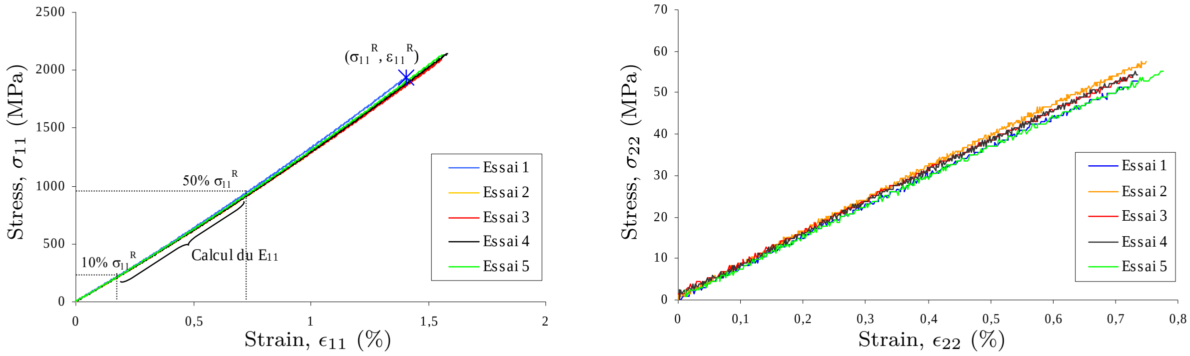

(a) Tensile test along fiber direction.

(b) Tensile test in transverse direction.

Figure A.11: Tensile testing of T700S/M21, curves from Gohorianu [65].

Table A.2: Results of tensile tests on T700S/M21 specimen, $[0°]_4$, [65].

Test	Young's Modulus	Failure stress	Failure strain
	E_{11} (MPa)	σ_{11}^r (MPa)	ϵ_{11}^r (%)
1	131499	1936	1.41
2	128536	2080	1.55
3	131936	2094	1.56
4	129261	2146	1.58
5	130391	2135	1.56
Average	130324	2078	1.58
Std. Dev.	1289	75	0.06

Table A.3: Results of tensile tests on T700S/M21 specimen, $[90°]_8$, [65].

Test	Young's Modulus	Failure stress	Failure strain
	E_{22} (MPa)	σ_{22}^r (MPa)	ϵ_{22}^r (%)
1	7509	53	0.736
2	7825	58	0.749
3	7644	54	0.728
4	7977	55	0.736
5	7493	55	0.777
Average	7689	55	0.745
Std. Dev.	186	1.6	0.018

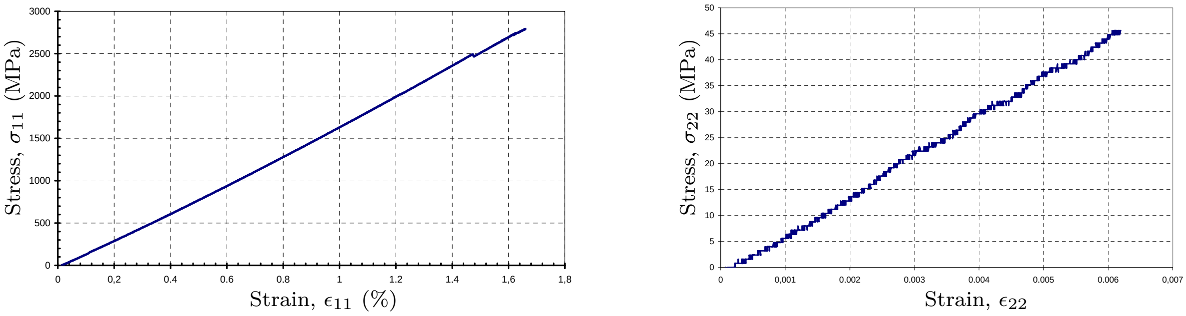

(a) Tensile test along fiber direction.

(b) Tensile test in transverse direction.

Figure A.12: Tensile testing of T800S/M21, curves from Rahmé [129].

Table A.4: Results of tensile tests on T800S/M21 specimen, $[0^\circ]_4$, [129].

Test	Young's Modulus E_{11} (MPa)	Failure stress σ_{11}^r (MPa)	Failure strain ϵ_{11}^r (%)
1	160957	2787	1.657
2	158073	2832	1.651
3	162856	2581	1.357
4	164756	2655	1.566
5	154178	2632	1.537
Average	160164	2698	$1,557$
Std. Dev.	4158	107	0.114

Table A.5: Results of tensile tests on T800S/M21 specimen, $[90^\circ]_8$, [129].

Test	Young's Modulus E_{22} (MPa)	Failure stress σ_{22}^r (MPa)	Failure strain ϵ_{22}^r (%)
1	7125	48	0.644
2	7687	50	0.578
3	8261	45	0.630
4	8292	48	0.585
Average	7841	48	0.6
Std. Dev.	552	2	0.03

$\mathcal{B}$

$\mathcal{G}_{Ic}$ and $\mathcal{G}_{IIc}$ for T800S/M21

In the appendix, we present the strain energy release rates in mode I and Mode II for T800S/21. The results presented here are based on the quasi-static tests.

B.1 DCB tests

The quasi-static DCB tests were carried out according to ISO–15024 [83] standard. A traveling microscope and KRAK GAGES from RUMUL© were used to follow the crack propagation (as shown in Figure 2.26). These crack gages are measure the variation in voltage when a crack propagates through them. A few recorded signals for these gages are shown in Figure B.1(a). The crack length a as a function of load point opening displacement δ is shown. The crack gage signals show an coherent response for $5-15$ mm. The fluctuations observed after that can be attributed to the extensive bending of the gages.

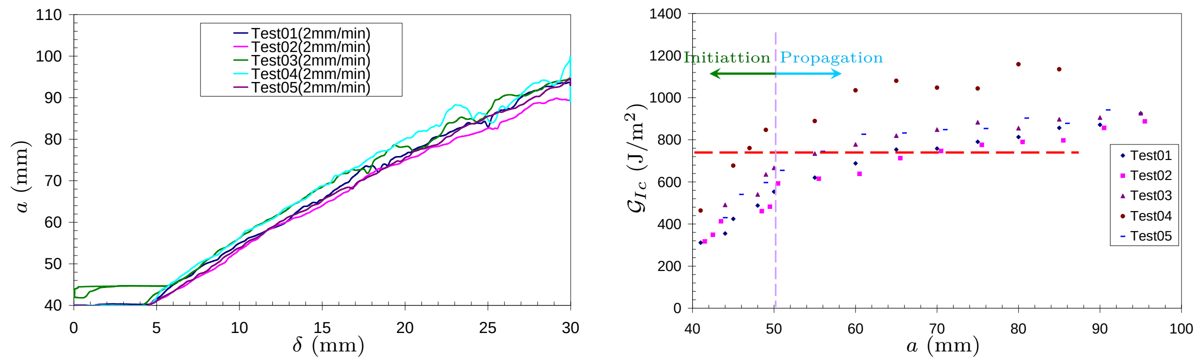

(a) (b)

Figure B.1: DCB test curve (a) crack length versus opening displacement (b) Critical Strain energy release rate versus opening displacement.

An R-curve ($\mathcal{G}_{Ic}$ as a function of a) for a DCB test is shown in Figure B.1(b). The test number 4 exhibits a considerable deviation from the otherwise less dispersive tests. For T800S/M21, one can consider that $a = 40 - 50$ mm gives the initiation and $a > 50$ mm gives the propagation values of $\mathcal{G}_{Ic}$. The dashed line in red color corresponds to $\mathcal{G}_{Ic} = 765$ J/m^2, the value used for numerical simulation of DCB and impact simulations of T800S/M21.

B.2 ELS tests

The ELS tests were carried out on a screw driven tension-compression machine. The crack gages cannot be employed for ELS specimen. These gages are best suited for an opening mode crack propagation, in case of a sliding crack propagation the closing contact of gage to itself gives the false readings. A typical $F - \delta$ curve for ELS specimen is shown in Figure B.2(a). The pink dots are the points corresponding to the $\mathcal{G}_{IIc}$ calculation.

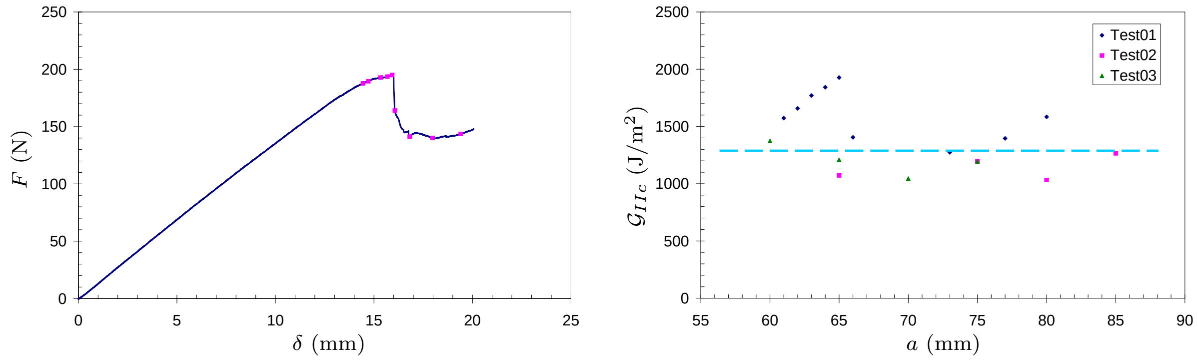

(a)

(b)

Figure B.2: ELS tests curve (a) Force versus specimen end displacement (b) Critical strain energy release rate $\mathcal{G}_{IIc}$ versus end displacement.

The R-curve for ELS tests is shown in Figure B.2(b). The dashed line in blue color shows the $\mathcal{G}_{IIc}$ value of 1250 J/m^2 used for numerical simulations of impact problems.

C

Impact Tests

The stacking sequences for numerical simulations are shown in Figures C.1 and C.2. Location of the cohesive finite element layers is also shown in these figures. Cohesive elements were only place between layers of the different orientations. In the case of T700S/M21 the individual ply thickness is 0.125 mm, but for simulations we have chosen a ply thickness of 0.25 mm (twice the ply thickness) in order to reduce the number of finite elements and CPU time.

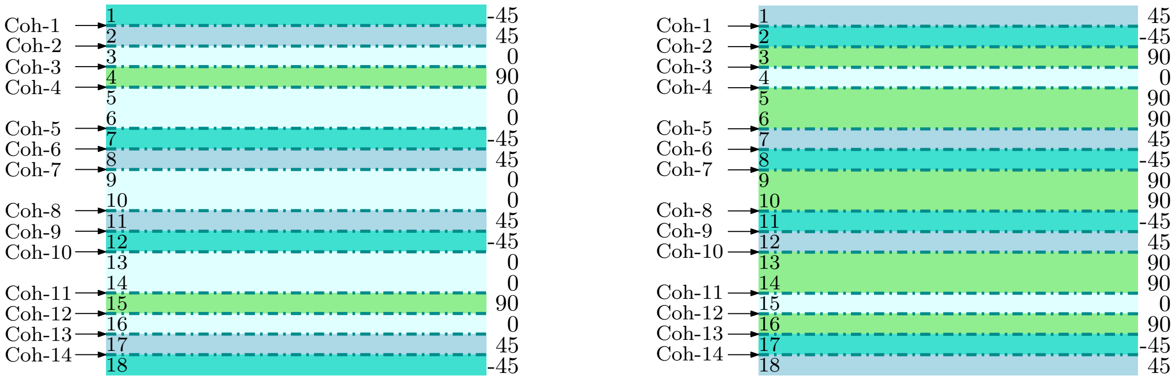

(a) 18 Ply laminate-1 (b) 18 Ply laminate-2

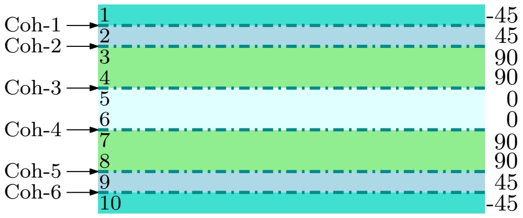

(c) 10 Ply laminate

Figure C.1: Stacking sequences of T800S/M21 impact specimen.

The impact tests carried out during this study are presnted in Table C.1. The absorbed energy (E_{abs}) is the difference of impact energy (E_{imp}) and rebound energy. This

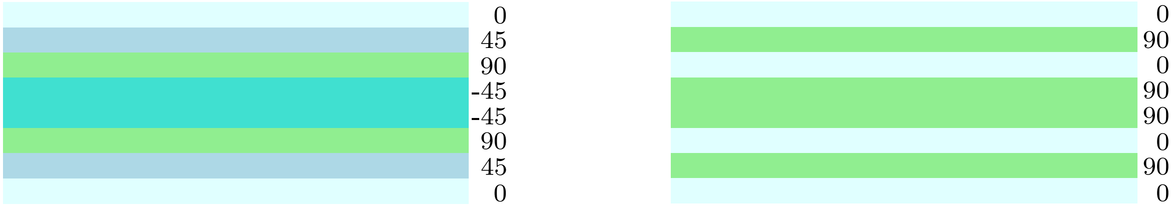

(a) Quasi-isotropic stacking sequence.

(b) Balanced ply sequence.

Figure C.2: Stacking sequences of T700S/M21 impact specimen.

measurement was only reliably available for the cases of canon impact tests where impact energy is measure by high speed camera.

Table C.1: Impact experiments on T700S/M21 and T800S/M21 specimen.

Plate Material	Lay-up Sequence	E_{imp} (J)	v (m/sec)	M (kg)	E_{abs} (J)
T700/M21	$[0_2, 45_2, 90_2, -45_2]_s$	3.87	2.527	1.213	xx
T700/M21	$[0_2, 45_2, 90_2, -45_2]_s$	8.17	3.671	1.213	xx
T700/M21	$[0_2, 90_2, 0_2, 90_2]_s$	4.25	2.647	1.213	xx
T700/M21	$[0_2, 90_2, 0_2, 90_2]_s$	9.37	3.931	1.213	xx
T800/M21	$[-45, 45, 90, 90, 0]_s$	10.34	2.955	2.368	xx
T800/M21	$[-45, 45, 90, 90, 0]_s$	19.88	4.098	2.368	xx
T800/M21	$[45, -45, 90, 0, 90, 90, 45, -45, 90]_s$	10.23	2.94	2.368	xx
T800/M21	$[45, -45, 90, 0, 90, 90, 45, -45, 90]_s$	19.90	4.10	2.368	xx
T800/M21	$[-45, 45, 0, 90, 0, 0, -45, 45, 0]_s$	9.62	2.850	2.368	xx
T800/M21	$[-45, 45, 0, 90, 0, 0, -45, 45, 0]_s$	14.25	3.470	2.368	xx
T800/M21	$[-45, 45, 0, 90, 0, 0, -45, 45, 0]_s$	20.63	4.175	2.368	xx
T800/M21	$[-45, 45, 0, 90, 0, 0, -45, 45, 0]_s$	21.11	4.223	2.368	xx
T800/M21	$[-45, 45, 0, 90, 0, 0, -45, 45, 0]_s$	20.80	4.191	2.368	xx
T800/M21	$[-45, 45, 0, 90, 0, 0, -45, 45, 0]_s$	20.67	4.178	2.368	xx

T800/M21	$[-45, 45, 0, 90, 0, 0, -45, 45, 0]_s$	20.88	4.200	2.368	xx
T800/M21	$[-45, 45, 0, 90, 0, 0, -45, 45, 0]_s$	20.69	4.181	2.368	xx
T800/M21	$[-45, 45, 0, 90, 0, 0, -45, 45, 0]_s$	29.55	4.996	2.368	xx
T800/M21	$[-45, 45, 0, 90, 0, 0, -45, 45, 0]_s$	32++	xx	2.368	xx
T800/M21	$[-45, 45, 0, 90, 0, 0, -45, 45, 0]_s$	14.16	40.816	0.017	8.57
T800/M21	$[-45, 45, 0, 90, 0, 0, -45, 45, 0]_s$	20.00	50.000	0.016	12.43
T800/M21	$[-45, 45, 0, 90, 0, 0, -45, 45, 0]_s$	27.68	58.824	0.016	17.72
T800/M21	$[-45, 45, 0, 90, 0, 0, -45, 45, 0]_s$	29.41	58.824	0.017	18.82
T800/M21	$[-45, 45, 0, 90, 0, 0, -45, 45, 0]_s$	39.51	68.182	0.017	26.94
T800/M21	$[-45, 45, 0, 90, 0, 0, -45, 45, 0]_s$	100	108.77[1]	0.019	xx

---

[1] Value used for simulation

D

Mathematical Formulation of SPH method

This appendix presents the basic mathematical principles of SPH method, different formulations which can be used and some particular characteristics of the method such as sphere of influence and pseudo viscosity.

The SPH method is based on three essential steps which will be presented in following paragraphs:

- The representation of a function by its integral with the definition of “kernel approximation”
- The particle approximation by passing from integral form to a discrete sum of contributions of particles present in domain of influence
- The application of formulation to conservation equations for desired application

Representation of a function by its integral

The concept of representation of a function by its integral utilized in SPH is based on the equality in Equation D.1 where f is definite and continuous over Ω

$$f(x) = \int_{\Omega} f(x')\delta(x - x')dx' \tag{D.1}$$

where f is a function of position vector x and $\delta(x - x')$ the Dirac function is defined as follows:

$$\delta(x-x') = \begin{cases} 1 & x = x' \\ \\ 0 & x \neq x' \end{cases} \tag{D.2}$$

By replacing the Dirac function δ by an interpolation $W(x-x',h)$, we obtain the interpolation integral of function $f(x)$ over Ω denoted as $\langle f(x) \rangle$ and written as:

$$\langle f(x) \rangle = \int f(x') W(x-x',h) \cdot \mathrm{d}x' \tag{D.3}$$

where W is to be verified over Ω the unity condition, Equation D.4, the convergence towards the Dirac where as the smoothing length h tends towards 0, Equation D.5, and the support has to be compact, Equation D.6:

$$\int_{\Omega} W(x-x',h) \cdot \mathrm{d}x' = 1 \tag{D.4}$$

$$\lim_{h \to 0} W(x-x',h)\mathrm{d}x' = \delta(x-x') \tag{D.5}$$

$$W(x-x',h)\mathrm{d}x' = 0 \qquad \text{if} \qquad |x-x'| > \kappa h \tag{D.6}$$

where κ is the constant of interpolation function

If the interpolation kernel can be differentiated, we can construct the differential interpolation of function f denoted as $\langle \nabla \cdot f(x) \rangle$, Equation D.7. We note immediately that the gradient operator is transmitted to the interpolation function and the derivation of the function can therefore be determined from the function values and derivative of kernel.

$$\langle \nabla \cdot f(x) \rangle = \int \nabla f(x') \cdot W(x-x',h) \cdot \mathrm{d}x' = -\int f(x') \cdot \nabla W(x-x',h) \cdot \mathrm{d}x' \tag{D.7}$$

Principle of particle approximation

The interpolate of the function f described above has a continuous integral form and can be converted to a discrete form by adding the values of f over all the particles of the domain Ω: the particle approximation.

By replacing the infinitesimal volume $\mathrm{d}x'$ of the particle j by the volume ΔV_j, and defining for particle j the mass m_j and density ρ_j, we have:

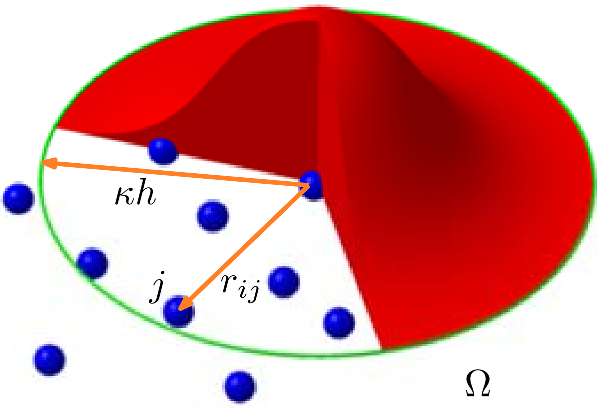

Figure D.1: Particle approximation over a domain Ω by the interpolation kernel W.

$$m_j = \Delta V_j \cdot \rho_j \tag{D.8}$$

By summing over N neighboring particles of particle i in domain Ω, the particle approximations of f and its gradient $\nabla \cdot f$ for this particle can be written as:

$$\langle f(x_i) \rangle = \sum_{j=1}^{N} \frac{m_j}{\rho_j} f(x_j) \cdot W_{ij} \tag{D.9}$$

$$\langle \nabla \cdot f(x_i) \rangle = \sum_{j=1}^{N} \frac{m_j}{\rho_j} f(x_j) \cdot \nabla_i W_{ij} \tag{D.10}$$

where

$$W_{ij} = W(x_i - x_j, h) = W(|x_i - x_j|, h) \tag{D.11}$$

and

$$\nabla_i W_{ij} = \frac{x_i - x_j}{r_{ij}} \frac{\partial W_{ij}}{\partial r_{ij}} \qquad \text{with} \qquad r_{ij} = |x_i - x_j| \tag{D.12}$$

We note that the notion of variable support (variable smoothing length) to determine the number of neighbors has two possible approximations: (i) scatter type and (ii) gather type. Each approximation can generate the numerical errors. For the purpose of clarity in conservation equations, we shall adopt the scatter approximation, the one used in LS-Dyna. For further details, reader is invited to consult ref. [106] on this subject. It is to be noted that different forms are possible when SPH formulation is applied to partial differential equations. Furthermore, by introducing density of particles in expression of gradient of a function and then applying the particle approximation, we can obtain two formulations for gradient approximation, Equations D.13 and D.14. Once again each formulation has its advantages and disadvantages in terms of numerical errors, [104].

$$\langle f(x_i)\rangle = \frac{1}{\rho_i}\left[\sum_{j=1}^{N} m_j\left[f(x_j) - f(x_i)\right]\cdot\nabla_i W_{ij}\right] \tag{D.13}$$

$$\langle f(x_i)\rangle = \frac{1}{\rho_i}\left[\sum_{j=1}^{N} m_j\left[\frac{f(x_j)}{\rho_j^2} - \frac{f(x_i)}{\rho_i^2}\right]\cdot\nabla_i W_{ij}\right] \tag{D.14}$$

These remarks explain the diverse conservation equations in SPH formulations found in literature.

Application to the conservation equations

The continuum mechanics equations can be written in the form:

$$\frac{\mathrm{D}\rho}{\mathrm{D}t} = -\rho\frac{\partial v^\alpha}{\partial x^\beta} \qquad \textbf{Mass conservation} \tag{D.15}$$

$$\frac{\mathrm{D}v^\alpha}{\mathrm{D}t} = \frac{1}{\rho}\frac{\partial\sigma^{\alpha\beta}}{\partial x^\beta} \qquad \textbf{Momentum conservation} \tag{D.16}$$

$$\frac{\mathrm{D}e}{\mathrm{D}t} = \frac{\sigma^{\alpha\beta}}{\rho}\frac{\partial v^\alpha}{\partial x^\beta} \qquad \textbf{Energy conservation} \tag{D.17}$$

where ρ is the density, e the internal energy, v^α a component of velocity, $\sigma^{\alpha\beta}$ the stress tensor, x^α the spatial coordinates and t is time. We also have $\sigma^{\alpha\beta} = -p\delta^{\alpha\beta} + \tau^{\alpha\beta}$

By applying the SPH method to the conservation equations presented earlier (and using the expression of derivative presented in Equation D.13), we obtain the relations Equation D.18, Equation D.19 and Equation D.20. A detailed description on derivation of these relations can be found in [104].

$$\frac{\mathrm{D}\rho}{\mathrm{D}t}(x_i) = \sum_{j=1}^{N} m_j(v(x_i^\beta) - v(x_j^\beta))\frac{\partial W_{ij}}{\partial x_i^\beta} \tag{D.18}$$

$$\frac{\mathrm{D}v^\alpha}{\mathrm{D}t}(x_i) = \sum_{j=1}^{N} m_j\left[\frac{\sigma^{\alpha\beta}(x_i)}{\rho_i^2} + \frac{\sigma^{\alpha\beta}(x_j)}{\rho_j^2} + \Pi_{ij}\right]\cdot\frac{\partial W_{ij}}{\partial x_i^\beta} \tag{D.19}$$

$$\frac{\mathrm{D}e}{\mathrm{D}t}(x_i) = \frac{1}{2}\sum_{j=1}^{N} m_j\left(\frac{p_i}{\rho_i^2} + \frac{p_j}{\rho_j^2} + \Pi_{ij}\right)\left[v^\beta(x_j) - v^\beta(x_i)\cdot\frac{\partial W_{ij}}{\partial x_i^\beta}\right] + \frac{1}{\rho}\tau^{\alpha\beta}(x_i)\cdot\dot{\epsilon}^{\alpha\beta}(x_i) \tag{D.20}$$

where $\dot{\epsilon}^{\alpha\beta}$ is the strain rate tensor and Π_{ij} is the pseudo viscosity.

By using the formulation of LS-Dyna over the expression of derivative, Equation D.21, the conservation equations take the forms as described in Equation D.23, Equation D.24 and Equation D.25, [101].

$$\langle \nabla \cdot f(x_i) \rangle = \sum_{j=1}^{N} \frac{m_j}{\rho_j} \left[f(x_j) A_{ij} - f(x_i) A_{ji} \right] \tag{D.21}$$

with

$$A_{ij} = \frac{1}{h^{d+1}} \theta' \left(\frac{\| x_i - x_j \|}{h} \right) \tag{D.22}$$

$$\frac{\mathrm{D}\rho}{\mathrm{D}t}(x_i) = \sum_{j=1}^{N} m_j (v(x_j) - v(x_i)) A_{ij} \tag{D.23}$$

$$\frac{\mathrm{D}v^{\alpha}}{\mathrm{D}t}(x_i) = \sum_{j=1}^{N} m_j \left[\left(\frac{\sigma^{\alpha\beta}(x_j)}{\rho_i^2} + \Pi_{ij} \right) A_{ij} - \left(\frac{\sigma^{\alpha\beta}(x_i)}{\rho_j^2} + \Pi_{ij} \right) A_{ji} \right] \tag{D.24}$$

$$\frac{\mathrm{D}e}{\mathrm{D}t}(x_i) = -\frac{P_i}{\rho_i^2} \sum_{j=1}^{N} m_j \left(v(x_j) - v(x_i) \right) A_{ij} + \frac{1}{2} \sum_{j=1}^{N} m_j \left(\frac{\Pi_{ij}}{2} \cdot A_{ij} - \frac{\Pi_{ji}}{2} \cdot A_{ji} \right) \tag{D.25}$$

Numerical viscosity or pseudo viscosity

If we try to solve an equation by classical numerical methods, it is frequently observed that the oscillations arise without real physical sense. These types of problems surely intervene when we try to simulate a system containing shocks, i.e a system showing high variations in dynamic parameters (necessarily the pressure). In classical resolutions (finite differences or finite volumes), it is sufficient to apply a some what arbitrary viscosity and to determine the diffusion which it engenders. In SPH method, it is indispensable to use a formulation adapted to include this numerical viscosity in conservation equations. There exist different types of numerical viscosities for SPH, [104]. The most widely used is shown in Equation D.26. This form permits to reproduce the kinetic energy dissipation in the form of heat at shock fronts and to avoid the “non-physical” behavior of particles approaching each other, [104].

$$\Pi_{ij} = \begin{cases} \dfrac{-\alpha_{\Pi} \cdot \bar{c}_{ij} \cdot \mu_{ij} + \beta_{\Pi} \cdot \mu_{ij}^2}{\bar{\rho_{ij}}} & \text{if} \quad v_{ij} \cdot x_{ij} < 0 \\ 0 & \text{if} \quad v_{ij} \cdot x_{ij} \geq 0 \end{cases} \tag{D.26}$$

$$\mu_{ij} = \frac{h_{ij} v_{ij} \cdot x_{ij}}{|x_{ij}|^2 + 0.01 h_{ij}^2} \tag{D.27}$$

$$c_{ij} = \frac{1}{2}(c_i + c_j) \tag{D.28}$$

$$\bar{\rho}_{ij} = \frac{1}{2}(\rho_i + \rho_j) \tag{D.29}$$

$$h_{ij} = \frac{1}{2}(h_i + h_j) \tag{D.30}$$

$$v_{ij} = v_i - v_j \qquad \text{and} \qquad x_{ij} = x_i - x_j \tag{D.31}$$

in the above equations, α_{Π} and β_{Π} are the constants near to 1, and v is the velocity vector of the particle and c is the speed of sound.

Choice of interpolation kernel

The choice of interpolation function is very important as it determines the model approximation and conditions the domain of influence for a particle. The properties of stability and convergence of solutions also depend upon the kernel. Many functions can therefore be used as long as they respect the conditions of Equation D.4, Equation D.5 and Equation D.6. The "cubic B–spline" and "quartic" form are two of the widely used forms, [104]. The form chosen by LS-DYNA® is "cubic B–spline", which is defined by following equations.

Let us consider an interpolation kernel which can be written in a general form as:

$$W(r_{ij}, h) = \frac{1}{h(r_{ij})^d} \cdot \theta(r_{ij}) \tag{D.32}$$

where d designates the spatial dimension of the system being modeled, h is the smoothing length which can vary in time and according to the position of particle and $r = |x_i - x_j|$.

The conditions of Equation D.4 and Equation D.5 impose certain conditions on the function $\theta(x)$:

$$\int\limits_{\Omega} \theta(r_{ij}, h) \mathrm{d}V = 1 \tag{D.33}$$

$$\lim_{h \to 0} (r_{ij}, h) = \delta(r_{ij}) \tag{D.34}$$

The supports also have to be compact, and the cubic B–spline kernel is written as:

$$\theta(r) = C \times \begin{cases} 1 - \frac{3}{2}r^2 + \frac{3}{4}r^3 & \text{for} \quad r \leq 1 \\ \frac{1}{4}(2-r)^3 & \text{for} \quad 1 < r \leq 2 \\ 0 & \text{for} \quad r > 2 \end{cases} \tag{D.35}$$

where C is a normalization constant depending upon the number of dimensions of model.

Variable smoothing length h

The introduction of smoothing length permits to resolve a number of problems posed by SPH method. The evolution of h in time should permit the conservation of a reasonable number of neighboring particles to assure the convergence of approximative calculations. A commonly used approach to keep the number of neighbors constant consists of keeping the total mass of neighbors constant:

$$h = h_0 \left(\frac{\rho_0}{\rho}\right)^{\frac{1}{d}} \tag{D.36}$$

where h_0 and ρ_0 the initial smoothing length and initial density for each particle, respectively, and d is the spatial dimension of the system being modeled.

Even if there are no specific implications of time in this equation, it is necessary to treat this modification in an explicit fashion. The forces arising due to shocks are violent and the response in terms of smoothing length will otherwise be very slow. One solution consists of differentiating the Equation D.36 w.r.t time and substituting in conservation equation, Equation D.15:

$$\frac{\mathrm{d}h(x_i)}{\mathrm{d}t} = -\frac{1}{d}h(x_i) \cdot \mathrm{div}[v(x_i)] \tag{D.37}$$

This evolution equation is then added to the system of conservation equations and permits, for each particle, to have a satisfactory number of neighbors.

Résumé en Français

Un certain nombre d'accidents dramatiques sont survenus dans l'aviation civile comme illustré figure 5, où l'éjection d'un éclat de moteur à travers la structure d'un avion a crée un accident mortel.

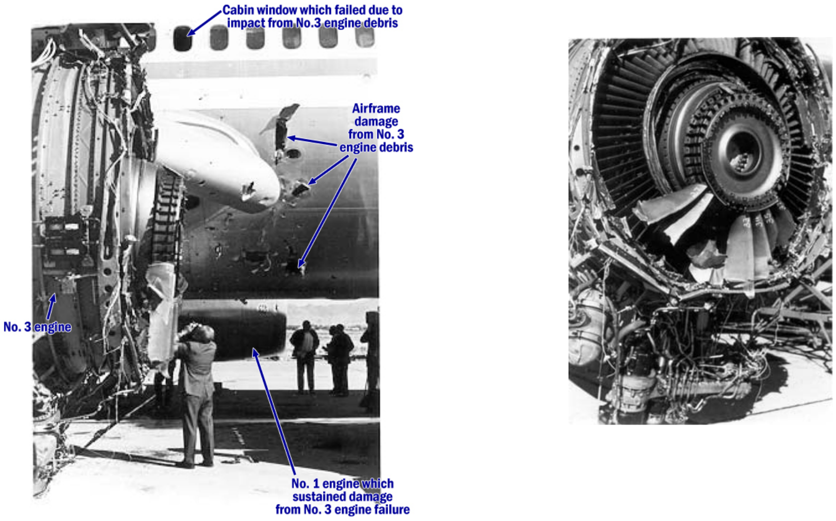

Figure 5 – Rupture d'une pale, National Airlines DC-10(November 3, 1973).

Les travaux réalisés pendant cette étude sont présentés suivant une structure pyramidale similaire à la pyramide des essais (figure 7). Le chapitre 1 présente brièvement les recommandations en termes de tolérance aux dommages issues de la certification aéronautique. Le chapitre 2 présente les résultats des essais de caractérisation des énergies de propagation de délaminage et des corrélations essais calculs basées sur le développement d'un modèle numérique cohésif. Le chapitre 3 présente un modèle de comportement multicritères proposé et développé pour simuler l'endommagement couplé inter et intralaminaire d'un stratifié sous impact. Les essais de caractérisation des effets de saturation de l'endommagement et de vitesse de déformation sur la limite élastique sont également présentés. Le chapitre 4 présente les résultats des essais d'impact non perforants réalisés au laboratoire pour différentes combinaisons de masses et de vitesse de projectile. Enfin le chapitre 5 permet de comparer les résultats des simulations d'impact d'une part avec le modèle cohésif seul, d'autre part avec le modèle d'endommagement multicritères, et des essais.

Chapitre 1 : Introduction

Contexte industriel

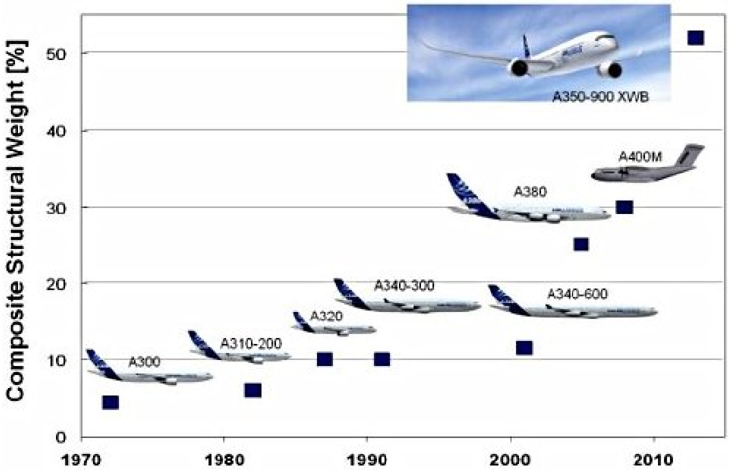

Figure 6 – Usage des composites dans les avion commerciaux par Airbus.

Depuis les 30 dernières années l'utilisation des matériaux composites dans les structures des avions ne cesse d'augmenter. Ce succès est essentiellement dû au très bon rapport raideur spécifique (E/ρ) des matériaux composites, la réduction significative du poids des avions étant un facteur important de réduction des coûts opérationnels. La figure 6 illustre le pourcentage en masse des composites dans les avions de la gamme Airbus.

Cependant, le comportement fragile plutôt que plastique des matériaux composites à l'impact est problématique. On estime aujourd'hui à environ 350 millions de dollars le coût annuel des essais de certification menés par les constructeurs aéronautiques. Pour utiliser de manière sûre, les structures composites dans des zones travaillantes, ceux-ci se tournent par conséquent vers une meilleure maîtrise du comportement multi-échelle via la simulation numérique ; le « virtual testing ».

Traditionnellement l'industrie aéronautique utilise la pyramide des essais illustrée sur la figure 7 pour déterminer les propriétés admissibles des matériaux et des structures. De plus en plus d'essais sur les coupons et les éprouvettes élémentaires, les essais les plus nombreux en fait, sont déjà remplacés par des simulations numériques. Les essais structuraux seront remplacés dans les années à venir.

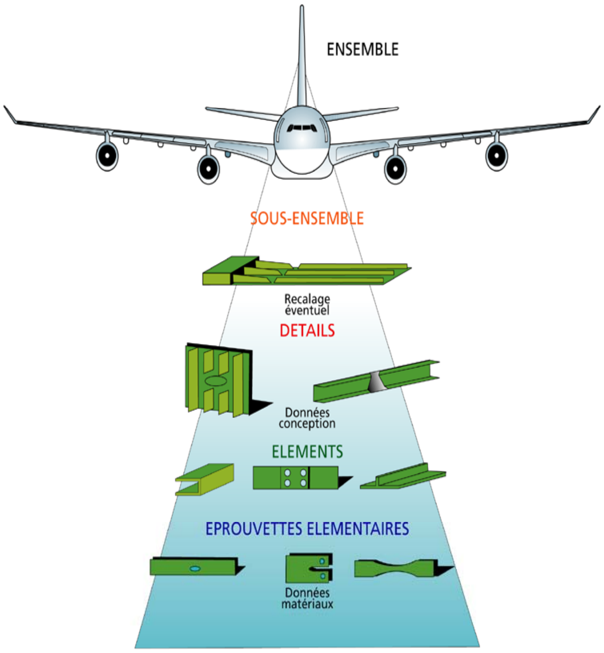

Figure 7 – Synoptique de la pyramide des essais [29].

Nous n'entrerons pas ici dans le détail de toutes les règles de certification qui concernent les composites sous impact. D'un point de vue général, nous pouvons résumer les prescriptions en disant que les impacts non perforants non admis en aéronautique sont ceux qui ne sont pas visibles et provoquent pourtant des dégâts à l'intérieur des structures susceptibles de provoquer sa ruine par fatigue. Par conséquent, il existe un risque non négligeable de rompre une structure composite en service si l'inspection de l'avion n'a pas permis de déceler l'occurrence d'un impact.

Contexte scientifique

Un nombre impressionnant de recherches a été et est encore mené dans le monde pour étudier le comportement des structures composites. En ce qui concerne le comportement à l'impact, ces recherches se sont intensifiées depuis une vingtaine d'années. Malgré tout, aucune méthodologie complètement validée n'a été proposée qui serait capable de prédire le comportement de structures composites sous impact incluant les différents endommagements susceptibles de conduire à sa ruine. Ceci est principalement dû à la nature complexe du comportement des matériaux dépendant de paramètres déterministes déterminés comme par exemple la nature des composants élémentaires, le séquence d'empilement, les conditions d'essais ; mais aussi de paramètres déterminés indéterministes ou présentant une forte variabilité tels que les modes de fabrication ou les conditions d'assemblage.

Le potentiel de résistance d'une structure composite est une caractéristique d'ensemble macroscopique intègre nominal qui passe sous le contrôle de la résistance des composants élémentaires et de leurs assemblages dès que l'endommagement apparait. Il n'existe donc pas un modèle type d'endommagement ou de rupture. Il existe autant de comportements que de combinaisons d'endommagements et de ruines des composants et de leurs assemblages. On distingue cependant deux approches philosophiquement différentes pour définir le potentiel de résistance : une représentation continue par des modèles de comportements, et une représentation discontinue par l'intermédiaire de liaisons internes qui peuvent se rompre.

Modélisation du comportement

Dans le cadre de la mécanique des milieux continus, le modèle de comportement est une relation utilisée pour caractériser leurs propriétés physiques macroscopiques et la réponse de structures élémentaires supposées représentatives du comportement du « matériau » face à des charges qui leurs sont appliquées. Les modèles explicites se fondent sur des observations phénoménologiques et sont donc limités par ce que l'on peut observer et mesurer. Les modèles implicites utilisent des formules mathématiques ou des interpolations dont les coefficients ne sont pas directement reliés à des propriétés intrinsèques donc difficilement identifiables. Les modèles hybrides ou mixtes combinent les deux approches précédentes. Parmi ces derniers, citons les méthodes dites DED (Dissipated Energy Density) basées sur la quantité d'énergie dissipée par l'endommagement considéré alors comme un début de rupture. Cette catégorie de méthodes aboutit souvent à l'introduction de liaisons cassables, notamment pour le délaminage. Les modèles continus incluant des critères de ruptures locales décrites ci-dessous font aussi partie des modèles hybrides.

Rupture locale des composites

La caractérisation expérimentale des contraintes et déformations seuils d'apparition des endommagements passe par l'introduction de critères de ruptures locaux associés aux modes de rupture des composants et de leurs assemblages : ruptures de fibres, décohésion fibres-matrice, flambage de fibres en compression, fissures dans la matrice et dans le sens de l'épaisseur des plis, délaminage ou décohésion interlaminaire. Les essais de traction par exemple sont traditionnellement utilisés pour caractériser une ou deux propriétés physiques. Des essais standardisés (ASTM ou ESIS) sont utilisés pour limiter les dispersions et incertitudes liés aux paramètres indéterministes ou indéterminés. Lors d'impacts, ces mécanismes de ruptures locales sont néanmoins affectés par les effets de vitesses de déformation, de masse du projectile, de rapport épaisseur de plaque cible sur diamètre du projectile pour certaines vitesses, c'est à dire des caractéristiques dynamiques de la sollicitation.

Effets de vitesse d'impact

L'impact sur une structure composite est défini comme l'application « relativement soudaine » d'une force d'impulsion dans un volume « limité » ou réduit de matière dans la structure. Les termes « relativement » et « limité », littéralement subjectifs, peuvent avoir différentes interprétations scientifiques comme le démontre Hancox [10]. Dans le domaine aéronautique, les impacts sont classifiés par gammes d'énergies ou de vitesses de projectiles, [5] :

– « faibles énergies » (chute d'outils), « d'énergie intermédiaire » (débris, cailloux, grêlons), ou « haute énergie » (Fane Blade Out ou éclat non contenus de débris moteurs) ;

– faibles vitesses de 0 à 50 m/s, vitesses intermédiaires de 50 à 200 m/s, hautes vitesses de 200 à 1000 m/s, hyper vitesses au-delà de 4000 m/s.

Dans le domaine des hautes et hyper vitesses, on introduit la notion de limite balistique pour les impacts perforants, et de limite d'écaillage pour les impacts provoquant des éclats face arrière sans perforation (matériaux fragiles).

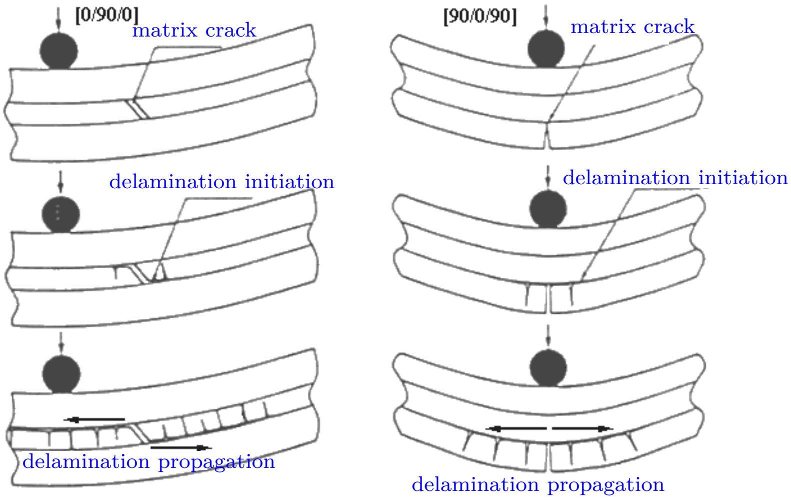

Figure 8 – Illustration de cinétique d'initiation et de propagation lors d'un impact basse vitesse sur une stratifié $[0, 90]_s$.

Les dégâts sont illustrés figures 8 et 9. Il est admis dans la communauté scientifique que le délaminage ne se produit jamais sans fissuration translaminaire alors qu'il peut y avoir fissuration sans délaminage. Ceci a surtout été observé pour des charges quasi-statiques et semble également être le cas pour des sollicitations d'impacts.

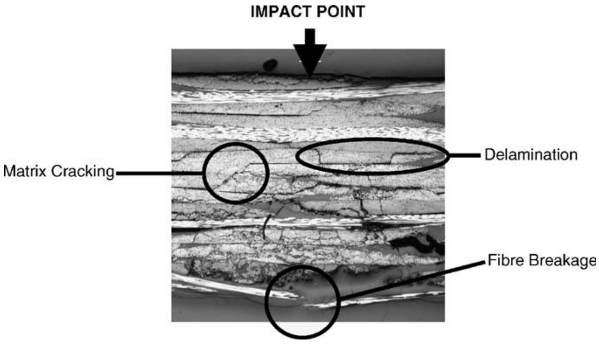

Figure 9 – Les Différents types d'endommagement après impact, Mitrevski et al. [25].

Modélisation et prédiction des dommages par simulation numérique

La majorité des approches de modélisation débouchant sur la simulation numérique utilise et est conforme aux hypothèses de la méthode des éléments finis. Les modèles de comportement utilisant la mécanique des milieux continus introduisent l'endommagement par des critères de ruptures locales, et altèrent les propriétés physiques du matériau. Le volume élémentaire représentatif dont les propriétés sont affectées est très souvent la maille du modèle éléments finis. Ces approches basées sur des critères de résistance sont simples et les dommages sont irréversibles.

Les modèles relaxant des liaisons pour modéliser la génération d'ouvertures dans la structure s'intéressent principalement à la modélisation du délaminage, et utilisent aussi la méthode des éléments finis. Ils sont basés sur la pré localisation d'éléments assurant une liaison cohésive qui se rompe progressivement ou brutalement en dissipant de l'énergie. Ces méthodes utilisent la mécanique classique de la rupture et considèrent l'endommagement comme une propagation de rupture. Des modèles intègrent des effets retards pour stabiliser la progression des ouvertures en dynamique. Là encore la rupture est irréversible. Ces modèles sont plus complexes à mettre en œuvre car il est nécessaire d'introduire des « contacts » numériques entres les lèvres des plis délaminés après ouverture.

On note quelques premiers travaux sur des méthodes sans maillage (SPH), non étendus pour le moment aux matériaux composites sous impacts basses vitesses. Depuis quelques années ces méthodes ont été appliquées avec succès à la modélisation de comportement en grandes déformations et grands déplacements et permettent de gérer plus « naturellement » la création de décohésions dans la matière [15, 22, 24]. Elles utilisent des modèles de comportement continus et des critères d'état du matériau pour définir la cohésion de la matière. Ces méthodes semblent prometteuses car elles ne nécessitent pas de pré localiser les zones de fissuration quel que soit le mode de rupture locale.

Objectifs

Pour certifier des structures composites aérospatiales, le fabricant a besoin de savoir le comportement de structures dans le cadre de sollicitations « normales », et démontrer la capacité de ces structures à résister au chargement pour une période minimum, par exemple jusqu'à la prochaine inspection technique, même après le début d'endommagement entre deux intervalles d'entretien. Ainsi les besoin spécifique de l'industrie aéronautique choisi pour cette étude sont : 1) comprendre de formuler et améliorer le comportement sous impact de structures composites pour les diverses configurations d'impacts caractéristiques rencontrés pendant la durée d'utilisation d'avion, 2) déterminer l'étendue de dommages après impact pour quelques types d'impacts caractéristiques, 3) relier quantitativement les dommages d'impact mesurés externes et non observables internes. D'un point de vu scientifique, la question que nous avons choisies d'étudier est : quelle sont les phénomènes physiques prédominent la résistance de la structure et comment on devrait les modéliser pour prédire l'extension interne des dommages pour les configurations différentes d'impact : les chocs bas énergie, l'impact haute énergie sur un fuselage. Un autre point clé est de la capacité prédictive de modèles mécaniques numériques, cela est le but de cette étude pour éviter les choix à priori d'outils numériques ou des paramètres numériques. Pour analyser l'effet de dommages inter-pli et les dommages dans le pli sur le comportement global d'échantillons composites, nous avons décidé de suivre une méthodologie parallèle de ces deux dommages. Premièrement nous proposons de modéliser le délaminage utilisant une méthode cohésive. L'homologue de ce modèle est qu'il doit être défini à priori, ainsi limitant la prédictibilité du modèle. Alors nous proposons d'utiliser une approche basée sur mécanique d'endommagement pour le pli, qui prend aussi en compte l'effet de délaminage sur la réduction d'effort. L'effet de vitesse de déformation est pris en compte sur les limites élastiques et aussi pour l'évolution de vitesse d'endommagement. Une analyse et la comparaison sont faites entre ces deux modèles et les tests d'impact sur les plaques composites différentes (T700S/M21, T800S/M21, différentes séquences d'empilement, différents épaisseurs, énergies différentes et vitesses différentes).

Chapitre 2 : Loi bilinéaire cohésif

Les composites unidirectionnels contiennent souvent une couche riche en résine entre deux plis comme on le voit sur figure 10. Cette couche ou l'interface riche en résine a été modélisée par des éléments d'interface. Ce chapitre se fixe principalement sur la validation d'un modèle matériau développé pour la simulation du comportement inter-laminaire.

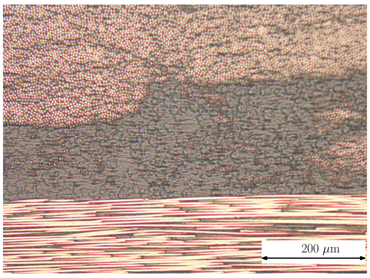

Figure 10 – Couche riche en résine d'un stratifié T800S/M21.

Modèle cohésif développé

Dans les paragraphes suivants la loi matériau cohésif a été développée et implémentée dans LS-DYNA® (le code commercial de calcul par éléments finis), comme une subroutine utilisateur. Au début de ce projet cette loi matériau n'existait pas comme un matériau standard dans LS-DYNA®. Comme première étape, la loi bilinéaire est choisie.

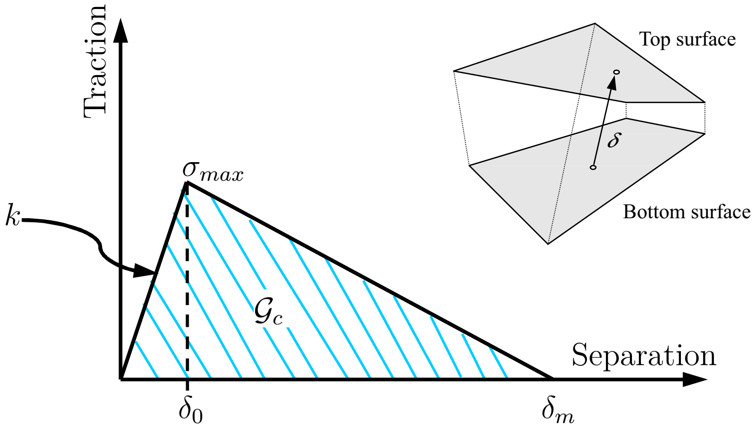

Figure 11 – Loi cohésive, traction vs. déplacement relatif.

Les éléments d'interface dans LS-DYNA® sont formulés en termes de traction vs. le déplacement relatif au lieu de contrainte vs. déformation [19]. Deux surfaces (le sommet et le fond) sont considérées (figure 11). Chaque point dans ces surfaces a un point correspondant dans l'autre surface, désignée comme le point homologue. Ces points homologues ont de mêmes coordonnées spatiales avant que l'interface soit chargée. Le déplacement relatif entre chaque paire de points homologues est projeté dans un système de référence local, qui exprime le déplacement relatif en termes d'ouverture et de glissement. Le glissement peut être en mode II (le cisaillement), III (la déchirure) ou une combinaison des deux.

Avant le début d'adoucissement/délaminage, une loi élastique relie le déplacement relatif des surfaces du sommet et fond avec la traction (l'effort divisé par section). Pour les modes purs I ou II, l'interface possède un comportement élastique linéaire jusqu'à la traction admissible. Ensuite, la raideur est réduite de telle façon que l'énergie absorbée est égale au taux de restitution d'énergie critique correspondant ($\mathcal{G}_{Ic}$ ou $\mathcal{G}_{IIc}$, respectivement, figure 12).

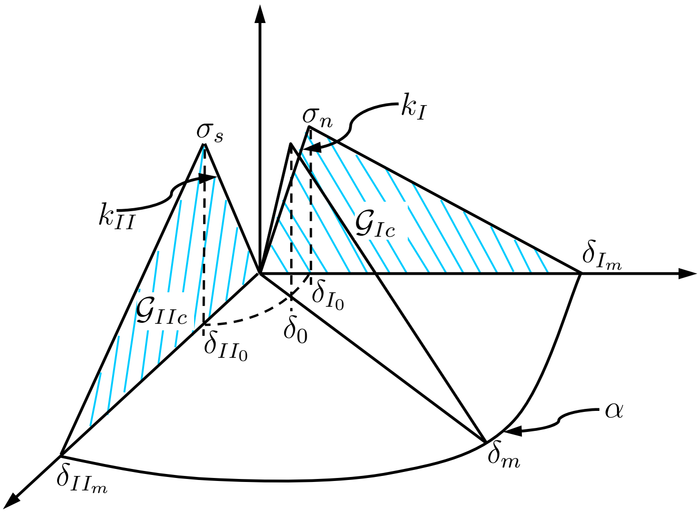

Figure 12 – Loi cohésif en mode mixte.

Le début de délaminage est défini par des déplacements relatifs qui sont calculés par $\delta_{I_0} = \dfrac{\sigma_n}{k_I}$ et $\delta_{II_0} = \dfrac{\sigma_s}{k_{II}}$, où σ_n et σ_s sont les contraintes maximal respectivement pour le mode I et II pur. k_I et k_{II} sont des rigidités des éléments cohésifs pour le mode d'ouverture et le mode de cisaillement. Les déplacements purs de rupture de mode sont définis par $\delta_{I_m} = \dfrac{2\mathcal{G}_{Ic}}{k_I \delta_{I_0}}$ et $\delta_{II_m} = \dfrac{2\mathcal{G}_{IIc}}{k_{II} \delta_{II_0}}$.

Le mode mixte modèle est fondé sur le début de délaminage et l'approche de propagation proposé par Camanho et al. [7]. Ils proposent l'interaction quadratique entre les tractions pour prédire le début d'adoucissement. La relation élastique est valide jusqu'à ce qu'un critère d'initiation basé sur contrainte est vérifié. Après cette étape, la réduction de raideur arrive pour chaque mode dans une telle façon qu'un critère de propagation définit l'énergie absorbée dans la situation de mode mixte. Un critère capable de représenté la taux de restitution d'énergie sous mode mixte est utilisé. Dans cette formulation particulière d'élément d'interface, le mode de glissement (II) est considéré représenter les deux modes II (cisaillement) et III (déchirure) parce que la distinction entre le mode II et III dépend de la direction du déplacement relatif entre les points homologues par rapport à l'orientation du devant de fissure. Le déplacement relatif est défini par :

$$\delta = \sqrt{\langle \delta_I \rangle^2 + \delta_{II}^2} \tag{1}$$

où

$$\delta_{II} = \sqrt{\delta_{\text{shear}}^2 + \delta_{\text{tear}}^2} \tag{2}$$

Dans le cas du mode mixte on introduit le paramètre β :

$$\beta = \max\left(0, \frac{\delta_{II}}{\delta_I}\right) \tag{3}$$

L'initiation en mode mixte est décrit par :

$$\delta_0 = \delta_{I_0}\delta_{II_0}\sqrt{\frac{1+\beta^2}{(\delta_{II_0})^2 + (\beta\delta_{I_0})^2}} \tag{4}$$

La propagation en mode mixte est décrit par une loi en puissance comme proposé par Mi et al. [23] et Allix et al. [6] :

$$\left(\frac{\mathcal{G}_I}{\mathcal{G}_{Ic}}\right)^\alpha + \left(\frac{\mathcal{G}_{II}}{\mathcal{G}_{IIc}}\right)^\alpha = 1 \tag{5}$$

Qui se traduit dans par :

$$\delta_m = \begin{cases} \dfrac{1+\beta^2}{\delta_0}\left[\left(\dfrac{k_I}{\mathcal{G}_{Ic}}\right)^\alpha + \left(\dfrac{k_{II}\beta^2}{\mathcal{G}_{IIc}}\right)^\alpha\right]^{-\frac{1}{\alpha}} & \Longleftarrow \delta_I > 0 \\ \delta_{II_m} & \Longleftarrow \delta_I \leq 0 \end{cases} \tag{6}$$

$$d = \frac{\delta_m(\delta - \delta_0)}{\delta(\delta_m - \delta_0)} \tag{7}$$

Pour les composites unidirectionnels carbone époxy, il est commun de représenter le mode mixte typiquement par l'utilisation de α comprise entre 1 et 2.

Les deux discontinuités qui existent dans la loi bilinéaire (à la valeur maximum et complète decohésion) peut produire des instabilités numériques dans une implémentation explicite. Dans les certaines situations, une vague de tension pourrait être produite à ces points, et exciter les oscillations de haute fréquence qui peuvent casser complètement les éléments de decohésion dans le voisinage. Ce problème peut être surmonté par l'utilisation d'étouffer les algorithmes, le plus hauts raffinement à mailles, abaissent la force d'interface, la plus haute solidité de fracture ou abaisse le chargement-taux. Toutefois, le modèle d'éléments finis particulier qui n'est pas affecté par ces ondes de propagation n'est pas toujours facile pour définir [27].

Identification des paramètres

Les paragraphes suivants abordent la corrélation essais/calculs sur plusieurs cas tests de mécanique de la rupture. Les éprouvettes utilisées pour la mise au point des lois cohésives sont de type DCB (Double Cantilever Beam) pour le mode I, ELS (End Loaded Split) pour le mode II et MMB (Mixed Mode Bending) pour le couplage mode I/mode II. Le modèle éléments finis est un modèle volumique (3 ddl par nœud, 1 point d'intégration par volume) où un seul élément est utilisé suivant la largeur de chaque bras de l'éprouvette. Les éléments cohésifs (sans épaisseur modélisée) possèdent 8 nœuds et sont placés en aval du front de fissure (figure 13). Ces éléments sont supprimés lorsque le déplacement à rupture est atteint sur un point de Gauss. Le modèle s'apparente donc à un modèle en déformation plane. Les conditions aux limites sont détaillées pour chaque type d'éprouvette.

Mode I : éprouvette DCB

Le matériau des éprouvettes DCB est constitué de nappe UD T800/M21 où tous les plis sont orientés à 0°. Les dimensions de l'éprouvette sont $L = 120 \times b = 25 \times 2h = 3.1$ mm^3. La fissure initiale (a_0) est de 40 mm et est réalisée par insertion lors de la fabrication d'un film de Téflon de 13 μm d'épaisseur. Le pli est supposé comme un matériau isotrope de module de flexion (E_f) 120 GPa et de coefficient de Poisson 0.3. Les essais ont été réalisés sur une machine de traction à déplacements imposés de 2 mm/min pour les essais statiques [14] et à 30 m/min pour les essais dynamiques. Pour les essais dynamiques, une pré craquage a été réalisée afin de minimiser le pic d'effort initial lors de la propagation dû à l'amat de résine présent en front de fissure (surtout pour le mode II [20]).

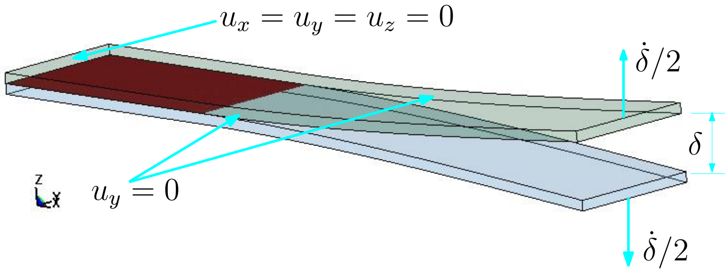

Figure 13 – Modèle numérique retenu, conditions aux limites de simulation (DCB).

La raideur de traction et de cisaillement des éléments cohésifs est de 100 kN/mm^3 ; valeur identifiée pour le recalage de la raideur initial de l'essai. Les contraintes à rupture en traction et en cisaillement sont égales à 60 MPa. La valeur du taux de restitution d'énergie critique en mode I est de 765 J/m^2. Le chargement est réalisé à vitesse imposée égale à 0.5 m/sec. Afin d'éliminer les déformations à énergie nulle (hourglass) les déplacements suivant y (en bord d'éprouvette) ont été bloqués (plan xz).

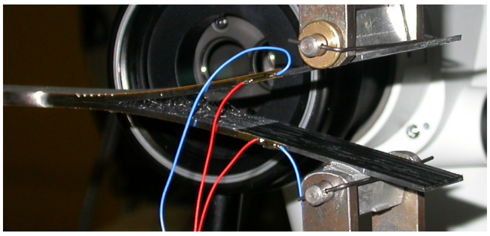

Figure 14 – Éprouvette DCB chargé par une machine hydraulique.

La figure 15 présente les résultats globaux du comportement force-ouverture des essais pour deux vitesses de chargement ainsi que le modèle numérique associé. Le comportement donné par le modèle numérique est similaire au comportement relevé lors des essais mais ne reproduit pas les non linéarités lors de l'initiation du délaminage. Ces non linéarités ne sont que peu présentes sur le matériau T700S/M21. Le procédé de fabrication du T800S/M21 étant différente de celui du T700S/M21 (présence de thermoplastique importante à l'interface), il est envisagé de modifier la loi d'interface pour prendre en compte ces non linéarités (plasticité).

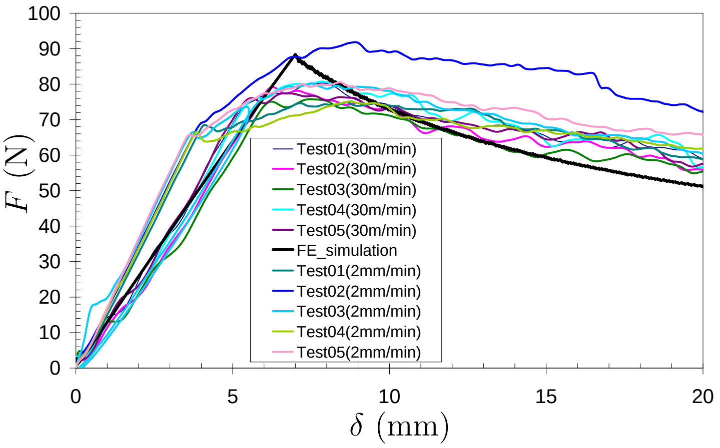

Figure 15 – DCB : courbes effort vs. déplacement, comparaison des résultats numériques et expérimentaux, [11].

Mode II : éprouvette ELS

Les résultats expérimentaux corrélés à cette étude numérique sont ceux de précédents travaux réalisés dans notre laboratoire sur un matériau T700S/M21. Les dimensions des éprouvettes sont de $L = 140 \times b = 20 \times 2h = 4.68$ mm^3. La fissure (a_0) est de 80 mm. Le pré craquage est de 4 mm. Les caractéristiques mécaniques du pli sont données dans le tableau 1. Les propriétés des éléments cohésifs sont identiques à ceux des modèles en mode I. Le taux de restitution d'énergie critique en mode II est 1387 J/m^2.

Pour les essais ELS, un montage d'essai spécifique est nécessaire afin de mesurer correctement l'effort appliqué : l'encastrement de l'éprouvette est mobile, le point d'application

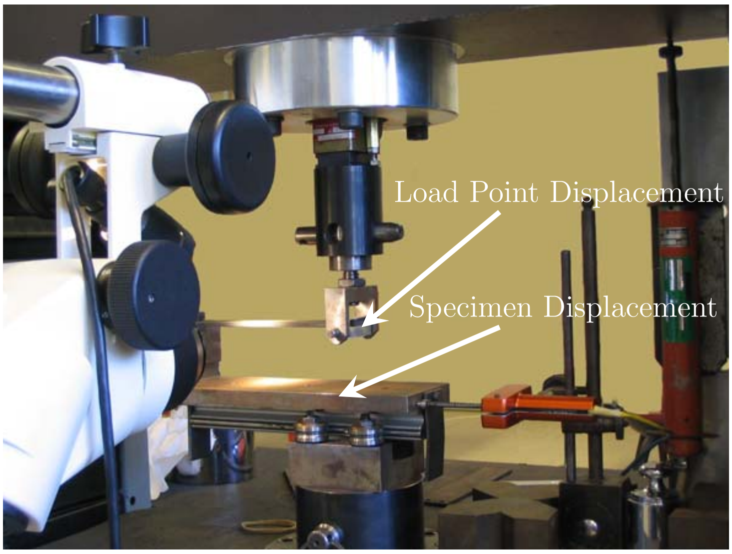

Figure 16 – Eprouvette ELS chargée par une machine électro-mécanique.

Tableau 1 – Propriétés matériaux pour les simulations des éprouvettes ELS et MMB de T700S/M21.

E_f (GPa)	E_{22} (GPa)	E_{33} (GPa)	ν_{12}	ν_{23}	ν_{13}	G_{12} (GPa)	G_{23} (GPa)	G_{13} (GPa)
98.62	7.69	7.69	0.33	0.4	0.33	4.75	2.75	4.75

de l'effort est fixé longitudinalement (figure 17). Les conditions aux limites du modèle numérique sont différentes : l'encastrement est fixé, le point d'application du chargement est libre de se déplacer longitudinalement. Le chargement est appliqué à déplacement imposé et égale à 240 mm/sec.

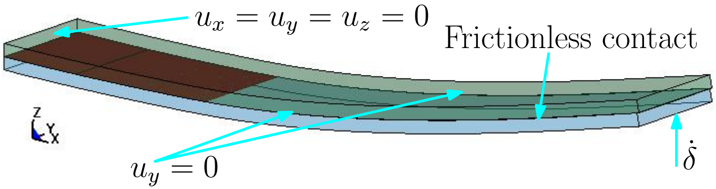

Figure 17 – Modèle numérique et conditions aux limites (ELS).

La comparaison du comportement expérimentale et numérique en termes de force en fonction du déplacement, montre, figure 18, un faible écart. La forme est identique et l'écart sur la valeur de l'effort à l'initiation du délaminage est inférieur à 10% ; cet écart étant attribué à la différence de conditions aux limites entre les essais et le modèle numérique.

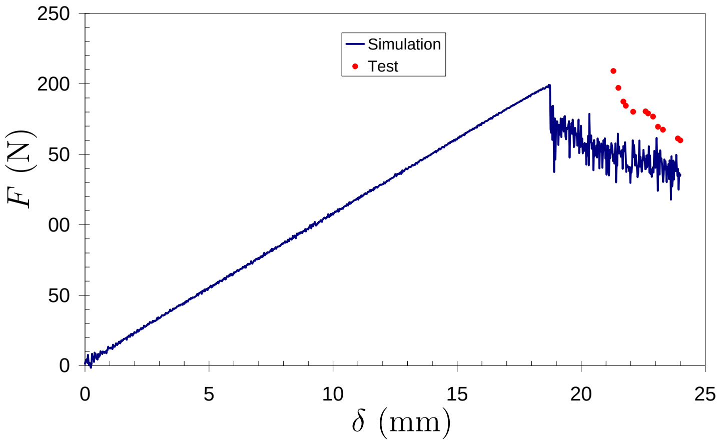

Figure 18 – ELS : courbes effort vs. déplacement, comparaison des résultats numériques et expérimentaux, [12].

Mode mixte : éprouvette MMB

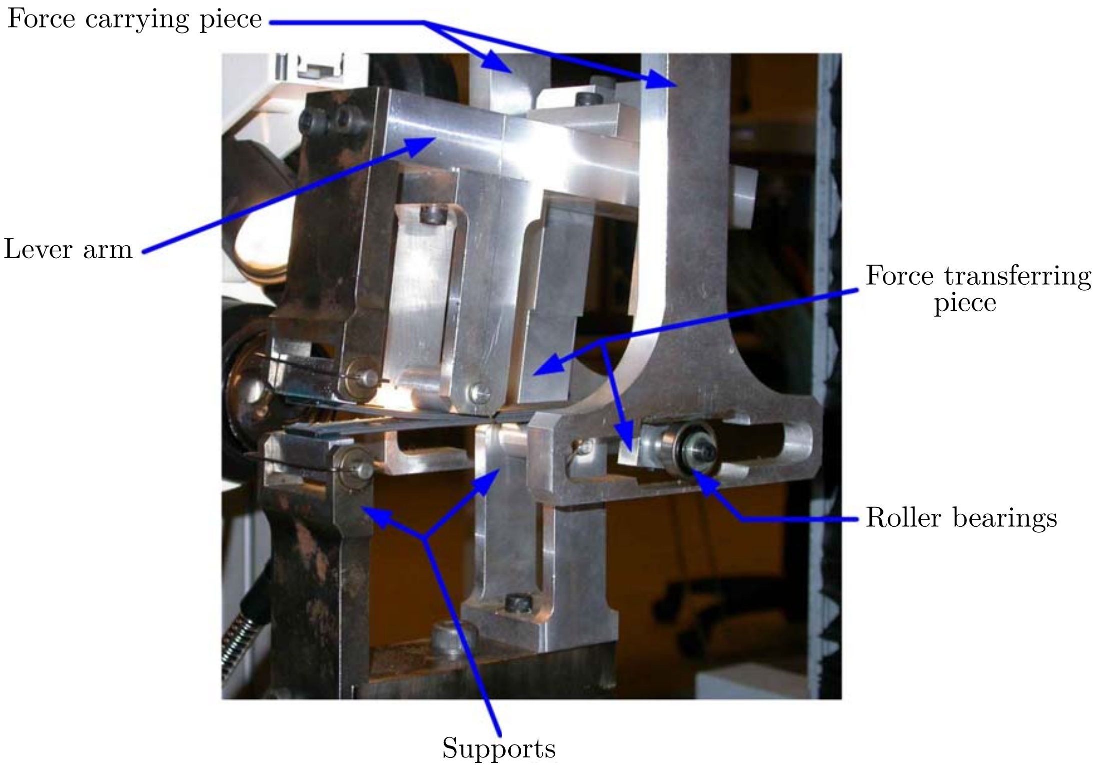

Figure 19 – Dispositif d'essais MMB, Prombut [28].

L'objectif de cette comparaison essais/calculs sur éprouvette MMB est de valider les paramètres de la loi d'interface sur le couplage mode I, mode II. Les essais comparés sont ceux obtenus lors d'une étude expérimentale précédente [28], où les essais sont réalisés pour une partition du mode I égale à 50% de l'énergie totale, obtenue à l'aide d'un montage spécifique (figure 6). Les dimensions des éprouvettes sont de $2L = 100 \times b = 20 \times 2h = 4.68$ mm^3. La fissure (a_0) est de 25 mm et le pré fissure de 4 mm (obtenue en mode I).

Les taux de restitution d'énergie critique en mode I et en mode II sont respectivement égale à 545 J/m^2 et 1387 J/m^2 ; valeurs moyennes des essais. Le paramètre α définissant la forme du critère de propagation (équation 6) est égal à 1.5.

Tableau 2 – Paramètres matériau des élément d'interface.

k_I (kN/mm^3)	k_{II} (kN/mm^3)	σ_n (MPa)	σ_s (MPa)	$\mathcal{G}_{Ic}$ (J/m^2)	$\mathcal{G}_{IIc}$ (J/m^2)	α
100	100	60	60	545	1387	1.5

La figure 21 présente la comparaison essai/calcul du comportement effort déplacement du point d'application de l'effort. Le modèle numérique rend bien compte du comportement expérimentale, autant sur l'effort à la propagation que sur la forme du comportement lors de la propagation du délaminage.

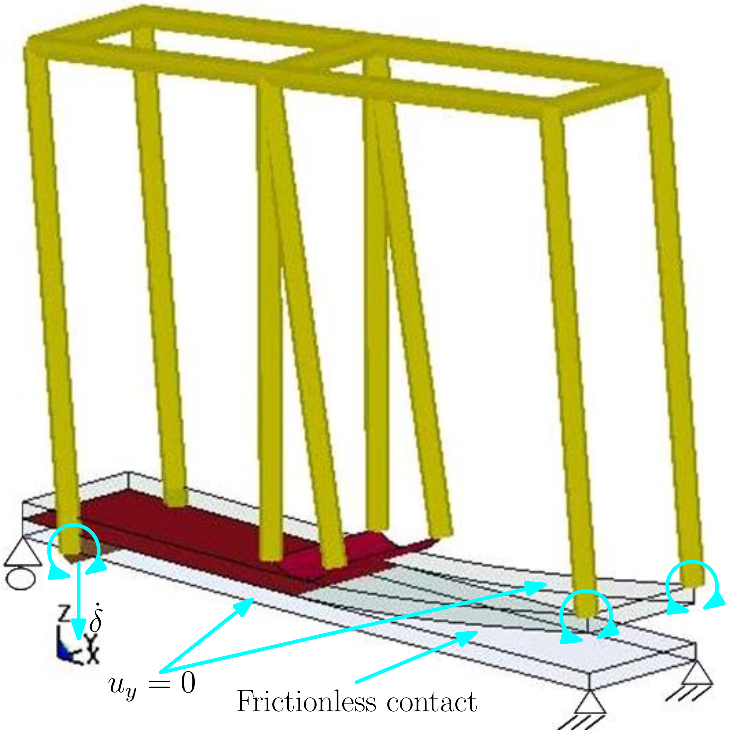

Figure 20 – MMB : modèle numérique et conditions aux limites.

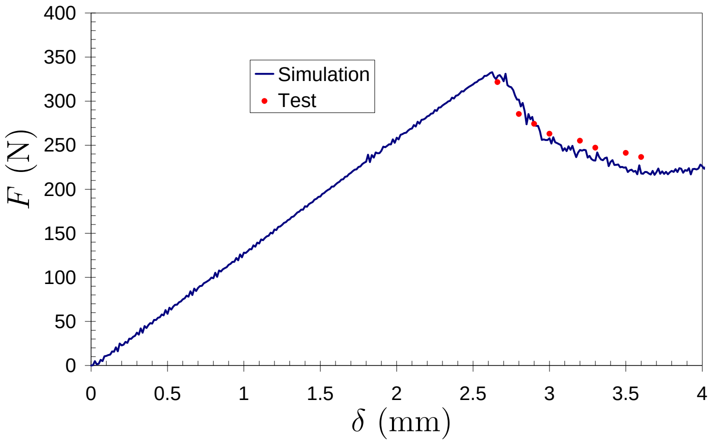

Figure 21 – MMB : courbes d'effort vs. déplacement comparaison des résultats numériques et expérimentaux, [12].

Chapitre 3 : Loi de comportement du pli

Ce chapitre présente un modèle d'endommagement basé sur mécanique des milieux continus et le modèle de Matzenmiller-Lubliner-Taylor [21]. Des essais de caractérisation réalisés en quasi-statique et en dynamique sont également présentés dans ce chapitre. Le système de barres d'Hopkinson a été utilisé pour la caractérisation en dynamique. Les essais ont été menés pour identifier les caractéristiques du matériau T800S/M21. La comparaison des essais et des simulations numériques est également présenté dans ce chapitre.

Une bibliographie a été réalisée concernant les modèles numériques et les essais de caractérisation pour matériaux composites. Cette étude bibliographique n'est pas présenté dans le rapport en français pour plus d'informations le lecteur est invité à se reporter au document en anglais qui synthétise essentiellement les équations des modèles.

Caractérisation

La caractérisation des propriétés physiques est présentée dans ce paragraphe. Les essais quasi-statiques et les essais dynamiques sont présentés. Les essais quasi-statiques au paragraphe 3.2.1 concernent des éprouvettes de T700S/M21 et T800S/M21 avec les dimensions utiles $L = 150$ mm, $b = 20$ mm et 2 mm. Les détails de préparation et d'instrumentation sont fourni en annexe A du rapport en anglais. Les plaques présentent un taux de fibre de 65%. La figure 22 présente le comportement des matériaux T700S/M21 et T800S/M21 $[\pm 45]_{2s}$. Une partie du comportement quasi-linaire est identifié avec une contrainte maximale de l'ordre 50 MPa au delà le comportement devient élastique non-linéaire. A partir de 60 MPa les UD T700S/M21 et T800S/M21 ont un comportement très différents. La déformation élastique à 50 MPa est de l'ordre de 1.2%. A 60 MPa le

T800S/M21 présente un plateau donc un effet de saturation de la contrainte, alors que T700S/M21 a un comportement différent et la contrainte continue à augmenter.

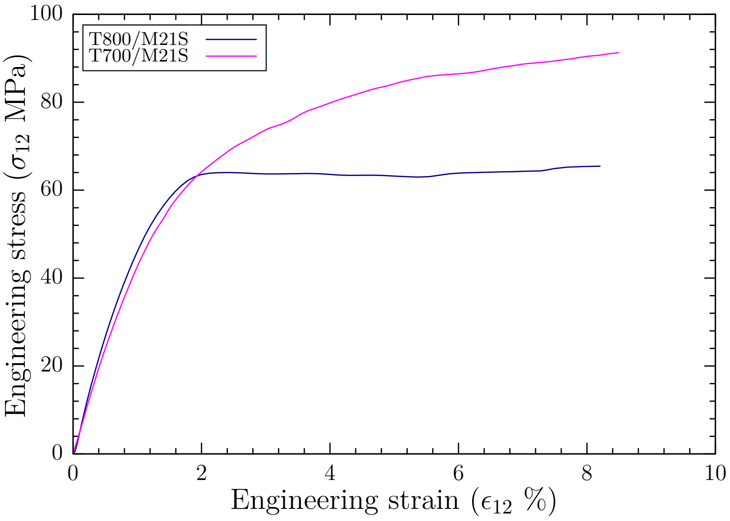

Figure 22 – La réponse typique des stratifiés T700S/M21 [9] et T800S/M21 $[\pm 45]_{2s}$.

Pour mieux comprendre les effets de saturation des coupes microscopiques ont été réalisées sur les éprouvettes de T700S/M21 etT800S/M21 avant expérimentation. On se rend compte que le T800S/M21 présente une épaisseur de résine beaucoup plus importante entre les plis que T700S/M21. Une épaisseur de l'ordre 66 μm pour T800S/M21 et 24 μm pour T700S/M21. L'analyse de la figure 22 qui permet de mesurer le module G_{12} nous amène à penser que c'est l'effet de couche de résine importante dans le cas du T800S/M21 qui amène la saturation de contrainte à 60 MPa dans les interfaces à [±45°]. En conséquence on décide de prendre en compte cette résistance particulière dans le modèle du comportement avec de l'endommagement.

Le paragraphe 3.2 présente les essais de compression dynamique et le système de barres d'Hopkinson. Une série des essais de compression dynamique a été réalisé pour les stratifiés $\pm\theta$, $\theta \in \{15, 30, 45, 60, 75\}$. Une ensemble des angles a été ballait. Aucune étude spécifique a été faite sur le choix d'angle à priori. Donc l'étude été systématique tous les 15° pour essayer de caractériser l'influence de variation de l'angle et de la vitesse de déformation. Le détaille des essais et la courbe expérimentale est présenté dans le document en anglais, le lecteur est invité à se reporter à la thèse complète pour voire l'ensemble des courbes. Globalement on distingue deux comportement différente pour les vitesses de déformations de l'ordre $200 - 300s^{-1}$ et vitesse de déformations qui s'approche $1000s^{-1}$.

Ce paragraphe résume l'analyse qui a été faite sur les courbes expérimentale pour les $\pm\theta$. Il apparait que T800S/M21 présente une forte sensibilité à la vitesse de déformation. Le lecteur est invité a se reporter encore une fois au document en anglais.

Nous avons choisi de synthétiser les résultats obtenus sur les essais T800S/M21 en fonction de valeur de l'angle et vitesse de déformation. Deux niveaux de vitesse de déformation une de l'ordre de grandeur de $200 - 300s^{-1}$ une autre de l'ordre de $1000s^{-1}$. La première s'appelle la vitesse de déformation quasi-statique et la deuxième nous l'intitulons la vitesse de déformation dynamique. Trois valeurs ont été relevées pour modéliser le comportement global des plis. La première valeur est une limite élastique, la deuxième valeur est un module d'Young et la troisième valeur c'est une contrainte à rupture.

L'objectif de cette analyse est d'identifier s'il est nécessaire ou pas de prendre en compte les effets de vitesse de déformation dans le modèle de comportement de matériau avec endommagement. Si oui, sous quelle forme avec quel critère. Pour les éprouvettes faiblement orientés avec $\theta \in \{0, 15, 30\}$, le module élastique dynamique en compression diminue avec la vitesse de déformation d'environ $20 - 40\%$, figure 23. Dans les trois cas $(0°, 15°, 30°)$, la déformation à limite élastique est de l'ordre de 0.6% en quasi-statique et de 1.2% end dynamique. Des déformation typiques à rupture sont de l'ordre de 1.0% en quasi-statique et $1.5 - 1.7\%$ en dynamique. A ce moment d'analyse nous ne savons pas si les effets de vitesse de déformation viennent de la résine à l'intérieur du pli ou à l'interface.

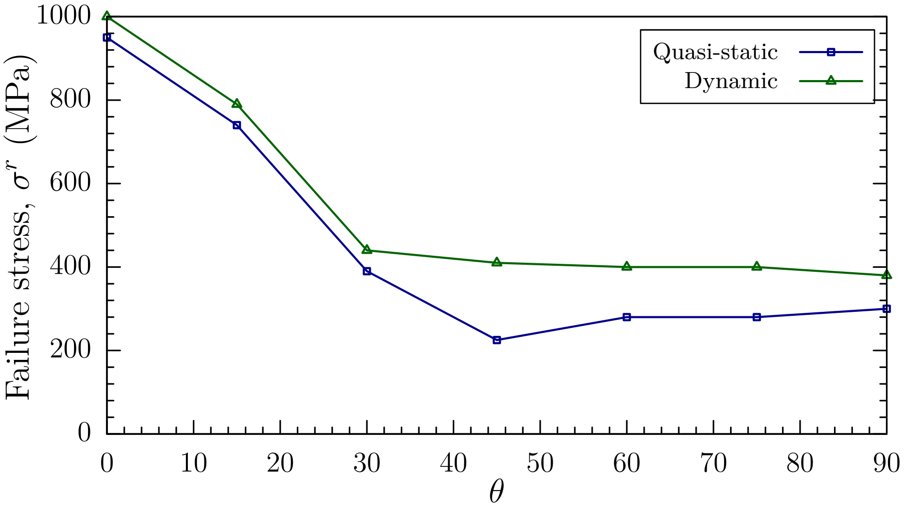

Figure 23 – Evolution de contrainte à rupture en fonction de l'angle et de la vitesse de déformation.

Loi de comportement du pli

Cette section est dédié au modèle du comportement développé et utilisé pour les simulations de système du banc d'essais d'Hopkinson et les simulations d'impact sont présenté dans le chapitre 5. Les modifications et les améliorations dans le modèle de MLT fondamental sont d'abord présentées.

Modèle proposé

Dans le paragraphe 3.1.2.2 le modèle de MLT basé sur les critères de rupture comme trouvé dans la littérature est présenté. Le modèle identifie 6 modes d'endommagement d_i, $i = 1 \cdots 6$, qui affectent 6 modules du matériau orthotrope (l'équation 11), et 5 modes de ruine, $r_i = 1 \cdots 5$. Quatre modifications sont proposées : les critères de ruptures pour incorporer la compression dans la direction transversale (2) le calcul de contrainte de test (iii) la matrice de couplage d'endommagement couple d_5 avec le mode de ruine de délaminage et (iv) la saturation d'endommagement pour introduire la rupture. Ces modifications sont discutées dans les paragraphes suivants.

Pour l'endommagement, il est proposé

$$d_i = q_{ij}\phi_j, j = 1 \cdots 5 \text{ and } \phi_j = 1 - \mathrm{e}^{\frac{1}{m_j}\left(1-r_j^{m_j}\right)}, r_j \geq 1 \tag{8}$$

La fonction d'évolution d'endommagement ϕ reste le même que [31] Pour d_1 on obtient par exemple :

$$d_1 = (1 - \phi_1) + (1 - \phi_2) + (1 - \phi_3) \tag{9}$$

Lachaud [16] a montré que le paramètre d'endommagement, d, pour les matériaux composites unidirectionnels n'atteint jamais une valeur de 1, mais il existe une limite de saturation d'endommagement pour ces matériaux surtout dans la direction transverse. Une fois que cette saturation d'endommagement est atteinte, la rupture peut arriver à n'importe quel instant sans augmentation discernable dans les dommages. Cette observation a été notamment implémentée pour le paramètre d_2, quand $d_2 > d_{max}$, d_2 est égal à 1, donc le matériau ne résistent pas au chargement dans la direction transverse. Par conséquence les paramètres d_4 et d_5 sont aussi réglé à une valeur de 1.

En se basant sur les observations expérimentales dans le paragraphe 3.2.1 et la littérature examiné [8, 25] il est proposé de coupler d_5 avec le mode de ruine r_5 car les fissures à l'intérieur du pli unidirectionnelles ne sont pas toujours perpendiculaire au plan $1-2$ du pli surtout sous le chargement d'impact bas énergie. Donc la matrice de couplage q devient :

$$q = \begin{bmatrix} 1 & 1 & 1 & 0 & 0 \\ 0 & 0 & 1 & 1 & 0 \\ 0 & 0 & 1 & 0 & 1 \\ 1 & 1 & 1 & 1 & 1 \\ 0 & 0 & 1 & 1 & \underline{\boldsymbol{\mathit{1}}} \\ 1 & 1 & 1 & 0 & 1 \end{bmatrix} \tag{10}$$

La matrice de souplesse du pli en 3D est montrée dans équation 11 pour prendre en compte les dommages hors plan.

$$C^{-1} = \begin{bmatrix} \frac{1}{(1-d_1)E_{11}^0} & \frac{-\nu_{21}}{E_{22}} & \frac{-\nu_{31}}{E_{33}} & & & \\ \frac{-\nu_{12}}{E_{11}} & \frac{1}{(1-d_2)E_{22}^0} & \frac{-\nu_{32}}{E_{33}} & & & \\ \frac{-\nu_{13}}{E_{11}} & \frac{-\nu_{23}}{E_{22}} & \frac{1}{(1-d_3)E_{33}^0} & & & \\ & & & \frac{1}{(1-d_4)G_{12}^0} & & \\ & & & & \frac{1}{(1-d_5)G_{23}^0} & \\ & & & & & \frac{1}{(1-d_6)G_{13}^0} \end{bmatrix} \tag{11}$$

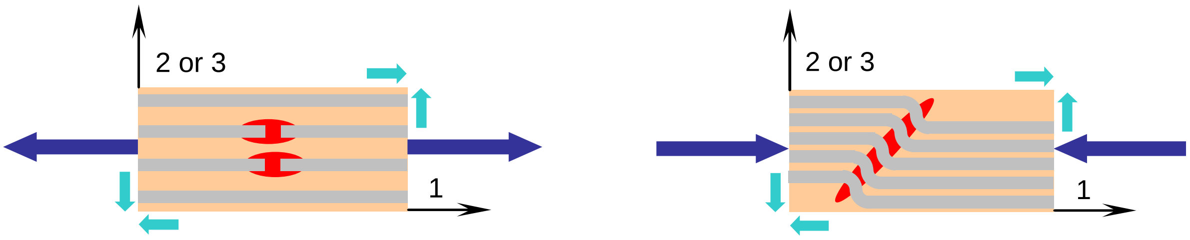

(a) Rupture en traction.

(b) Rupture en compression.

Figure 24 – Traction et compression dans la direction des fibres.

$$f_1(\sigma, d, r) = \left(\frac{\langle \sigma_{11} \rangle}{X_T}\right)^2 + \frac{\sigma_{12}^2 + \sigma_{13}^2}{S_{fs}^2} - r_1^2 = 0 \tag{12}$$

Le critère de rupture en traction est présenté dans l'équation 12. L'effet du cisaillement est pris en considération. X_T est la contrainte à rupture en traction dans la directions de fibres.

L'équation 13 décrit la rupture de fibres en compression. Ce critère prend en compte le chargement par le matériau adjacent qui exerce des tractions normales compressives dans les direction transverse et hors plan.

$$f_2(\sigma, d, r) = \left[\frac{\left\langle -\sigma_{11} + \frac{\langle -\sigma_{22} - \sigma_{33} \rangle}{2} \right\rangle}{X_C} \right]^2 - r_2^2 = 0 \tag{13}$$

ou X_C est la contrainte à rupture en compression sens fibre.

Le troisième mode de rupture représente l'écrasement du matériau comme décrit dans l'équation 14. Ce critère de rupture est utilisés pour représenter l'écrasement du matériau au dessous de l'impacteur dans un chargement de type impact.

$$f_3(\sigma, d, r) = \left[\frac{\langle -(\sigma_{11} + \sigma_{22} + \sigma_{33}) \rangle}{3Z_C} \right]^2 - r_3^2 = 0 \tag{14}$$

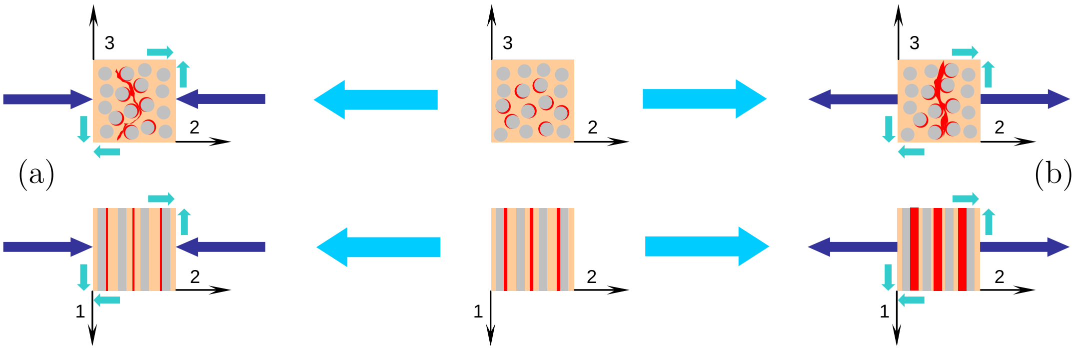

Figure 25 – (a) Compression et (b) traction dans la direction transverse.

$$\begin{aligned} f_4(\sigma, d, r) = \Bigg[& \left(\frac{\langle \sigma_{22} \rangle}{Y_T} \right)^2 + \left(\frac{\langle -\sigma_{22} \rangle}{Y_C} \right)^2 \\ & + \left(\frac{\sigma_{12}}{S_{12} + \langle -\sigma_{22} \rangle \tan\varphi} \right)^2 + \left(\frac{\sigma_{23}}{S_{23} + \langle -\sigma_{22} \rangle \tan\varphi} \right)^2 \Bigg]^2 - r_4^2 = 0 \end{aligned} \tag{15}$$

La fissuration transverse dû à σ_{22} est couplée avec le cisaillement dans le plan dû à σ_{12} et hors plan (perpendiculaire à la direction des fibres) dû à σ_{23} (figure 25). L'équation 15 a été modifiée pour prendre en compte l'effet de compression pure sens (2-)transverse. Y_T et Y_C sont les limites élastiques en traction et compression dans la direction transverse. S_{12}

et S_{23} sont les limites élastiques de cisaillement dans et hors plan. Le critère de rupture prend en compte la différence dans le comportement mécanique lier à l'ouverture ou à la fermeture des fissures. Le paramètre $\tan\varphi$ peut être considéré comme un coefficient de friction pour le matériau et intervient seulement quand le matériau est chargé en compression. Ce paramètre a une effet d'amélioration de résistance au cisaillement.

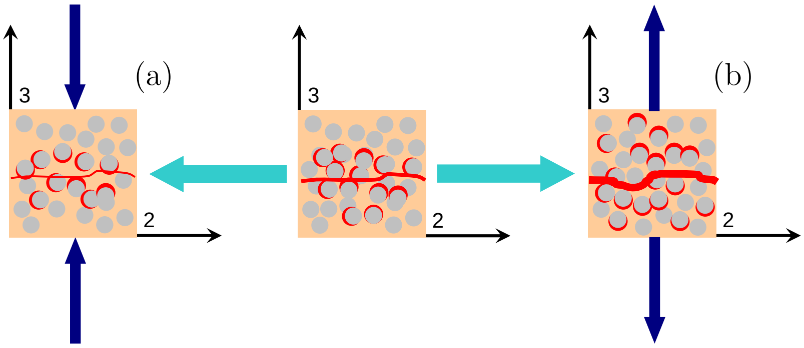

Figure 26 – (a) Compression et (b) traction hors plan.

$$f_5(\sigma,d,r) = S_{del}\left[\left(\frac{\langle\sigma_{33}\rangle}{Z_T}\right)^2 + \left(\frac{\sigma_{13}}{S_{13}+\langle-\sigma_{33}\rangle\tan\varphi}\right)^2 + \left(\frac{\sigma_{23}}{S_{23}+\langle-\sigma_{33}\rangle\tan\varphi}\right)^2\right]^2 - r_5^2 = 0 \tag{16}$$

La contrainte normale hors plan σ_{33} est couplé avec le cisaillement hors plan σ_{13} (parallèle avec direction de fibre) et le cisaillement hors plan σ_{23} (perpendiculaire à la direction de fibre), voir équation 16. Z_T est la limite élastique en (3-)direction et S_{13} est la limite élastique de cisaillement dans le plan $1-3$. Ce critère de rupture représente le délaminage. Le paramètre S_{del} donne la possibilité pour inclure l'approche non locale dépendant des contraintes des éléments adjacents pour modifier la surface délaminée. Ce paramètre n'a pas été utilisé pour l'instant.

Les jeux de données utilisé pour les simulations sont données dans les tableaux 3 et 4

Tableau 3 – Material model data for T700S/M21 simulation.

E_{11} (GPa)	E_{22} (GPa)	E_{33} (GPa)	ν_{12}	ν_{23}	ν_{13}	G_{12} (GPa)	G_{23} (GPa)	G_{13} (GPa)
135	7.69	7.69	0.34	0.4	0.34	4.75	2.75	4.75
X_T (GPa)	X_C (GPa)	Y_T (GPa)	Y_C (GPa)	Z_T (GPa)	Z_C (GPa)	S_{12} (GPa)	S_{23} (GPa)	S_{13} (GPa)
2.2	1.2	0.04	0.25	0.04	0.7	0.045	0.045	0.045
-	S_{fs} (GPa)	S_{del}	m_i	φ	d_{max}	$\mathcal{C}_1$	$\dot{\epsilon}_{ref}$ (s^{-1})	-
–	1.5	1.0	1.75	10	0.87	–	–	–

Tableau 4 – Material model data for T800S/M21 simulation.

E_{11} (GPa)	E_{22} (GPa)	E_{33} (GPa)	ν_{12}	ν_{23}	ν_{13}	G_{12} (GPa)	G_{23} (GPa)	G_{13} (GPa)
165	7.64	7.64	0.35	0.4	0.35	5.61	2.75	5.61
X_T (GPa)	X_C (GPa)	Y_T (GPa)	Y_C (GPa)	Z_T (GPa)	Z_C (GPa)	S_{12} (GPa)	S_{23} (GPa)	S_{13} (GPa)
2.2	1.2	0.045	0.28	0.045	0.7	0.05	0.05	0.05
-	S_{fs} (GPa)	S_{del}	m_i	φ	d_{max}	$\mathcal{C}_1$	$\dot{\epsilon}_{ref}$ (s^{-1})	-
–	1.5	1.0	10	10	0.87	4.7	750	–

Chapitre 4 : Essais d'impact sur éprouvette coupon

Ce chapitre présente les résultats des essais d'impact réalisés sur les plaques composites. Dans littérature on trouve que la réponse de la plaque est différente dans le cas d'impact grande masse ou faible masse à iso-énergie [2–4, 18, 26].

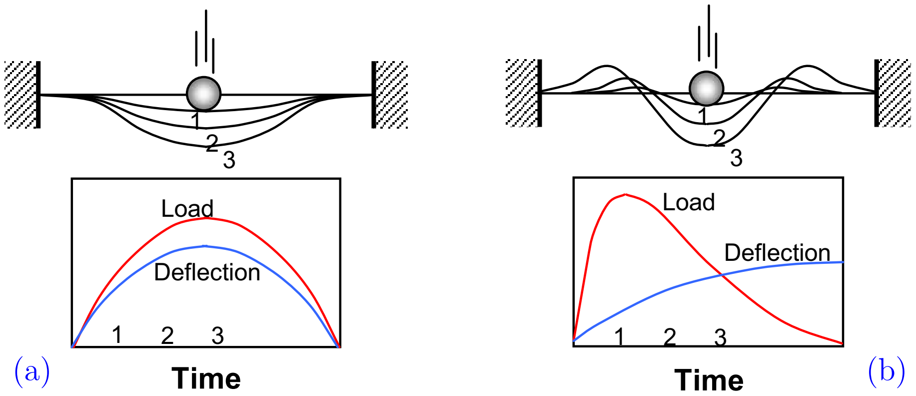

Figure 27 – Typical (a) large mass and (b) small mass impact response, [26]

Dans cette étude le comportement des éprouvettes sous les sollicitions de types différentes en masse et vitesse est étudié. Ici l'auteur décrit les essais de grande masse par tour de chute et faible masse par essais au canon. La masse de l'éprouvette utilisée dans cette étude est égale à 10 g. Dans le cas de la tour de chute, la masse de l'impacteur est $M \in \{1.213, 2.369\}$ Kg et pour les essais au canon la masse $M \in \{0.016, 0.017\}$ Kg.

Préparation de l'éprouvette

La préparation des éprouvettes est décrite en annexe-A du document en anglais. Les dimensions de l'éprouvette sont les $L = 150^{0.5}_{-0} \times b = 100^{0.5}_{-0} \times h$. Les longueurs et largeurs sont mêmes pour toutes les éprouvettes mais l'épaisseur varie en fonction du nombre de plis utilisé et des matériaux T700S/M21 ou T800S/M21.

Tableau 5 – Matériaux et séquences d'empilement.

Material	lay–up sequence
T700S/M21	$[0_2, 90_2, 0_2, 90_2]_s$
T700S/M21	$[0_2, 45_2, 90_2, -45_2]_s$
T800S/M21	$[-45, 45, 90, 90, 0]_s$
T800S/M21	$[-45, 45, 0, 90, 0, 0, -45, 45, 0]_s$
T800S/M21	$[45, -45, 90, 0, 90, 90, 45, -45, 90]_s$

Dans le cas des essais au canon, il n'est pas possible de mesurer l'effort global et le déplacement de la face non impactée de l'éprouvette. Donc, trois jauges de déformations ont été collé sur la face non impactée.

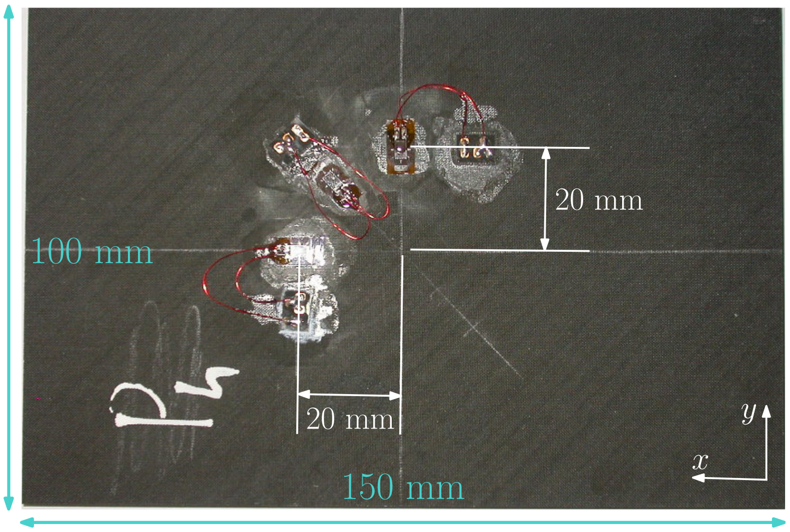

Figure 28 – Position de jauges de déformation (face non impactée).

Essais sur tour de chute

Le dispositif de tour de chute est détaillé figure 29. L'impacteur est un chariot équipé d'un capteur d'effort avec un embout hémisphérique de 16 mm.

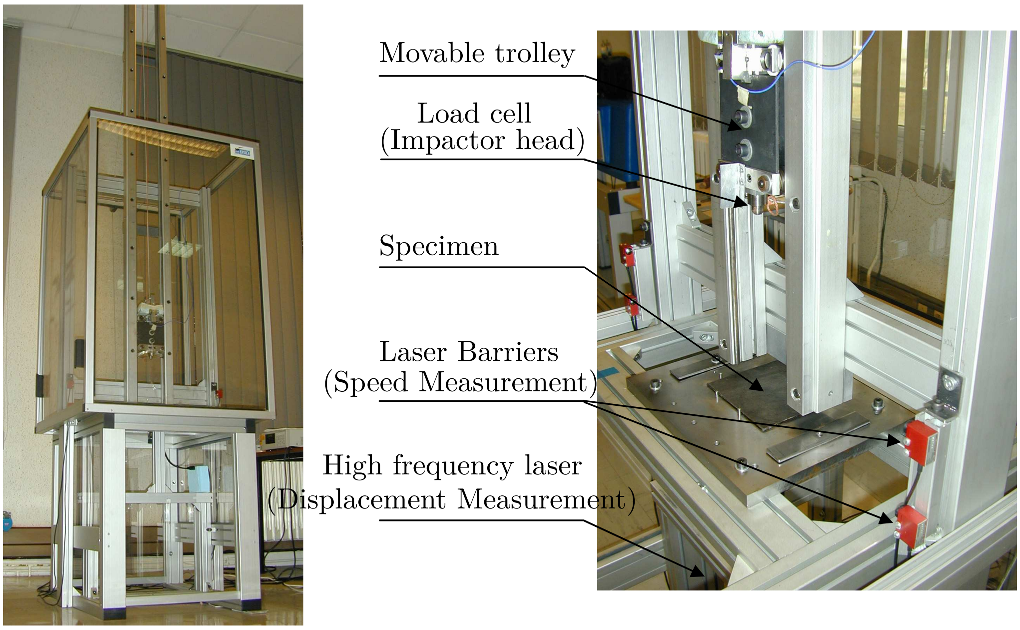

Figure 29 – Dispositif des essais grande masse faible vitesse (tour de chute).

Les éprouvettes sont placées en appui simple sur une plaque en acier 300×200 mm^2 $\times$ 20 mm^3 épaisse. Cette plaque support possède une fenêtre de 125×75 mm^2.

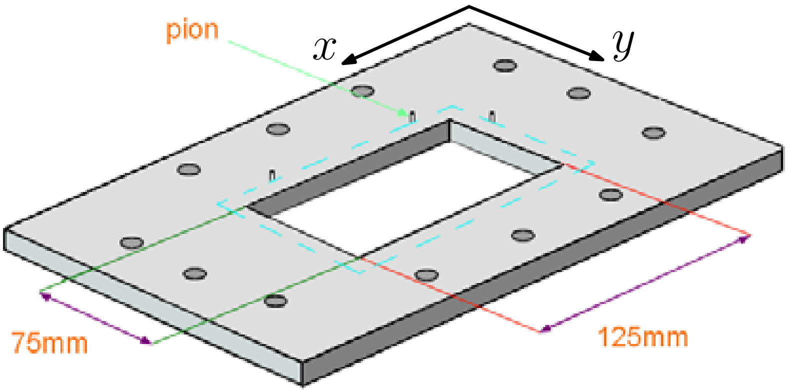

Figure 30 – Plaque de support avec une fenêtre rectangulaire.

Effort global et déplacement transitoire

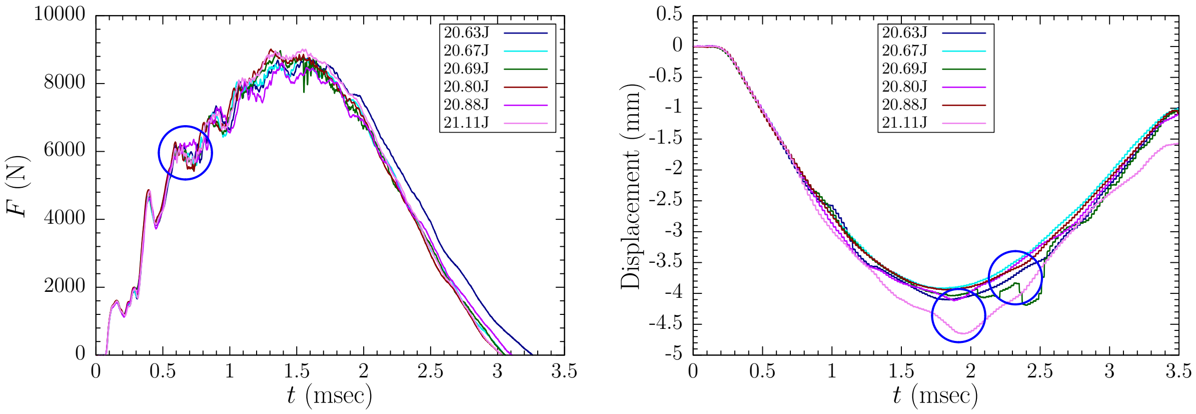

(a) Force–time response. (b) Displacement–time response.

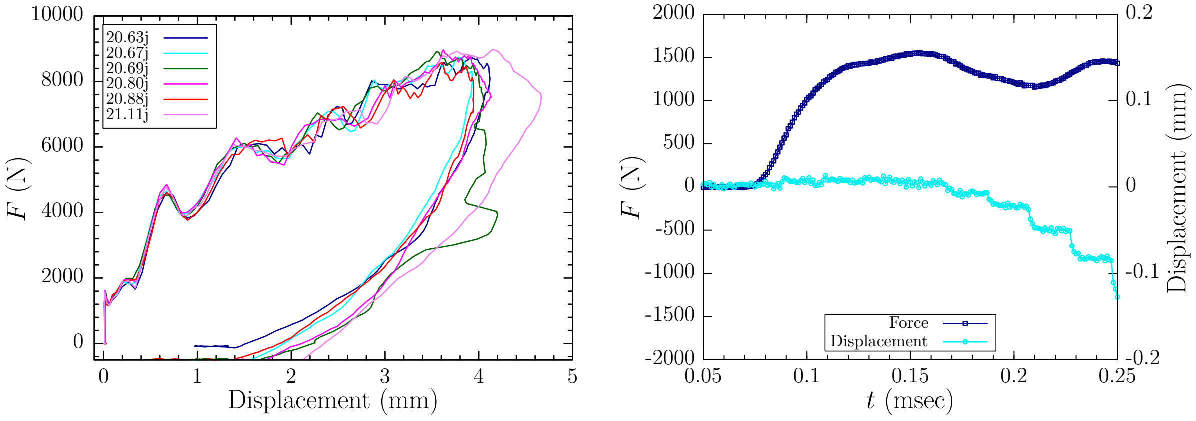

(c) Force–displacement (d) Start of force/displacement–time curves

Figure 31 – Courbes d'effort vs. déplacement, $E_{imp} \approx 20$ J sur un stratifié T800S/M21 4.5 mm épaisse.

La figure 31 montre les résultats de six essais réalisés à 20 J sur un stratifié de 4.5 mm d'épaisseur avec $[-45, 45, 0, 90, 0, 0, -45, 45, 0]_{2s}$ de T800S/M21. L'effort mesuré par le capteur d'effort augmente en fonction du temps, puis diminue après une valeur maximale. Le déplacement de la face non impactée montre un comportement similaire. L'effort maximal moyen de ces tests est 8854 N. La dispersion de l'effort maximal n'est pas significative (figure 31(a)), ce qui n'est pas le cas pour le déplacement, en fonction du temps (figure 31(b)).

Le cercle bleu, figure 31(a), indique le temps (0,5 ms après le contact) attribué à la propagation du délaminage aussi observé par divers auteurs [30, 32].

Analyses post-impact

Plusieurs examens post-impact ont été réalisés pour étudier l'impact des défauts induits. En début, les profils des indentations résiduelles (BVID) sont étudiés comme décrit dans [1]. Ensuite, des examens par ultrasons (C-Scan) et rayons X ont été réalisés pour quantifier les orientations et les tailles de délaminage. Et enfin, un examen microscopique a été réalisé pour observer les fissures matricielles et l'interaction avec le délaminage.

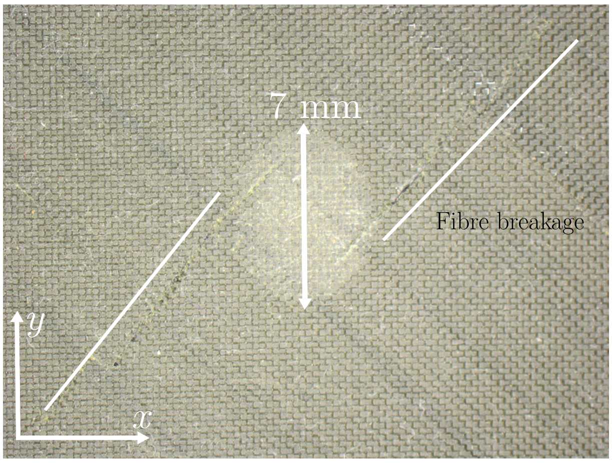

Figure 32 – Indentation résiduelle typique d'un stratifié T800S/M21, $E_{imp} \approx 20$ J.

Essais au canon

Le dispositif d'essais au canon à air comprimée est donné figure 33(a). Le projectile est illustré figure 33(c). Le projectile est une bille de diamètre 16 mm en acier.

(a) Dispositif des essais au canon à ISAE.

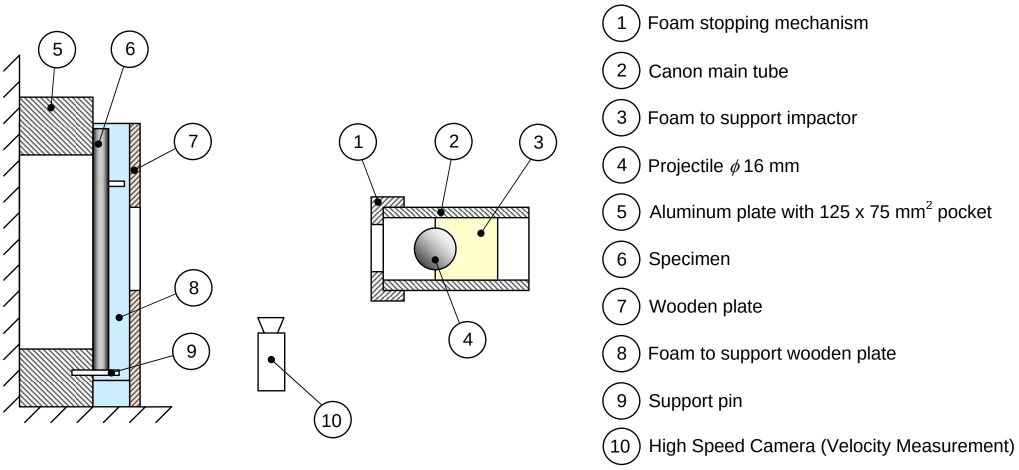

(b) Schéma représentatif du canon à air comprimé.

(c) Impactor used for canon tests.

Figure 33 – Dispositif des essais petite masse, vitesse moyen.

Signaux des jauges de déformation

Le support du dispositif d'essais au canon n'est pas équipé d'un capteur d'effort ou de mesure de déplacement. Par conséquent, des jauges de déformation ont été collées sur la face non impactée en vue d'obtenir des déformations sur des points particuliers. La figure 34 montre les résultats de certains tests au canon.

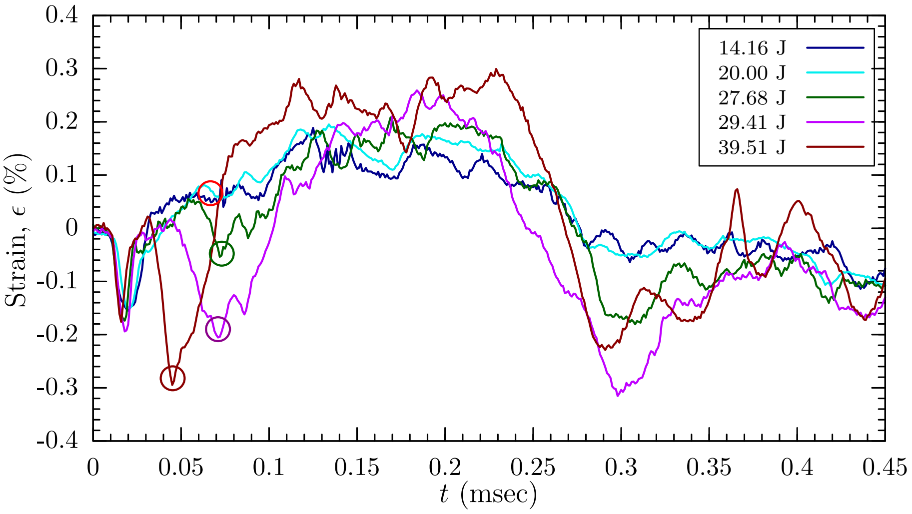

Figure 34 – Déformation (ϵ_x) de T800S/M21, $[-45, 45, 0, 90, 0, 0, -45, 45, 0]_s$, stratifié à différents énergie d'impact.

Différents points (cercles sur figure 34) montrent quelques points particuliers de ces signaux pour plus des détails, le lecteur est invité à se reporter au document en anglais.

Conclusions

Les énergies d'impact sont de 4, 8, 10, 15, 20, 30 et 100 J et les vitesses d'impact varient de 4 m/sec à 100 m/sec. Deux matériaux sont étudiés : le premier est une fibre de carbone de haute résistance (T700S/M21) avec une matrice à ténacité améliorée et fabriqué par le procédé de voie solvant, le second est un module intermédiaire (T800S/M21) où l'interface entre les couches est enrichie par des nodules de thermoplastiques (mode de fabrication hot melt). Deux types de séquences d'empilement sont utilisés, une classique appelée « quasi-isotrope » (T700S/M21) et les autres moins classiques $[\pm 45, 0, 0, 90, 90, 0, 0, \pm 45]$ qui ne respectent pas les règles d'empilement, mais développée pour des applications fuselage d'avion.

En ce qui concerne la cinétique d'initiation d'endommagement pour l'empilement quasi-isotrope, le défaut après l'impact est globalement sous forme d'un cône dans l'épaisseur et elliptique dans le plan. Il est observé que les dommages obtenus à basses énergies et faibles vitesses sont initiés par des fissures dans l'épaisseur du pli (cisaillement hors plan). Ces micro-fissures par la suite entraînent le délaminage entre les couches de différentes orientations. L'orientation du délaminage est guidée par l'angle relatif entre les plis situés de part et d'autre du délaminage. Pour ces types d'éprouvette, la présence de macro-fissures sur le côté non impacté favorise la propagation du délaminage.

En ce qui concerne les impacts à vitesse élevée, il apparaît que les défauts (délaminage) observés après l'impact pour une même énergie, ont des tailles plus petites en comparaison aux dommages observés après impact faible vitesse. La flexion due au impact sur tour de chute est plus important par rapport aux essais au canon, et par conséquent la surface délaminée est plus grande. Ces observations se retrouvent également sur la profondeur de l'indentation qui est faible après un impact à grande vitesse de sollicitation.

Chapitre 5 : Modélisation d'impact

Dans ce chapitre, les deux modèles développés, modèle bilinéaire cohésif (chapitre 2) et le modèle continu (chapitre 3), sont appliqués pour simuler l'impact sur plaques.

Les simulations utilisant la loi cohésive sont d'abord présentées, puis les simulations introduisant l'endommagement couplé. Les comparaisons essais calculs sont réalisées sur le comportement effort/déplacement–temps et sur la taille des défauts.

La dernière partie de ce chapitre présente une première étude de l'impact sur composites par l'utilisation de méthodes numériques sans maillages [17]. Dans ce cadre, des modèles numériques utilisant des Smoothed Particles Hydrodynamics (SPH) orthotrope on été développés.

Simulations numériques

Les résultats présentés dans les paragraphes suivants sont ceux pour un stratifié $[-45, 45, 0, 90, 0, 0, -45, 45, 0]_s$. Les simulations sont réalisées pour les 2 cas de charge : grand masse, faible vitesse et faible masse, grande vitesse.

Modèles éléments finis

Les modèles numériques par éléments finis sont illustrés aux figures 35(a) et 35(b). Le positionnement des couches des éléments d'interface est indiqué dans la figure 35(c). Le comportement des plis est linéaire orthotrope et le comportement des éléments d'interface est celui décrit au chapitre 2.

Dans le cas d'impact grande masse, la vitesse d'impact, $v_{imp} = 3,47$ m/sec et l'impacteur possède une masse $M = 2,369$ Kg. Afin d'être conforme au modèle physique, le projectile est libre dans les trois directions pour les impact au canon. La masse de projectile est de $0,017$ Kg et la vitesse d'impact est $40,82$ m/sec, mesurée par une caméra rapide. Le nombre des éléments finis déformables pour la simulation avec le modèle continu est de 374.400 et 665.600 pour modèle bilinéaire cohésif. Le maillage est raffiné au dessous de projectile. Les paramètres matériau utilisés pour les simulations d'endommagement

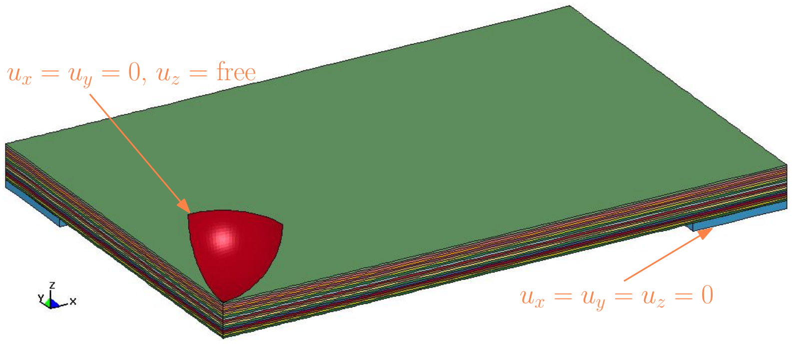

(a) Tour de chute.

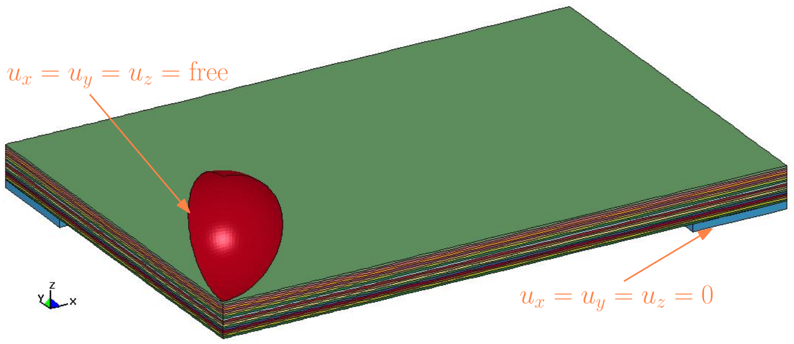

(b) Canon au gaz.

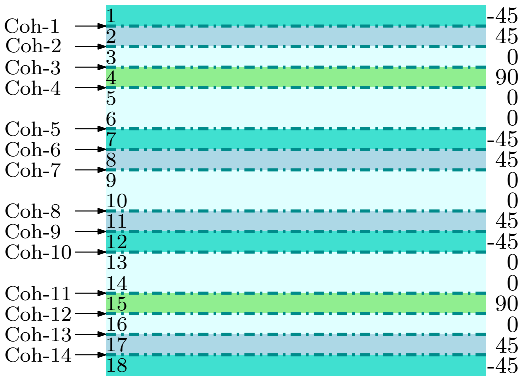

(c) Stacking sequence.

Figure 35 – Modèles éléments finis et séquence d'empilement.

continu sont présentés dans le tableau 6. Ces constantes du matériau sont essentiellement les mêmes que celles décrites dans le chapitre 3.

Comparaison : essais et simulations

Comportement global

Les résultats expérimentaux disponibles pour les comparaisons essais-calculs sont l'effort et le déplacement en fonction du temps pour les essais sur tour de chute et les signaux des jauges de déformation pour les essais au canon.

Tableau 6 – Données matériaux pour simulation d'impact sur T800S/M21.

E_{11} (GPa)	E_{22} (GPa)	E_{33} (GPa)	ν_{12}	ν_{23}	ν_{13}
165	7.64	7.64	0.35	0.4	0.35
G_{12} (GPa)	G_{23} (GPa)	G_{13} (GPa)	X_T (GPa)	X_C (GPa)	Y_T (GPa)
5.61	2.75	5.61	2.2	1.2	0.045
Y_C (GPa)	Z_T (GPa)	Z_C (GPa)	S_{12} (GPa)	S_{23} (GPa)	S_{13} (GPa)
0.28	0.045	0.7	0.05	0.05	0.05
S_{fs} (GPa)	S_{del}	m_i	φ	d_{max}	$\mathcal{C}_1$
1.5	1.0	10	10	0.87	4.7
$\dot{\epsilon}_{ref}$ (s^{-1})	$S_{12}^{dyn} = S_{23}^{dyn} = S_{13}^{dyn}$ (GPa)				
750	0.12				

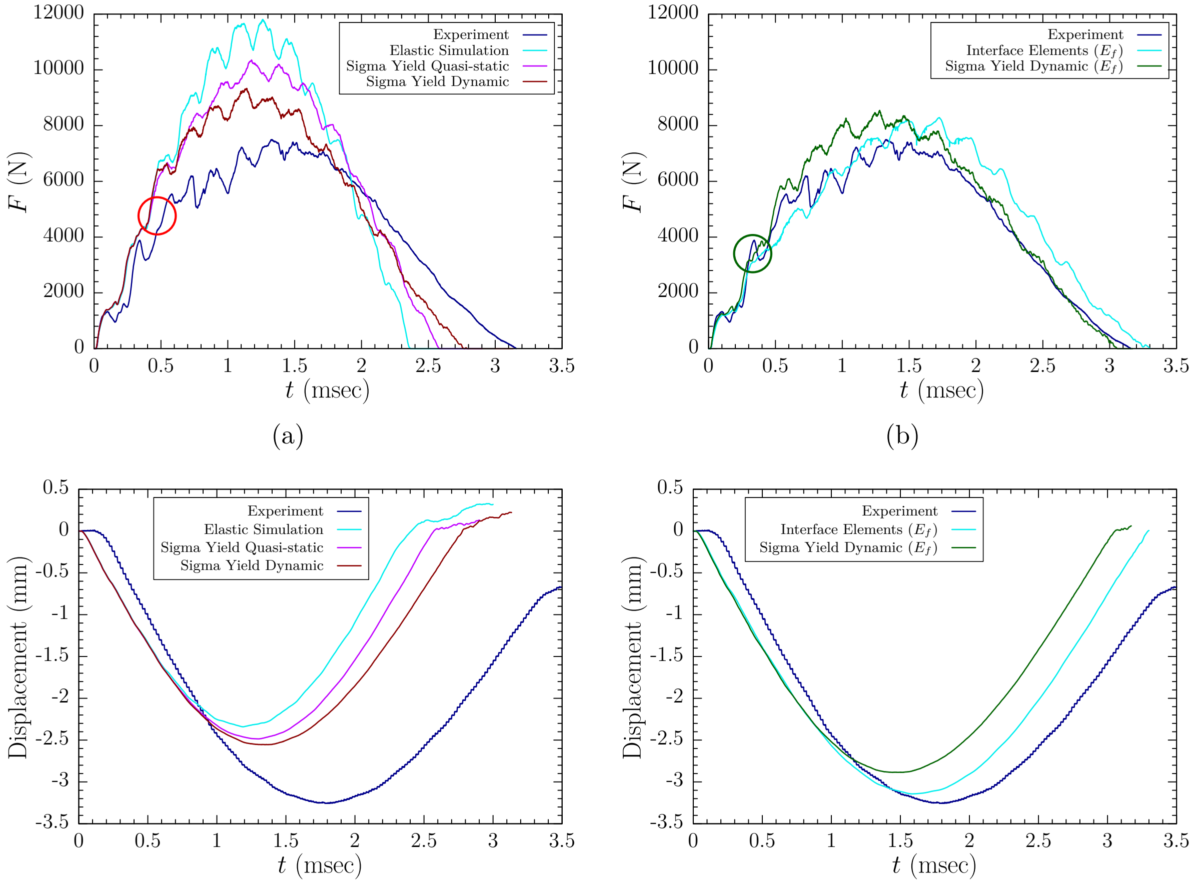

(a) (b)

(c) (d)

Figure 36 – Effort/déplacement en fonction du temps.

La figure 36 présente l'évolution de l'effort d'impact et du déplacement maximal la de face non impactée en fonction du temps. Les modèles linéaires élastiques donnent des efforts d'impact et des déplacements supérieurs. Ensuite les résultats pour les simulations introduisant une limite élastique quasi-statique (Sigma Yield Quasi-statique) et limite élastique dynamique (Sigma Yield Dynamique) sont comparés. Pour le $1^{\text{èr}}$ cas les contraintes de cisaillement S_{12}, S_{23} et S_{13} ont une valeur fixe de 50 MPa. Pour le $2^{\text{ème}}$ cas les contraintes de cisaillement ont une valeur seuil de 120 MPa et évolue en fonction de vitesse de déformation par l'introduction d'une loi logarithmique identifiée au paragraphe 3.2.2.3 du chapitre 3.

Il est observé que pour le $1^{\text{èr}}$ cas la réponse est plus rigide que pour le $2^{\text{ème}}$ (figures 36(a) et 36(c)). Il est à noter que tous les résultats numériques prédisent une plus grande rigidité initiale (figure 36(a)). De l'avis de l'auteur, le comportement à l'impact sur tour de chute est très lié à la flexion de la plaque. Pour l'instant, le modèle continu d'endommagement ne fait pas de distinction entre les modules de traction et de compression. Par conséquent, dans un premier temps le module de flexion, E_f, de 112 GPa est utilisé pour les simulations (figures 36(b) et 36(d)).

Tableau 7 – Résultats effort (N) versus temps (msec).

	Effort maximal (N) / temps (msec)	Temps de contact (msec)
Elastic Simulation	12.000 / 1,25	2,35
Sigma Yield Quasi-static	10.400 / 1,20	2,58
Sigma Yield Dynamic	9.400 / 1,15	2,75
Interface elements (E_f)	8.200 / 1,75	3,30
Sigma Yield Dynamic (E_f)	8.300 / 1,30	3,05
Experiment	7.800 / 1,32	3,15

Dans les figures 36(a), on peut voir que les simulations montrent un écart plus important dès le début de la simulation, comme souligné par un cercle rouge. D'autre part en utilisant E_f au lieu de E_{11}, la rigidité initiale de l'échantillon est mieux estimée, figure 36(b). Le changement de la rigidité dû à l'endommagement de la plaque commence à $0,7$ ms, ce qui est bien approché par le modèle continu d'endommagement (courbe de couleur vert foncé dans la figure 36(b)). Les endommagements dans le modèle éléments finis contenant des éléments d'interface arrivent plus tôt, à environ $0,4$ ms. Par rapport à toutes les simulations, le modèle continu reproduit mieux les fréquences de vibrations de la plaque. À $1,5$ msec le modèle continu d'endommagement et la courbe expérimentale possèdent le même comportement (petit plateau jusqu'à $1,75$ ms) puis une diminution presque linéaire jusqu'à 3 ms.

Le déplacement de la face non impactée est mieux approché par la simulation avec des éléments d'interface. La différence entre expérimentation et simulation peut être attribuée à l'absence de déformation permanente dans le modèle numérique.

Endommagement local et vitesse de déformation

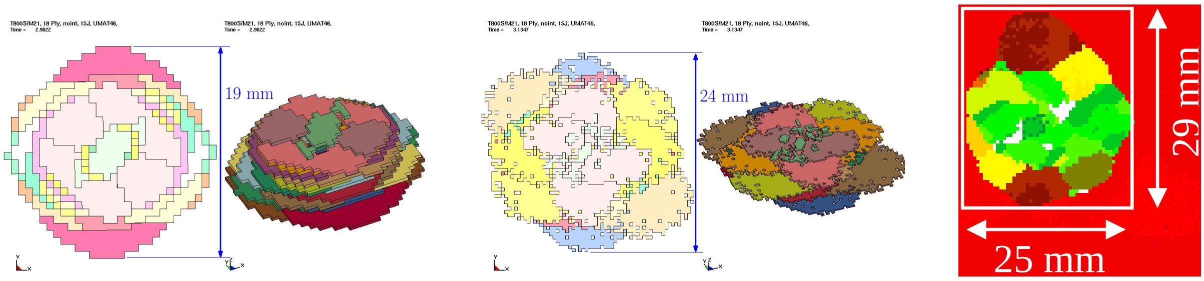

(a) Quasi-static yield stress. (b) Dynamic yield stress. (c) Image ultrasons.

Figure 37 – Eléments avec variable d'endommagement $d_4 \in \{0.87, 1.0\}$, essai sur tour de chute à 15 J.

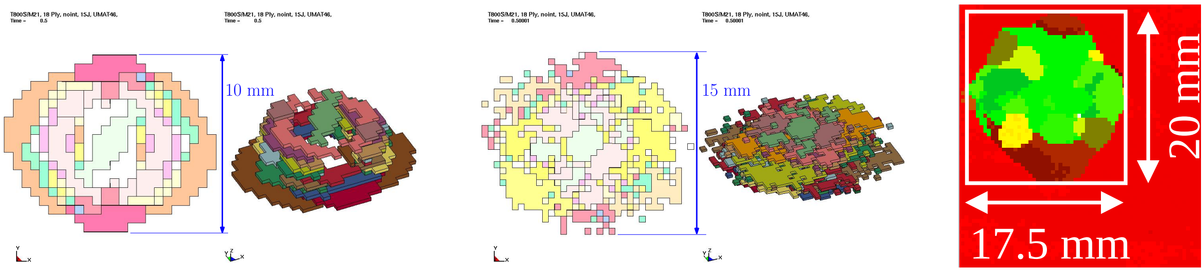

(a) Quasi-static yield stress. (b) Dynamic yield stress. (c) Image ultrasons.

Figure 38 – Eléments avec variable d'endommagement $d_4 \in \{0.87, 1.0\}$, essai au canon à 15 J.

La variable d'endommagement d_4 peut être considérée comme une variable représentant à la fois le délaminage et la fissuration matricielle. Les figures 37 et 38 comparent d_4 avec les résultats expérimentaux pour les impacts sur tour de chute et au canon. L'énergie d'impact est de 15 J. Les éléments où l'endommagement est saturé ($d_4 > d_{max}$), sont présentés sur ces deux figures. Ces deux figures montrent que la taille et l'orientation des éléments endommagés sont cohérentes avec les essais quand on utilise le modèle à effet de vitesse de déformation sur les limites élastiques.

Les résultats locaux confirment encore une fois que non seulement l'orientation mais aussi l'arrêt de la fissuration matricielle sont bien prédis par le modèle d'endommagement continu (figure 39).

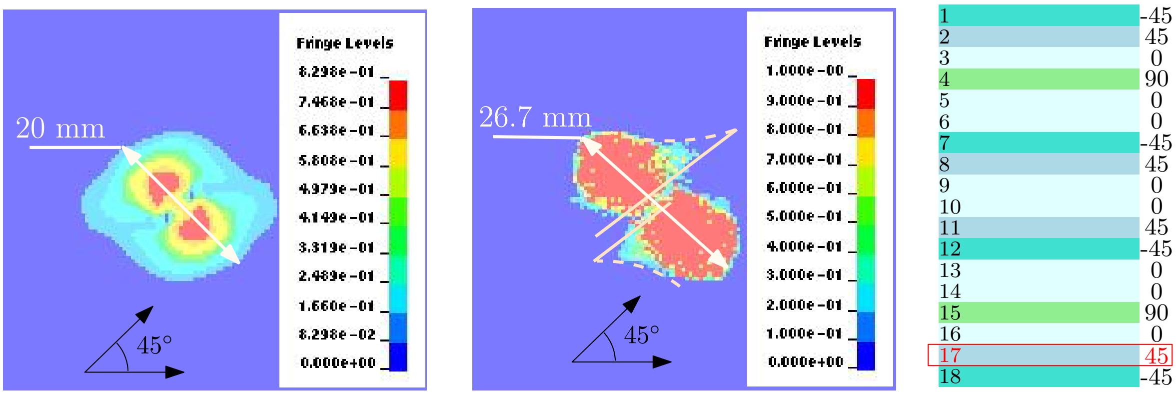

(a) d_4 (Quasi-static yield stress).   (b) d_4 (Dynamic yield stress).   (c) Lay-up sequence.

Figure 39 – Variable d'endommagement d_4 pour le pli avant dernière par rapport à face impactée.

Le tableau 8 résume la comparaison des résultats expérimentaux et numériques. On constate qu'une meilleure corrélation est obtenue en utilisant le modèle continu d'endommagement. Les simulations d'impacts à l'aide du modèle cohésif surestime la taille d'endommagement avec un écart important.

Tableau 8 – Comparaison des surfaces délaminés mesurés par essais et prédit par simulations.

Séquence d'empilement	Energie (J)	Surface délaminé (mm×mm)			Ecart int[1]		Ecart umat[2]		Ecart général	
		Interface[1]	Umat[2]	Essai	L_x	L_y	L_x	L_y	Umat	Interface
$[45, -45, 90, 0, 90, 90, 45, -45, 90]_s$	10.23[3]	30×32	24×26.5	26×20	15.4%	60%	-7.7%	32.5%	22.3%	84.6%
$[45, -45, 90, 0, 90, 90, 45, -45, 90]_s$	19.90[3]	48.8×67.6	32.5×39	38×31	28.4%	118%	-14.5%	25.8%	7.6%	180%
$[-45, 45, 0, 90, 0, 0, -45, 45, 0]_s$	9.62[3]	28×31	25×22	22×22	27.2%	4.1%	13.6%	0%	13.6%	79.3%
$[-45, 45, 0, 90, 0, 0, -45, 45, 0]_s$	14.25[3]	33.5×39	26.5×24.1	25.5×29	31.4%	34.5%	3.9%	-16.7%	-13.6%	76.7%
$[-45, 45, 0, 90, 0, 0, -45, 45, 0]_s$	20.63[3]	45.6×52	37.5×36	38×36	20%	44.4%	-1.3%	0%	-1.3%	73.3%
$[-45, 45, 0, 90, 0, 0, -45, 45, 0]_s$	29.55[3]	76.8×83	47×43	45.5×51.5	68.8%	61.2%	3.3%	-16.5%	-13.8%	172%
$[-45, 45, 0, 90, 0, 0, -45, 45, 0]_s$	14.16[4]	32.6×33.5	17.5×15	17.5×20	86.3%	67.5%	0%	-25%	-25%	67.4%
$[-45, 45, 0, 90, 0, 0, -45, 45, 0]_s$	20.00[4]	44.1×46.9	19.6×17.6	37.5×30.5	17.6%	53.8%	-47.7%	-42.3%	-69.8%	80.8%
$[-45, 45, 0, 90, 0, 0, -45, 45, 0]_s$	29.41[4]	61.3×71.8	23×19.5[5]	44.5×39.5	37.8%	81.8%	-48.3%	-50.6%	-74.5%	150%
$[-45, 45, 0, 90, 0, 0, -45, 45, 0]_s$	39.51[4]	82.2×88.3	37×25[5]	55.5×39.5	48.1%	124%	-33.3%	-36.7%	-57.8%	67.4 %
$[-45, 45, 0, 90, 0, 0, -45, 45, 0]_s$	100.0[4]	150×100[6]	114.6×82.1	145.2×83.7	×	×	-21.1%	-1.9%	-22.5%	×

---

1. Loi cohésive bilinéaire
2. Modèle continu d'endommagement
3. Tour de chute
4. Canon
5. Valeurs conservatives
6. Séparation en deux sous stratifiés

Prédiction de défaut d'indentation

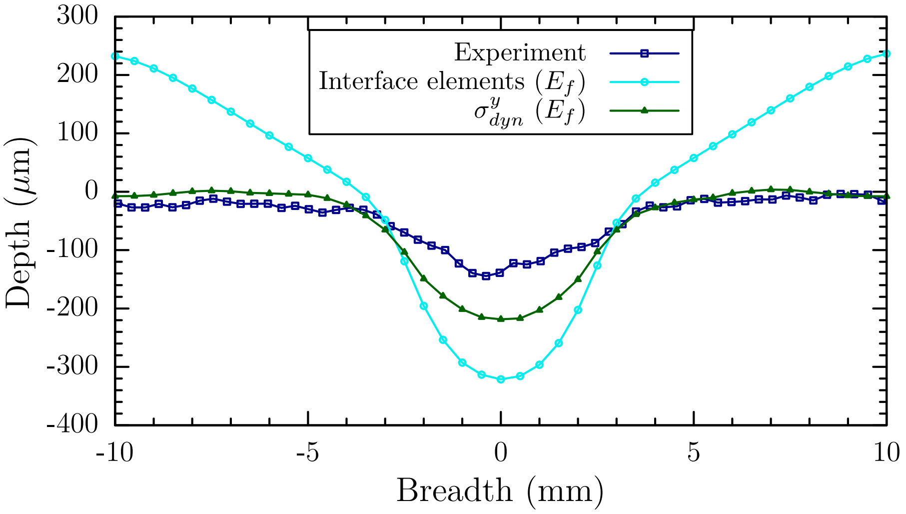

Figure 40 – Dent depth, numerical models predictions compared with experimental value, $E_{imp} = 15J$.

La figure 40 compare le profil d'indentation prédit par les deux modèles d'endommagement. On constate que l'écart entre la mesure et la simulation à l'aide du modèle continu d'endommagement est moins important qu'avec les éléments cohésifs. Le modèle continu d'endommagement ne prend pas en compte les déformation résiduelles pour l'instant. Les résultats donnés par le modèle continu sont prometteurs.

Conclusions

Les prédictions du délaminage par le modèle cohésif sont quantitativement cohérent. Qualitativement, l'écart entre les essais et la simulation est plus important. Les surfaces délaminées prédites par modèle cohésif sont toujours supérieures aux valeurs expérimentales. En ce qui concerne les interfaces ±45, pour initier l'endommagement les contraintes maximales dans ces interfaces doivent être inférieures aux contraintes maximales dans les interfaces $[0, 90]$.

Le modèle continu d'endommagement utilisant le module de flexion (E_f), au lieu de module de traction (E_{11}), et la limite élastique dynamique en cisaillement donnent des résultats cohérents pour les essais sur tour de chute. Un écart important est observé pour les simulations des essais au canon. Cette différence peut être réduite une identification plus exhaustive des effets de vitesses de déformation au delà de $1000s^{-1}$.

Parmi les perspectives une méthode sans maillage Smoothed Particle Hydrodynamics (SPH) a été testée pour explorer la faisabilité de cette méthode pour modéliser le comportement à l'impact des composites stratifiés. Les résultats obtenus sont encourageant

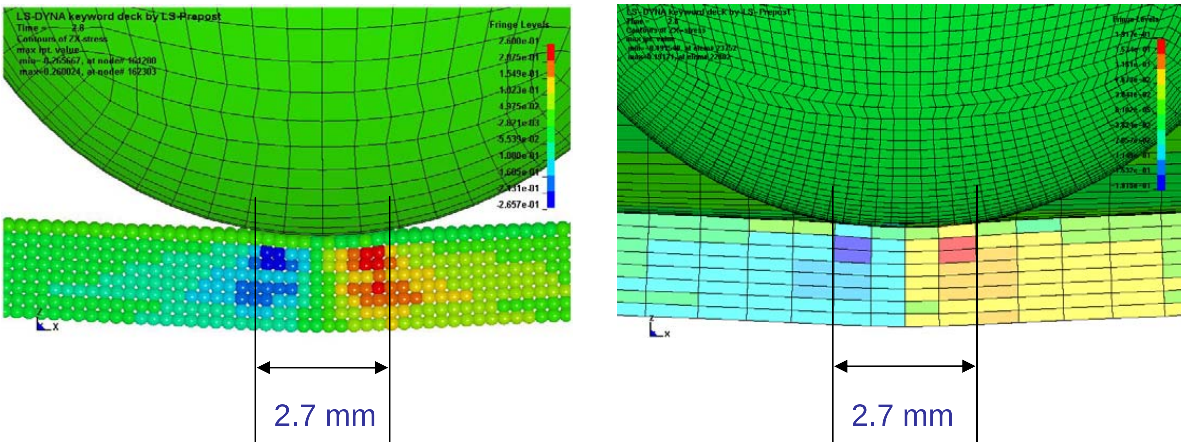

(a) Modèle numérique couplé EF–SPH. (b) Modèle numérique EF sans SPH.

Figure 41 – Surface de contact, FE et FE–SPH modèles numériques.

comme le montre la figure 41. Pour plus des détails le lecteur est invité à se reporter au document en anglais et à la référence [13].

Conclusion générale et perspectives

Afin de certifier les structures composites aéronautiques, les concepteurs ont besoin de connaître le comportement des structures lors de sollicitations normales pendant la vie des aéronefs, et de démontrer la capacité de ces structures à supporter la charge pendant une période minimale (intervalle d'inspection technique), même après l'apparition des dommages. Dans le cas particulier des impacts, il est nécessaire de comprendre le comportement des structures en matériaux composites pour des chargements différents. La détermination de l'étendue des dommages en cas de choc est une question clé.

Du point de vue scientifique, la question abordée dans cette étude est la suivante : est-il possible de prédire l'étendue des dommages internes (et la localisation) en se basant sur la mesure de l'indentation externe, la connaissance du taux et de l'intensité du chargement. Dans ce cadre, cette étude a pour but de proposer un modèle prédictif robuste capable de représenter les dommages accidentels, les effets du chargement de structures composites typiques des structures aéronautiques. Deux approches numériques ont été étudiées sur des échantillons de laboratoire : un modèle représentant les ouvertures (délaminage) et un modèle continu.

La méthodologie suivie a été de caractériser expérimentalement le comportement de composites UD T700S/M21 et T800S/M21 à plusieurs vitesses de chargement. Ensuite, des modèles numériques ont été proposés pour les deux approches numériques. Enfin, les dommages d'impact prédits numériquement sont comparés aux essais de choc. Une attention particulière est portée sur l'influence de la masse et de la vitesse de chargement sur l'étendue des dommages. Les conclusions importantes de chaque partie de cette étude sont détaillées ci-après.

L'objectif principal de la caractérisation expérimentale a été de mettre en évidence les effets de vitesse de déformation sur les contraintes seuils d'endommagement et les contraintes à ruptures mais aussi sur la propagation du délaminage. Un choix délibéré a été fait à priori pour caractériser séparément le comportement inter et intra laminaire.

Le comportement de l'interface est bien connu pour être lié au délaminage lorsque les bifurcations de fissures ne sont pas prises en compte. Le choix a été fait d'utiliser la mécanique linéaire de la rupture afin de développer une loi cohésive pour les deux matériaux utilisés. Le protocole expérimental de détermination des paramètres de la loi cohésive passe par des essais DCB, ENF et MMB. Tous les paramètres de la loi bilinéaire développée ont été identifiés. D'autre part, des essais dynamiques ont été réalisés afin de déterminer l'influence de la vitesse de sollicitations sur la propagation de délaminage, mais les montages réalisés n'ont pas permis de donner des résultats satisfaisants. Néanmoins, de l'avis de l'auteur l'utilisation d'éléments cohésifs est un choix approprié pour la modélisation de l'initiation et de la propagation des fissures. Un modèle numérique pour éléments finis cohésifs a été élaboré et mis en œuvre dans le code de calculs explicite LS-DYNA®. Une étude paramétrique a été effectuée afin de déterminer le meilleur choix des paramètres numériques ayant le moins d'influence sur le comportement mécanique. Pour les deux matériaux T700S/M21 et T800S/M21, le même type de loi a été utilisée. Pour les corrélations essais-calculs, il est nécessaire de différentier le comportement en traction sens fibres et en compression sens fibres. Dans notre cas, pour simplifier la loi le module de flexion a été utilisé. De même, les taux de restitution d'énergie critique introduits ne sont pas fonction de l'angle relatif des plis adjacents. Enfin, il est conclu que, malgré leur simplicité d'utilisation, ces modèles ne sont pour l'instant pas très prédictifs ni robustes.

Pour identifier le comportement inter laminaire, des matériaux utilisés, des essais quasi-statiques et dynamiques ont été effectués pour plusieurs stratifications de type $[\pm\theta]_{3s}$, θ variant de 0 à 90 par pas de 15°. En quasi-statique le comportement des matériaux T700S/M21 et T800S/M21 pour la stratification $[\pm 45]_{3s}$ en traction, est très différent : 50 MPa représente un niveau de contrainte seuil de saturation pour le matériau T800/M21 alors que cette saturation n'est pas relevée sur le matériau T700/M21. Il est suggéré que ce phénomène est dû à l'importance de nodules de thermoplastiques à l'interface entre les plis pour le matériau T800/M21.

Dans les essais dynamiques, trois valeurs globales sont proposées pour caractériser le comportement à la rupture : le module d'élasticité, la limite élastique et une contrainte de rupture maximale. Quelle que soit l'angle étudié, la limite d'élasticité globale et la contrainte à rupture dynamique sont toujours 30% à 50% supérieures aux valeurs quasi-statiques. On suppose que ces deux contraintes sont les propriétés de plis. Les valeurs dynamiques du module d'élastique global sont par contre plus faibles que celles obtenues en quasi-statique pour des angles inférieurs à 45°. Au-delà de cet angle critique, les modules élastiques et dynamiques sont du même ordre de grandeur quelque soit la vitesse de déformation et restent à peu près constante.

Pour étudier l'effet des taux de déformation sur le comportement des plis de T800S/M21, des essais dynamiques au banc d'essais d'Hopkinson ont été réalisés sur des stratifiés $[\pm 45]_{3s}$. Les résultats présentés ont permis de conclure que les effets de vitesse de déformation sur la limite d'élasticité sont importants lorsque la vitesse de déformation dépasse $750/s$. L'évolution identifiée est une évolution de type exponentielle. Pour des vitesses de déformation comprises entre $200/s$ et $750/s$, la limite d'élasticité quasiment constante.

La loi de comportement proposé pour modéliser le comportement des matériaux étudiés est basée sur mécanique de l'endommagement des milieux continus. Ce modèle prend en compte les effets de vitesse de déformation sur les contraintes seuils d'endommagement et les variables d'endommagement sont déterminées par des critères de rupture couplés. Ces critères de rupture ont été identifiés à partir d'études bibliographiques et des modifications importantes ont été proposées sur la base des observations expérimentales pour caractériser les matériaux dans diverses directions de chargement et pour les gammes de sollicitation étudiées. Conforme avec les données expérimentales, la saturation des dommages a été introduite dans le modèle. Les effets de vitesses de déformation sur les seuils d'endommagement ont été implémentés. De nouveaux termes de couplage entre les endommagements ont été introduits. Le modèle matériau a ensuite été utilisé pour prédire les essais sur le banc d'essais d'Hopkinson. Les données quasi-statiques matériau ont été relevé par une campagne d'essais.

Deux types de configurations d'essais de choc ont été utilisés pour l'étude expérimentale L'objectif de cette étude expérimentale a été de déterminer les dommages générés lors de chocs à basse vitesse / grande masse (tour de chute), et moyenne vitesse / petite masse (Canon à air comprimé). Les énergies d'impact ont été 4 J à 100 J et les vitesses d'impact varient de 4 m/s à 100 m/s. Pour chaque type d'essais, les défauts ont été relevés par Ultra-sons, RX et observation au MEB. La cinétique d'endommagement lors d'impact a été identifiée. De manière globale, les défauts créés lors des essais au canon possèdent des dimensions plus faibles que ceux observés sur la tour de chute.

Deux types d'effets induits approches de modélisation des dommages ont été étudiées. La première approche a été la loi des dommages et solidaire dans laquelle le dommage a été considéré comme localisé dans l'interface et la seconde approche a été par les dégâts continuum projet de loi mécanique des matériaux où les dommages ont été considérées comme distribuées de façon continue dans la nappe et l'interface. En cas de simulations de l'impact avec le modèle de dommages cohérente, les résultats qualitatifs ont été satisfaisants. Il a été observé que les paramètres bilinéaire cohésion nécessaire pour engager des dommages dans (±45 interfaces) devait être différente de [0/90] interfaces afin d'atteindre ces résultats qualitatifs. Quantitativement, la différence, par rapport aux valeurs expérimentales, est un exemple plus côté au-dessus de 50%. Le modèle d'endommagement de cohésion au cours prédit la taille délaminage. De l'avis de l'auteur, il est important de prendre en compte les effets de vitesse de déformation et de dommages à l'intérieur avion plis.

Les modélisations numériques introduisant la loi de comportement du modèle continu ont donnés des résultats très satisfaisants en termes de prévision du comportement global (force-temps, déplacement-temps) mais aussi en termes de prévision de la taille des défauts (délaminage). Le modèle d'endommagement continuum a également montré des résultats prometteurs en termes de prédiction de l'indentation. Il a également été démontré que les effets de la vitesse de déformation sont importants pour une meilleure corrélation des surfaces délaminées avec relevés expérimentaux pour les deux types d'expérimentation. La prédiction de l'indentation peut encore être améliorée par l'introduction du comportement plastique des plis.

Enfin, une nouvelle méthode numérique sans maillage a été proposée pour modéliser la tenue à l'impact des composites stratifiés. La méthode SPH développée en orthotrope a été utilisée pour la modélisation en linéaire matériau d'impacts basse vitesse. L'analyse des contraintes le long d'une section transversale des plaques impactées a permis la prédiction qualitative de l'apparition de fissure. Des contraintes techniques (difficultés d'implémentation de la loi d'endommagement développée dans la partie numérique SPH du code de calculs utilisé) ont limité le couplage du modèle d'endommagement avec la méthode SPH. Par conséquent, l'apparence « naturelle » du couplage entre la méthode SPH et les dommages mécanique des matériaux reste à faire.

Perspectives :

Plusieurs possibilités peuvent être envisagées pour poursuivre cette étude.

La partie expérimentale concernant l'étude de l'influence de la vitesse de sollicitation sur la propagation du délaminage doit être améliorée. Ceci passe par la modification du banc d'essais d'Hopkinson. L'instrumentation doit être plus poussée et doit prévoir l'enregistrement de la propagation du délaminage par caméra rapide. La loi cohésive doit prendre en compte les effets de vitesse de déformation.

De même, une configuration du banc d'Hopkinson en traction est nécessaire pour identifier la vitesse de déformation en traction. Une étude détaillée doit alors être effectuée pour améliorer la compréhension et la corrélation des stratifiés $[\pm\theta]$. Les paramètres du modèle développé doivent être caractérisés pour une plus grande plage de vitesse de déformation. Enfin, le couplage de l'endommagement avec la pseudo plasticité dans le modèle doit permettre une meilleure prévision de l'indentation résiduelle.

Concernant les essais au canon, l'instrumentation du banc d'essais doit être amélioré (mesure de l'effort et du déplacement des échantillons impactés) afin d'améliorer la comparaison essais-calculs. Enfin le modèle d'endommagement développé doit être couplé à la méthode SPH afin de permettre la représentation de la rupture.

Bibliographie

[1] Aboissiere, J. (2003). *Propagation de dommages d'impact dans un materiau compoiste stratifié a fibres de carbonne et résine époxyde.* PhD thesis, Ecole Nationale Supérieure d'Ingénieurs de Constructions Aéronautiques, Département Génie Mécanique, 1, Place Emile Blouin - 31056 Toulouse Cedex 5.

[2] Abrate, S. (1991). Impact on laminated composite materials. *Applied Mechanics Reviews*, 44 :155–190.

[3] Abrate, S. (1994). Impact on laminated composites : Recent advances. *Applied Mechanics Reviews*, 47 :517–544.

[4] Abrate, S. (2001). Modeling of impacts on composite structures. *Composite Structures*, 51 :129–138.

[5] Al-Maghribi, A. (2008). *Comportement des matériaux composites à fibres courtes : Application à l'impact basse vitesse.* PhD thesis, Institut Supérieure de l'Aéronautique et de l'Espace, Département de Mécanique des Structures et Matériaux, 10 Avenue Edouard Belin, 31055 Toulouse Cedex 04.

[6] Allix, O., Ladevèze, P., and Corigliano, A. (1995). Damage analysis of interlaminar fracture specimens. *Composite Structures*, 31 :61–74.

[7] Camanho, P. P., Dávila, C. G., and De Moura, M. F. (2003). Numerical simulation of mixed-mode progressive delamination in composite materials. *Journal of Composite Materials*, 37 :1415–1438.

[8] Espinosa, C. and Collombet, F. (1991). Impact de plaques composites : caractérisation et modèles. *Journal de Physique III*, pages 1953–1968.

[9] Gohorianu, G. (2008). *Influence des défauts de perçage sur la tenue en matage des stratifiés carbone/epoxy.* PhD thesis, Institut Supérieur de l'Aéronautique et de l'Espace, 1, Place Emile Blouin - 31056 TOULOUSE Cedex.

[10] Hancox, N. L. (2000). *Impact Behavior of Fibre-reinforced Composite Materials and Structures*, chapter An overview of the impact behaviour of fibre-reinforced composites, pages 1–32. Woodhead Publishing.

[11] Ilyas, M., Espinosa, C., Lachaud, F., and Salaün, M. (2009a). Dynamic delamination modeling using cohesive finite elements. In *9th International Conference on the Mechanical and Physical Behaviour of Matrerials under Dynamic Loading*, pages 1567–1573. DYMAT2009, EDP Sciences.

[12] Ilyas, M., Lachaud, F., Espinosa, C., and Salaün, M. (2009b). Dynamic delamination of aeronautic structural composites by using cohesive finite elements. In *17th International Conference on Composite Materials*. ICCM-17, IOM3.

[13] Ilyas, M., Limido, J., Lachaud, F., Espinosa, C., and Salaün, M. (2009c). Modélisation SPH 3D de l'impact basse vitesse sur plaque composite. In *19ème Congrès Français de Mécanique*. CFM-19.

[14] ISO–15024 (2001). *Fiber-reinforced plastic composites - Determination of Mode I interlaminar fracture toughness, G_{IC}, for unidirectionally reinforced materails*. International Organization for Standardization.

[15] Jacquet, E. (2003). Etude numérique de l'endommagement induit par l'impact de débris sur des structures composites. Master's thesis, Ecole Nationale Supérieure d'Ingénieurs de Constructions Aéronautiques.

[16] Lachaud, F. (1997). *Délaminage de matériaux composites à fibres de carbonne et à matrice organiques : étude numérique et expérimental, suivi par emission acoustique*. PhD thesis, Ecole Nationale Supérieur d'Ingénieurs de Constructions Aéronautique, 1, Place Emile Blouin - 31056 TOULOUSE Cedex.

[17] Liu, G. R. and Liu, M. B. (2003). *Smoothed Particle Hydrodynamics – A Meshfree Particle Method*. World Scientific Publishing Co.

[18] López-Puente, J., Zaera, R., and Navarro, C. (2002). The effect of low temperatures on the intermediate and high velocity impact response of CFRPs. *Composites : Part B*, 33 :559–566.

[19] LSTC (2007). *LS-Dyna Keyword Manual*. Livermore Software Technology Corporation.

[20] Maikuma, H., Gillespie, Jr, J. W., and Wilkins, D. J. (1990). Mode II interlaminar fracture of the center notch flexural specimen under impact loading. *Journal of Composite Materials*, 24 :124–149.

[21] Matzenmiller, A., Lubliner, J., and Taylor, R. L. (1995). A constitutive model for anisotropic damage in fiber-composites. *Mechanics of Materials*, 20(2) :125–152.

[22] Medina, D. F. and Chen, J. K. (2000). Three-dimensional simulations of impact induced damage in composite structures using the parallelized SPH method. *Composites : Part A*, 31 :853–860.

[23] Mi, Y., Crisfield, M., and Davies, G. (1998). Progressive delamination using interface elements. *Journal of Composite Materials*, 32 :1246–1272.

[24] Michel, Y. (2007). *Phenomene d'impact à haute vitesse sur cibles minces fragiles - Application au projet de laser megajoule et à la problematique des debris spatiaux*. PhD thesis, Université de Toulouse III - Paul Sabatier.

[25] Mitrevski, T., Marshall, I. H., and Thomson, R. (2006). The influence of impactor shape on the damage to composite laminates. *Composite Structures*, 76 :116–122.

[26] Olsson, R. (2003). Closed form prediction of peak load and delamination onset under small mass impact. *Composite Structures*, 59 :341–349.

[27] Pinho, S. T., Iannucci, L., and Robinson, P. (2006). Formulation and implementation of decohesion elements in an explicite finite element code. *Composites : Part A*, 37 :778–789.

[28] Prombut, P. (2007). *Caracterisation de la propagation de delaminage des stratifiés composites multidirectionnels.* PhD thesis, Ecole Nationale Supérieur d'Ingénieurs de Constructions Aéronautique, 1, Place Emile Blouin - 31056 TOULOUSE Cedex.

[29] Rouchon, J. (2006). Certification of aircraft composite structures. EUROSAE Formation Continue.

[30] Sjöblom, P. O., Hartness, J. T., and Cordell, T. M. (1988). On low-velocity impact testing of composite materials. *Journal of Composite Materials*, 22(1) :30–52.

[31] Xiao, J. R., Gama, B. A., and Gillespie Jr, J. W. (2007). Progressive damage and delamination in plain weave S-2 glass/SC-15 composites under quasi-static punch-shear loading. *Composite Structures*, 78 :182–196.

[32] Zhang, Y., Zhu, P., and Lai, X. (2006). Finite element analysis of low-velocity impact damage in composite laminated plates. *Materials and Design*, 27 :513–519.